



**HAL**  
open science

# Study and diagnostic of the physicochemical properties of new $\pi$ -conjugated (metallo)supramolecular architectures for nonlinear optics

Karolina Waszkowska

► **To cite this version:**

Karolina Waszkowska. Study and diagnostic of the physicochemical properties of new  $\pi$ -conjugated (metallo)supramolecular architectures for nonlinear optics. Mathematical Physics [math-ph]. Université d'Angers, 2021. English. NNT : 2021ANGE0070 . tel-03881069

**HAL Id: tel-03881069**

**<https://theses.hal.science/tel-03881069v1>**

Submitted on 1 Dec 2022

**HAL** is a multi-disciplinary open access archive for the deposit and dissemination of scientific research documents, whether they are published or not. The documents may come from teaching and research institutions in France or abroad, or from public or private research centers.

L'archive ouverte pluridisciplinaire **HAL**, est destinée au dépôt et à la diffusion de documents scientifiques de niveau recherche, publiés ou non, émanant des établissements d'enseignement et de recherche français ou étrangers, des laboratoires publics ou privés.

# THESE DE DOCTORAT DE

L'UNIVERSITE D'ANGERS

ECOLE DOCTORALE N° 596

*Matière, Molécules, Matériaux*

Spécialité : *Physique*

Par

**Karolina Waszkowska**

**Study and diagnostic of the physicochemical properties of new  $\pi$ -conjugated (metallo)supramolecular architectures for nonlinear optics**

Thèse présentée et soutenue à Angers, le 25 Novembre 2021

Unité de recherche : Laboratoire MOLTECH-Anjou, UMR CNRS 6200

Thèse N° :

## Rapporteurs avant soutenance :

Isabelle Ledoux-Rak  
Dobrosława Kasprowicz

Professeur, ENS Paris-Saclay, Gif-sur-Yvette, France  
Professeur, Poznań University of Technology, Poznań, Poland

## Composition du Jury :

Examineurs : Anna Zawadzka  
Konstantinos Iliopoulos

Abdelkrim El-Ghayoury  
Adam Szukalski

Professeur, Nicolaus Copernicus University, Toruń, Poland  
Maître de conférences (HDR), Institut Fresnel Marseille, Marseille, France  
Maître de conférences (HDR), Université d'Angers, Angers, France  
Maître de conférences, Wrocław University of Science and Technology, Wrocław, Poland  
Professeur, Université d'Angers, Angers, France

Dir. de thèse : Bouchta Sahraoui



**L'auteur du présent document vous autorise à le partager, reproduire, distribuer et communiquer selon les conditions suivantes :**



- Vous devez le citer en l'attribuant de la manière indiquée par l'auteur (mais pas d'une manière qui suggérerait qu'il approuve votre utilisation de l'œuvre).
- Vous n'avez pas le droit d'utiliser ce document à des fins commerciales.
- Vous n'avez pas le droit de le modifier, de le transformer ou de l'adapter.

**Consulter la licence creative commons complète en français :**  
**<http://creativecommons.org/licences/by-nc-nd/2.0/fr/>**

## ACKNOWLEDGEMENTS

I would like to extend my sincere thanks to the director of my doctoral thesis, Prof. Bouchta Sahraoui, for his invaluable help in the implementation of doctoral research and valuable comments during the 4 years of doctorate.

I am also grateful all the PhD students and the team of the MOLTECH-Anjou laboratory, with whom I had the opportunity to work in a good and pleasant atmosphere, in particular Dr. Abdelkrim El-Ghayoury and Dr. Yohan Cheret for the synthesis of chemical compounds, Prof. Denis Gindre and Mr. Theo Travers for SHG Imaging measurements, Dr. Dominique Guichaoua and Dr. Christophe Cassagne for each technical assistance, as well as directors of laboratories.

I must thank Prof. Ali Trabolsi from New York University Abu Dhabi, United Arab Emirates, and the team of the University of Strasbourg for the synthesis of modified pyrene-based chemical complexes.

Furthermore, thanks should also go to Dr. Oksana Krupka and her team from the Taras Shevchenko University of Kiev, Ukraine, for all help in the field of chemistry.

I am extremely grateful to Prof. Anna Zawadzka, Dr. Przemysław Płóciennik and Mr. Andrzej Korcala from Nicolaus Copernicus University in Toruń, Poland, for the opportunity to provide the research included in this doctoral thesis, as well as Dr. Janusz Strzelecki for any help in AFM research.

I would like particularly thank to Prof. Anna Migalska-Zalas from Jan Długosz University in Częstochowa, Poland, for help in quantum chemical calculations for nonlinear optics.

Many thanks also to Prof. Andriy Kityk and his team from Częstochowa University of Technology, Poland, for the opportunity to conduct additional experimental research as part of the IMAGE project.

I would also like to extend my gratitude to Dr. Konstantinos Iliopoulos from Aix-Marseille University, Institute Fresnel Marseille, France, for a great help in understanding the Z-scan method.

Moreover, I am also grateful Dr. Petra Göring and Mrs. Monika Lelonek and the entire SmartMembranes team in Halle, Germany, and Prof. Patrick Huber and his team from University of Hamburg, Germany, for introducing to the science of nanoporous membranes.

Special thanks to all my friends, my family, for their support and patience during the realization of my doctoral dissertation.

The presented results in this doctoral thesis are part of a project that has received funding from European Union's Horizon 2020 research and innovation program under Marie Skłodowska-Curie grant agreement No 778156, as well as was supported by the European Cooperation in Science and Technology through COST Action MP1403 Nanoscale Quantum Optics. Experimentation presented in this manuscript was done using Interdisciplinary Centre for Modern Technologies facilities, NCU, Toruń, Poland. Calculations have been carried out in



# OUTLINE

<b>INTRODUCTION</b> .....	<b>1</b>
<b>CHAPTER 1: NONLINEAR OPTICS</b> .....	<b>7</b>
1.1 Wave Description .....	7
1.2 Second Harmonic Generation .....	11
1.3 Second-order Nonlinear Optical Susceptibility Tensor $\chi^{(2)}$ .....	15
1.4 Third Harmonic Generation .....	18
1.5 Third-order Nonlinear Optical Susceptibility Tensor $\chi^{(3)}$ .....	20
1.6 Nonlinear Absorption .....	25
1.7 Nonlinear Refractive Index .....	30
1.8 Applications .....	32
Literature .....	35
<b>CHAPTER 2: SUPRAMOLECULAR CHEMISTRY</b> .....	<b>40</b>
2.1 History of Supramolecular Chemistry .....	40
2.2 Main Concepts .....	40
2.3 Applications .....	49
2.4 Supramolecular Systems .....	50
2.4.1 Crown Ethers .....	50
2.4.2 Cryptands .....	51
2.4.3 Cyclophanes .....	52
2.4.4 Cyclodextrins .....	53
2.4.5 Rotaxanes .....	54
2.4.6 Fullerenes .....	55
2.4.7 Peptides, Proteins and Helicates .....	56
2.4.8 Metal Organic Frameworks .....	59
2.4.9 Porphyrins .....	61
Literature .....	62

<b>CHAPTER 3: THIN FILMS PHYSICS .....</b>	<b>78</b>
3.1 Luminescence .....	78
3.2 Electronic Properties of Materials .....	81
3.3 Thin Film Structures .....	83
3.4 Spin Coating .....	86
3.5 Physical Vapor Deposition .....	87
3.6 Pulsed Laser Deposition .....	91
Literature .....	92
<b>CHAPTER 4: EXPERIMENTAL TECHNIQUES .....</b>	<b>94</b>
4.1 Theoretical Models .....	94
4.1.1 Lee .....	94
4.1.2 Kurtz – Perry .....	95
4.1.3 Herman – Hayden .....	95
4.1.4 Kubodera – Kobayashi .....	99
4.1.5 Reintjes .....	100
4.1.6 Kajzar – Messier .....	104
4.2 SHG/THG Experiments .....	109
4.3 Corona Poling .....	112
4.4 Z-scan Technique .....	114
4.4.1 Closed Aperture Z-scan .....	116
4.4.2 Open Aperture Z-scan .....	118
4.4.3 Divided Z-scan .....	119
4.5 Spectroscopy Characterization .....	120
4.6 Atomic Force Microscopy .....	122
4.7 Ellipsometry .....	127
Literature .....	130
<b>CHAPTER 5: PORPHYRIN COMPLEXES .....</b>	<b>134</b>
5.1 Sample Preparation .....	134



5.2	Surface Characterization .....	135
5.3	Spectroscopic Studies .....	138
5.4	Second Harmonic Generation .....	143
5.5	Third Harmonic Generation .....	147
5.6	Z-Scan Results .....	150
5.7	Conclusions .....	155
	Literature .....	156
<b>CHAPTER 6: TRIPLE STRANDED HELICATES .....</b>		<b>158</b>
6.1	Sample Preparation .....	158
6.2	Surface Characterization .....	159
6.3	Spectroscopic Studies .....	162
6.4	Second Harmonic Generation .....	166
6.5	Third Harmonic Generation .....	170
6.6	Z-Scan Results .....	173
6.7	Quantum Chemical Calculations .....	177
6.8	Conclusions .....	183
	Literature .....	185
<b>CHAPTER 7: MODIFIED PYRENE-BASED COMPLEXES .....</b>		<b>187</b>
7.1	Sample Preparation .....	187
7.2	Surface Characterization .....	188
7.3	Spectroscopic Studies .....	192
7.4	Second Harmonic Generation .....	197
7.5	Third Harmonic Generation .....	202
7.6	Z-Scan Results .....	207
7.7	Conclusions .....	211
	Literature .....	212
<b>CHAPTER 8: NANOPOROUS MEMBRANES .....</b>		<b>214</b>
8.1	Nanoporous Membranes versus Thin Films .....	214

8.2	Samples Preparation .....	216
8.3	Porphyrin Complex Nanocomposite .....	218
8.4	Triple Stranded Helicate Nanocomposite .....	220
8.5	Modified Pyrene-Based Complex Nanocomposite .....	221
8.6	SHG Imaging .....	224
8.7	Conclusions .....	226
	Literature .....	227
	<b>SUMMARY .....</b>	<b>229</b>
	<b>LIST OF SYMBOLS .....</b>	<b>234</b>
	<b>LIST OF FIGURES .....</b>	<b>238</b>
	<b>LIST OF TABLES .....</b>	<b>251</b>
	<b>LIST OF PUBLICATIONS .....</b>	<b>254</b>
	<b>LIST OF COMMUNICATIONS .....</b>	<b>257</b>
	<b>LIST OF POSTERS .....</b>	<b>260</b>

## INTRODUCTION

With the construction of the first laser in 1960, the opportunities to observe new properties in materials appeared. A year later, the generation of the second harmonic was observed, it was the first discovery of nonlinear optics [1]. Nonlinear phenomenon appears in the case when applying high radiation power, the response of the medium, for example electric polarization, is a nonlinear field function. Usually, second and third order nonlinear effects are studied, since radiation sources of sufficient power effectively achieve these responses. Why nonlinear optics is important? As a matter of fact current daily life without nonlinear optics would be more difficult. For instance, without nonlinear optics, telecommunication would be missing of high-quality fibre systems that power the internet. Moreover, current medicine is rich in advanced technology, based on laser analytical tools that are used for medical diagnosis. Furthermore, nonlinear optical effects are used to monitor water and air pollution. Besides, new materials are characterized using nonlinear optical phenomena. In addition to telecommunications, medicine and environmental protection, scientific instruments, new laser colours, advanced spectroscopy, data storage are important. All these applications have a significant impact on everyday life. Materials that have unique nonlinear responses are in the spotlight of scientists research because they are used in fields such as photonics, optoelectronics, optical calculations, optical signal processing and more. The extraordinary nonlinear properties often result from conjugated  $\pi$  –electron bonding networks in materials.

The science of supramolecular systems is a relatively new field of knowledge, which includes not only chemistry, but also physics, biochemistry and material engineering. Supramolecular chemistry, which is about 60 years old, is currently a very dynamically developing field of organic chemistry dealing with structures composed of many subunits that arise spontaneously as a result of weak intermolecular interactions [2]. The study of noncovalent interactions is key to understanding

inherently all processes in living cells. The voluminous macromolecular biological systems have been the inspiration for similar systems created by humans. On the one hand, supramolecular chemistry deals with the study of already existing, natural supramolecular structures, such as ionophore antibiotics, cell membranes or nucleic acids, and on the other, on the design and synthesis of completely new, non-naturally occurring structures such as nanotubes, liquid crystals, dendrimers, macrocyclic compounds and many others. The main objectives of this work lies on the design and elaboration of new multifunctional supramolecular architectures for nonlinear optical applications. In this respect, dynamic metal-ligand (M-L) interaction is continuously emerging as a powerful tool for the design and the development of various types of multi-responsive material properties. Such materials can therefore be classified to the kind of stimuli that they respond to, such as thermo-, photo-, chemo-, electro-, mechano-, and offer applications in diverse fields, including biomedicine, nanoelectronics and catalysis [3-6]. Recently a huge interest has been devoted to the preparation of different supramolecular assemblies by the use of suitable ligands that leads to the formation through self-assembly processes to self-assembled metal complexes and/or metallo-supramolecular networks.

On the other hand, there is no doubt that the phenomenal increase in thin film research is due to their versatile applications in various fields, such as electronics, optics, space industry, and aviation [7]. These studies gave rise to numerous inventions, for example, in the form of active and passive elements, piezoelectric devices, power microminiaturization, elements for solar energy processing and storage, magnetic memories, superconductors, reflective and antireflective coatings. Why are thin film structures important? One of the simplest reasons is the desire to produce materials with properties that differ significantly from those of bulk homogeneous materials. It often happens that the properties of bulky materials required for non-engineering applications differ significantly for their corresponding thin films materials and nanomaterials. An example of such unique properties is the relatively easy protection of electrical contacts between semiconductor devices by

depositing a thin layer on the contact surface. Construction materials intended for high temperatures are often coated with appropriate coatings based on thin film technology, due to which it is possible to reduce wear of the element and extend its life. Thin film deposition technology has an effect on increasing efficiency, reducing costs, and control over various surfaces. These features allow the development of completely new products, improving the design and production process. This allows achieving better functionality of products, thus saving resources and materials and reducing the amount of waste encountered in traditional production. The electronic, magnetic and optical properties of thin layers are the key to creating communication electronics. It is therefore clear that thin films play an important role in shaping society in the future.

This doctoral thesis consists of 8 chapters divided into subsections. The first chapter discusses mathematically nonlinear optical phenomena using a wave equation. Second- and third-order nonlinear phenomena have been characterized, which include the generation of the second harmonic (SHG) and the generation of the third harmonic (THG). Tensors characterizing nonlinear optical susceptibility for these effects were derived. The other part of this chapter describes other effects that are characterized by complex nonlinear electrical susceptibility. Imaginary part present phenomena of nonlinear absorption, which is divided into saturable absorption (SA) and reverse saturable absorption (RSA). The real part is described by variations in the refractive index, which were described using forced birefringence, the electro-optical Kerr phenomenon, as well as self-focusing and self-defocusing.

The second chapter describes what the title supramolecular compounds are. The chapter began with the history of the development of supramolecular chemistry. Then, the most important features and assumptions were presented, and examples of chemical structures that are classified in supramolecular chemistry are presented as well. Their applications in everyday life and in

nonlinear optics are also described, which is also the main topic of this work. In the following, various types of supramolecules are described, which include helicates, metal organic frameworks (MOF) called also coordinating polymers, and porphyrins, from which supramolecular architectures are very often built. The unique properties of these structures and their applications are represented.

The third chapter is a description of thin films and their properties and manufacturing methods. The phenomenon of luminescence and what is its lifetime are described, as well as electronic properties of materials. In this thesis, thin films based on a two-dimensional structure model and are described mathematically. The following three most popular methods for producing thin films are presented. The first is the spin coating method. This method is based on the production of layers from a solution. The other two methods allow the production of powder layers in a vacuum, they are physical vapor deposition (PVD) and pulsed laser deposition (PLD) also known as laser ablation.

The next chapter, fourth, consists of descriptions of experimental techniques. First, theoretical models were described, from which it is possible to determine the second and third order nonlinear susceptibility from experimental data depending on the given parameters and the method of measurement. The following are experimental apparatus that were used to study the second and third harmonic generation. The next part describes what the corona poling method is, which allows possibility of SHG measurements. Next, the Z-scan technique is described, which is divided into 3 ways. This method allows the determination of nonlinear absorption and nonlinear refractive index during one measurement. Further in the fourth chapter, spectroscopic devices were described, where the absorption and luminescence spectra of the studied thin films were obtained. The surfaces of the investigated layers were characterized by means of an atomic force microscope (AFM) and the next section describes its operation. The last experimental technique presented in

this work is ellipsometry, which allows to determine constants such as the extinction coefficient or refractive index.

The next three chapters present the experimental results of the studied chemicals, which are triple stranded helicates with different metal cations:  $\text{Fe}^{2+}$ ,  $\text{Co}^{2+}$ ,  $\text{Ni}^{2+}$  and  $\text{Zn}^{2+}$  [8], and metalloporphyrins with different metals : Fe, Ru, Pd and Pt, as well as modified pyrene-based complexes contacting zinc Zn(II) and cadmium Cd(II) cations. The method of sample preparation was first presented and then samples were characterized by AFM. The following sections present spectroscopic results: absorption and their luminescence. Then, the nonlinear properties of the supramolecular systems studied, which are the generation of the second and third harmonics, and the effects determined using the Z-scan technique are presented. Each of these chapters ends with a summary of the obtained experimental results.

Chapter 8 presents the nonlinear optical properties research of nanoporous membranes on which second harmonic generation studies were performed for each type of the investigated samples: porphyrin complexes, triple stranded helicates and modified pyrene-based supramolecular complexes. One sample was selected from each type of studied complexes.

The presented doctoral dissertation ends with a conclusion and analysis of the obtained experimental data. The results obtained for each supramolecular system presented in this paper were summarized and their potential applications, usefulness in nonlinear optics and perspectives for further research are presented.

## Literature

- [1] R. W. Boyd, Nonlinear Optics, Academic Press, 2008.
- [2] H. Dodziuk, Introduction to Supramolecular Chemistry, Kluwer Academic Publishers, 2002

- [3] P. Sutar, V.M. Suresh, T.K. Maji, Tunable emission in lanthanide coordination polymer gels based on a rationally designed blue emissive gelator, *Chem. Commun.* 51, 9876-9879, 2015
- [4] D. D. Diaz, D. Kuhbeck, R. J. Koopmans, Stimuli-responsive gels as reaction vessels and reusable catalysts, *Chem. Soc. Rev.* 40, 427-448, 2011.
- [5] T. Vermonden, R. Censi, W.E. Hennink, Hydrogels for Protein Delivery *Chem. Rev.* 112, 2853-2888, 2012.
- [6] S. Zhang, M.A. Greenfield, A. Mata, L. C. Palmer, R. Bitton, J. R. Mantei, C. Aparicio, M.O. de La Cruz, S.I. Stupp, A self-assembly pathway to aligned monodomain gels, *Nat. Mater.* 9, 594-601, 2010.
- [7] L. B. Freund, S. Suresh, *Thin Film Materials: Stress, Defect Formation and Surface Evolution*, Cambridge University Press, 2003.
- [8] K. Waszkowska, Y. Cheret, A. Zawadzka, A. Korcala, J. Strzelecki, A. El-Ghayoury, A. Migalska-Zalas, B. Sahraoui. Photoluminescence and nonlinear optical properties of triple stranded helicates based metallo-supramolecular architectures. *Dyes and Pigments*, 186 (2021) 109036.



## CHAPTER 1: NONLINEAR OPTICS

Visible light is a small but very important part of the electromagnetic wave spectrum. Generally, the propagation of the light in the free space can be described by classical physics, nevertheless interactions between matter and light (for instance absorption and emission) can be described only by quantum physics. The classical relevant description is in form of Maxwell's equations, which describe the velocity of propagation the electromagnetic waves in a vacuum. This velocity is in close relation to the measured speed of light. This observation strongly determines the light in the field of electromagnetic waves.

### 1.1. Wave Description

All of electromagnetic phenomena including light propagation can be fully written in relation to Maxwell's equations (in SI units) [1.1 – 1.3]:

$$\nabla \cdot \vec{D} = \rho \quad (1.1)$$

$$\nabla \cdot \vec{B} = 0 \quad (1.2)$$

$$\nabla \times \vec{E} = -\frac{\partial \vec{B}}{\partial t} \quad (1.3)$$

$$\nabla \times \vec{H} = \frac{\partial \vec{D}}{\partial t} + \vec{j} \quad (1.4)$$

where:  $\vec{E}$  describes vector of electric field strength,  $\vec{H}$  – vector of magnetic field strength,  $\vec{D}$  is a vector of electric induction,  $\vec{B}$  describes vector of magnetic induction,  $\rho$  is a volumetric density of charge and  $\vec{j}$  is a vector of total current density. Material equations allow us to determine vectors  $\vec{D}$  and  $\vec{H}$  by using the vectors  $\vec{E}$  and  $\vec{B}$ . They depend on the properties of the material. However, we can write those vectors as follows:

$$\vec{D} = \varepsilon_0 \vec{E} + \vec{P} \quad (1.5)$$

$$\vec{B} = \mu \vec{H} + \vec{M} \quad (1.6)$$

Vector  $\vec{P}$  describes electric polarity and it can be written by:

$$\vec{P} = \varepsilon_0 \chi_e \vec{E} \quad (1.7)$$

where  $\chi_e$  is known as electrical susceptibility,  $\varepsilon_0 = 8,85 \cdot 10^{-12} \text{C}^2/(\text{N} \cdot \text{m}^2)$  and is known as electric permittivity of the vacuum. The magnetic polarization vector  $\vec{M}$  is expressed by the following relation:

$$\vec{M} = \chi_m \vec{H} \quad (1.8)$$

where  $\chi_m$  describes magnetic susceptibility. Specifically interesting are the solutions of Maxwell's equations in areas of free space where there are no free charges and there are no conduction currents, that means:

$$\rho = 0 \quad (1.9)$$

$$\vec{j} = 0 \quad (1.10)$$

It is also important that we should have non-magnetic medium, so that means the vector of magnetic polarization  $\vec{M}$  is equal to zero. In this case, the vector of magnetic induction  $\vec{B}$  is equal to:

$$\vec{B} = \mu \vec{H} \quad (1.11)$$

where  $\mu$  is magnetic permittivity of the medium. Equivalently important is fact, that electrical polarization  $\vec{P}$  cannot be ignored. In strong electric fields, the response of the material medium to

the applied field changes its nature, and beside the linear response  $\vec{P}_L$  there is also nonlinear response  $\vec{P}_{NL}$ , that means:

$$\vec{P} = \vec{P}_L + \vec{P}_{NL} \quad (1.12)$$

where the linear dependence of the electric field is expressed as follows:

$$\vec{P}_L = \epsilon_0 \chi_e^{(1)} \vec{E} \quad (1.13)$$

$\chi_e^{(1)}$  describes linear electric susceptibility. In spite of this, nonlinear polarization is a complex function of the electric field  $\vec{E}$ :

$$\vec{P}_{NL} = \epsilon_0 \left[ \chi_e^{(2)} \cdot \vec{E}^2 + \chi_e^{(3)} \cdot \vec{E}^3 + \dots \right] \quad (1.14)$$

where  $\chi_e^{(2)}$  and  $\chi_e^{(3)}$  are second- and third-order nonlinear electrical susceptibilities, respectively.

Now electric polarization can be written as follows:

$$\vec{P} = \vec{P}^{(1)} + \vec{P}^{(2)} + \vec{P}^{(3)} + \dots \quad (1.15)$$

where  $\vec{P}^{(n)}$  describes n-order polarization,  $n = 1, 2, 3, \dots$ . Currently we can look at the output of the optical wave equation. Let us take the curl of the curl of the electric field  $\vec{E}$  from the (1.3). As a consequence of the continuity of the function we substitute the order of the derivative after time and space on the right of the resulting equation, and then using equations (1.4), (1.10) and (1.11) to express  $\nabla \times \vec{B}$  with  $\mu_0 (\partial \vec{D} / \partial t)$  we have the following result:

$$\nabla \times \nabla \times \vec{E} + \mu_0 \frac{\partial^2}{\partial t^2} \vec{D} = 0 \quad (1.16)$$

Under certain conditions, equation (1.16) can be simplified. For example, using a vector calculus we can write the first element of the equation as:

$$\nabla \times \nabla \times \vec{E} = \nabla(\nabla \cdot \vec{E}) - \nabla^2 \vec{E} \quad (1.17)$$

In the case of nonlinear optics exist a relation between  $\vec{D}$  and  $\vec{E}$ , so it cannot be assumed that  $\nabla \cdot \vec{E} = 0$  as a resulting from  $\nabla \cdot \vec{D} = 0$ . Nevertheless we can assume that  $\nabla(\nabla \cdot \vec{E})$  is negligible in (1.17) so that equation (1.16) can be written as follows:

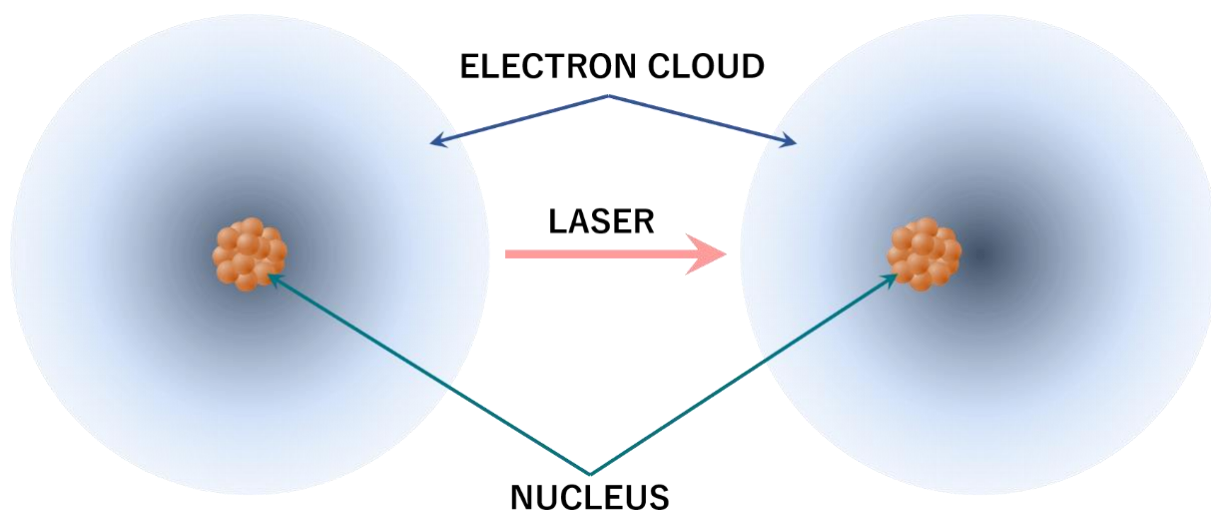
$$\nabla^2 \vec{E} - \mu_0 \frac{\partial^2}{\partial t^2} \vec{D} = 0 \quad (1.18)$$

To eliminate  $\vec{D}$  from the (1.18), we can use equation (1.5) and replace, for convenience  $\mu_0$  as  $1/\epsilon_0 c^2$ , where  $c$  is the speed of light in vacuum. In this way, the most general wave equation in nonlinear optics takes form:

$$\nabla^2 \vec{E} - \frac{1}{c^2} \frac{\partial^2}{\partial t^2} \vec{E} = \frac{1}{\epsilon_0 c^2} \frac{\partial^2}{\partial t^2} \vec{P} \quad (1.19)$$

While electromagnetic radiation passes through matter, the electric field of this radiation causes a periodic shift of electric charges with the frequency of the radiation, however, these oscillating displacements in turn generate electromagnetic radiation (Fig. 1.1). When the intensity of the incident light is low, the deviations of the electric charges from the rest position are also small - they behave like harmonic oscillators driven by a frequency other than resonance: motion contains only the same frequency components as excitation. The potential that drives the dipole back to its original position is approximately parabolic-shaped only for small charge displacements. However, in the case of large displacements, the potential deviates from this parabolic behavior, because the nuclear charge of the neighboring atoms acts. This deviation is called nonlinearity because it denotes a nonlinear relationship between the deflection and the restoring force. The shape and strength of the nonlinearity depends on the structure of the material through which the light passes. The moving charge is accelerated towards the zero position by the potential, resulting in a sinusoidal velocity waveform only for the square potential. In the event of deviations, the load is

in the meantime accelerated too slowly or too quickly, which leads to deviations from the sinusoidal shape in the velocity curve and consequently to deviations in the electric field of the light emitted by the load. In the spectrum of light, this means that not only the incidence frequency, but also its harmonics are contained in different powers. As the conversion efficiency drops sharply with the harmonic degree, only the second (SHG) or third (THG) is mainly of technical importance.



**Figure 1.1:** The nucleus and the electron cloud are shifted relative to each other under the influence of light.

## 1.2. Second Harmonic Generation

Nonlinear second-order processes occur in the case of specific combinations of frequency, intensity and phase in the relation to the electric field and its manifestation in a nonlinear medium. The laser beam whose electric field, dependent on the time  $t$  and coordinates  $r$  which propagates towards  $\vec{k}$  direction, is represented as [1.1 – 1.3]:

$$\vec{E}(r, t) = E \cdot \sin(\omega t - \vec{k} \cdot r) \quad (1.20)$$

This laser beam appears in the medium for which the electrical second-order susceptibility  $\chi_e^{(2)}$  is not equal to zero. The nonlinear polarization that arises in such medium is given by relation:

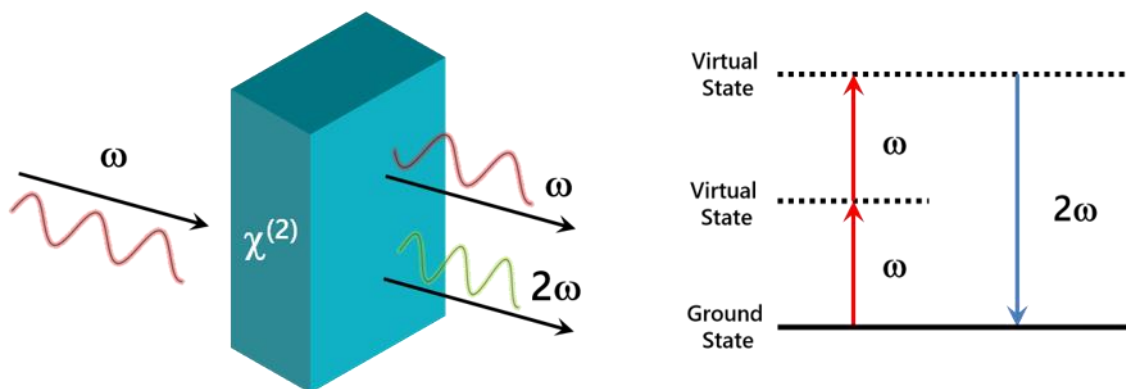
$$\vec{P}^{(2)}(r, t) = \epsilon_0 \chi_e^{(2)} \cdot \vec{E}^2 \quad (1.21)$$

Taking into account the wave equation (1.20) we get following relation:

$$\vec{P}^{(2)}(r, t) = \frac{1}{2} \epsilon_0 \chi_e^{(2)} E^2 [1 - \cos 2(\omega t - \vec{k} \cdot r)] \quad (1.22)$$

We see therefore, that the second order polarity consists of a member independent of the time  $t$  in which there is frequency zero and the member changing with the frequency of  $2\omega$  at time  $t$ . It should be also noted that the first component of the equation does not indicate electromagnetic radiation, because the second derivative disappears, however it leads to the formation of a static electric field through a nonlinear medium.

The second harmonic generation effect is illustrated schematically in Fig. 1.2. The nonlinear medium on which an electromagnetic wave propagates in the  $\vec{k}$  direction with a frequency  $\omega$ , the new wave with a doubled frequency is created.



**Figure 1.2:** Geometry of generated second harmonic and energy level diagram described SHG process.

Second harmonic generation can be also described by energy diagram level, where two photons of frequency  $\omega$  are destroyed from the virtual state to the frequency  $2\omega$  in single quantum-mechanics process (Fig. 1.2).

The intensity of generated second harmonic in a nonlinear medium with a thickness  $d$  can be expressed by:

$$I(2\omega, d) \approx I_{\omega}^2 (\chi_e^{(2)})^2 \left[ \frac{\sin\left(\frac{1}{2}d\Delta k\right)}{\frac{1}{2}d\Delta k} \right]^2 \quad (1.23)$$

where  $I_{\omega}$  describes the intensity of the incident light, while  $\Delta k$  is the phase matching parameter:

$$|\Delta k| = |\vec{k}_2 - 2\vec{k}_1| = \left(\frac{2\omega}{c}\right) (n_{2\omega} - n_{\omega}) \quad (1.24)$$

where  $\vec{k}_1$  and  $\vec{k}_2$  are vectors of fundamental wavelength and generated second harmonic, respectively. It can be also noted, that the intensity of generated second harmonic increases quadratically with the intensity of incident light  $I_{\omega}$ . The influence on increase of the intensity have also the condition which for phase velocities of fundamental and generated harmonic wavelength are equal, which means  $\Delta k = 0$ . Besides, for small values of any  $x$ , the  $\sin x$  function in Maclaurin's theorem takes form:

$$\sin x = x - \frac{x^3}{3!} + \frac{x^5}{5!} - \frac{x^7}{7!} + \dots$$

This means, when the phase matching condition (1.24) is met, it can be expressed by:

$$\Delta k = 0 \Rightarrow n_{2\omega} = n_{\omega} \quad (1.25)$$

Then, along with the square of the thickness  $d$  of the medium, the intensity of the generated second harmonic will increase. Otherwise, if this condition is not met, we have to deal with the periodicity of the SHG intensity as a function of the thickness  $d$  of the medium. The phase matching condition (1.24) is often difficult to achieve because the refractive index is a function of the frequency, and this is associated with an effect known as dispersion. Generally, phase matching is be divided into two types. Type I occurs in case when two polarizations vector (fundamental and generated

harmonic) are in parallel position:  $n_z^{2\omega} = n_{xy}^\omega$ , while type II appears in case when polarizations vector are in orthogonal position:  $n_z^{2\omega} = \frac{1}{2}(n_{xy}^\omega + n_z^\omega)$ .

It should be also noted that for a given value of thickness  $d$ , the mismatch parameter  $\Delta k$  is not proportional to  $d$ . For a mismatch  $\Delta k$ , a value called the coherence length  $L_c$  is included, which is a measure of the maximum length within which the parametric cooperation process is effective. This value is expressed by the formula [1.4]:

$$L_c = \frac{\pi}{|\Delta k|} \quad (1.26)$$

The behavior described by equation (1.23) was firstly experimentally observed in 1962 by P. D. Maker [1.5]. The experiment consisted in the fact that the ruby laser beam was focused on the surface of the quartz crystal, and then was measured how the intensity of the generated second harmonic signal changes when the crystal is rotating, thus changing the effective length of the optical path through the crystal. The phase mismatch  $\Delta k$  was different from zero and more or less the same for all orientations used in the experiment, which is not true for all nonlinear materials.  $\Delta k$  in general strongly depends on crystal orientation, as well as with respect to polarization of fundamental and generated harmonic wavelengths.

As it turns out, the process of second harmonic generation strongly depends on the crystal structure of the material. It was noted earlier, that the second order polarization is the square of the electric field (1.21). In centrosymmetric medium must appear an inversion, that is:

$$\begin{aligned} -\vec{P}^{(2)} &= \varepsilon_0 \chi_e^{(2)} \cdot (-\vec{E})^2 \\ -\vec{P}^{(2)} &= \varepsilon_0 \chi_e^{(2)} \cdot \vec{E}^2 \end{aligned} \quad (1.27)$$



It means that  $\vec{P}^{(2)} = -\vec{P}^{(2)}$  only if the second-order nonlinear susceptibility is equal to zero  $\chi_e^{(2)} = 0$ . As the result, only materials devoid of the symmetry center exhibit nonlinear optical properties.

The second harmonic generation has many applications. One of them is strict diagnostics of surface properties of optical materials. As mentioned above, coherent SHG is impossible to obtain in medium that are centrosymmetrical. The intensity as a function of the incident angle depends to the large extent on the morphology of the surface and the presence of impurities on the surface of the material.

### 1.3. Second-order nonlinear optical susceptibility tensor $\chi^{(2)}$

In previous paragraph we already said that second-order polarization is equal to (1.21):

$$\vec{P}^{(NL)} = \varepsilon_0 \chi_e^{(2)} \cdot \vec{E} \cdot \vec{E}$$

Taking into account electromagnetic plane wave equation:

$$E(z, t) = E(z) \exp(-i\omega t) + c. c. \quad (1.28)$$

where *c.c.* is a complex conjugate, we can also write relation (1.21) as:

$$P^{(NL)}(t) = 2\varepsilon_0 \chi_e^{(2)} \cdot EE^* + \varepsilon_0 \chi_e^{(2)} [E^2 \exp(-2i\omega t) + c. c.] \quad (1.29)$$

An expression with a double frequency of  $2\omega$  appears, which is responsible for generating the second harmonic. Basically, the second order nonlinear optical susceptibility  $\chi_e^{(2)}$  is a three-rank tensor made up of 27 components  $ijk$  along the axes ( $x, y, z$ ) which express three perpendicular directions. The components of the tensor  $\chi_{ijk}^{(2)}$  exhibit an invariance during the permutation of the indices  $j$  and  $k$ . Indeed, the commutativity of the elements  $E_j(\omega)E_k(\omega) = E_k(\omega)E_j(\omega)$  (which is

true for non-resonant materials) makes it possible to reduce the number of independent components to a number equal to 18 and to write the polarization by following expression:

$$\begin{bmatrix} P_x^{NL} \\ P_y^{NL} \\ P_z^{NL} \end{bmatrix} = \varepsilon_0 \begin{bmatrix} \chi_{111} & \chi_{122} & \chi_{133} & \chi_{123} & \chi_{113} & \chi_{112} \\ \chi_{211} & \chi_{222} & \chi_{233} & \chi_{223} & \chi_{213} & \chi_{212} \\ \chi_{311} & \chi_{322} & \chi_{333} & \chi_{323} & \chi_{313} & \chi_{312} \end{bmatrix} \begin{bmatrix} E_x^2(\omega) \\ E_y^2(\omega) \\ E_z^2(\omega) \\ 2E_y(\omega)E_z(\omega) \\ 2E_x(\omega)E_z(\omega) \\ 2E_x(\omega)E_y(\omega) \end{bmatrix} \quad (1.30)$$

According to Kleinman symmetry [1.6 – 1.7], in the pulsation domain outside of the absorption resonance, tensor  $\chi_e^{(2)}$  is symmetrical with respect to the permutations of the three indices  $ijk$ .

Taking that claim into account we obtain following relation:

$$\chi_{ijk} = \chi_{ikj} = \chi_{jik} = \chi_{jki} = \chi_{kij} = \chi_{kji} \quad (1.40)$$

**Table 1.1:** Relation between indices  $jk$ .

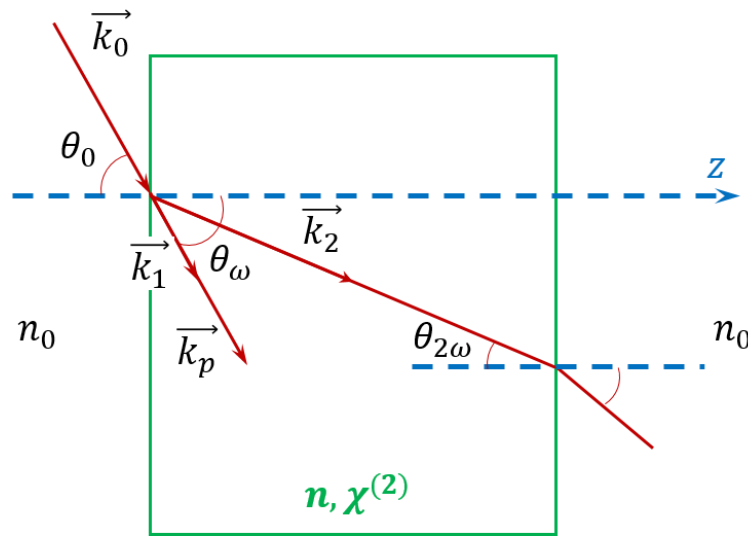
$jk$	11	22	33	23=32	13=31	12=21
$l$	1	2	3	4	5	6

And it leads to fact that only 10 components of the tensor remain independent. The elements of the polarization  $P^{(NL)}$  in the coordination system  $(x, y, z)$  can be now written in following matrix expression:

$$\begin{bmatrix} P_x^{NL} \\ P_y^{NL} \\ P_z^{NL} \end{bmatrix} = \varepsilon_0 \begin{bmatrix} \chi_{111} & \chi_{122} & \chi_{133} & \chi_{123} & \chi_{113} & \chi_{112} \\ \chi_{112} & \chi_{222} & \chi_{233} & \chi_{223} & \chi_{123} & \chi_{122} \\ \chi_{113} & \chi_{223} & \chi_{333} & \chi_{233} & \chi_{133} & \chi_{123} \end{bmatrix} \begin{bmatrix} E_x^2(\omega) \\ E_y^2(\omega) \\ E_z^2(\omega) \\ 2E_y(\omega)E_z(\omega) \\ 2E_x(\omega)E_z(\omega) \\ 2E_x(\omega)E_y(\omega) \end{bmatrix} \quad (1.41)$$

Generally, instead of components of second-order nonlinear optical susceptibility tensor  $\chi_{ijk}$ , the notation  $d_{il}$  is used, where  $\chi_{ijk} = 2d_{il}$ , and indices  $jkl$  are replaced by the indices presented in Tab. 1.1 [1.8]. Using notation shown in tab. 1.1, relation (1.41) can be written as follows:

$$\begin{bmatrix} P_x^{NL} \\ P_y^{NL} \\ P_z^{NL} \end{bmatrix} = 2\varepsilon_0 \begin{bmatrix} d_{11} & d_{12} & d_{13} & d_{14} & d_{15} & d_{16} \\ d_{16} & d_{22} & d_{23} & d_{24} & d_{14} & d_{12} \\ d_{15} & d_{24} & d_{33} & d_{23} & d_{13} & d_{14} \end{bmatrix} \begin{bmatrix} E_x^2(\omega) \\ E_y^2(\omega) \\ E_z^2(\omega) \\ 2E_y(\omega)E_z(\omega) \\ 2E_x(\omega)E_z(\omega) \\ 2E_x(\omega)E_y(\omega) \end{bmatrix} \quad (1.42)$$



**Figure 1.3:** Geometric representation of the propagation of the fundamental and second harmonic waves in a nonlinear medium.

By considering a monochromatic plane wave propagating in a linear medium with an index  $n_0$  and wave vector  $\vec{k}_0$  (Fig. 1.3) after enter to nonlinear medium with index  $n$ , wave vector  $\vec{k}_1$  locally creates a macroscopic polarization with oscillating component  $2\omega$ . This forced wave is expressed by wave vector  $\vec{k}_p$  with amplitude [1.9]:

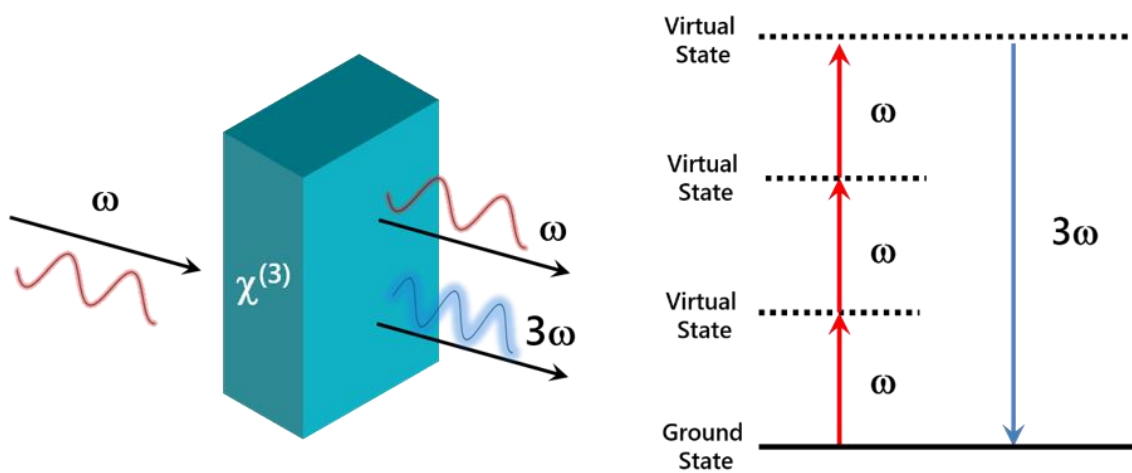
$$k_p = 2k_1 = \frac{2\omega}{c} n(\omega) \quad (1.43)$$

Therefore, this wave propagates collinearly and at the same speed as the fundamental wave  $\omega$ :

$$\vec{P}_{2\omega} = \varepsilon_0 [\chi^{(2)} E(\omega) E(\omega)] \exp(ik_p z) \quad (1.44)$$

These two waves will therefore interfere throughout their propagation within the material. The energy transfer  $\omega \rightarrow 2\omega$  will be maximum when these two waves oscillate in phase, that is to say when  $\vec{k}_2 = \vec{k}_p$  or  $\vec{k}_2 = 2\vec{k}_1$ . That relation describes the condition of phase matching.

#### 1.4. Third Harmonic Generation



**Figure 1.4:** Interaction geometry during the third harmonic generation process and energy level diagram described THG process.

Third-order nonlinear optical interactions give a rich variety of the phenomena that can provide both basic and useful information about the structure and dynamics of molecules, and can be used to create new devices. There are many third-order processes that can be distinguished based on the frequency of input and output waves as well as on the nature of the resonance material encountered. Third harmonic generation process (THG) is schematically presented in Fig. 1.4.

The nonlinear polarization, which is created as a result of the relationship with the electric field and the function of nonlinear optical susceptibility, can be expressed as follows [1.1 – 1.3]:

$$\vec{P}^{(3)}(r, t) = \varepsilon_0 \chi_e^{(3)} \cdot \vec{E}^3 \quad (1.45)$$

Taking into account the wave equation, we get the following result:

$$\vec{P}^{(3)}(r, t) = \frac{1}{4} \varepsilon_0 \chi_e^{(3)} E^3 \cos 3(\omega t - \vec{k} \cdot r) + \frac{3}{4} \varepsilon_0 \chi_e^{(3)} E^3 \cos(\omega t - \vec{k} \cdot r) \quad (1.46)$$

The first polarization element describes the response at frequency of  $3\omega$ , which is created by the frequency field  $\omega$  (Fig. 1.4). It provides to the third harmonic generation process, which can be schematically presented by energy diagram. Three photons of frequency  $\omega$  are destroyed from the virtual state and in microscopic nature of this effect one photon of frequency  $3\omega$  is created.

As it can be observed, third harmonic generation process is similar to the second-order nonlinear optical process. Analogously, the intensity of generated third harmonic in a nonlinear medium with the thickness  $d$  is expressed by:

$$I(3\omega, d) \approx I_\omega^3 (\chi_e^{(3)})^2 \left[ \frac{\sin\left(\frac{1}{2} d \Delta k\right)}{\frac{1}{2} d \Delta k} \right]^2 \quad (1.47)$$

In this case, the value of mismatch parameter is given by:

$$|\Delta k| = |\vec{k}_3 - 3\vec{k}_1| = \left(\frac{3\omega}{c}\right) (n_{3\omega} - n_\omega) \quad (1.48)$$

where  $\vec{k}_1$  and  $\vec{k}_2$  are vectors of fundamental wavelength and generated third harmonic,  $n_{3\omega}$  and  $n_\omega$  are refractive indexes of this vector values. The rules for obtain the maximum intensity in third harmonic generation process are the same as for SHG. The difference is that there is no structural restriction for THG process. Generation of third harmonic is possible in both: noncentrosymmetric and centrosymmetric materials.

### 1.5. Third-order nonlinear optical susceptibility tensor $\chi^{(3)}$

Considering the situation, where three monochromatic plane waves propagate in medium, their electric field can be described as follows:

$$\vec{E}(t) = \vec{E}_1 \exp(-i\omega_1 t) + \vec{E}_2 \exp(-i\omega_2 t) + \vec{E}_3 \exp(-i\omega_3 t) + c. c. \quad (1.49)$$

In this case, third-order nonlinear polarization P:

$$P^{(3)} = \chi_{ijkl}^{(3)} E_j E_k E_l \quad (1.50)$$

is composed of 44 elements including 22 elements whose direction is the same as the direction of propagation of the waves (and 22 elements with opposite direction of propagation as well):

$$\begin{aligned} &\omega_1, \omega_2, \omega_3, 3\omega_1, 3\omega_2, 3\omega_3, (\omega_1 + \omega_2 + \omega_3), (\omega_1 + \omega_2 - \omega_3), \\ &(\omega_1 + \omega_3 - \omega_2), (\omega_2 + \omega_3 - \omega_1), (2\omega_1 \pm \omega_2), (2\omega_1 \pm \omega_3), \\ &(2\omega_2 \pm \omega_1), (2\omega_2 \pm \omega_3), (2\omega_3 \pm \omega_1), (2\omega_3 \pm \omega_2) \end{aligned} \quad (1.51)$$

At this time we can describe nonlinear polarization as a sum of partial polarizations:

$$\vec{P}^{(3)} = \sum_n \vec{P}(\omega_n) \exp(-i\omega_n t) \quad (1.52)$$

However, in isotropic medium, the nonlinear optical response of electromagnetic waves appears only after taking into consideration the third order nonlinear electrical polarization written in the form:

$$P_i^{(3)}(\vec{r}, t) = \chi_{ijkl}^{(3)} E_j E_k E_l(\vec{r}, t) \quad (1.53)$$

Moreover, elements of the tensor  $\chi_{ijkl}^{(3)}$  are non-zero even in the case of isotropic medium. Taking that into account isotropic second-order tensor  $\delta_{ij}$ , we obtain following relation:

$$\chi_{ijkl}^{(3)} = \chi_{xxyy}^{(3)} \delta_{ij} \delta_{kl} + \chi_{xyxy}^{(3)} \delta_{ik} \delta_{jl} + \chi_{xyyx}^{(3)} \delta_{il} \delta_{kj} \quad (1.53)$$

$$\chi_{iii}^{(3)} = \chi_{jjj}^{(3)} = \chi_{kkk}^{(3)} = \chi_{xxyy}^{(3)} + \chi_{xyxy}^{(3)} + \chi_{xyyx}^{(3)} \quad (1.54)$$

The interaction between nonlinear medium and with three electromagnetic waves  $\omega_1, \omega_2, \omega_3$  associated with the wave vectors  $\vec{k}_1, \vec{k}_2, \vec{k}_3$ , respectively, generates third-order polarization, which is described by:

$$P_i^{(3)}(\omega_4, \vec{k}_4) = \chi_{ijkl}^{(3)}(-\omega_4, \omega_1, \omega_2, \omega_3) E_j(\omega_1, \vec{k}_1) E_k(\omega_2, \vec{k}_2) E_l(\omega_3, \vec{k}_3) \quad (1.55)$$

This relation is fulfilled provided that the principle of energy conservation and phase matching are fulfilled, that means:

$$\omega_4 = \omega_1 + \omega_2 + \omega_3 \quad (1.56)$$

$$\vec{k}_4 = \vec{k}_1 + \vec{k}_2 + \vec{k}_3 \quad (1.57)$$

Third-order nonlinear optical susceptibility tensor  $\chi^{(3)}$  is dependent on interaction between frequencies of the applied electric fields with the medium, and the spatial components of the nonlinear polarization can be written as follows:

$$P_i^{(3)}(\omega_4) = K \chi_{ijkl}^{(3)}(-\omega_4, \omega_1, \omega_2, \omega_3) E_j(\omega_1) E_k(\omega_2) E_l(\omega_3) \quad (1.58)$$

where the indices  $j, k, l$  can take the values from  $x, y, z$  and  $K$  describes degeneration factor:

$$K = \begin{cases} 1 & \text{for } \omega_1 = \omega_2 = \omega_3 \\ 3 & \text{for } \omega_1 = \omega_2 \neq \omega_3 \\ 6 & \text{for } \omega_1 \neq \omega_2 \neq \omega_3 \end{cases} \quad (1.59)$$

The coefficients 1,3 and 6 come from number of permutations of the applied fields which introduce a contribution to the component of the electric field at the considered frequency. The third-order nonlinear electrical polarization is, in fact, a sum function of the frequencies (1.56) and

is a source of a new wave with frequency  $\omega_4$ . Complexed amplitudes of the polarization  $P(\omega_n)$  for positive frequencies can be written as form:

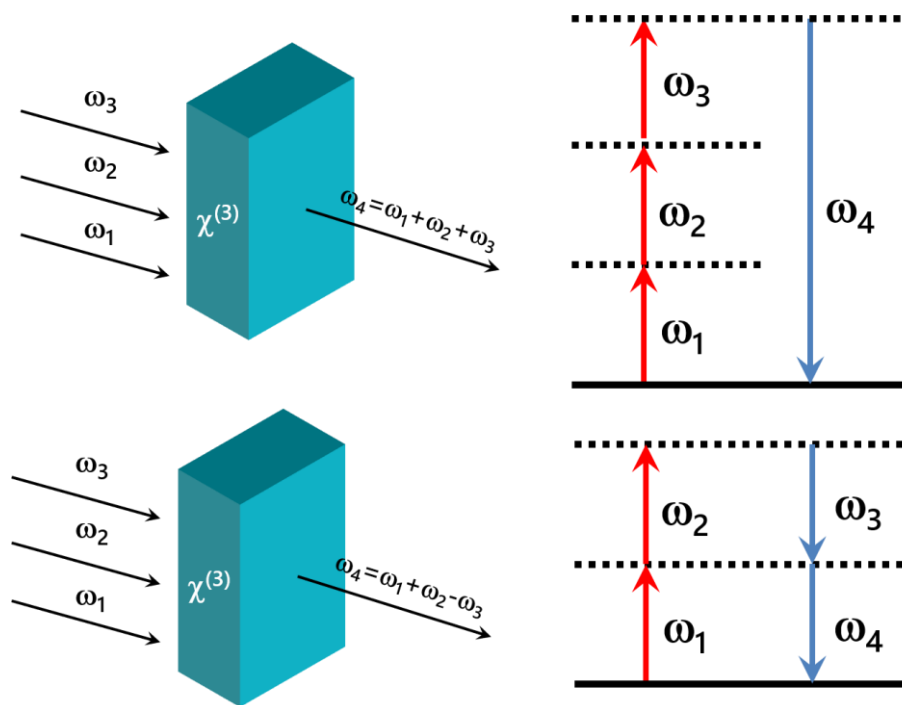
$$\begin{aligned}
P(\omega_1) &= \chi^{(3)}(3E_1E_1^* + 6E_2E_2^* + 6E_3E_3^*)E_1, \\
P(\omega_2) &= \chi^{(3)}(6E_1E_1^* + 3E_2E_2^* + 6E_3E_3^*)E_2, \\
P(\omega_3) &= \chi^{(3)}(6E_1E_1^* + 6E_2E_2^* + 3E_3E_3^*)E_3, \\
P(\omega_1) &= \chi^{(3)}E_1^3, \\
P(\omega_2) &= \chi^{(3)}E_2^3, \\
P(\omega_3) &= \chi^{(3)}E_3^3, \\
P(\omega_1 + \omega_2 + \omega_3) &= 6\chi^{(3)}E_1E_2E_3, \\
P(\omega_1 + \omega_2 - \omega_3) &= 6\chi^{(3)}E_1E_2E_3^*, \\
P(\omega_1 + \omega_3 - \omega_2) &= 6\chi^{(3)}E_1E_2^*E_3, \\
P(\omega_2 + \omega_3 - \omega_1) &= 6\chi^{(3)}E_2E_3E_1^*, \\
P(2\omega_1 + \omega_2) &= 3\chi^{(3)}E_1^2E_2, \\
P(2\omega_2 + \omega_1) &= 3\chi^{(3)}E_2^2E_1, \\
P(2\omega_1 + \omega_3) &= 3\chi^{(3)}E_1^2E_3, \\
P(2\omega_3 + \omega_1) &= 3\chi^{(3)}E_3^2E_1, \\
P(2\omega_2 + \omega_3) &= 3\chi^{(3)}E_2^2E_3, \\
P(2\omega_3 + \omega_2) &= 3\chi^{(3)}E_3^2E_2, \\
P(2\omega_1 - \omega_2) &= 3\chi^{(3)}E_1^2E_2^*, \\
P(2\omega_2 - \omega_1) &= 3\chi^{(3)}E_2^2E_1^*, \\
P(2\omega_1 - \omega_3) &= 3\chi^{(3)}E_1^2E_3^*, \\
P(2\omega_3 - \omega_1) &= 3\chi^{(3)}E_3^2E_1^*, \\
P(2\omega_2 - \omega_3) &= 3\chi^{(3)}E_2^2E_3^*, \\
P(2\omega_3 - \omega_2) &= 3\chi^{(3)}E_3^2E_2^*,
\end{aligned} \tag{1.60}$$

The particular elements of polarization are responsible for various nonlinear effects that appear in material. For instance, two different processes where three electromagnetic waves propagate in nonlinear medium are schematically illustrated in Fig. 1.5.



The third-order nonlinear optical susceptibility tensor  $\chi_{ijkl}^{(3)}$  describes the third-order optical effects at the macroscopic and  $\chi_{ijkl}^{(3)}$  is a four-rank tensor with a total 81 components. That means while determining the nonlinear optical susceptibility of a medium, we have to determine all the elements of the tensor. In case of isotropic medium, the tensor  $\chi_{ijkl}^{(3)}$  has following characteristics of symmetry (according to Kleinman symmetry):

$$\begin{aligned}
 \chi_{xxxx} &= \chi_{yyyy} = \chi_{zzzz} = \chi_{xxyy} + \chi_{xyxy} + \chi_{xyyx} \\
 \chi_{yyzz} &= \chi_{zzyy} = \chi_{zzxx} = \chi_{xxzz} = \chi_{xxyy} = \chi_{yyxx} \\
 \chi_{yzyz} &= \chi_{zyzy} = \chi_{zxzx} = \chi_{xzzx} = \chi_{xyxy} = \chi_{yxxy} \\
 \chi_{yzzz} &= \chi_{zyyz} = \chi_{zxxz} = \chi_{xzzx} = \chi_{xyyx} = \chi_{yxxy}
 \end{aligned}
 \tag{1.61}$$



**Figure 1.5:** Schematic representation of two processes that can take place during interaction of three incident waves with nonlinear medium.

This properties of symmetry allows to reduce the number of elements of tensor  $\chi_{ijkl}^{(3)}$ . Consequently, the third-order nonlinear optical susceptibility tensor has only three independent components:  $\chi_{xxxx}$ ,  $\chi_{xyxy}$  and  $\chi_{xxyy}$ .

Basically, the elements of third-order nonlinear optical susceptibility tensor are complex of real and imaginary part [1.1]:

$$\chi^{(3)} = \chi'^{(3)} + i\chi''^{(3)} \quad (1.62)$$

where:  $\chi'^{(3)}$  is the real part responsible for nonlinear variations in the refractive index and  $\chi''^{(3)}$  is the imaginary part related to nonlinear absorption of light and stimulated scattering.

Moreover, during experiments of nonlinear optical properties of isotropic medium subjected to the action of laser pulses of short duration, we can consider that only two effects contribute to the third-order electrical nonlinear optical susceptibility: deformation of the electronic cloud and movements of the molecule (translations, rotations and vibrations). Furthermore, when we consider Born-Oppenheimer approximation, which means that the frequency of the incident beam is far from the resonant frequencies of the medium, the contributions due to the deformation of the electronic cloud can be separated from the movements of the molecule. Consequently, we can describe third-order nonlinear optical susceptibility as the arithmetic sum of two terms:

$$\chi^{(3)} = \chi_{elec}^{(3)} + \chi_{mol}^{(3)} \quad (1.63)$$

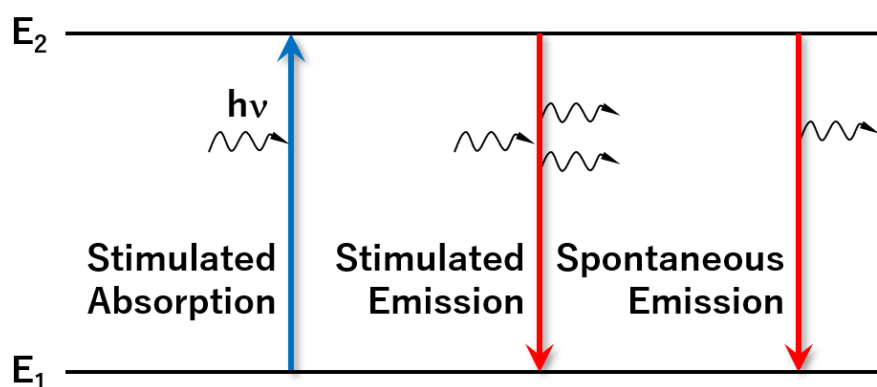
where:  $\chi_{elec}^{(3)}$  and  $\chi_{mol}^{(3)}$  denote the electronic component linked to the deformation of the electronic cloud and the molecular component linked to the movements of the molecule, respectively. Besides, the components of the tensor for isotropic medium can be written as follows [1.10 – 1.11]:

$$\chi_{xxxx}^{(3)elec} = 3\chi_{xxyy}^{(3)elec} = 3\chi_{yyxx}^{(3)elec} = 3\chi_{yxyx}^{(3)elec} \quad (1.64)$$

$$\chi_{xxxx}^{(3)mol} = 8\chi_{xxyy}^{(3)mol} = 8\chi_{yyxx}^{(3)mol} = \frac{4}{3}\chi_{yxyx}^{(3)mol} \quad (1.65)$$

## 1.6. Nonlinear Absorption

As we have already mentioned, light propagation in free space is described by classical physics, while light absorption and emission is described by quantum mechanics. During the interaction between the electromagnetic wave and the system of molecules with energy levels  $E_1$  and  $E_2$  in thermodynamic equilibrium, a number of different processes can occur, what is schematically illustrated in Fig. 1.6.



**Figure 1.6:** Interaction of the electromagnetic field with a two-level system.

In the process of photon absorption with energy:

$$h\nu = E_2 - E_1 \quad (1.66)$$

where:  $h$  is a Planck's constant and  $\nu$  is the frequency, the particle is excited to the energy level  $E_2$  from level  $E_1$ . This process is called stimulated absorption (see Fig. 1.6) [1.12]. The energy of the electromagnetic radiation absorbed by the molecule is strictly defined, that means molecule can only receive certain specific energy values. These energy values correspond to energy levels of the

molecule. Transitions between energy levels only take place between permitted levels. Absorption occurs only for those quanta, whose energy is strictly determined by the energies of the allowed energy levels [1.13]. Moreover, when a molecule passes from a higher energy level  $E_2$  to a lower level  $E_1$  under the influence of a radiation field, a photon is emitted with energy  $h\nu$ . This means that the number of photons increases by one – besides to the incident photon, another one with the same frequency is emitted. This process is called stimulated emission. In the case of returning system from a higher  $E_2$  energy to a lower level  $E_1$  irrespective of the external field, while radiating the appropriate photon, the process called spontaneous emission occurs.

In the spectroscopic experiment, a signal is recorded in the form of bands corresponding to the amount of energy absorbed by the sample from radiation passing through the sample. The absorption spectrum is characterized by three parameters:  $I$  – intensity,  $\nu$  – frequency corresponding to the position of the band and the width at half maximum (FWHM) [1.14]. Absorption intensity is determined by two quantities that are proportional:  $T$  – transmittance and  $A$  – absorbance, which determine the percentage number of transmission and absorption, respectively. Transmittance is a quantity that determines the ratio of the intensity of radiation passing through sample  $I$  to the intensity of radiation falling on sample  $I_0$ , which can be expressed by:

$$T = \frac{I}{I_0} \quad (1.67)$$

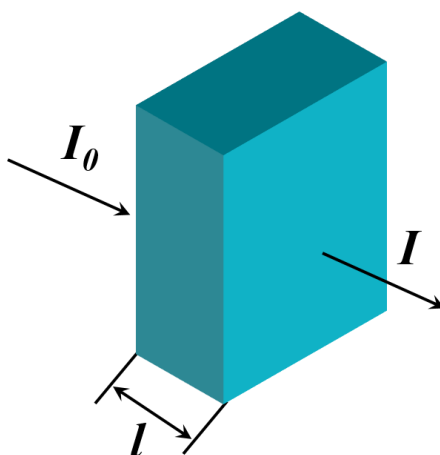
At the moment, when the radiation has completely passed through the medium, transmittance is equal to 1, otherwise this value is equal to 0. Absorbance  $A$  defines the amount of energy that has been absorbed by the medium. This quantity is recorded as the logarithm of the inverse transmittance:

$$A = \log \frac{1}{T} = \log \frac{I_0}{I} \quad (1.68)$$

When all the radiation passes through the material, the absorbance value is 0 whereas when the radiation has been absorbed, this value tends to infinity. The values of transmittance and absorbance are usually written as a percentage form, as follows:

$$\%T = 100 \frac{I}{I_0}, \quad A = \log \frac{100}{\%T} \quad (1.69)$$

The absorption spectrum can also be characterized by two parameters, which are: the wavelength that corresponds to the maximum intensity  $\lambda_{\max}$  and the specific absorption coefficient  $\alpha$  at the point  $\lambda_{\max}$ . The relation between the coefficient  $\alpha$ , and the thickness of the absorbing medium  $l$  is described by the Lambert-Beer law.



**Figure 1.7:** Transmission in a medium of thickness  $l$ .

The beam of radiation passing through the absorbing medium  $I$  decreases exponentially with the thickness  $l$  of the sample in relation to the primary radiation  $I_0$  (Fig. 1.7) according to the equation:

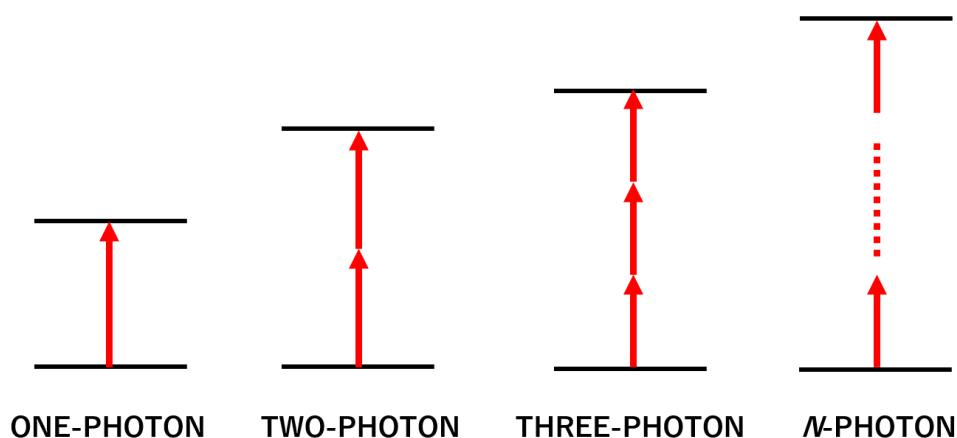
$$I = I_0 \cdot e^{-k \cdot l} \quad (1.70)$$

where  $k$  is the radiation absorption coefficient. By transforming this equation and inserting it into equation (1.68), we obtain the relation:

$$A = \ln \frac{I_0}{I} = k \cdot l; \quad A = \log \frac{I_0}{I} = \alpha \cdot l \quad (1.71)$$

where  $\alpha = 0.4343 \cdot k$  is called the correct absorption coefficient and its value is given in  $[\text{cm}^{-3}]$ .

This is the characteristic value for a given substance. Generally, the value of the factor  $\alpha$  is determined at the wavelength at which the highest absorption occurs, however, it can be calculated for any wavelength of the absorption spectrum. Equation (1.71) is called the Lambert-Beer law.



**Figure 1.8:** Numerous processes of multiphoton absorption.

At the moment when the medium is excited by very high laser radiation, it happens that more than one photon is absorbed (see Fig. 1.8). This phenomenon is called multi-photon absorption, but from the perspective of this work, the most important phenomenon is two-photon absorption (TPA), which is a third-order phenomenon, and in this paper we will denote it as nonlinear absorption. In that case the absorption coefficient becomes nonlinear:

$$\alpha = \alpha_0 + \beta I \quad (1.72)$$

where  $\alpha_0$  is the linear absorption coefficient and  $\beta$  nonlinear absorption coefficient. As we already said in previous paragraph, components of third-order nonlinear optical susceptibility tensor is a complex of real and imaginary part:

$$\chi^{(3)} = \chi'^{(3)} + i\chi''^{(3)}$$

where  $\chi''^{(3)}$  is the imaginary part related to nonlinear absorption of light and stimulated scattering and is described as [1.15]:

$$\chi''^{(3)} = \frac{n_0^2 \varepsilon_0 c \lambda}{3\pi} \beta \text{ [mW}^{-1}\text{]} \quad (1.73)$$

where:  $n_0$  is linear refractive index,  $c$  – speed of light.

Basically, we distinguish two types of nonlinear absorption depending on the change in the amount of radiation passing through the material: saturable absorption (SA) and reverse saturable absorption (RSA).

Saturable absorption (SA) characterizes decreasing of light absorption while light intensity increases. Saturable absorber can be characterized as a two-level electron system in which the electrons are in the ground state. When irradiating electrons with a low intensity source, these electrons are excited to a higher energy level - the light is absorbed. By applying a sufficiently high intensity of the incident light, molecules in the ground state of the saturable material are excited to the energy  $E_I$  with high speed that they do not have enough time to return to the ground state  $E_0$ . Additionally, in an ion-doping medium, the high intensity applied leads to exhaustion of the ground state of these ions. Another example is the effect found in semiconductors, where the excitation of electrons from the conductivity band causes a reduction in the absorption of photon energy just above the band gap. The SA property is bound to all high-power materials, however the advantage of the saturable absorber is the low-power absorption. The main application of saturable absorbers are Q-switching lasers. Insertion of a saturable absorbent into the laser cavity causes significant losses in the cavity until the absorbent is saturated. When the absorbent is saturated, it practically does not cause major losses, so laser amplification becomes very important.

The opposite process to SA is Reverse Saturation Absorption (RSA). In this case, the material's transmittance decreases as the incident radiation intensity increases, where strong radiation absorption occurs from higher energy levels. In the matter of RSA, the absorption cross section of the saturated absorber from the excitation level to the higher level must be larger compared with the absorption cross section from the ground state to the excited state. Moreover, the cross section of the ground state absorption must be that large enough so as the first excited level can be completely filled. Subsequently, excitation to a higher energy level should be fast enough for the electrons to be reabsorbed.

## 1.7. Nonlinear Refractive Index

Generally in optics, the refractive index of a medium is a measure of the change in the velocity of propagation of a wave in a given medium in relation to the velocity in another (reference) medium. A strong electric field of high intensity light can cause changes in the refractive index of the medium as the light passes through the medium. Such phenomena are described by nonlinear optics. If the coefficient changes in proportion to the square of the electric field strength (linearly with the light intensity), such a phenomenon is called the optical Kerr effect and causes further phenomena such as self-focusing and phase self-modulation, and if the coefficient changes linearly with the field strength (this only occurs in crystals without a center of symmetry) is called the Pockels effect.

As we previously said, we can describe third-order nonlinear optical susceptibility as:

$$\chi^{(3)} = \chi'^{(3)} + i\chi''^{(3)}$$

where:  $\chi'^{(3)}$  is the real part responsible for nonlinear variations in the refractive index [1.16]:

$$\chi'^{(3)} = \frac{4n_0^2 \epsilon_0 c}{3} n_2 [m^2 W^{-1}] \quad (1.74)$$



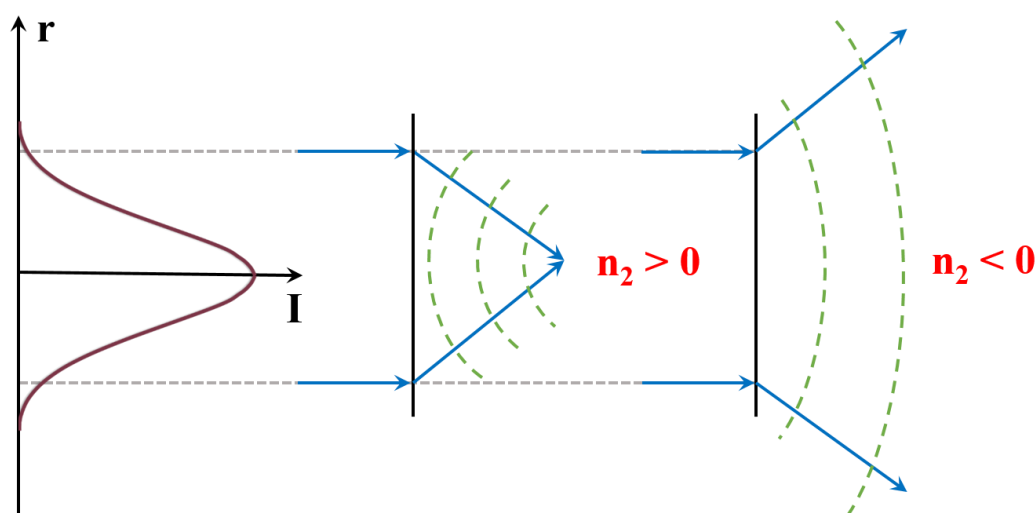
The value of  $n_2$  which is nonlinear refractive index is expressed in units [ $\text{m}^2\text{W}^{-1}$ ]. Pockels effect is called a linear electro-optical effect – forced birefringence. The phenomenon consists in changing the refractive index in proportion to the external electric field. Occurs only in crystals that do not show inversion symmetry (and therefore exhibit a piezoelectric effect). One of the properties of the linear electro-optical effect is the low inertia, which allows to modulate light in the high frequency range of several dozen gigahertz. This effect is described by a linear relationship between the change of the crystal optical indicator coefficients and the external electric field. The external electric field causes the ellipsoid's refractive indexes to rotate and deform. In general, the main axes of the ellipsoid do not coincide with the primary main axes. Equation describing Pockels effect is given in form of refractive index:

$$n(E) = n_0 + n_1 E \quad (1.75)$$

The Kerr electro-optical phenomenon is the appearance of birefringence in an isotropic medium under the influence of an applied electric field. It arises as a result of the arrangement of polar molecules of the medium towards the external electric field, due to which the medium becomes birefringent. After switching off the field, the material loses this property again becoming an optically isotropic medium. The ordering of the particles is counteracted by their thermal movements, which is why the Kerr coefficient decreases as the temperature increases. To observe the Kerr phenomenon, application an electric field is carried out perpendicular to the running beam of linearly polarized light at an angle of  $45^\circ$  to the electric field. At the cell output, the light is polarized elliptically depending on the light path in the medium, the electric field strength and the type of substance. The device built in this way is called a Kerr cell. Therefore, refractive index is given by following equation [1.17]:

$$n(E) = n_0 + \frac{n_2}{2} E^2 \quad (1.76)$$

Self-focusing is a nonlinear optical process induced by changing the refractive index of materials exposed to intense electromagnetic radiation. The medium, whose refractive index increases with the intensity of the electric field, acts as a focusing lens for the electromagnetic wave characterized by the initial transverse intensity gradient, as in a laser beam. The peak intensity of the self-focused region is steadily increasing as the wave passes through the medium until defocusing effects or medium damage interrupt this process. The opposite situation is when the refractive index increases while the intensity of laser beam decreases. This effect is called self-defocusing. Fig. 1.8 presents phenomena of both effects.



**Figure 1.9:** Schematic illustration of self-focusing ( $n_2 > 0$ ) and self-defocusing ( $n_2 < 0$ ) effect.

## 1.8. Applications

Generally, nonlinear optics has a huge influence on everyday life [1.18]. One of the most distinctive uses of nonlinear optics is frequency doubling and second harmonic generation. An example is the use of Nd: YAG laser light with a wavelength of 1064 nm, which, upon contact with a nonlinear material, is converted into visible light with a wavelength of 532 nm (green color). Although there exist many nonlinear materials and new materials with strong nonlinearity are still being sought,

the most commonly used in this process are crystals such as BBO (beta-barium borate), KTP (potassium titanyl phosphate), KDP (potassium dihydrogen phosphate), and also  $\text{LiNbO}_3$  (lithium niobate) [1.19 – 1.22]. These crystals are distinguished due to their unique properties, which is strong birefringence, thanks to which the phase matching described in subsection 1.2 is obtained. Besides, the crystals have a certain symmetry, which is necessary to obtain a nonlinear second-order effect, and are optically transparent to laser light with the incident wavelength and the generated harmonic.

Another application that uses second-order nonlinear optical phenomena is high-resolution microscopic SHG imaging, most often used in biological and medical sciences [1.23]. One of the non-centrosymmetric SHG-emitting structures is collagen, which is found in most tissues. By comparing the images of the generated second harmonic, it is possible to see the microstructure of collagen, identify changes in its structure and recognize tumor characteristics (breast cancer, ovarian cancer, skin cancer, lung cancer, and other neoplasms), as well as its progression. Apart from neoplastic changes detected in collagen tissues, thanks to SHG microscopy, it is possible to diagnose pathologies occurring in tissues, cartilage or skin with separation of SHG polarization [1.24]. Other examples of applications of SHG imaging are the study of the eye structure [1.25], as well as tissue engineering that allows for the design of artificial tissues by imaging the orientation and amount of distribution of materials in the tissue [1.26].

In addition to the aforementioned second order effect applications, SHG is commonly used to characterize both organic and inorganic materials. As mentioned before, this effect is only possible in materials that do not contain a center of symmetry. Therefore, thanks to the SHG technique, it is possible to easily and quickly detect material noncentrosymmetry, both in crystals and in powdered form, using the apparatus constructed by Kurtz and Perry [1.27].

Additionally to second-order nonlinear phenomena, third-order NLO effects are used in many applications in everyday life. One of them is, among others, phase conjugation, which uses, inter alia, mixing four waves, mixing three waves, and holography. In this process, two incident waves interact simultaneously in a nonlinear optical material, and the third (or fourth) wave at this time deflects in the resulting dynamic hologram and reads the conjugated phase [1.28]. Besides, another example of applications using  $\chi^{(3)}$  is mode-locking, consisting in generating pulses of laser light in a very short time, on the order of pico- and femtoseconds [1.29], which are commonly used in medicine and nonlinear optics.

Materials with strong nonlinear absorption are used, among other things, for optical 3D data storage and imaging. Due to the phenomenon of two-photon absorption (TPA) in the depths of the material, it is possible to record and read information not only on its surface [1.30]. Another example is semiconductor imaging, thanks to which we obtain information about the properties of charge transfer in semiconductor devices. Moreover, TPA is widely used in medicine, in imaging with dyes showing a strong absorption nonlinearity [1.31], and in photodynamic therapy, which is a method of cancer treatment, by using materials characterized by a strong NLO absorption in the infrared range [1.32]. Furthermore, materials with strong reverse saturable absorption (RSA) find potential applications as optical limiters, which are widely used as detectors to protect the eyes from strong laser radiation. Optical limiting is based on the phenomena when the intensity of the laser light is increased, the transmittance of such material decreases [1.33]. Moreover, materials showing nonlinear absorption and/or nonlinearity in refractive index find applications in Q-switching: the optical element of the laser, thanks to which it is possible to create a pulsed beam of high power, much higher than the continuous beam. This method differs from the above-mentioned mode locking due to lower frequencies and longer pulse durations (ns). There are two main types of Q-switching: active, which often uses magneto-optic effects and the Pockels effect and the Kerr effect; passive - a saturable absorber is used, i.e. a material whose transmittance

increases when the light intensity reaches a certain value. Q-switching lasers are most often used when very high intensity laser beams with short pulses, usually nanoseconds, are required, including in holography or metal cutting, as well as for data storage.

Another effect that is based on NLO is optical bistability, which is used in optical devices such as memory devices, optical transmitters. This effect is obtained in two ways, the first being absorption bistability, in which the absorber blocks the laser light depending on its intensity [1.34]. Then two transmission states occur, in which once the absorber is not used at a given intensity, and in the second case the state occurs when, for a certain intensity, the light crosses the blockage of the absorber. Another way is to use the changes in the refractive index in the same way [1.35].

Other phenomena that exploit the nonlinear refractive index is the photorefractive effect, in which the material (most often a crystal) reacts to light by changing  $n_2$ , using, for example, the electro-optical effect and the formation of interference gratings. The most common application of photorefractive effect is creating dynamic holography [1.36]. Moreover, another application of the Kerr effect, in which the nonlinear refractive index changes, is self-phase modulation, which is the phase shift of the pulse, causing the pulse frequency spectrum to change with the change of  $n_2$ . This effect is commonly used in optical fibers [1.37].

## Literature

- [1.1] R. W. Boyd, Nonlinear Optics, Academic Press, 2008.
- [1.2] S. Kielich, Molekularna optyka nieliniowa, Polish Scientific Publishers PWN, Warsaw – Poznan, 1977.
- [1.3] Y. R. Shen, The principles of nonlinear optics, John Wiley and Sons Inc. 1984.
- [1.4] J. F. Reintjes, Nonlinear optical parametric processes in liquids and gases, Academic Press, 1984.

- [1.5] P. D. Maker, R. W. Terhune, M. Nisenoff, C. M. Savage, Effects of dispersion and focusing on the production of optical harmonics, Phys. Rev. Lett. Vol. 8, N. 1, 1962.
- [1.6] D. A. Kleinman, Theory of Second Harmonic Generation of Light, Phys. Rev. 128, 1761, 1962.
- [1.7] D. A. Kleinman, Nonlinear Dielectric Polarization in Optical Media, Phys. Rev. 126, 1997, 1962.
- [1.8] R. D. Guenther, Modern Optics, Ed. John Wiley and Sons, 1990.
- [1.9] M. Braun, F. Bauer, T. Vogtmann, S. Schwoerer, Precise second-harmonic generation Maker fringe measurements in single crystals of the diacetylene NP/4-MPU and evaluation by a second-harmonic generation theory in  $4 \times 4$  matrix formulation and ray tracing, J. Opt. Soc. Am. B 14, 1699, 1997.
- [1.10] J. P. Bourdin, P. X. Nguyen, G. Rivoire, and J. M. Nunzi, Polarization properties of the orientational response in phase conjugation, Nonlinear Opt., 7, 1-6, 1994.
- [1.11] B. Sahraoui, X. Nguyen Phu, T. Nozdryn, and J. Cousseau, Electronic and nuclear contributions to the third-order nonlinear optical properties of new polyfluoroalkylsulfanyl-substituted tetrathiafulvalene derivatives, Synth. Met., 115, 261-264, 2000.
- [1.12] W. Demtröder, Laser Spectroscopy, Polish Scientific Publishers PWN, Warsaw, 1993.
- [1.13] R. P. Feynman, R. B. Leighton, M. Sands, The Feynman Lectures on Physics, Addison-Wesley, 1964.
- [1.14] J. R. Albani, Principles and Applications of Fluorescence Spectroscopy, Blackwell Science, 2007.
- [1.15] G. I. Stegeman and R. A. Stegeman, Nonlinear optics: phenomena, materials, and devices, John Wiley and Sons Inc., 2012.

- [1.16] R. del Coso and J. Solis, Relation between nonlinear refractive index and third-order susceptibility in absorbing media, *Journal of the Optical Society of America B* Vol. 21, Issue 3, pp. 640-644, 2004.
- [1.17] M. Sheik-Bahae, A. A. Said, T.-H. Wei, D. J. Hagan, E. W. Van Stryland, Sensitive measurement of optical nonlinearities using a single beam, *Quantum Electron. IEEE J. Of* 26, 760 (1990).
- [1.18] E. Garmire, Nonlinear optics in daily life, *Optics Express*, 21 (25), 2013.
- [1.19] S. N. C. Santos, J. M. P. Almeida, K. T. Paula, N. B. Tomazio, V. R. Mastelaro, C. R. Mendonca, Characterization of the third-order optical nonlinearity spectrum of barium borate glasses, *Optical Materials*, 73, 2017, 16-19.
- [1.20] N. Chauvet, M. Ethis de Corny, M. Jeannin, G. Laurent, S. Huant, T. Gacoin, G. Dantelle, G. Nogues, G. Bachelier, Hybrid KTP–Plasmonic Nanostructures for Enhanced Nonlinear Optics at the Nanoscale, *ACS Photonics* 2020, 7, 3, 665–672.
- [1.21] V. I. Bespalov, V. I. Bredikhin, V. P. Ershov, V. I. Katsman, L. A. Lavrov, KDP and DKDP crystals for nonlinear optics grown at high rate, *Journal of Crystal Growth*, 82(4), p. 776-778, 1987.
- [1.22] G. D. Boyd, R. C. Miller, K. Nassau, W. L. Bond, A. Savage, LiNbO<sub>3</sub>: An Efficient Phase Matchable Nonlinear Optical Material, *Appl. Phys. Lett.* 5, 234 (1964).
- [1.23] P. Pantazis, J. Maloney, D. Wu, S. E. Fraser, Second harmonic generating (SHG) nanoprobe for in vivo imaging, *PNAS*, 2010, 107 (33), 14535-14540.
- [1.24] J. C. Mansfield, C. P. Winlove, J. J. Moger, S. J. Matcher, Collagen fiber arrangement in normal and diseased cartilage studied by polarization sensitive nonlinear microscopy, *J. of Biomedical Optics*, 13(4), 044020 (2008).

- [1.25] H-Y. Tan, S-W. Teng, W-C. Lin, S-J. Lin, S-H. Jee, C-Y. Dong, Characterizing the thermally induced structural changes to intact porcine eye, part 1: second harmonic generation imaging of cornea stroma, *J. of Biomedical Optics*, 10(5), 054019 (2005)
- [1.26] P. J. Campagnola, A. C. Millard, M. Terasaki, P. E. Hoppe, C. J. Malone, W. A. Mohler, Three-Dimensional High-Resolution Second-Harmonic Generation Imaging of Endogenous Structural Proteins in Biological Tissues, *Biophysical Journal*, 103(3), 2012.
- [1.27] S. K. Kurtz, T. T. Perry, A Powder Technique for the Evaluation of Nonlinear Optical Materials, *Journal of Applied Physics* 39, 3798 (1968).
- [1.28] I. N. Papadopoulos, S. Farahi, C. Moser, D. Psaltis, Focusing and scanning light through a multimode optical fiber using digital phase conjugation, *Optics Express*, 20(10), 10583-10590 (2012).
- [1.29] Z. Luo, Y. Li, M. Zhong, Y. Huang, X. Wan, J. Peng, J. Weng, Nonlinear optical absorption of few-layer molybdenum diselenide ( $\text{MoSe}_2$ ) for passively mode-locked soliton fiber laser, *Photonics Research*, 3(3), pp. A79-A86 (2015).
- [1.30] A. M. McDonagh, M. G. Humphrey, M. Samoc, B. Luther-Davies, Organometallic Complexes for Nonlinear Optics. 17.<sup>1</sup> Synthesis, Third-Order Optical Nonlinearities, and Two-Photon Absorption Cross Section of an Alkynylruthenium Dendrimer, *Organometallics* 1999, 18, 25, 5195–5197.
- [1.31] W. Yang, P. S. Chan, M. S. Chan, K. F. Li, P. K. Lo, N. K. Mak, K. W. Cheah, M. S. Wong, Two-photon fluorescence probes for imaging of mitochondria and lysosomes, *Chemical Communications*, 33, 2013.



- [1.32] Y. Zhou, Y-K. Cheung, C. Ma, S. Zhao, D. Gao, P-C. Lo, W-P. Fong, K. S. Wong, D. K. P. Ng, Endoplasmic Reticulum-Localized Two-Photon-Absorbing Boron Dipyrromethenes as Advanced Photosensitizers for Photodynamic Therapy, *J. Med. Chem.* 2018, 61, 9, 3952–3961.
- [1.33] G. S. He, J. D. Bahwalkar, C. F. Zhao, P. N. Prasad, Optical limiting effect in a two - photon absorption dye doped solid matrix, *Appl. Phys. Lett.* 67, 2433 (1995).
- [1.34] A. Ghasedi, E. Koushki, J. Baedi, Optical nonlinearity, saturation in absorption and optical bistability of AZO films synthesized in presence of sodium hydroxide, *Physica B: Condensed Matter*, 587, 15, 2020, 412148.
- [1.35] P-Y. Chen, M. Farhat, A. Alu, Bistable and Self-Tunable Negative-Index Metamaterial at Optical Frequencies, *Phys. Rev. Lett.* 106, 105503, 2011.
- [1.36] E. Benoit a la Guillaume, U. Bortolozzo, J-P. Huignard, S. Residori, F. Ramaz, Dynamic ultrasound modulated optical tomography by self-referenced photorefractive holography, *Optics Letters*, 38(3), pp. 287-289 (2013).
- [1.37] E. P. Ippen, C. V. Shank, T. K. Gustafson, Self - phase modulation of picosecond pulses in optical fibers, *Appl. Phys. Lett.* 24, 190 (1974).

## CHAPTER 2: SUPRAMOLECULAR CHEMISTRY

### 2.1. History of Supramolecular Chemistry

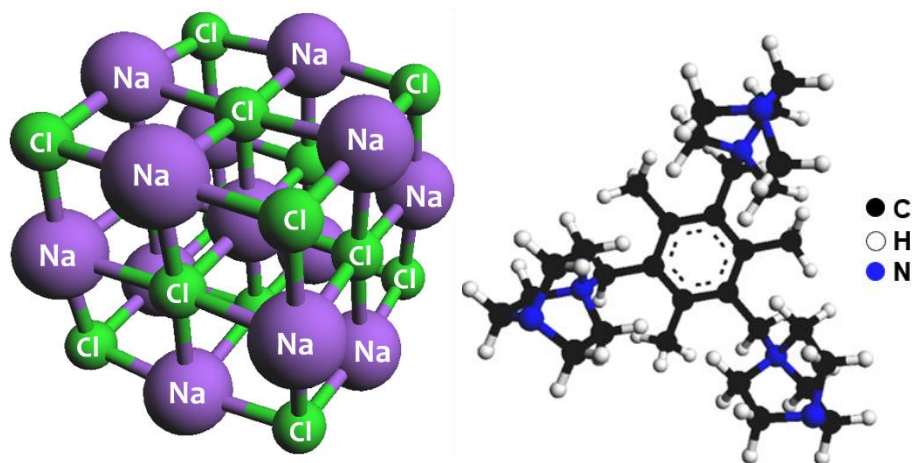
The first occurrence of intermolecular interactions was postulated by J. D. van der Waals in 1873 [2.1] but the first concept consistent with the supramolecular chemistry was the Lock-and-Key mechanism described by E. Fisher in 1894 [2.2]; proposed mechanism explained the recognition of the substrate by the enzyme. Further development of intermolecular interaction research took place at the beginning of the 20th century with the discovery of hydrogen bonds [2.3]. This research enabled a much better way to understand the structure of protein and nucleic acids, culminating in the discovery of DNA in 1953 by J. Watson and F. Crick [2.4]. During this period, research and synthesis of artificial systems based on noncovalent interactions began as well. However, another breakthrough was the synthesis of crown ethers by C. J. Pedersen in 1960s [2.5]. Based on his studies, successive chemists, such as D.J. Cram, J-M. Lehn, have investigated various kinds of artificial ion receptors and mechanically intertwined systems [2.6]. The importance of supramolecular chemistry had increased significantly while D. J. Cram, J-M. Lehn and C. J. Pedersen received the Nobel Prize in chemistry of their studies in 1987 [2.7].

Supramolecular chemistry is the chemistry of 21<sup>st</sup> century. It finds application in the areas of science: conversion of light by energy transfer [2.8], conductors of electricity [2.9], optical sensing [2.10], and others. Due to their unique properties, supramolecular complexes are promising in nonlinear optics as well as in nanophotonics.

### 2.2. Main Concepts

Supramolecular chemistry refers to systems composed of more than one molecule - complexes. In contrast to, *inter alia*, classical organic chemistry, supramolecular chemistry is based on noncovalent interactions, which include ion-ion interactions (the strongest), ion-dipole

interactions, dipole-dipole interactions, Hydrogen bonds, Halogen bonds, van der Waals forces, interactions involving  $\pi$ -systems, likewise metal-ligand coordination host-guest interactions and  $\pi$ - $\pi$  stacking, and hydrophobic effects (the weakest) [2.11 – 2.12]. These weak interactions play a very important role, inter alia, in polymers, charge transfer complexes, mono- and poly-layers, liquid crystals that fall within the scope of supramolecular chemistry. Each of these interactions has unique advantages. One of the most obvious advantages are their response to external factors including polarity of the medium, concentration and temperature, as well as their inherent nature. Hydrogen bonds seems to be most interesting according to their long lifetime, dynamic control and directionality [2.13].

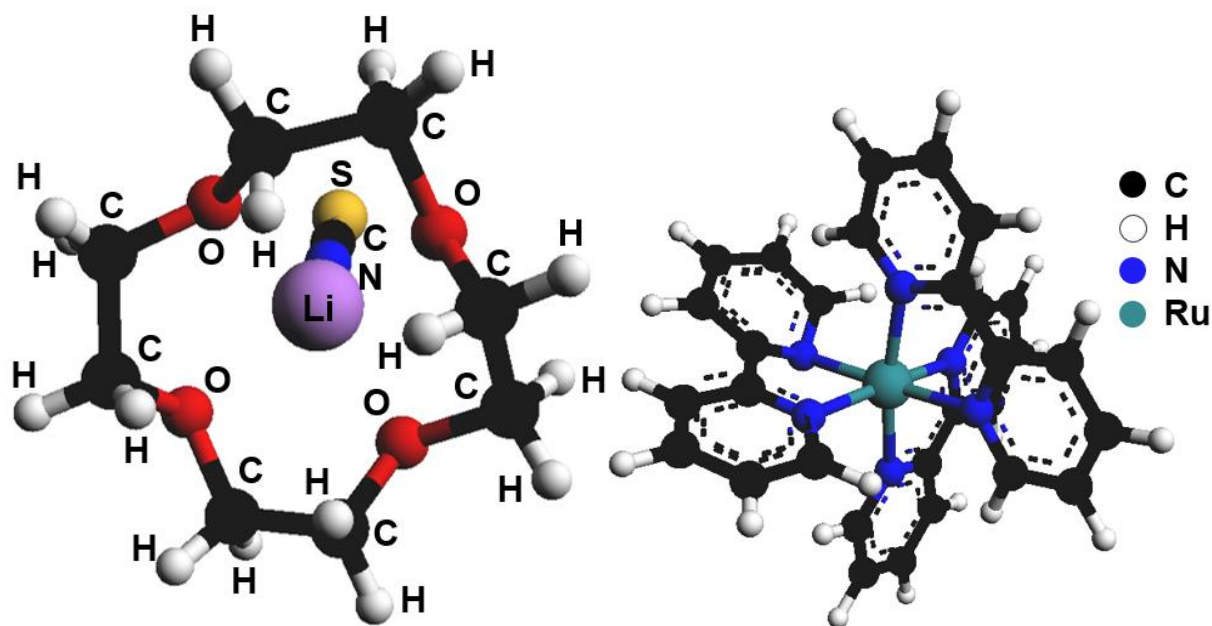


**Figure 2.1:** NaCl as an examples of material with ion-ion interactions (a) and chemical structure of tris(diazabicyclooctane) used as a host to build supramolecular systems (b).

Electrostatic ion-ion interactions take place between two differently charged molecules, for example NaCl (Fig. 2.1 a). Contrary to ionic bonds, the charge in the interacting molecules is not concentrated on one atom, but is delocalized (it occurs on several or a dozen atoms). The force of its interaction is proportional to  $1/r^2$  (where  $r$  is the distance between molecules), in the case of a medium containing other charges (e.g. electrolyte solution), the effect of the interaction is smaller. The bond energies are placed between  $100\text{--}350\text{ kJ mol}^{-1}$  making them the strongest non-covalent

interaction, however this energy is comparable in strength to covalent bonding. An example of an ion-ion interaction in supramolecular materials can be the interaction of a tris(diazabicyclooctane) (Fig. 2.1 b), present as a host, with anions such as  $\text{Fe}(\text{CN})_6^{3-}$  [2.14]

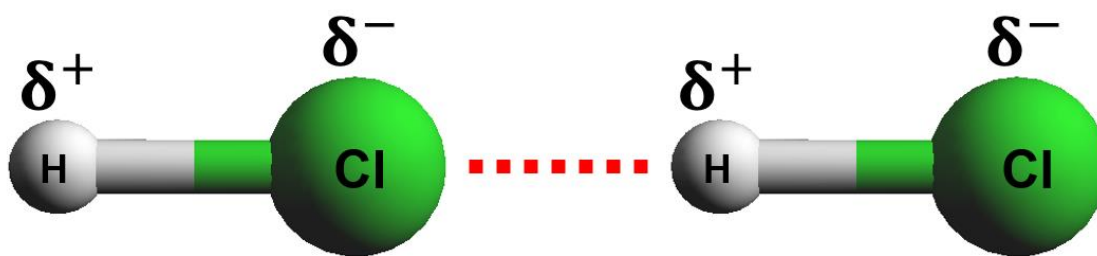
Ion-dipole interactions are characterized by the fact that they occur in both the liquid and solid state. Such an interaction occurs during the interaction of an ion (cation) with the free pairs (polar part) of a molecule on oxygen, nitrogen or sulfur atoms. This interaction is characterized by the energy of 50 - 200  $\text{kJ mol}^{-1}$ . Examples of supramolecular compounds in which an ion-dipole interaction occurs are, inter alia, metal-crown ether complexes [2.15] as well as  $[\text{Ru}(\text{BPY})_3]^{2+}$  [2.16]. Schematic chemical structures with ion-dipole interactions are presented in Fig. 2.2.



**Figure 2.2:** Schematic structures of 12-crown-4-Lithium complex ( $\text{LiSCN}$ ) and  $[\text{Ru}(\text{BPY})_3]^{2+}$ .

The dipole-dipole interaction is formed between molecules that have permanent dipole moments. Such particles have an excess of negative charge in some places, and its deficiency in others, and they also interact with each other like ions, but the interaction is weaker, because partial (not total) electric charges are involved, as well as the attraction of unlike charges. It is always accompanied by the repulsion of the homonymous charges, the interaction energy is between 5 - 50  $\text{kJ mol}^{-1}$ .

There are two types of dipole-dipole interaction: the first type occurs in the case of attraction resulting from the pairing of single pairs of poles of adjacent molecules, while the second type is the opposite orientation of one of the dipoles in relation to the other. Such an interaction is typical for organic carbonyl compounds [2.17]. The principle of dipole-dipole interactions is presented in Fig. 2.3.



**Figure 2.3:** Schematic example of dipole-dipole interaction.

The most important interaction - Hydrogen bonds are a kind of electrostatic interaction between a hydrogen atom and an electronegative atom containing free electron pair, which makes them a special type of dipole-dipole interaction. There are three types of hydrogen bonds [2.18]: a) strong hydrogen bonds – the interaction between two centre bonds are involved with short distance and bond energies higher than  $40 \text{ kJ mol}^{-1}$ ; b) medium and weak hydrogen bonds – the directionality is lost in part and the bond energies are placed between  $20\text{-}40 \text{ kJ mol}^{-1}$ ; c) unconventional hydrogen bonds – where  $\pi$ -systems or transition metals or boron hydrides plays acceptor role. Fig. 2.4 presents examples of two main types of hydrogen bonds. The bonds discussed are relatively strong interactions directed in a specific direction, so that they enable to obtain well-defined structures whose durability can be regulated based on the conditions in which they are located. The structure of the DNA double helix is based largely on the occurrence of a number of hydrogen bonds [2.19] (Fig. 2.5). Hydrogen bonds are ubiquitous in supramolecular chemistry.

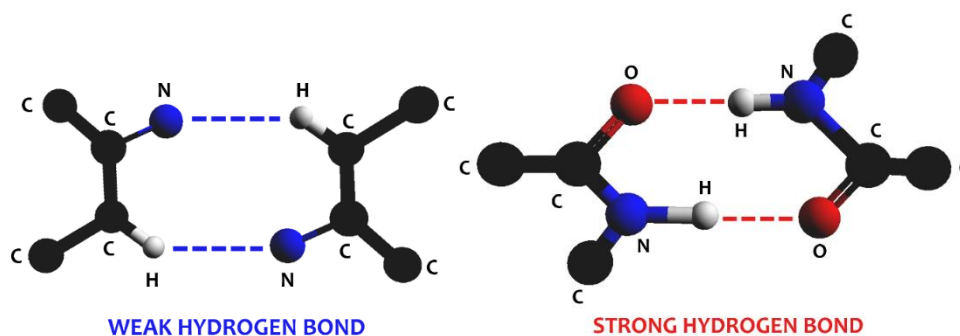


Figure 2.4: Schematic examples of strong and weak hydrogen bonds.

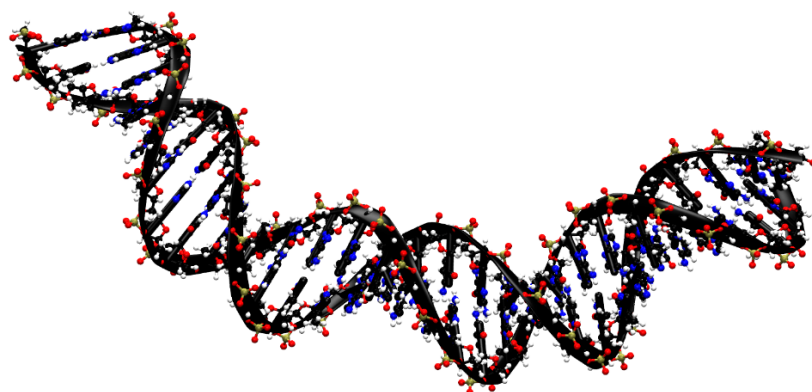


Figure 2.5: Schematic example of double helix DNA structure.

The Halogen bond is characterized by very low energy, around  $8 \text{ kJ mol}^{-1}$ . It is defined as a bonding interaction through the space between a bond donor atom and a halogen (acceptor) atom covalently bonded to any other non-hydrogen atom [2.20 – 2.23]. Schematic example of structure with Halogen-bond interactions are presented in Fig. 2.6.

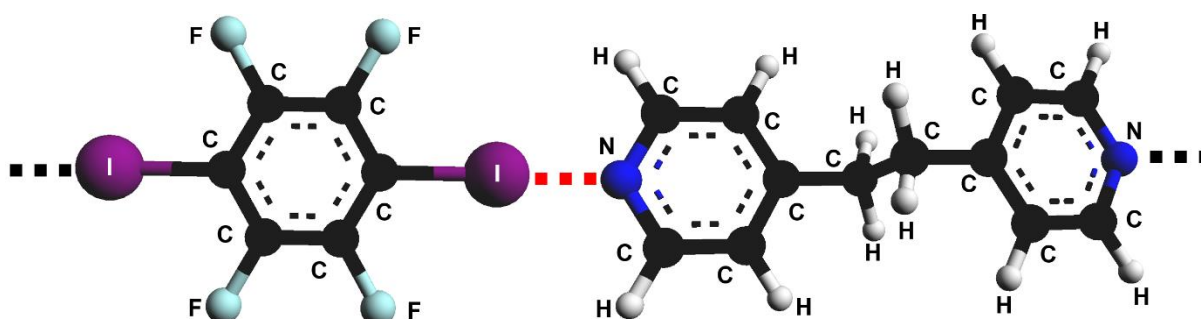
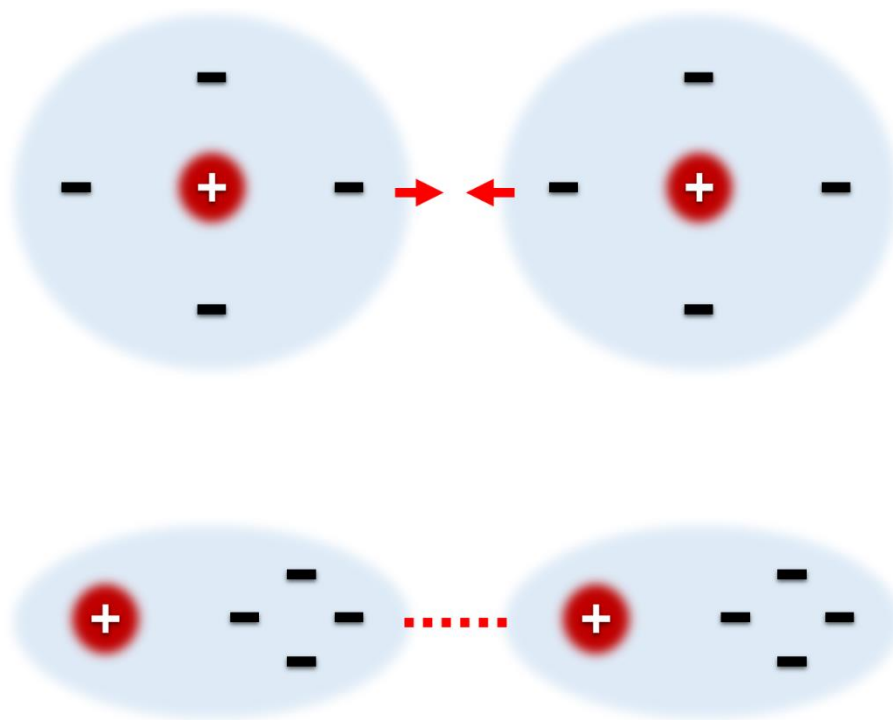


Figure 2.6: Schematic example of Halogen bond interaction (red bond).

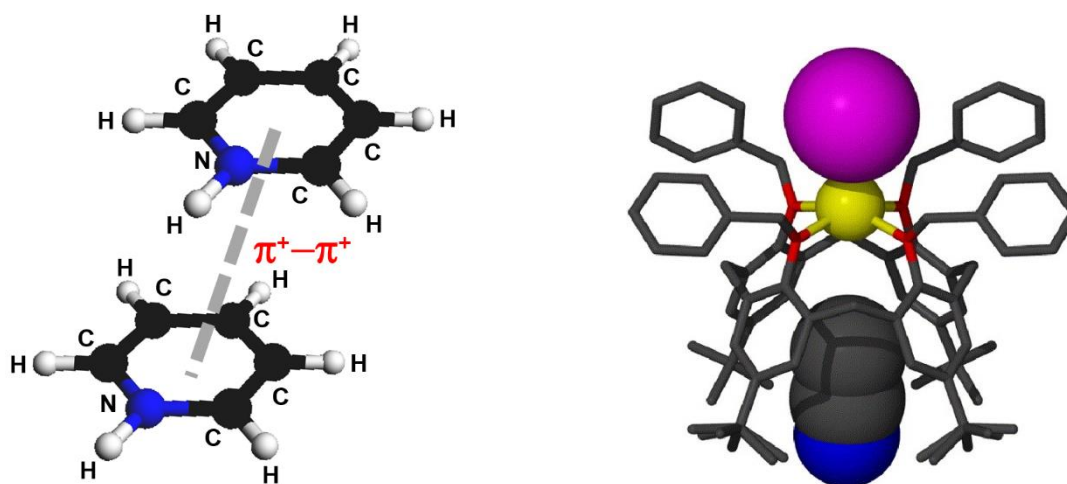
In contrast to hydrogen bond, van der Waals interactions [2.24] are the interactions between persistent and induced dipole. In molecules without a stable dipole moment, it can be excited by molecules with a permanent moment, then such an excited dipole and stable dipole interact as well as two persistent dipoles, with an energy less than  $5 \text{ kJ mol}^{-1}$ . A molecule with a momentary dipole moment can excite it in a neighbouring molecule, as a result of which both molecules can temporarily attract or repel one another. The averaging of repulsive and attractive forces gives an attractive impact proportional to distance between molecules  $r^{-6}$  [2.25]. Fig. 2.7 presents an schematic example of van der Waals interaction.



**Figure 2.7:** Schematic example of van der Waals interactions.

The interactions of  $\pi$ -systems are divided into three categories: the first is  $D - H \cdots \pi$ , the second is  $\pi - \pi$  stacking, and the third is cation- $\pi$ , however  $D - H \cdots \pi$  can be classified as hydrogen bonding. The  $\pi - \pi$  interactions are weak electrostatic interactions that occur between aromatic rings, often in situation where one compound is rich in electrons. Due to supramolecular chemistry, an

example is the interaction between the aromatic ring in nucleophilic nucleobases of a DNA helix [2.26 – 2.27]. The most popular  $\pi$ - $\pi$  interaction geometries are edge to face (herringbone pattern) and offset face to face. The energy of such stacking is 0-50 kJ mol<sup>-1</sup>. On the other hand, the cation- $\pi$  interactions may be slightly stronger and have an energy of 5-80 kJ mol<sup>-1</sup>, which may even be comparable to the energy of a hydrogen bond. These are non-covalent interactions between the  $\pi$  orbitals of an aromatic ring rich in electrons with the adjacent metallic or organic (for example pyrazolinium) cation [2.28]. Fig. 2.8 presents schematic examples of  $\pi$ - $\pi$  and cation- $\pi$  interactions in typical chemical structures.

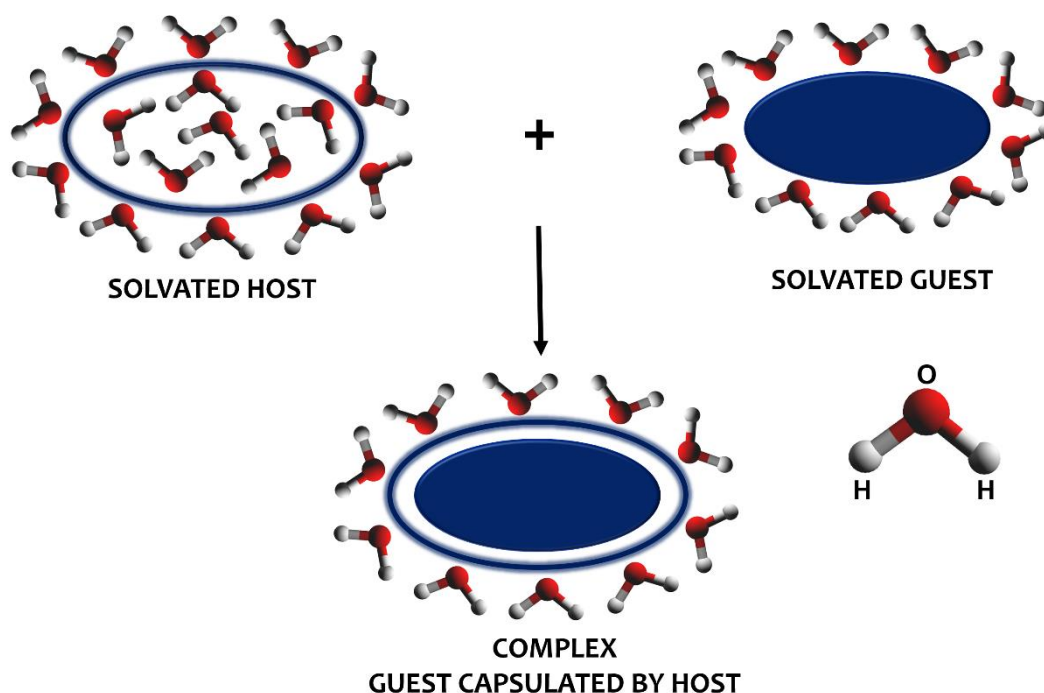


**Figure 2.8:** Schematic examples of complexes with face to face  $\pi$ - $\pi$  stacking (a) and cation- $\pi$  interaction (sodium tetrabenzoyloxy-p-tert-butylcalix[4]arene (3NaI) complex) [2.28] (b).

The weakest non-covalent effect is the hydrophobic effect (Fig. 2.9). This effect occurs when molecules lacking a dipole moment (nonpolar) repel the solvent, which is water, from each other. There are two effects: enthalpic, in which the polar solvent stabilizes excluded from the cavity upon guest binding, and entropic, in which the combination of guest and host results in less disruption in relation to the solvent structure. In hydrophobic effect, the entropy increases due to the exclusion of the non-polar substance by water, which interacts during dissolution and enters a



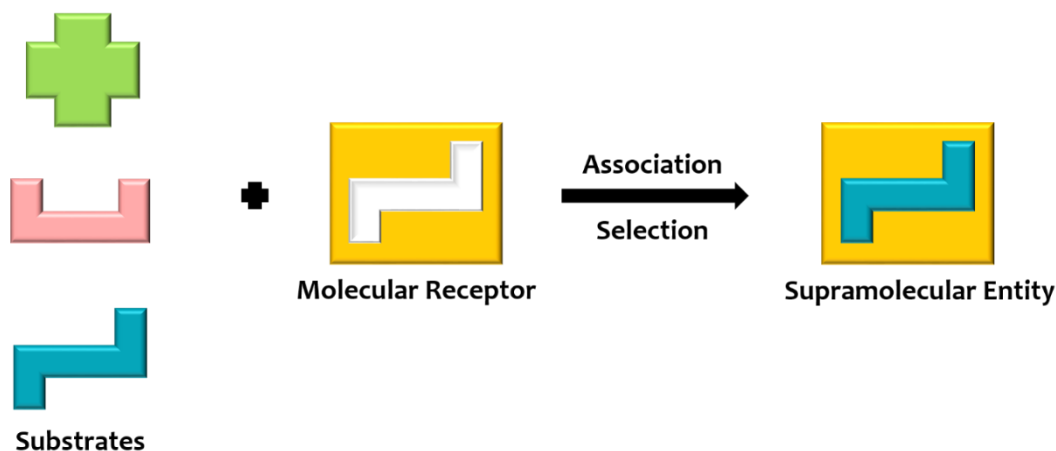
higher state of disorder. An example of supramolecular systems is the aforementioned cyclodextrins with attached organic guests in water [2.29 – 2.30].



**Figure 2.9:** Schematically presented mechanism of forming supramolecular complex caused by hydrophobic effect.

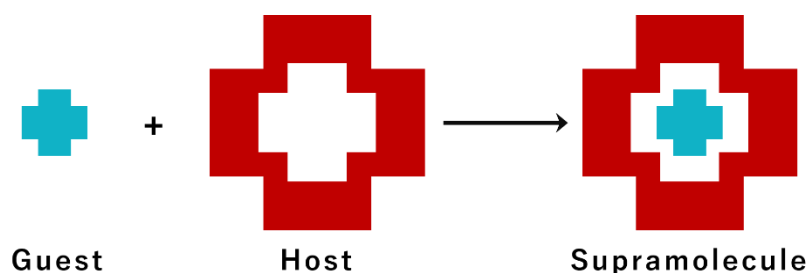
Generally, we distinguish two main concepts of supramolecular chemistry. The first of them is molecular self-organization. It involves spontaneous organization into more complex systems without external interference. Self-organization process may also refer to individual molecules that spontaneously adopt a specific structure, for example folding of proteins [2.31]. Self-assembly of molecular systems leads to self-association of complicated supramolecular systems. Supramolecular association is caused by weak intermolecular interactions, and the process is based on the template effect, which requires several stages to occur spontaneously. The second term is molecular recognition (Fig. 2.10), which means the specific of a compound coordinated by the larger structure – a ligand that results in a guest-host complex. The recognition consists in creating selective binding of the substrate molecule called a “guest” with a receptor, called the “host”. These terms are

arbitrary, usually the larger molecule is called the host and the smaller guest. The recognition of both molecules occurs due to non-covalent interactions and is very specific [2.32].



**Figure 2.10:** Schematic illustration of molecular recognition process.

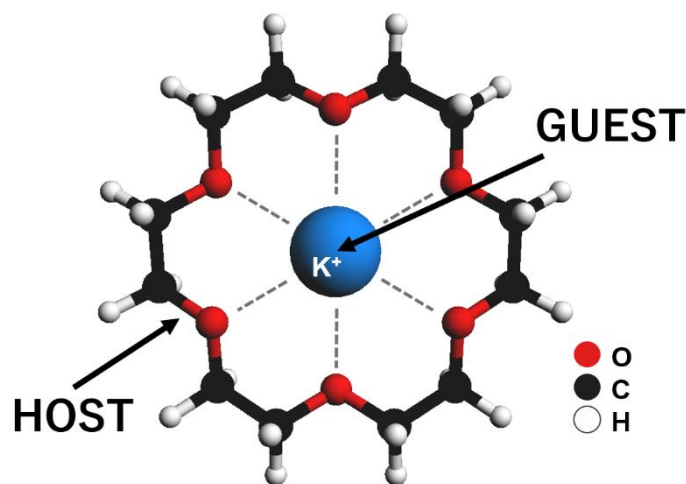
One of the main terms in supramolecular chemistry is the concept of a complex-forming ligand, called as molecular “host”. Such ligand is made of electron-donating atoms of oxygen, sulphur or nitrogen. These ligands can form complexes with, for example, metal ions, which are “guest” molecules. The resulting “guest-host” complexes are created on the basis of so-called concepts, including molecular recognition. Due to Fig. 2.11, when the “guest” molecule connects to the ligand molecule, the “lock and key” effect is created.



**Figure 2.11:** Scheme describing the formation of a supramolecule in guest-host interaction.

Guest-host complexes generally consist of several molecules (usually two) and the physicochemical methods used to study them are similar to those used in classical organic

chemistry. Complexes composed of a larger number of molecules are characterized by the fact that they are formed by a much larger and inaccurately defined number of molecules. They are similar in this respect to polymers whose molecular weight is only known approximately. Fig. 2.12 presents an example of a guest-host system.



**Figure 2.12:** Schematic example of guest-host supramolecular complex.

### 2.3. Applications

Modern supramolecular systems are refined and complex, and some of them are molecular machines modelled on such biomolecules as motor proteins or cancer system cells [2.33 – 2.34]. Therefore, there are increasingly frequent applications of the achievements of electrochemistry for the design of new supramolecular systems [2.35]. Processes of self-assembly of matter have been successfully used to create new materials. As an example may be various supramolecular polymers composed of organic molecules, connected to each other by noncovalent interactions [2.36]. Another example is the design of new porous materials made of small molecules connected by weak noncovalent forces as well [2.37]. Supramolecular materials play a very important role in medicine. Assemblies are used, for example, to study the interactions of ligands with biomolecules, such as proteins or nucleic acids [2.38]. The knowledge about these interactions is currently of great

importance in the design of drug delivery [2.39] or in the treatment of cancer [2.40]. One of the statutory tasks of supramolecular chemistry is the use of matter to perform calculations at the atomic scale. The storage of the information in supramolecular systems is usually done through use of the molecular switches. Many publications present data storage in supramolecular systems, such as two-photon induced data storage in supramolecular azopolymers [2.41] or in thin films formed by supramolecular assembly [2.42]. Supramolecular systems were studied for nonlinear optics as well. Studies of the second order nonlinearity in supramolecular polymers were described in [2.43], however other tests present the third order optical nonlinearity of metallo-supramolecular complexes based on phthalocyanine [2.44], fullerenes connected with rotaxanes [2.45] or of ammonium picrates [2.46]. Most of the experiments investigated nonlinear optical responses were examined by using the Z-scan technique [2.47 – 2.48]. Nevertheless, other studies of supramolecular systems were performed for light up-conversion [2.49].

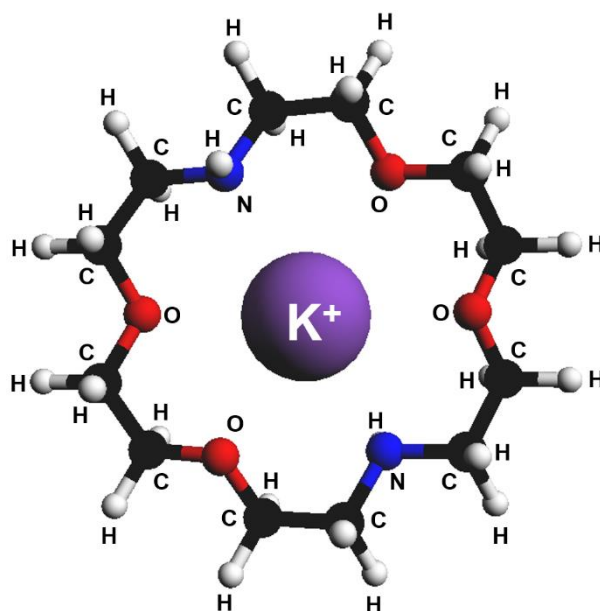
## 2.4. Supramolecular systems

Supramolecular chemistry is characterized by the fact that chemical compounds are rarely made from “zero”. For this purpose, the previously obtained systems are used as building blocks for new supramolecular structures. The following subchapters present some specific examples of chemical compounds from macrocyclic groups, compounds of metal complexes, as well as systems of biological origin. As mentioned before, most often these are guest-host systems, where the host is usually an organic macrocyclic compound, and the guest is a much smaller structure, that may be a cation or anion, which is located in a special place of the host, thus creating complex.

### 2.4.1. Crown Ethers

They belong to the group of macrocyclic organic compounds of synthetic origin. Most often they are cyclic polyethers with a regular structure, capable of selectively forming stable complexes with cations, most often with alkali metals. As mentioned earlier, the first crown ether was synthesized

by Charles Pedersen in 1967, who then received the 1987 Nobel Prize along with Donald Cram and Jean-Marie Lehn. The most important and interesting physicochemical properties of crown ethers are, first of all, their solubility in almost all known solvents, and they are also very good ligands for many ions, which combine relatively with weak ion-dipole interactions, but form a strong complex. What's more, they are used as catalysts to accelerate chemical reactions, as well as in environmental protection, by removing toxic heavy metal ions from water. Besides, they are widely researched in terms of nonlinear optics, Kerr effects, generation of higher harmonics or optical birefringence [2.50 – 2.52]. Fig. 2.13 presents example of crown ethers.

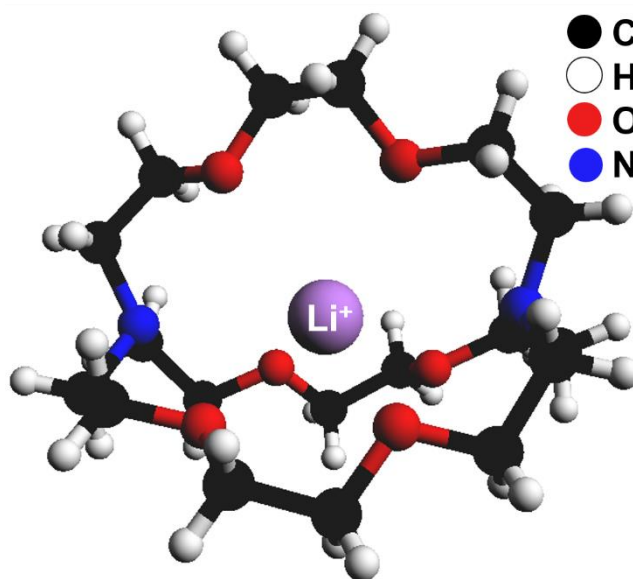


**Figure 2.13:** Schematic example of crown ether complex (1,10-Diaza-18-Crown-6) with potassium.

#### 2.4.2. Cryptands

Similarly to crown ethers, cryptands are organic chemical compounds obtained synthetically. They are characterized by a strong complexing action, creating chelate compounds (i.e. those where the organic ligand is combined with the central ion by more than one coordination bond), with a characteristic spherical structure, resembling a so-called crypt - hence the nomenclature. Due to

their coordination properties, they are often used with transition metals and rare earth ions. An example of a complex of cryptand with lithium  $\text{Li}^+$  is shown in Fig. 2.14. Cryptands, similarly to the supramolecular compounds mentioned above, were also studied for nonlinear optics, by means of the second-order nonlinear properties of the complexes with barium  $\text{Ba}^+$ , lithium  $\text{Li}^+$ , nickel  $\text{Ni}^{2+}$ , zinc  $\text{Zn}^{2+}$ , copper  $\text{Cu}^{2+}$ , as well as cadmium  $\text{Cd}^{2+}$  ions [2.53 – 2.54].



**Figure 2.14:** Schematic example of supramolecular cryptand  $\text{Li}^+$  complex.

### 2.4.3. Cyclophanes

Cyclophanes belong to the group of organic compounds derived from aromatic hydrocarbons in which the characteristic feature is at least two carbon atoms derived from at least one aromatic moiety, which are connected to each other by a system of covalent bonds. The first description of cyclophane was presented in the journal *Nature* by C. J. Brown and A. C. Farthing [2.55], which were then examined by the previously mentioned Nobel laureate D. J. Cram. Fig. 2.15 shows an exemplary supramolecular structure composed of cyclophane. Apart from the photochemical and luminescent properties, nonlinear optical properties were also reported, including for example the relationship between the structure of cyclophane derivatives and the SHG response [2.56 – 2.59].

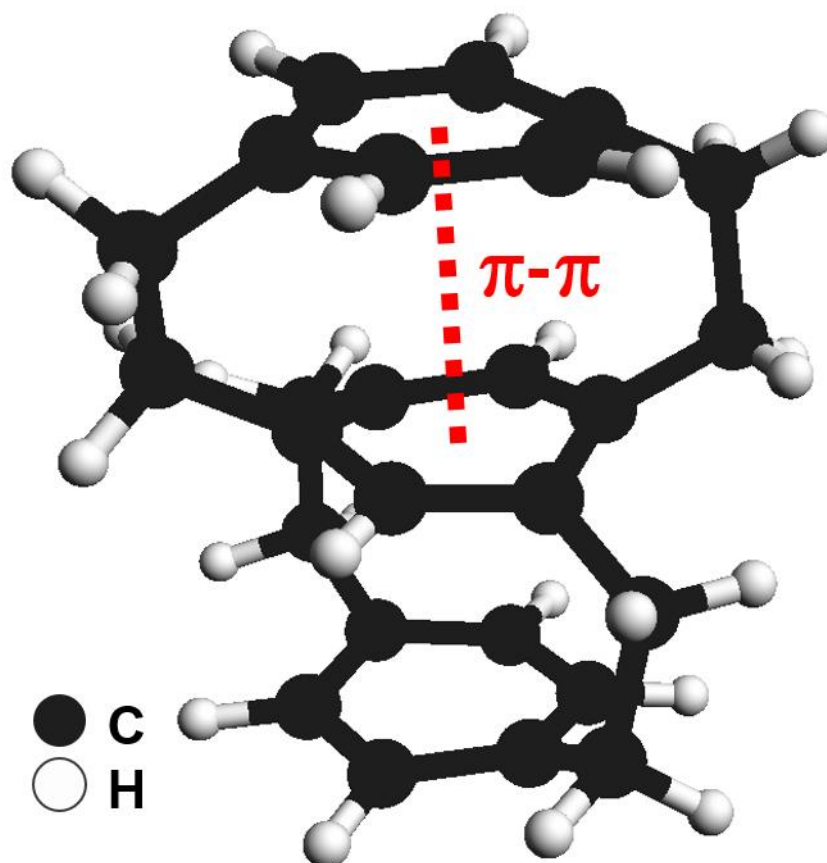


Figure 2.15: Schematic example of multi-layer chiral cyclophane.

#### 2.4.4. Cyclodextrins

This type of supramolecular system belongs to the group of dextrin (carbohydrates composed of simple sugar derivatives), forming a cyclic structure that is easily soluble in water. Due to the hydrophobicity of the interior, these compounds are able to form guest-host complexes with hydrophobic compounds. Cyclodextrins are widely used in pharmacy, where it is possible to reduce the doses of the drug due to the use of this compound. In addition, they are used in the hygiene industry where cyclodextrins are used to absorb or release odors. Current investigations present cyclodextrins research, inter alia, for NLO in the form of polymeric films, also as applications for optical limiting [2.60 – 2.63]. Fig. 2.16 shows an exemplary cyclodextrin.

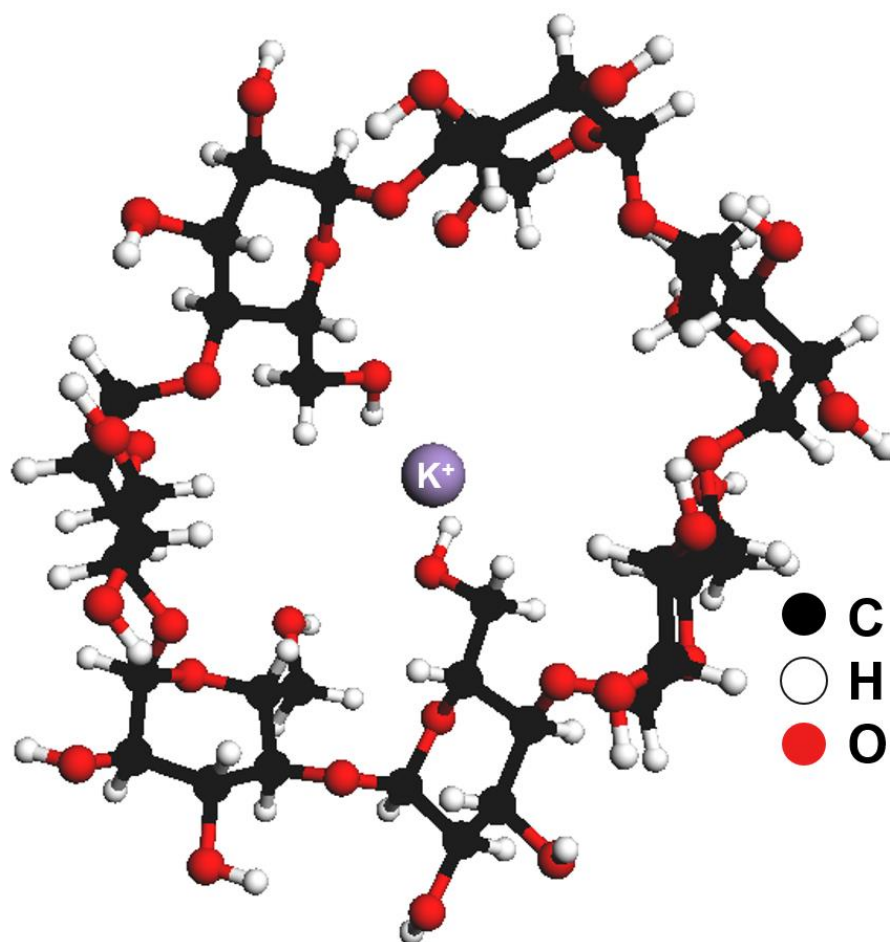


Figure 2.16: Schematic example of cyclodextrin complex.

#### 2.4.5. Rotaxanes

Rotaxane compounds belong to the class of chemical compounds in which the molecules are a system of two chemically unrelated molecules, one of which has a linear structure and the other is a macrocycle. The first linear molecule is the axis and is developed into functional groups at the ends (so-called stoppers) that prevent the macrocyclic structure from escaping the axis, which causes both structures to be mechanically linked, which is schematically shown in Fig. 2.17. Rotaxane compounds are very often used for the construction and research of molecular switches [2.64 – 2.65], but also in nonlinear optics as photonics materials, tested in terms of SHG, THG, nonlinear absorption and nonlinear refractive index described in [2.66 – 2.68].

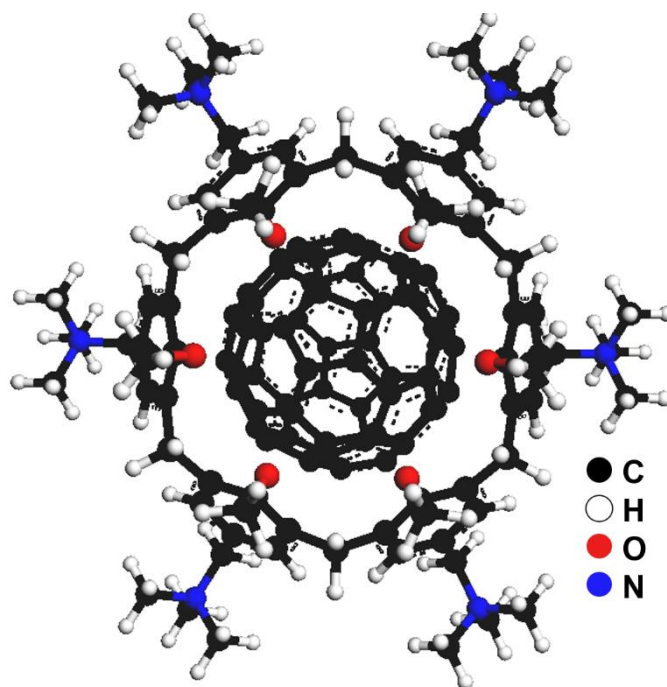




**Figure 2.17:** Schematically representation of rotaxanes.

#### 2.4.6. Fullerenes

Fullerenes are an allotropic form of carbon that consists of an even number of carbon atoms (from about 28 to even 1500 atoms), creating a closed, hollow geometric body whose properties are in many respects similar to aromatic hydrocarbons. The discovery of fullerenes by H. Kroto (University of Sussex, Brighton) and the team of R. E. Smalley, R. F. Curl Jr (Rice University) received the 1996 Nobel Prize in Chemistry. The surface of these molecules consists of a conjugated ring system of five and six carbon atoms. The best known is fullerene  $C_{60}$  containing 60 carbon atoms. It should be emphasized that nanotubes, i.e. cylinders of graphene layers, belong to isomeric varieties of fullerenes. Fullerenes have interesting conductive and semiconductor properties. Due to their ability to bind and accept electrons, they serve as building materials for multicomponent supramolecular architectures. They are widely used in research in the fields of optical limiting and optical switching [2.69], besides, due to their nonlinear properties, they have been studied in terms of higher harmonics and non-linear absorption, which was presented in [2.70] showing NLO supramolecular properties compounds of fullerenes with porphyrins. An example of a supramolecule containing a  $C_{60}$  molecule is shown in Fig. 2.18.

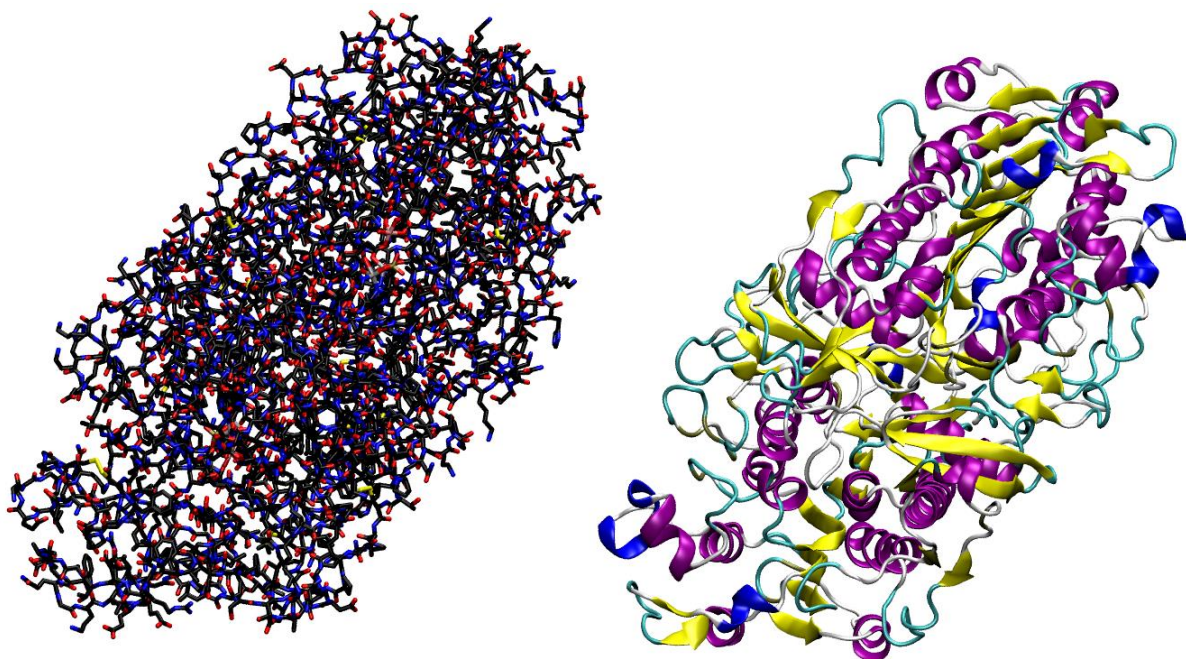


**Figure 2.18:** Schematic exemplary supramolecular calixarene structure with a  $C_{60}$  molecule in centre.

#### 2.4.7. Peptides, Proteins and Helicates

Peptides belong to the group of organic chemical compounds, so-called amides, formed by bonding two or more amino acid molecules with a peptide bond, i.e. one that connects the  $\alpha$ -amino group of one amino acid with the  $\alpha$ -carboxyl group of another amino acid. Short peptides are called oligopeptides, longer chains are called polypeptides or proteins, and the boundary between polypeptides and proteins is determined either by molecular weight or by functionality criteria. On the other hand, proteins are macromolecular biopolymers connected by peptide bonds, the composition of which, in addition to carbon, oxygen, hydrogen, nitrogen and sulfur, phosphorus, sometimes also includes metal cations such as zinc  $Zn^{2+}$ , magnesium  $Mg^{2+}$ , iron  $Fe^{2+}$ , cobalt  $Co^{2+}$ , manganese  $Mn^{2+}$  and copper  $Cu^{2+}$ . Apart from the fact that they have a building, transport, catalysis, storage, immunological etc. function, both peptides and proteins are widely studied in terms of physics, photonics, nonlinear optics. Some papers reported peptide nanostructures

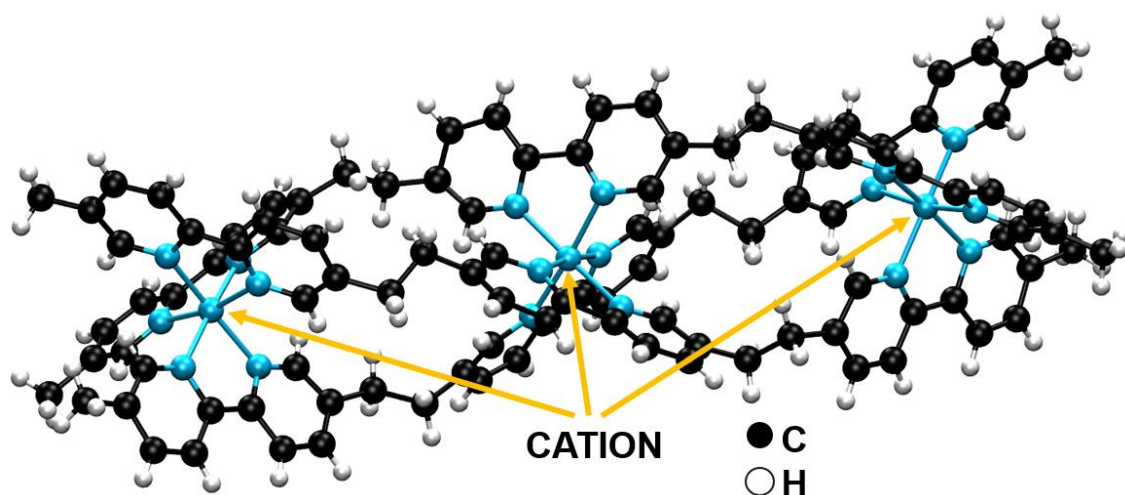
characterized by nonlinear optics through the SHG effect, as well as nanophotonics and nonlinear spectroscopy [2.71 – 2.75]. In the case of proteins, very interesting work has described nonlinear effects using Rayleigh scattering, and, inter alia, second harmonic generation of chiral crystals as well as fluorescent proteins FPs [2.76 – 2.79]. Fig. 2.19 presents example of supramolecular protein alkaline phosphatase [2.80].



**Figure 2.19:** The schematic exemplary illustration of a supramolecular protein: on the left - presentation of the arrangement of individual atoms, on the right - a ribbon model.

Helices are typical structures mainly for nucleic acids and proteins. As mentioned before, one of the most important discoveries is the DNA structure model proposed by J. Watson and F. Crick based on the work of R. Franklin. Moreover, since this discovery, DNA has been studied extensively in terms of nonlinear optics [2.81 – 2.85]. The double helix, which is the basic element of the structure of a DNA molecule, consists of two polynucleotide chains that run in opposite directions and wrap around a common axis. Inside the double helix there are nitrogen bases of nucleotides, which are connected by hydrogen bonds in complementary pairs. The formation of a

double helix is a process that can not be interrupted until the completion of the pairs is fully achieved. Some molecules spontaneously form as a result of complexation with a metal ion, forming a helix.



**Figure 2.20:** Schematic example of triple metallo-helicate.

Generally, in recent years there has been a great deal of interest in self-organized helicates and helical fibers. Understanding and using the rules associated with the formation of helicates, described by J-M Lehn's research groups, led to the formation of structures such as double helix, triple helix, as well as quadruple helix [2.86 – 2.88]. Fig. 2.20 presents example of self-assembled triple metallo-helicate. The already known helicates include, among others, heteronuclear helicates [2.89], helical circular structures [2.90], as well as mixed helices [2.91]. Under carefully selected experimental conditions, helicates with different structures are obtained, examples may be complexes, grid type structures or macrocyclic structures. Prior investigations have documented luminescent properties of ruthenium (II) triple-stranded helicates [2.92] and its potential application in medicine. Moreover, metallo-helicate built of from the same ligands, but with iron cation  $\text{Fe}^{2+}$ , was investigated for its electronic and magnetic properties and its spin-crossover behavior was checked [2.93]. S. V. Eliseeva et al. presented luminescent and two- and three-photon

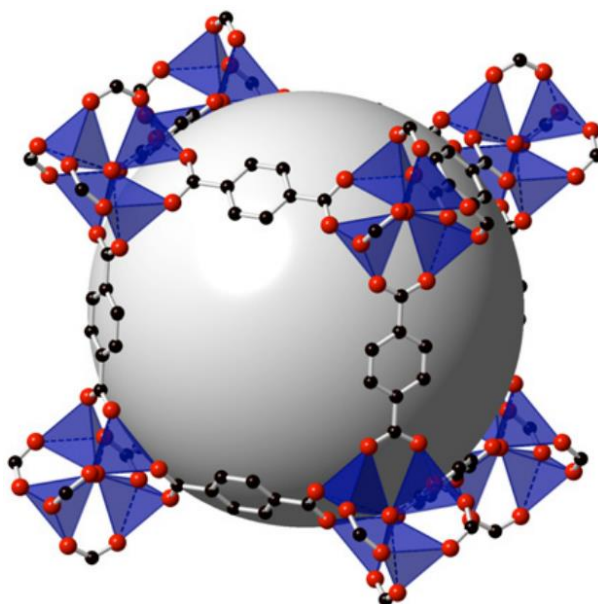
cross section of binuclear helicates [2.94]. Nevertheless, N. Kundu et al. reported in 2012 electrochemical and photophysical properties of triple-stranded helicates with  $\text{Cu}^{2+}$  and  $\text{Cd}^{2+}$  ions.

#### 2.4.8. Metal Organic Frameworks

MOFs are microporous materials that consist of inorganic building blocks (SBU – Secondary Building Units) and organic molecules (linker) which connect elements between the inorganic units [2.95]. Metal organic frameworks are also so-called coordination polymers or coordination networks with an open framework that contains possible pores. Usually they are in form of crystalline and based on Werner complexes. Complex (coordinate) compounds contain at least one central atom that is surrounded by other atoms or groups of atoms (ligands), wherein at least one central atom-ligand bond is a coordinate bond – a covalent bond, the essence of which is the commonality of the electron pair between two atoms, both of which are electrons formally derived from one atom. After synthesis, the pores of the three-dimensional structures are filled with guest molecules (solvents, unreacted linkers). MOF-5 is one of the most studied MOFs, its simplified empirical formula is  $\text{Zn}_4\text{O}(\text{BDC})_3$  (Fig. 2.21) [2.96]. MOFs serve as models from which they are built metallo-supramolecular architectures.

The large inner surface is important for possible applications as catalysts. The pore size can be precisely determined via the size of the organic ligands, so that only reactants of a certain size fit into it. A high selectivity can thus be expected. Some MOFs have very good adsorption properties [2.97], which make them interesting for use in adsorption chillers. In an adsorption refrigerator, heat or cold is generated by adsorption or evaporation of a solvent. For this purpose, the system is divided into two subsystems, one containing a solvent and the other the MOF. Both subsystems are connected to the valve by a connecting pipe. If the valve is opened, solvent can evaporate and extract heat from the environment (enthalpy of vaporization), while heat is released when the solvent is adsorbed on the MOF (enthalpy of adsorption). Moreover, MOFs can be used as

heterogeneous catalysts, due to their large surface area, the adjustable porosity and the diversity of the chemical composition [2.98]. Nevertheless, potential areas of application can be found in biological imaging and sensing, which are based on unique luminescent properties of MOFs [2.99]. Very often MOFs are combined with rare earth ions due to their photoluminescence, that make it ideal for imaging applications, such as the sharp and essentially non-overlapping emission bands characteristic in visible and near infrared (NIR) spectral areas, resistance to photobleaching or to flash and long luminescence time decays. Drug transport systems are another very important application of metal organic frameworks [2.100 – 2.102].



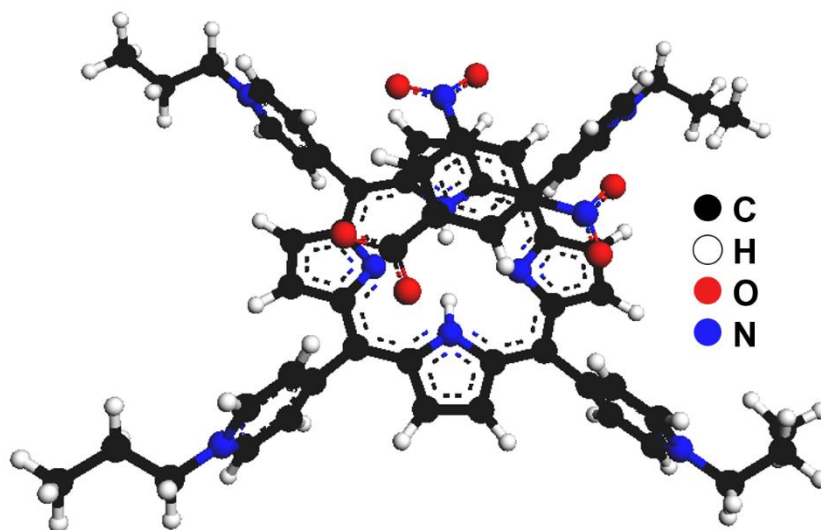
**Figure 2.21:** The structure of MOF-5 [2.96].

Metal-organic frameworks have been studied for nonlinear optics as well. C. Wang et al. reported second-order nonlinear effects in noncentrosymmetrical MOF architectures [2.103], however second-order nonlinear optical activity have been studied by J. Yu et. al [2.104]. Moreover, Y. Liu et al. presented nonlinear optical response dependent on used metal substituent [2.105].

### 2.4.9. Porphyrins

The most studied and frequently used building blocks in supramolecular chemistry include systems based on the porphyrin backbone and related compounds. These compounds have interesting electrochemical and photochemical properties that can be easily modified, they also have the ability to form very stable transition metal chelate complexes.

Porphyrin is a molecule made up of a characteristic aromatic macrocycle that consists of four pyrrole rings connected by methine bridges = CH – (Fig. 2.22). This combination creates a system of conjugated double bonds that contain 18 delocalized  $\pi$  electrons. In this arrangement, Huckle's aromatic rule is fulfilled ( $4n + 2$ );  $n = 4$ . Pyrrole rings form a closed aromatic plane that forms the nucleus of the molecule. One of the results of a large conjugate system is that porphyrin molecules usually very intensively absorb electromagnetic radiation in the visible area and can be deeply colored.



**Figure 2.22:** Schematic example of supramolecular structure with porphyrin ring.

It is well-known that natural porphyrins play a fundamental role in nature, for different roles that play in plant and animal organisms, as well as in industry and medicine. Naturally, such as

chlorophyll and heme groups, are essential for the vital functions of organisms. Chlorophyll in particular allows photosynthesis in plants - after absorption of light, transform it into chemical energy. However, heme group present in hemoglobin allows properly oxygenate various tissues in organisms acting as an oxygen transporter. The most important features characterizing porphyrins include their unique spectroscopic and luminescent properties, as well as magnetic and photoconductivity. Porphyrins are very reactive compounds which react in many types, for example coordination, polymerization, reaction redox, sorption, aggregation, and others. Porphyrins find application in many fields of science. In example in medicine, they exhibit the ability to selectively accumulate in cancerous tissues – in photodynamic therapy (PDT) [2.106 – 2.107]. Also they find application in toxicology - heme biosynthesis is used as biomarker in environmental toxicology studies [2.108]. On the other hand, porphyrin-based compounds are of interest as possible components of molecular electronics, photonics and nonlinear optics [2.109 – 2.116]. In example, synthetic porphyrin dyes that are incorporated in prototype dye-sensitized solar cells [2.117 – 2.119]. Moreover, phthalocyanines belong to the group of organic compounds with a structure similar to porphyrins. In combination with metals such as cobalt or copper, they are widely used as dyes [2.120]. Moreover, they are used in organic solar cells [2.121], as well as in studies of the effects of nonlinear optics [2.122].

## Literature

[2.1] J. D. Van der Waals, Over de continuïteit van den gas-en vloeistofoestand (on the continuity of the gas and liquid state). Ph.D. Thesis, University of Amsterdam, Amsterdam, 1873.

[2.2] E. Fischer, Einfluss der Configuration auf die Wirkung der Enzyme, Berichte der deutschen chemischen Gesellschaft, 27: 2985-2993, 1894.

[2.3] J. D. Watson, F. H. C. Crick, Molecular Structure of Nucleic Acids: A Structure of Deoxyribose Nucleic Acid, Nature, 171 (4356): 737-8, 1953.



- [2.4] J. D. Watson and F. H. C. Crick, A Structure for Deoxyribose Nucleic Acid, *Nature* (3), 171, 737-738, 1953.
- [2.5] C. J. Pedersen, Macrocyclic Polyethers: Dibenzo-18-Crown-6 Polyether and Dicyclohexyl-18-Crown-6 Polyether, *Organic Syntheses, Coll. Vol., 6*, p. 395, 1988.
- [2.6] J-M Lehn, *Supramolecular Chemistry: Receptors, Catalysts, and Carriers*, *Science* Vol. 227, Issue 4689, pp. 849-856, 1985.
- [2.7] "The Nobel Prize in Chemistry 1987". Nobelprize.org. Nobel Media AB 2014.  
[http://www.nobelprize.org/nobel\\_prizes/chemistry/laureates/1987/](http://www.nobelprize.org/nobel_prizes/chemistry/laureates/1987/)
- [2.8] T. Hasobe, Supramolecular nanoarchitectures for light energy conversion, *Phys. Chem. Chem. Phys.*, 12: 44-57, 2010.
- [2.9] Puigmartí-Luis, J., Laukhin, V., Pérez del Pino, Á., Vidal-Gancedo, J., Rovira, C., Laukhina, E. and Amabilino, David B., Supramolecular Conducting Nanowires from Organogels, *Angewandte Chemie International Edition*, 46: 238–241, 2007.
- [2.10] I. V. Kolesnichenko, E. V. Anslyn, Practical applications of supramolecular chemistry, *Chem. Soc. Rev.*, 46, 2385, 2017.
- [2.11] S. Seiffert, *Supramolecular Polymer Networks and Gels*, *Advances in Polymer Science* 268, Springer, 2015.
- [2.12] Z.-T. Li, L.-Z. Wu, *Hydrogen Bonded Supramolecular Structures*, *Lecture Notes in Chemistry*, Springer, 2015.
- [2.13] A. Harada, *Supramolecular Polymer Chemistry*, Wiley-VCH, 2012.
- [2.14] P. Xydias, S. Lymperopoulou, V. Dokorou, M. Manos, J. C. Plaatouras, Supramolecular networks derived from hexacyanoferrates and nitrogen heterocyclic cations, *Polyhedron*, Vol. 157 (2019) 341-357

- [2.15] P. Groth, On the Crystal Structure of the (1:1) Complex between Lithium Thiocyanate and 1,4,7,10-Tetraoxacyclododecane at Room Temperature, *Acta Chem.Scand. Ser.A*, 35, 463,1981.
- [2.16] J. A. Broomhead, C. G. Young, P. Hood, Tris(2,2-Bipyridine)Ruthenium(II) Dichloride Hexahydrate, *Inorganic Syntheses*. 28. pp. 338–340, (1990)
- [2.17] C. Hilger, M. Draeger, R. Stadler, Molecular origin of supramolecular self-assembling in statistical copolymers, *Macromolecules* 1992, 25, 9, 2498–2501
- [2.18] W. Binder, *Hydrogen Bonded Polymers*, 207 *Advances in Polymer Science*, Springer, 2007.
- [2.19] K. Pervushin, A. Ono, C. Frenandez, T. Szyperski, M. Kainosho, K. Wuthrich, NMR scalar couplings across Watson-Crick base pair hydrogen bonds in DNA observed by transverse relaxation-optimized spectroscopy, *Proc. Natl. Acad. Sci. USA* Vol. 95, pp. 14147–14151, 1998.
- [2.20] A. Priimagi, G. Cavalo, P. Metrangolo, G. Resnati, The Halogen Bond in the Design of Functional Supramolecular Materials: Recent Advances, *Acc. Chem. Res.* 2013, 46, 11, 2686–2695
- [2.21] A. Abate, M. Saliba, D. J. Hollman, S. D. Stranks, K. Wojciechowski, R. Avolio, G. Grancini, A. Petrozza, and H. J. Snaith, Supramolecular Halogen Bond Passivation of Organic–Inorganic Halide Perovskite Solar Cells, *Nano Lett.* 2014, 14, 6, 3247–3254
- [2.22] Q-N Zheng, X-H Liu, T. Chen, H-J Yan, T. Cook, D. Wang, P. J. Stang, and L-J Wan, Formation of Halogen Bond-Based 2D Supramolecular Assemblies by Electric Manipulation, *J. Am. Chem. Soc.* 2015, 137, 19, 6128–6131
- [2.23] H. Wang, H. K. Bisoyi, A. M. Urbas, T. J. Bunning, Q. Li, The Halogen Bond: An Emerging Supramolecular Tool in the Design of Functional Mesomorphic Materials, *Chem A Europ. J.* vol 25-6 (2019), 1369-1378

- [2.24] H. Ibach, H. Luth, *Solid-State Physics: An Introduction to Principles of Material Science*, Springer, 2009.
- [2.25] J. Szejtli, Introduction and General Overview of Cyclodextrin Chemistry, *Chem. Rev.* 98, 5, 1743-1754, 1998
- [2.26] E. T. Kool, Replacing the Nucleobases in DNA with Designer Molecules, *Acc. Chem. Res.* 35, 11, 936-943, 2002.
- [2.27] S. Martinez-Vargaz, J. Valdes-Martinez, A. I. Martinez, Supramolecular architectures of Cu(II) with terpyridine and pyridyl-carboxylates, *Journal of Molecular Structure*, Vol. 1006, 1–3, (2011), 425-433
- [2.28] R. Ferdani, L. J. Barbour, G. W. Gokel, Cation–Pi interactions in the crystal structures of alkali metal calixarene complexes, *Journal of Supramolecular Chemistry*, Vol. 2, 1–3, (2002), 343-348
- [2.29] F. Biedermann, W. M. Nau, H.-J. Schneider, The Hydrophobic Effect Revisited Studies with Supramolecular Complexes Imply High-Energy Water as a Noncovalent Driving Force, *Angew. Chem.* vol. 53, 42 (2014) 11158-11171
- [2.30] S. Liu, B. C. Gibb, High-definition self-assemblies driven by the hydrophobic effect: synthesis and properties of a supramolecular nanocapsule, *Chem. Commun.*, 2008, 3709-3716
- [2.31] B. S. Gerstman, P. P. Chapagain, Self-organization in protein folding and the hydrophobic interaction, *The Journal of Chemical Physics* 123, 054901, 2005.
- [2.32] J-M. Lehn, *Perspectives in Supramolecular Chemistry – From Molecular Recognition towards Molecular Information Processing and Self-Organization*, *Angewandte Chemie International Edition in English*. 29 (11), 1304–1319, 1990.

- [2.32] H. Qin, Ch. Zhao, Y. Sun, J. Ren, X. Qu, Metallo-supramolecular Complexes Enantioselectively Eradicate Cancer Stem Cells in Vivo, *J. Am. Chem. Soc.* 139, 16201-16209, 2017.
- [2.34] H. Wang, Z. Feng, D. Wu, K. J. Fritzsche, M. Rigney, J. Zhou, Y. Jiang, K. Schmidt-Rohr, B. Xu, Enzyme-Regulated Supramolecular Assemblies of Cholesterol Conjugates against Drug-Resistant Ovarian Cancer Cells, *J. Am. Chem. Soc.*, 138, 34, 10758-10761, 2016.
- [2.35] F. D'Souza, P. M. Smith, S. Gadde, A. L. McCarty, M. J. Kullman, M. E. Zandler, M. Ito, Y. Araki, O. Ito, Supramolecular Triads Formed by Axial Coordination of Fullerene to Covalently Linked Zinc Porphyrin–Ferrocene(s): Design, Syntheses, Electrochemistry, and Photochemistry, *J. Phys. Chem. B*, 108, 31, 11333-11343, 2004.
- [2.36] J. B. Beck, S. J. Rowan, Multistimuli, Multiresponsive Metallo-Supramolecular Polymers, *J. Am. Chem. Soc.* 125, 46, 13922-13923, 2003.
- [2.37] S. Lim, H. Kim, N. Selvapalam, K.-J. Kim, S. J. Cho, G. Seo, K. Kim, Cucurbit[6]uril: Organic Molecular Porous Material with Permanent Porosity, Exceptional Stability, and Acetylene Sorption Properties, *Angew Chem Int Ed Engl.* ;47(18):3352-5, 2008.
- [2.38] S. Kiyonaka, K. Sada, I. Yoshimura, S. Shinkai, N. Kato, I. Hamachi, Semi-wet peptide/protein array using supramolecular hydrogel, *Nature Materials*, vol. 3, 2004.
- [2.39] Y. Bae, S. Sukushima, A. Harada, K. Kataoka, Design of Environment-Sensitive Supramolecular Assemblies for Intracellular Drug Delivery: Polymeric Micelles that are Responsive to Intracellular pH Change, *Angewandte Chemie*, Vol. 42, Iss. 38, 4640-4643, 2003.
- [2.40] Z. Liu, A. C. Fan, K. Rakhra, S. Sherlock, A. Goodwin, X. Chen, Q. Yang, D. W. Felsher, H. Dai, Supramolecular Stacking of Doxorubicin on Carbon Nanotubes for In Vivo Cancer Therapy, *Angewandte Chemie*, Vol. 48, Iss. 41, 7668-7672, 2009.

[2.41] D. Hu, Y. Hu, W. Huang, Q. Zhang, Two-photon induced data storage in hydrogen bonded supramolecular azopolymers, *Optics Communications*, Vol. 285, Iss. 24, 4941-4945, 2012.

[2.42] Y. Q. Wen, Y. L. Song, G. Y. Jiang, D. B. Zhao, K. Ding, W. F. Yuan, X. Lin, H. J. Gao, L. Jiang, D. B. Zhu, Crystalline Thin Films Formed by Supramolecular Assembly for Ultrahigh-Density Data Storage, *Advanced Materials*, Vol. 16, Iss. 22, 2018-2021, 2004.

[2.43] M. Virkki, O. Tuominen, A. Forni, M. Saccone, P. Metrangolo, G. Resnati, M. Kauranen, A. Priimagi, Halogen bonding enhances nonlinear optical response in poled supramolecular polymers, *J. Mater. Chem. C*, 3, 3003, 2015.

[2.44] L. Dordević, T. Marangoni, F. De Leo, I. Papagiannouli, P. Aloukos, S. Couris, E. Pavoni, F. Monti, N. Armaroli, M. Prato, D. Bonifazi, [60]Fullerene-poryphyrin [n]pseudorotaxanes: self-assembly, photophysics and third-order NLO response, *Phys. Chem. Chem. Phys.*, 18, 11858, 2016.

[2.45] A. D. Grishina, Y. G. Gorbunova, T. V. Krivenko, L. A. Lapkina, V. V. Savel'ev, A. V. Vannikov, A. Y. Tsivadze, Photorefractive and Nonlinear Optical Properties of Indium(III)Tetra(15-Crown-5)Phthalocyaninate-Based Composites, *Protection of Metals and Physical Chemistry of Surfaces*, Vol. 50, No. 4, pp. 472–479, 2014.

[2.46] A. Aditya Prasad, S. Kalainathan, S. P. Meenakshisundaram, Supramolecular architecture of third-order nonlinear optical picrate: Crystal growth and DFT approach, *Optik* 127, 6134–6149, 2016.

[2.47] Z. Zheng, Z-P Yu, M-D Yang, F. Jin, L-N Ye, M. Fang, H-P Zhou, J-Y Wua, Y-P Tiana, Silver(I) supramolecular complexes generated from isophorone-based ligands: crystal structures and enhanced nonlinear optical properties through metal complexation, *Dalton Trans.*, 43, 1139, 2014.

- [2.48] H-Y Bie, J-H Yu, J-Q Xu, J. Lu, Y. Li, X-B Cui, X. Zhang, Y-H Sun, L-Y Pan, Synthesis, structure and non-linear optical property of a copper(II)thiocyanate three-dimensional supramolecular compound, *Journal of Molecular Structure* 660, 107–112, 2003.
- [2.49] X. Tong, J. Xiang, F. Shi, Y. Zhao, Near-Infrared Light-Sensitive Supramolecular Gel with Enhanced Visible Light Upconversion, *Adv. Optical Mater.*, 4, 1392–1396, 2016.
- [2.50] A. Datta, Role of Metal Ions ( $M = Li^+$ ,  $Na^+$ , and  $K^+$ ) and Pore Sizes (Crown-4, Crown-5, and Crown-6) on Linear and Nonlinear Optical Properties: New Materials for Optical Birefringence, *J. Phys. Chem. C* 2009, 113, 8, 3339–3344
- [2.51] H. Shirota, Ultrafast Dynamics of Liquid Poly(ethylene glycol)s and Crown Ethers Studied by Femtosecond Raman-Induced Kerr Effect Spectroscopy, *J. Phys. Chem. B* 2005, 109, 15, 7053–7062
- [2.52] D. A. Leigh, A. E. Moody, F. A. Wade, T. A. King, D. West, G. S. Bahra, Second Harmonic Generation from Langmuir-Blodgett Films of Fullerene—Aza-Crown Ethers and Their Potassium Ion Complexes, *Langmuir* 1995, 11, 2334-2336
- [2.53] P. Mukhopadhyay, P. K. Bharadwaj, A. Krishnan, P. K. Das, Synthesis and characterization of mono- and bis-D- $\pi$ -A cryptand derivatives for second-order nonlinear optics and its modulation with different metal ion inputs, *J. Mater. Chem.*, 2002, 12, 2786-2791
- [2.54] W. Chen, Z-R Li, D. Wu, Y. Li, C-C Sun, F. L. Gu, Y. Aoki, Nonlinear Optical Properties of Alkalides  $Li^+(\text{calix}[4]\text{pyrrole})M^-$  ( $M = Li, Na, \text{ and } K$ ): Alkali Anion Atomic Number Dependence, *J. Am. Chem. Soc.* 2006, 128, 4, 1072–1073
- [2.55] C. J. Brown, A. C. Farthing, Preparation and Structure of Di-p-Xylylene, *Nature* 164, 915–916 (1949)

- [2.56] L. N. Puntus, E. V. Sergeeva, D. Yu Antonov, K. Yu Suponitsky, I. Rau, F. Kajzar, K. A. Lyssenko, The correlation between SHG efficiency and structural peculiarities of [2.2]paracyclophane derivatives, *Mol. Cryst. Liq. Cryst.*, 2017, Vol. 655, 16-34
- [2.57] M. Shimada, Y. Yamanoi, T. Ohto, S-T Pham, R. Yamada, H. Tada, K. Omoto, S. Tashiro, M. Shionoya, M. Hattori, K. Jimura, S. Hayashi, H. Koike, M. Iwamura, K. Nozaki, H. Nishihara, Multifunctional Octamethyltetrasila[2.2]cyclophanes: Conformational Variations, Circularly Polarized Luminescence, and Organic Electroluminescence, *J. Am. Chem. Soc.* 2017, 139, 32, 11214–11221
- [2.58] J. Zyss, I. Ledoux, S. Volkov, V. Chernyak, S. Mukamel, G. P. Bartholomew, G. C. Bazan, Through-Space Charge Transfer and Nonlinear Optical Properties of Substituted Paracyclophane, *J. Am. Chem. Soc.* 2000, 122, 48, 11956–11962.
- [2.59] T. Häberle, J. Hirsch, F. Pöllinger, H. Heitele, M. E. Michel-Beyerle, C. Anders, A. Döhling, C. Krieger, A. Rückemann, H. A. Staab, Ultrafast Charge Separation and Driving Force Dependence in Cyclophane-Bridged Zn–Porphyrin–Quinone Molecules, *J. Phys. Chem.* 1996, 100, 46, 18269–18274
- [2.60] P. Fischer, M. Koetse, A. Laschewsky, E. Wischerhoff, L. Jullien, A. Persoons, T. Verbiest, Orientation of Nonlinear Optical Active Dyes in Electrostatically Self-Assembled Polymer Films Containing Cyclodextrins, *Macromolecules* 2000, 33, 26, 9471–9473
- [2.61] M. Konstantaki, E. Koudoumas, S. Couris, J. M. Janot, H. Eddaoudi, A. Deratani, P. Seta, S. Leach, Optical limiting behaviour of the water-soluble C60/ $\gamma$ -cyclodextrin complex, *Chem. Phys. Lett.*, Vol. 318, 4–5, 2000, 488-495
- [2.62] A. R. Dias, M. H. Garcia, M. P. Robalo, A. P. S. Tekheira, L. A. Bulygina, V. I. Sokolov, Synthesis of Cyclodextrin Inclusion Complexes with (h-Cyclopentadienyl)iron Derivatives as

Potential Nonlinear Optics Materials, Russian Journal of Organic Chemistry, Vol. 37, No. 5, 2001, pp. 6203623

[2.63] El Djouhar Rekaï, J-B Baudin, L. Jullien, I. Ledoux, J. Zyss, M. Blanchard-Desce, A Hyperpolar, Multichromophoric Cyclodextrin Derivative: Synthesis, and Linear and Nonlinear Optical Properties, Chem. A Europ. J. Vol. 7, 20, 2001, 4395-4402

[2.64] S. I. Jun, J. W. Lee, S. Sakamoto, K. Yamaguchi, K. Kim, Rotaxane-based molecular switch with fluorescence signaling, Tetrahedron Letters, vol. 41, (2000) 471-475

[2.65] W. Yang, Y. Li, H. Liu, L. Chi, Y. Li, Design and Assembly of Rotaxane-Based Molecular Switches and Machines, small 2012, 8, No. 4, 504–516

[2.66] J. Niziol, K. Nowicka, F. Kajzar, Linear and Nonlinear Optical Properties of Selected Rotaxanes and Catenanes, In: Papadopoulos M.G., Sadlej A.J., Leszczynski J. (eds) Non-Linear Optical Properties of Matter. Challenges and Advances in Computational Chemistry and Physics, vol 1. Springer, Dordrecht

[2.67] I. Rau, R. Czaplicki, A. Humeau, J. Luc, B. Sahraoui, G. Boudebs, F. Kajzar, D. A. Leigh, J. Berna-Canovas, Linear and nonlinear optical properties of a rotaxane molecule, Proc. SPIE 6343, Photonics North 2006, 63433C (2006)

[2.68] V. Bermudez, P-A Chollet, F. G. Gatti, F. Kajzar, D. A. Leigh, A. Lorin, S. Zhang, Linear and nonlinear optical properties of rotaxanes: novel versatile photonic materials, Proc. SPIE 4106, Linear, Nonlinear, and Power-Limiting Organics, (2000)

[2.69] R. Signorini, R. Bozio, M. Prato, in Fullerenes: From Synthesis to Optoelectronic Properties (Eds.: D. M. Guldi, N. Martin), Kluwer, Dordrecht, 2002, p. 295.



- [2.70] B. Kulyk, K. Waszkowska, A. Busseau, C. Villegas, P. Hudhomme, S. Dabos-Seignon, A. Zawadzka, S. Legoupy, B. Sahraoui, Penta(zinc porphyrin)[60]fullerenes: Strong reverse saturable absorption for optical limiting applications, *Applied Surface Science* 533 (2020) 147468
- [2.71] A. Handelman, S. Lavrov, A. Kudryavtsev, A. Khatchatourians, Y. Rosenberg, E. Mishina, G. Rosenman, Nonlinear Optical Bioinspired Peptide Nanostructures, *Adv. Opt. Mater.*, vol 1, 11 (2013) 875-884
- [2.72] B. Apter, N. Lapshina, A. Handelman, B. D. Fainberg, G. Rosenman, Peptide Nanophotonics: From Optical Waveguiding to Precise Medicine and Multifunctional Biochips, *Small*, vol 14, 34 (2018) 1801147
- [2.73] S. Woutersen, P. Hamm, Nonlinear two-dimensional vibrational spectroscopy of peptides, *Journal of Physics: Condensed Matter*, Vol. 14, No 39, 2002
- [2.74] A. Handelman, B. Apter, N. Turko, G. Rosenman, Linear and nonlinear optical waveguiding in bio-inspired peptide nanotubes, *Acta Biomaterialia*, Vol 30, 2016, 72-77
- [2.75] T. Xu, S. P. Wu, I. Miloradovic, M. J. Therien, J. K. Blasié, Incorporation of Designed Extended Chromophores into Amphiphilic 4-Helix Bundle Peptides for Nonlinear Optical Biomolecular Materials, *Nano Lett.* 2006, 6, 11, 2387–2394
- [2.76] K. Clays, E. Hendrickx, M. Triest, T. Verbiest, A. Persoons, C. Dehu, J.-L. Brédas, Nonlinear Optical Properties of Proteins Measured by Hyper-Rayleigh Scattering in Solution, *Science*, 1993, Vol. 262, 5138, pp. 1419-1422
- [2.77] L. M. Hauptert, G. J. Simpson, Screening of protein crystallization trials by second order nonlinear optical imaging of chiral crystals (SONICC), *Methods*, vol. 55, 4 (2011) 379-386

- [2.78] J. M. Perry, A. J. Moad, N. J. Begue, R. D. Wampler, G. J. Simpson, Electronic and Vibrational Second-Order Nonlinear Optical Properties of Protein Secondary Structural Motifs, *J. Phys. Chem. B* 2005, 109, 42, 20009–20026
- [2.79] E. De Meulenaere, I. Asselberghs, M. de Wergifosse, E. Botek, S. Spaepen, B. Champagne, J. Vanderleyden, K. Clays, Second-order nonlinear optical properties of fluorescent proteins for second-harmonic imaging, *J. Mater. Chem.*, 2009, 19, 7514-7519
- [2.80] E. E. Kim, H. W. Wyckoff, Reaction mechanism of alkaline phosphatase based on crystal structures: Two-metal ion catalysis, *J. Mol. Biol.* 218 (1991) 449
- [2.81] J. G. Grote, N. Ogata, J. A. Hagen, E. Heckman, M. J. Curley, P. P. Yaney, M. O. Stone, D. E. Diggs, R. L. Nelson, J. S. Zetts, F. K. Hopkins, L. R. Dalton, Deoxyribonucleic acid (DNA)-based nonlinear optics, *Proc. SPIE 5211, Nonlinear Optical Transmission and Multiphoton Processes in Organics*, (2003)
- [2.82] J. Balapanuru, J-X Yang, S. Xiao, Q. Bao, M. Jahan, L. Polavarapu, J. wei, Q-H Xu, K. Ping Loh, A Graphene Oxide–Organic Dye Ionic Complex with DNA-Sensing and Optical-Limiting Properties, *Angew. Chem.* vol 49, 37 (2010), 6549-6553
- [2.83] R. Khazaeinezhad, S. H. Kassani, B. Paulson, H. Jeong, J. Gwak, F. Rotermund, D-I Yeom, K. Oh, Ultrafast nonlinear optical properties of thin-solid DNA film and their application as a saturable absorber in femtosecond mode-locked fiber laser, *Sci Rep* 7, 41480 (2017)
- [2.84] A. Szukalski, M. Moffa, A. Camposeo, D. Pisignano, J. Myśliwiec, All-optical switching in dye-doped DNA nanofibers, *J. Mater. Chem. C*, 2019, 7, 170-176
- [2.85] B. Derkowska, O. Krupka, V. Smokal, B. Sahraoui, Optical properties of oxazalone derivatives with and without DNA–CTMA, *Opt. Mater.* vol. 33 (2011) 1429-1433

- [2.86] C. Piguet, G. Bernardinelli, G. Hopfgartner, Helicates as Versatile Supramolecular Complexes, *Chem. Rev.*, 1997, 97, 2005.
- [2.87] S. Rigault, C. Piguet, G. Bernardelli, G. Hopfgartner, Lanthanide-Assisted Self-assembly of an Inert, Metal Containing Nonadentate Tripodal Receptor, *Angew. Chem. Int. E.*, 37, 169, 1998.
- [2.88] P. N. W. Baxter, J.-M. Lehn, G. Baum, D. Fenske, Self Assembly and Structure of Interconverting Multinuclear Inorganic Arrays: A<sub>4</sub>[4x5]AgI<sub>20</sub> Grid and an AgI<sub>10</sub> Quadruple Helicate, *Chem. Eur. J.* 6, 4510, 2000.
- [2.89] E.C. Constable, A. J. Edwards, P. R. Raithby, J. V. Walker, The First Structurally Characterized Heterodinuclear Double-Helicate Complex, *Angew. Chem. Int. Ed. Vol 32*, 10, 1465, 1993
- [2.90] B. Hasenknopf, J.-M. Lehn, B.O. Kneisel, G. Baum, D. Fenske, Self-Assembly of a Circular Double Helicate, *Angew. Chem. Int. Ed.*, 1996, 35, 1838.
- [2.91] M. Greenwald, D. Wessely, E. Katz, I. Willner, Y. Cohen, From Homoleptic to Heteroleptic Double Stranded Copper(I) Helicates: The Role of Self-Recognition in Self-Assembly Processes, *J. Org. Chem.*, 2000, 65, 1050.
- [2.92] G. I. Pascu, A.C. G. Hotze, C. Sanchez-Cano, B. M. Kariuki, M. J. Hannon, Dinuclear Ruthenium(II) Triple-Stranded Helicates: Luminescent Supramolecular Cylinders That Bind and Coil DNA and Exhibit Activity against Cancer Cell Lines, *Angewandte Chemie*, Vol 46, 23, 4374-4378, 2007.
- [2.93] F. Tuna, M. R. Lees, G. J. Clarkson, M. J. Hannon, Readily Prepared Metallo-Supramolecular Triple Helicates Designed to Exhibit Spin-Crossover Behaviour, *Chem. Eur. J.* 2004, 10, 5737 –5750.

- [2.94] N. Kundu, S. M. T. Abtab, S. Kundu, A. Endo, S. J. Teat, M. Chaudhury, Triple-Stranded Helicates of Zinc(II) and Cadmium(II) Involving a New Redox-Active Multiring Nitrogenous Heterocyclic Ligand: Synthesis, Structure, and Electrochemical and Photophysical Properties, *Inorg. Chem.* 2012, 51, 4, 2652-2661.
- [2.95] H. Garcia, S. Navalon, *Metal-Organic Frameworks: Applications in Separations and Catalysis*, John Wiley & Sons, 2018.
- [2.96] Q. Li, T. Thonhauser, A theoretical study of the hydrogen-storage potential of (H<sub>2</sub>)<sub>4</sub>CH<sub>4</sub> in metal organic framework materials and carbon nanotubes, *J. Phys.: Condens. Matter* 24 (2012) 424204 (8pp).
- [2.97] D. Saha, Z. Bao, F. Jia, S. Deng, Adsorption of CO<sub>2</sub>, CH<sub>4</sub>, N<sub>2</sub>O, and N<sub>2</sub> on MOF-5, MOF-177, and Zeolite 5A, *Environ. Sci. Technol.* 2010, 44, 5, 1820-1826.
- [2.98] JY Lee, O. K. Fahra, J. Roberts, K. A. Scheidt, SB T. Nguyen, J. T. Hupp, Metal-organic framework materials as catalysts, *Chem. Soc. Rev.*, 2009, 38, 1450-1459.
- [2.99] Y. Wang, Y. Zhu, A. Binyam, M. Liu, Y. Wu, F. Li, Discovering the enzyme mimetic activity of metal-organic framework (MOF) for label-free and colorimetric sensing of biomolecules, *Biosensors and Bioelectronics* 86 (2016) 432-43.
- [2.100] N. L. Torad, Y. Li, S. Ishihara, K. Ariga, Y. Kamachi, H-Y Lian, H. Hamoudi, Y. Sakka, W. Chaikittisilp, K. C.-W. Wu, Y. Yamauchi, MOF-derived Nanoporous Carbon as Intracellular Drug Delivery Carriers, *Chem. Lett.* 2014, 43, 717-719.
- [2.101] C. Orellana-Tavra, E. F. Baxter, T. Tian, T. D. Bennett, N. K. H. Slater, A. K. Cheetham, D. Fairen-Jimenez, Amorphous metal-organic frameworks for drug delivery, *Chem. Commun.*, 2015, 51, 13878-13881.

- [2.102] F. Ke, Y-P Yuan, L-G Qiu, Y-H Shen, A-J Xie, J-F Zhu, X-Y Tian L-D Zhang, Facile fabrication of magnetic metal–organic framework nanocomposites for potential targeted drug delivery, *J. Mater. Chem.*, 2011, 21, 3843-3848
- [2.103] C. Wang, T. Zhang, W. Lin, Rational Synthesis of Noncentrosymmetric Metal–Organic Frameworks for Second-Order Nonlinear Optics, *Chem. Rev.* 2012, 112, 2, 1084-1104.
- [2.104] J. Yu, Y. Cui, C. Wu, Y. Yang, Z. Wang, M. O'Keeffe, B. Chen, G. Qian, Second-Order Nonlinear Optical Activity Induced by Ordered Dipolar Chromophores Confined in the Pores of an Anionic Metal–Organic Framework, *Angew. Chem.* 51, 42, 2012, 10542-10545
- [2.105] Y. Liu, G. Li, X. Li, Y. Cui, Cation-Dependent Nonlinear Optical Behavior in an Octupolar 3D Anionic Metal–Organic Open Framework, *Angew. Chem*, 46, 33, 2007, 6301-6304
- [2.106] D. A. James, N. Swamy, N. Paz, R. N. Hanson, R. Ray, Synthesis and estrogen receptor binding affinity of a porphyrin-estradiol conjugate for targeted photodynamic therapy of cancer, *Bioorganic & Medicinal Chemistry Letters* 9 (1999) 2379-2384
- [2.107] E. Fagadar-Cosma, L. Cseh, V. Badea, G. Fagadar-Cosma, D. Vlascici, Combinatorial Synthesis and Characterization of New Asymmetric Porphyrins as Potential Photosensitizers in Photodynamic Therapy, *Combinatorial Chemistry & High Throughput Screening*, Volume 10, Number 6, 2007, pp. 466-472(7)
- [2.108] L. Lake, L. E. Gerschenson, Cellular and molecular toxicology of lead. III. Effect of lead on heme synthesis, *Journal of Toxicology and Environmental Health*, Vol 4, (4), 1978
- [2.109] M. Jurow, A. E. Schuckman, J. D. Batteas, C. M. Drain, Porphyrins as molecular electronic components of functional devices, *Coordination Chemistry Reviews*, Vol 254, 19–20, 2297-2310, 2010

- [2.110] A. K. Burrell, M.I R. Wasielewski, Porphyrin-based nanostructures: routes to molecular electronics, *Journal of Porphyrins and Phthalocyanines*, Vol 4, 4, 401-406, 2000
- [2.111] P. A. Liddell, G. Kodis, A. L. Moore, T. A. Moore, D. Gust, Photonic Switching of Photoinduced Electron Transfer in a Dithienylethene–Porphyrin–Fullerene Triad Molecule, *J. Am. Chem. Soc.* 2002, 124, 26, 7668-7669
- [2.112] K. Yoshiaki, O. Kazuya, Porphyrin Supramolecules for Artificial Photosynthesis and Molecular Photonic/Electronic Materials, *Bulletin of the Chemical Society of Japan*, Vol 76, No 4, 689-708, 2003
- [2.113] S. I. Yang, J. Seth, J-P Strachan, S. Gentemann, D. Kim, S. Holten, J. S. Lindsey, D. F. Bocian, Ground and excited state electronic properties of halogenated tetraarylporphyrins. Tuning the building blocks for porphyrin-based photonic devices, *Journal of Porphyrins and Phthalocyanines*, Vol 3, No 2, 117-147, 1999
- [2.114] F. Z. Henari, W. J. Blau, L. R. Milgrom, G. Yahioğlu, D. Phillips, J. A. Lacey, Third-order optical non-linearity in Zn(II) complexes of 5,10,15,20-tetraarylethynyl-substituted porphyrins, *Chemical Physics Letters*, Vol 267, No 3–4, 229-233, 1997
- [2.115] T. E. O. Screen, K. B. Lawton, G. Scott Wilson, N. Dolney, R. Ispasoiu, T. Goodson III, S.J. Martin, D. D. C. Bradley, H. L. Anderson, Synthesis and third order nonlinear optics of a new soluble conjugated porphyrin polymer, *J. Mater. Chem.*, 2001, 11, 312-320
- [2.116] K. S. Suslick, C. T. Chen, G. R. Meredith, L. T. Cheng, Push-pull porphyrins as nonlinear optical materials, *J. Am. Chem. Soc.* 1992, 114, 17, 6928-6930
- [2.117] L-L Li, E. Wei-Guang Diao, Porphyrin-sensitized solar cells, *Chem. Soc. Rev.*, 2013, 42, 291-304

[2.118] S. Mathew, A. Yella, P. Gao, R. Humphry-Baker, B. F. E. Curchod, N. Ashari-Astani, I. Tavernelli, U. Rothlisberger, Md. K. Nazeeruddin, M. Gratzel, Dye-sensitized solar cells with 13% efficiency achieved through the molecular engineering of porphyrin sensitizers, *Nature Chemistry* 6, 242–247, 2014

[2.119] A. Yella, H-W Lee, H. N. Tsao, C. Yi, A. K. Chandiran, Md. K. Nazeeruddin, E. Wei-Guand Diao, C-Y Yeh, S. M. Zakeeruddin, M. Gratzel, Porphyrin-Sensitized Solar Cells with Cobalt (II/III)–Based Redox Electrolyte Exceed 12 Percent Efficiency, *Science*, Vol 334, No 6056, 629-634, 2011

[2.120] M. Zhang, C. Shao, Z. Guo, Z. Zhang, J. Mu, P. Zhang, T. Cao, Y. Liu, Highly Efficient Decomposition of Organic Dye by Aqueous-Solid Phase Transfer and In Situ Photocatalysis Using Hierarchical Copper Phthalocyanine Hollow Spheres, *ACS Appl. Mater. Interfaces* 2011, 3, 7, 2573–2578

[2.121] M. G. Walter, A. B. Rudine, C. C. Wamser, Porphyrins and phthalocyanines in solar photovoltaic cells, *J. Porp. Phth.* Vol. 14, No. 09, pp. 759-792, 2010

[2.122] A. Zawadzka, K. Waszkowska, A. Karakas, P. Plóciennik, A. Korcala, K. Wiśniewski, M. Karakaya, B. Sahraoui, Diagnostic and control of linear and nonlinear optical effects in selected self-assembled metallophthalocyanine chlorides nanostructures, *Dyes and Pigments*, 157, 151-162, 2018

## CHAPTER 3: THIN FILMS PHYSICS

### 3.1. Luminescence

The luminescence of a material is the emission of radiation that occurs from a state with energy higher than the basic state. There are many types of luminescence, depending on the caused factor, the phenomenon of light wave emission as a result of chemical reactions, however, electroluminescence is a phenomenon that occurs under the influence of current flow. Nonetheless, in this work we will focus on photoluminescence - phenomenon in which light acts as an excitatory stimulus. Photoluminescence, due to its duration, is divided into fluorescence and phosphorescence. The processes leading to these phenomena related to light absorption are best illustrated by the Jabłoński diagram (Fig. 3.1).

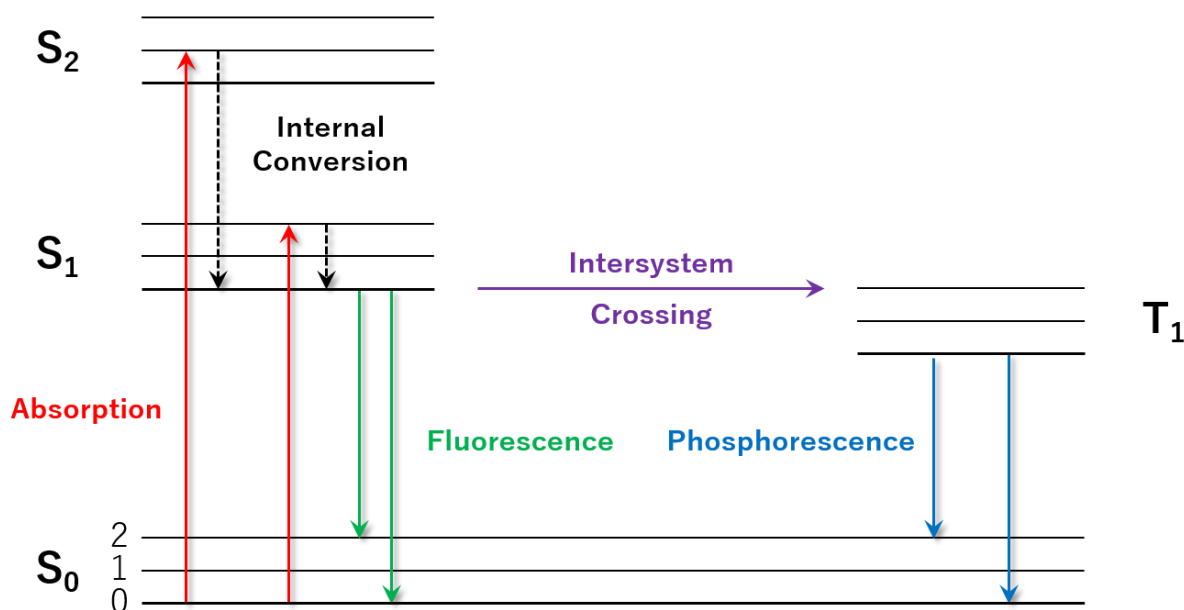


Figure 3.1: Jabłoński diagram.

States  $S_0$ , as well as  $S_1$  and  $S_2$  represent the basic level as well as the first and second singlet excited levels, respectively. At each of these energy levels, fluorspar may occur in different vibrational states, designated 0, 1 and 2, respectively. Absorption transitions between ground and excited states



are represented by vertical lines directed upwards. There are several processes after light absorption. An interesting phenomenon is the internal conversion, in which there is a radiative relaxation from the singlet excited state  $S_2$  to  $S_1$ . The transition from  $S_1$  excited singlet state to  $S_0$  ground state is called fluorescence. Its duration usually does not exceed  $10^{-8}$  seconds [3.1]. The conversion in which the transition from the singlet excited state  $S_1$  to the triplet excited state  $T_1$  occurs is called the intersystem crossing. However, if from the triplet excited state  $T_1$  there is a transition to the ground state  $S_0$ , in a time not shorter than  $10^{-8}$  seconds [3.1], then we deal with phosphorescence. The energy differences between higher excited states of a given  $S_2$  and  $S_1$  multiplet are usually much smaller than between the lowest singlet  $S_1$  or triplet  $T_1$  and the ground state  $S_0$ , which means that the rate of internal conversion significantly exceeds the rate of fluorescence and phosphorescence.

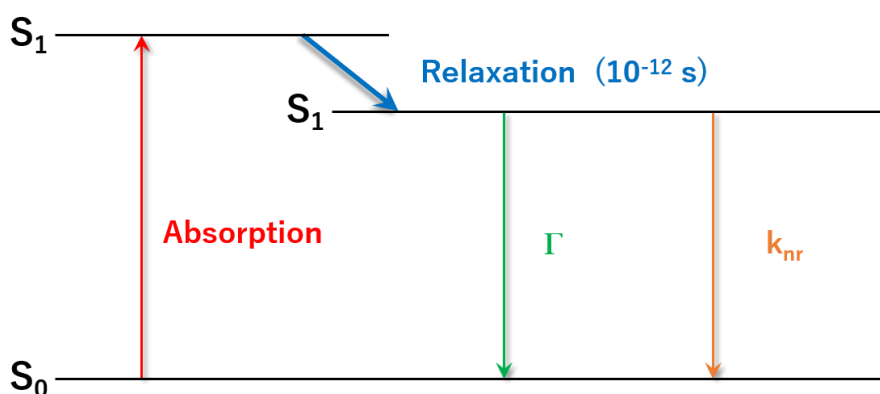
The name fluorescence was first used by G. G. Stokes, who discovered in 1852 that mineral fluorite emits visible light when it is illuminated by UV light [3.2]. It turns out that the maximum emission is mainly shifted towards longer waves in relation to the maximum absorption. This effect is called Stokes shift. In addition, the analysis of the Jabłoński diagram shows that the absorption energy exceeds the emission energy. In fact, the total energy absorbed by the molecule is released in the substrate in various ways, including photon emission, so the energy of the emitted photons is therefore smaller than the energy of the absorbed photons.

Another property is that fluorescence itself is observed regardless of the excitation wavelength. This principle was described in 1950 by M. Kasha [3.3]. Investigating the emission properties of complex molecules, he discovered that when a photon is absorbed from the  $S_0$  base level, it can be excited to any higher  $S_N$  energy level. However, photon emission occurs only from the lowest excited state  $S_1$ , therefore it is correct to say that it does not depend on the excitation wavelength (needs a minimum energy of photon). Kasha's rule is important in understanding the emission

spectrum of an excited molecule. The law of S. Wawilow is connected with Kasha's rule, which says that the excitation wave length also does not affect the quantum efficiency of fluorescence [3.4].

An interesting phenomenon is also the Mirror - Image Rule. It occurs when the fluorophore emission spectrum is a mirror reflection of the absorption spectrum [3.5]. This happens when the probability of transition from  $S_1$  excited singlet level to  $S_0$  base level is identical to  $S_0$  to  $S_1$  transition.

One of the most important parameters of the fluorophore is the fluorescence lifetime, which characterizes the average time during which the molecule remains in the excited state  $S_1$  shortly before returning to the ground state  $S_0$  [3.5]. Fluorescence lifetime is best described by the simplified Jabłoński diagram (Fig. 3.2).



**Figure 3.2:** Simplified Jabłoński diagram illustrating the fluorescence lifetime.

In the situation presented in Fig. 3.2 the excited fluorophore is characterized by two main parameters: radiation emission rate ( $\Gamma$ ) and non-radiative decay to ground state  $S_0$  ( $k_{nr}$ ). The fluorescence lifetime ( $\tau_L$ ) is therefore described by the equation:

$$\tau_L = \frac{1}{\Gamma + k_{nr}} \quad (3.1)$$

In general, the values of  $\tau_L$  are very small, on the order of 10 ns [3.1]. In many cases, fluorescence lifetimes depend on the fluorophore structure. Lifetime can also be modified by factors affecting one of the speed parameters. For example, the molecule may be non-fluorescent due to high internal conversion rates or slow emissions.

### 3.2. Electronic Properties of Materials

A very important feature of all materials is their ability to conduct electricity or lack thereof. Under the influence of the applied voltage, the phenomenon of electric current through materials occurs. Conductivity occurs through charge carriers that can be positively charged - then their displacement occurs in the direction of field strength, or negatively charged - they move in the opposite direction. The basic charge carriers are electrons (negative) and holes (positive), which indicate the absence of an electron in a solid at the binding site. Electron conductivity occurs in materials with a covalent bond, i.e. one in which electron pairs belonging to the two nearest atoms bind together. It is different in the case of ionic bonds, in which conductivity takes place through ions. In such a system, positive carriers are cations, while negative carriers are anions.

It is convenient to discuss the electronic properties of materials using solid state band theory. When the atoms approach each other over very small distances, the discrete energy levels of the electrons change to form a solid. The electrons that surround the atomic nucleus can only fill precisely defined energy states with the lowest possible energy. According to the Pauli principle, two identical fermions cannot be in the same quantum state at the same time, which means that a maximum of two electrons with opposite spins can occupy one energy state [3.6]. Therefore, as the atoms approach each other, the valence electrons interact with each other, which causes the energy level to split. Generally, the differences between energy states are very small, so they are said to form continuous energy bands. The band resulting from the split of the base band is called the valence

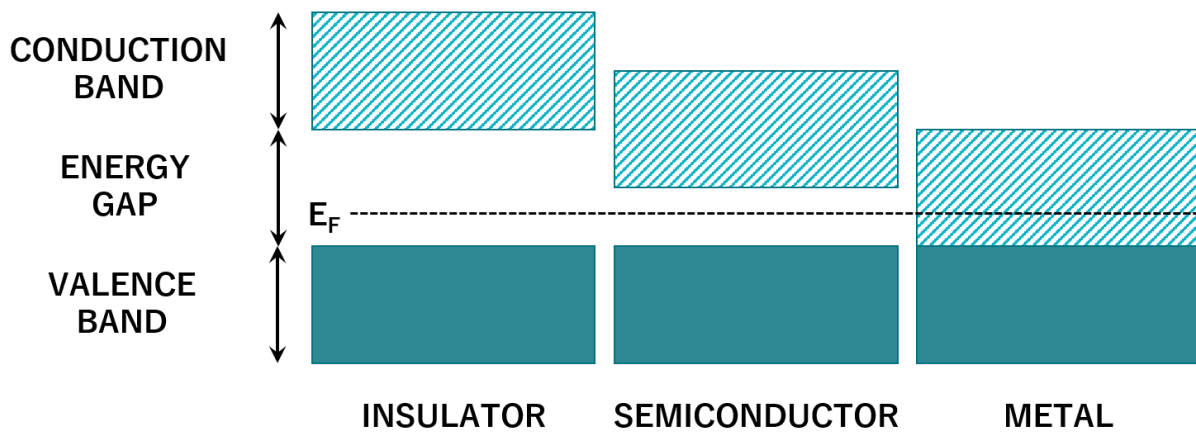
band, while the band above it is the conductivity band. The energy gap, i.e. the area between these bands, is forbidden for electrons.

It turns out, however, that these bands can be filled completely, partly or not at all. Then the quantity, called Fermi  $E_F$  energy, is entered, which determines the energy of the highest occupied level in the energy band at 0 K. Fermi energy is from 2 eV to 12 eV [3.7]. This energy distribution of a large number of particles and its changes with temperature  $T$  can be calculated by statistical considerations. The kinetic energy of the electron gas is regulated by the Fermi-Dirac distribution, which gives information that the Fermi energy  $E_F$  is determined by the probability of filling a certain energy level  $E$  by electrons  $f(E)$ :

$$f(E) = \frac{1}{\exp\left(\frac{E - E_F}{k_B T}\right) + 1} \quad (3.2)$$

where:  $k_B$ - Boltzmann constant,  $T$  - absolute temperature. If the energy level  $E$  is completely occupied by electrons, then the Fermi-Dirac distribution is 1. In turn, for the empty energy level  $f(E) = 0$ . Electricity conduction occurs for electrons with energy similar to Fermi energy.

There are two types of molecular orbitals: HOMO (Highest Occupied Molecular Orbital), which means the highest occupied molecular orbital and LUMO (Lowest Unoccupied Molecular Orbital), which means the lowest unfilled molecular orbital [3.6]. In solid state physics, HOMO means the maximum valence band, LUMO means the minimum conductivity band (Fig. 3.3). The difference between them determines the value of the energy gap. A large energy break is associated with insulators. Partial filling of the energy band can lead to a situation where the value of the energy gap is zero. Metals are characterized by having empty levels directly above double-occupied valence levels. Due to the zero energy gap they are conductors of electric current. The Fermi level is particularly interesting in metals because there are ways to change its position on the energy scale, which is done by injecting electrons or by causing a shortage of electrons in the material.



**Figure 3.3:** Valence bands (highest occupied by electrons) and conduction bands (empty). The electrical properties of the solid depend on the energy gap between them (difference between HOMO - LUMO). A large energy gap is typical for an insulator, medium describes semiconductor, while a zero energy gap is typical for metals.


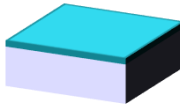
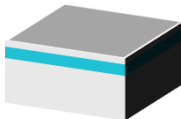
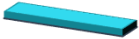
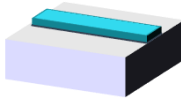
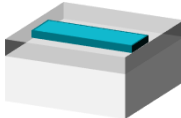

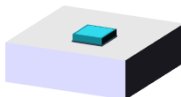
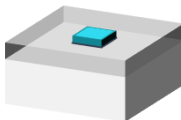
Generally, the band structure, along with information about the location of the Fermi level, tells us a lot about the electrical properties of the material (insulator, metal, semiconductor). The band structure also gives information about the basic optical properties, including the energy gap indicates what absorption spectrum we can expect.

### 3.3. Thin Film Structures

Over the last few decades, there has been a significant increase in the interest in thin films. Used in many types of engineering systems, thin films make an important contribution to technological processes, including accelerating the development of highly integrated electronic systems.

In order to understand the definition of the thin film, it is convenient to introduce a general classification of structures in terms of their geometrical configuration and character of spatial constraints, as it is shown in Fig. 3.4. These configurations are classified in terms of structure limitation in three perpendicular directions, where coordinate reference orientation depends on the

configuration. The degree of limitation is defined as the interaction of the structure with other solid states to which it may be attached or with which it may be in contact. The layer or film is often called a two-dimensional structure, a quantum wire is a one-dimensional structure and a quantum dot a zero-dimensional structure. However, it is not standard terminology [3.8]. The adoption of the classification scheme which is shown on Fig. 3.4. makes it easier to distinguish low-dimensional structures.

	UNRESTRICTED AREA	PARTLY RESTRICTED AREA	RESTRICTED AREA
THIN FILM			
QUANTUM WIRE			
QUANTUM DOT			

**Figure 3.4:** Division of low-dimensional structures in terms of their general shapes and level of spatial restrictions.

Generally, a thin film is defined as a low-dimensional material created by applying single atoms, molecules or ions to the substrate. The thin film technology applies to a wide spectrum covering from a few nanometres to several microns. It is believed that thin films act to as a “bridge” between monolayers and volume structures. There are no rigid rules that allow you to classify films as thick or thin. However, the dependence of film properties on the dimension is important.

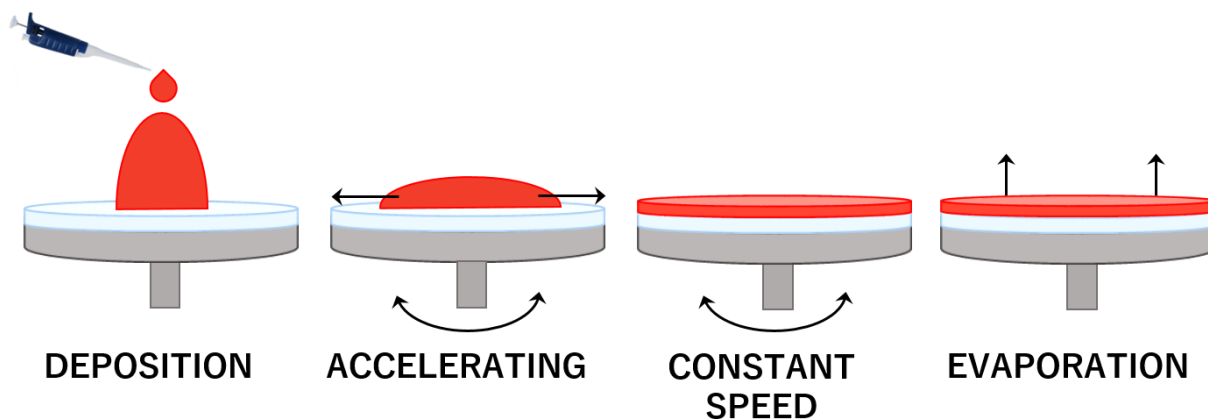
Regardless of the thickness boundary, the ideal film can be defined mathematically as a homogenous solid material contained between two parallel planes and stretched infinitely in two directions, for example  $x$  and  $y$ , but bounded along the third direction  $z$  which is perpendicular to the  $x$ - $y$  plane. The dimension along the direction  $z$  denotes the film thickness  $d$  [3.9]. This value can vary from  $d \rightarrow 0$  to any value up to 10 microns or more, but always remains much smaller than those that are along the order two directions  $x$  and  $y$ . In fact, this deviates significantly from the ideal case, because the two planes are never exactly parallel, even when they were created in the best setting conditions, and the material contained between two planes is rarely homogenous, evenly distributed, or the same species. It is also known that the film may contain many defects, impurities, dislocations, grain boundaries and other defects and discontinuities. The upper surface of the film often exhibits some topographic characteristics which are characteristic of growth conditions, which are often noticeable by the sense of sight. Some of these features can be undoubtedly minimized by adequate control of deposition, but they can not be avoided. The bottom surface of the layer exhibits topographical features of the substrate with which is in contact.

As mentioned before, all films produced in various techniques are invariably associated with some of the defects in layer growth. The surface state of the layer plays a dominant role in modifying, inter alia, electrical properties. In addition, due to the high surface-to-volume ratio of the thin film, the newly formed surface of the layer becomes highly reactive. Due to imbalance of forces close to the surface, such phenomena as thermal emission, gas adsorption, solid state reactions and other surface-related features are often observed. That is why it is extremely important to study thin films not only because of the enormous technological importance, but also because of insufficient knowledge about their interaction with electric, magnetic and electromagnetic fields. Often new phenomena appear in thin films. So far, many factors have been observed determining, among others, the physical, electrical or optical properties of thin films, such as: sedimentation rate,

substrate temperature, environmental condition, material purity which is deposited, layer heterogeneity and others.

### 3.4. Spin Coating

One of the most important, well-known and cheapest method of thin films deposition is spin coating technique. Deposition is divided into 4 steps (Fig. 3.5): in this method, the layers are applied from a solution, so before applying the layers it is necessary to dissolve the studied compounds in a suitable solvent; (1) in the first step, a specific amount of solution is spread on substrate, which is held by vacuum through a spinning device; (2) when the rotatable stage is accelerating, most of the solution is spun outside the substrate, however part of the solution remains on the ground and covers its entire surface; (3) followed by rotation in constant speed, making the layer thinner and homogenous; (4) after evaporation of the solvent, additional drying is carried out on a special hot plate, at a temperature depending on the material used.



**Figure 3.5:** Spin coating technique.

The sample thickness is influenced by many parameters, both from the samples and from spinning parameters: viscosity, amount of solution, covering time, spinning speed, acceleration, surface



tension. However, the final thickness  $d_f$  of the sample can be estimated from the semi-empirical equation of Meyerhofer [3.10]:

$$d_f = \left(\frac{3}{2}\right)^{1/3} c_0(1 - c_0)^{-1/3} \omega_r^{-2/3} v_0 e^{1/3} \quad (3.3)$$

where  $c_0$  describes initial coating concentration,  $\omega_r$  is connected to the angular rotation speed (in  $s^{-1}$ ),  $v_0$  is the initial kinetic viscosity (in  $m^2 s^{-1}$ ),  $e$  describes the evaporation rate (in  $m s^{-1}$ ).

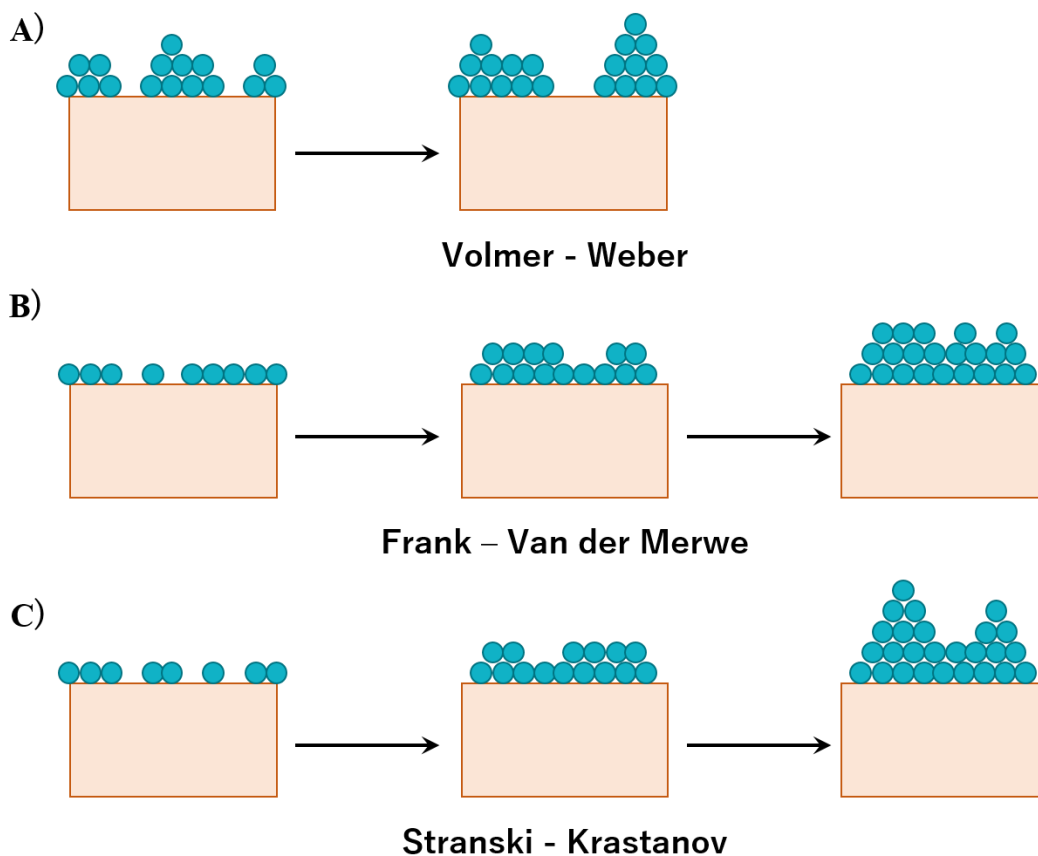
Spin coating technique is very popular in the production of photoresistive layers, devices including LEDs, photovoltaic cells, light-sensitive and conjugated polymers, semiconductor wafers, emerging industries of organic electronics. Moreover, is widely used in the preparation of samples for investigations in nonlinear optics [3.11 – 3.12]. This method has many advantages: uses low-cost equipment, is very simple and it is possible to use various kinds of substrates. However, also has its drawbacks. One of them is the fact that each sample should be prepared separately, so mass production of samples of the same thickness is almost impossible. Also the fact that the production of thin layers is carried out only for laboratory samples - of small size. For successful coating, the following conditions must be met: first, prepared solvent must wet substrate, otherwise all of the solution will be ejected during acceleration; secondly, the material that we want to apply to the substrate must be soluble; besides, the solvent we use must be volatile. In addition, spin speed versus thickness correlations should be observed, otherwise wrong calculations can lead to structure defects such as pinhole, air bubbles, uneven sample thickness at the center and at the edges.

### 3.5. Physical Vapor Deposition

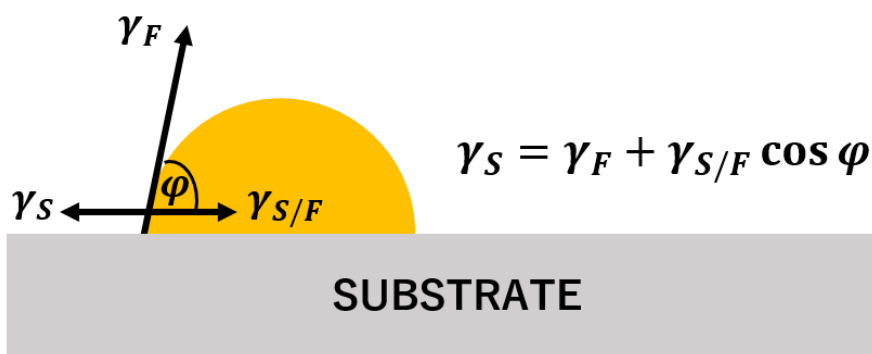
PVD process generally takes place in three stages. The first is the production of the proper particles: atoms, molecules or ions. In the second stage, the particles are transported to the substrate in the

form of vapor by low gas or plasma pressure. In the last stage, condensation occurs on the substrate, the aim of which is to create a stable layer. The final product may be in the form of a single crystal layer as well as a polycrystalline layer, as well as an amorphous layer. Typically, the gas-phase deposition is used to deposit films with thicknesses ranging from a few to thousands of nanometres, but it can also be used to form multilayer coatings and thick layers. Typical deposition rates are 1-10 nm per second [3.13].

Extensive experimental and theoretical studies of the deposition process at different stages of growth allowed to observe that there are three different types of nucleation and layer growth. The three basic types are: the Volmer – Weber model, the Frank – Van der Merwe model and the Stranski – Krastanov model [3.14]. A diagram illustrating each of these three types of thin film growth is presented on Fig. 3.6. In the Volmer – Weber model (Fig. 3.6a), the balance exists between the three-dimensional crystal of the layer in contact with the substrate, while the rest of the substrate is depleted of any condensed phase. The growth process takes place in the form of islands on the surface of the substrate until the atoms do not form a continuous layer. In the Frank – Van der Merwe model (Fig. 3.6b) nucleation takes place in the form of a single-layer island. Finally, monolayers grow together, forming a complex monolayer. This process is repeated in a multi-layered manner. In this growth model, the layer after the layer of interaction between the substrate and the atoms of the layer are stronger than between adjacent atoms of the layer. The Stranski – Krastanov model (Fig. 3.6c) combines the features of layered growth and nucleation in three dimensions. In this model, nucleation and growth occur as in the Frank – Van der Merwe model, therefore a finite number of monolayers is created. Subsequent formation of the layer occurs by creating separate nuclei. The mismatch between the substrate and the resulting layer can not be taken into account when the thickness of the layer increases so that the three-dimensional growth promotes the growth of the layer by layer. Alternatively, the symmetry of orientation over the layers relative to the substrate may be responsible for producing growth in this mode.



**Figure 3.6:** Types of layer growth: A) Volmer - Weber island growth; B) Frank - Van der Merwe layer growth; C) Stranski - Krastanov island-layer growth.



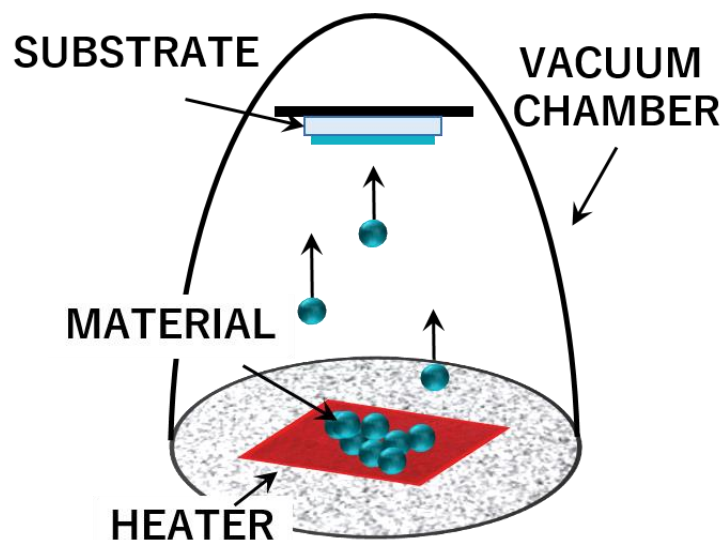
**Figure 3.7:** Schematic of forming island film on the substrate.

The differences between these models can be determined by the surface tension or interface tension ( $\gamma$ ), which can be interpreted as the work per unit area needed to form the inter-surface

(see Fig. 3.7), where  $\gamma_S$  is the surface tension of the substrate,  $\gamma_F$  is the surface tension of film under vacuum, and  $\gamma_{S/F}$  is the surface tension of substrate-film interface, and  $\varphi$  describes island wetting angle. For the Volmer-Weber  $\varphi > 0$ , therefore  $\gamma_S < \gamma_F + \gamma_{S/F}$ . However, for Frank – Van der Merwe growth  $\varphi$  is equal to 0, hence  $\gamma_S \geq \gamma_F + \gamma_{S/F}$ . According to Fig. 3.7, during Stranski-Krastanov growth it is necessary assuming that there is a lattice mismatch between the deposited film and the substrate. The condition for Frank-Van der Merwe growth is initially fulfilled, however, the formation of layers causes indirect changes in the values of  $\gamma_S$  and  $\gamma_{S/F}$ , which leads to the condition for Volmer-Weber growth.

The scheme of deposition from the gas phase is shown in Fig. 3.8. The vacuum deposition process, also often referred to as a vacuum evaporation, is a PVD process in which material from a thermal source of evaporation reaches the substrate, with little interference with gas molecules in the space between the source and the substrate. In this process, thermal energy is supplied to the source (radiator), from which the atoms are evaporated to the substrate. The material vaporized from the source has a composition that is proportional to the relative vapors of the material in the molten source material. The configuration of the steam source is to accelerate the heat near the source material and avoid warming up the environment. Heating the source material can be achieved by any of several methods. The easiest way is the resistance heating of the wire on which the source material is located. Larger amounts of this material can be heated in suitable crucibles by resistance heating, high frequency induction heating or electron beam evaporation. The evaporated atoms pass through a reduced background pressure in the vacuum chamber and settle on the surface of the substrate. The vacuum environment also allows reduction of impurities of the deposition system to the lowest possible level. Typical vacuum deposition occurs in the  $10^{-5} \sim 10^{-9}$  Torr pressure range [3.13] which depends on the level of gaseous pollution and that can be tolerated in the deposition system. The deposition rate is commonly determined by the number of atoms

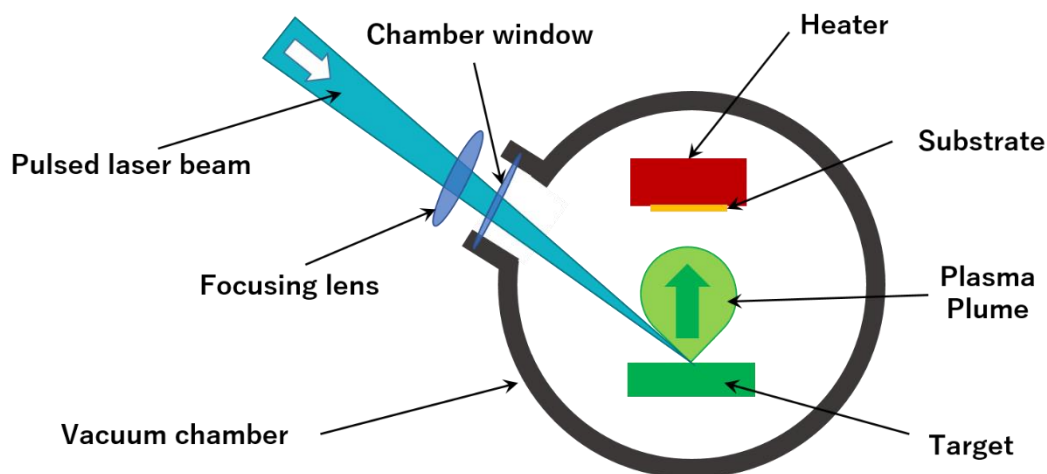
reaching the substrate per unit area of the substrate per unit on time. Generally, the substrates are placed at a significant distance from the source of evaporation to reduce their radiation of the substrate heating by the source of evaporation. The PVD method is widely used as a method of sample preparation for testing non-linear optics of both inorganic and organic samples [3.15].



**Figure 3.8:** Diagram showing the basic features of the vapor deposition system.

### 3.6. Pulsed Laser Deposition

Pulsed Laser Deposition (PLD), called as well Laser Ablation (Fig. 3.9) is one of the most famous techniques of thin film deposition. In this method deposition takes place from the gas phase in the vacuum system. This is a technique that uses a pulse laser which is focused on the purpose of the deposited material [3.16]. In the next step the surface is heated by the laser's interaction, which initiates the evaporation process. By evaporating a small amount of material with each material impulse, a plasma plume is formed and begins to expand. Plasma is moving towards the substrate, where it condenses. In this way, a thin film is formed. In the case of inorganic materials, the laser desorption conditions are chosen such that the plasma plume is composed of atoms and other low-mass particles.



**Figure 3.9:** Experimental setup for Pulsed Laser Deposition technique.

## Literature

[3.1] J. R. Lakowicz, Principles of Fluorescence Spectroscopy: Third Edition, Springer Science & Business Media, 2006.

[3.2] G. G. Stokes, On the Change of Refrangibility of Light, Phil. Trans. R. Soc. Lond. 1852 142, 463-562.

[3.3] M. Kasha, Characterization of electronic transitions in complex molecules, Discussions of the Faraday Society, 1950.

[3.4] P. Klan, J. Wirz, Photochemistry of Organic Compounds, From Concepts to Practice, Wiley, 2009.

[3.5] J. R. Albani, Principles and Applications of Fluorescence Spectroscopy, Blackwell Science, 2007.

[3.6] L. Piel, Ideas of Quantum Chemistry, Elsevier Inc, 2014

[3.7] R. E. Hummel, Electronic Properties of Materials, Springer Science & Business Media, 2005.

- [3.8] L. B. Freund, S. Suresh, *Thin Film Materials: Stress, Defect Formation and Surface Evolution*, Cambridge University Press, 2003.
- [3.9] A. Goswami, *Thin Film Fundamentals*, New Age International Publishers, 1996.
- [3.10] D. Meyhofer, Characteristics of resist films produced by spinning, *J Appl Phys* 49 (7):3993-3997, 1978.
- [3.11] B. Kulyk, A. P. Kerasidou, L. Soumahoro, C. Moussallem, F. Gohier, P. Frere, B. Sahraoui, Optimization and diagnostic of nonlinear optical features of p-conjugated benzodifuran-based derivatives, *RSC Adv.*, 2016, 6, 14439.
- [3.12] A. Ayadi, A. Szukalski, A. El-Ghayoury, K. Haupa, N. Zouari, J. Myśliwiec, F. Kajzar, B. Kulyk, B. Sahraoui, TTF based donor-pi-acceptor dyads synthesized for NLO applications, *Dyes and Pigments*, 5599, 2016.
- [3.13] D. M. Mattox, *Handbook of Physical Vapor Deposition (PVD) Processing*, Noyes Publications, 1998.
- [3.14] K. S. Sree Harsha, *Principles of Physical Vapor Deposition of Thin Films*, Elsevier Inc, 2006.
- [3.15] A. Zawadzka, K. Waszkowska, A. Karakas, P. Płóciennik, A. Korcala, K. Wisniewski, M. Karakaya, B. Sahraoui, Diagnostic and control of linear and nonlinear optical effects in selected self-assembled metallophthalocyanine chlorides nanostructures. *Dyes Pig.*, Vol. 157, 151-162, 2018.
- [3.16] P. Płóciennik, D. Guichaoua, A. Korcala, A. Zawadzka, Studies of aluminium oxide thin films deposited by laser ablation technique, *Optical Materials* (2016).

## CHAPTER 4: EXPERIMENTAL TECHNIQUES

### 4.1. Theoretical Models

#### 4.1.1 Lee

The Lee model is used to determine the second-order nonlinear susceptibility [4.1]. Quartz glass is the most commonly material used as a reference. Second-order nonlinear optical susceptibility  $\chi^{(2)}$  of sample with thickness  $d$  can be calculated by:

$$\chi^{(2)} = \chi_{Quartz}^{(2)} \left(\frac{2}{\pi}\right) \left(\frac{L_{Quartz}^{coh}}{d}\right) \sqrt{\frac{I^{2\omega}}{I_{Quartz}^{2\omega}}} \quad (4.1)$$

where  $I^{2\omega}$  and  $I_{Quartz}^{2\omega}$  are the maximum amplitudes of SHG of the investigated material and quartz, respectively,  $\chi_{Quartz}^{(2)} = 1.0 \text{ pm} \cdot \text{V}^{-1}$  [4.2] is nonlinear optical susceptibility of quartz and  $L_{Quartz}^{coh} = 21 \mu\text{m}$  is the coherent length of the reference material:

$$L_{Quartz}^{coh} = \frac{\lambda_{\omega}}{4 \cdot |n_{2\omega} - n_{\omega}|} \quad (4.2)$$

where  $\lambda_{\omega}$  is the wavelength of the fundamental beam, while  $n_{2\omega}$  and  $n_{\omega}$  are refractive indexes of the reference material for the fundamental beam and the generated second harmonic, respectively.

In the case where the optical absorption of the material is not negligible, the formula (4.1) takes form:

$$\chi^{(2)} = \chi_{Quartz}^{(2)} \left(\frac{2}{\pi}\right) \left(\frac{L_{Quartz}^{coh}}{d}\right) \sqrt{\frac{I^{2\omega}}{I_{Quartz}^{2\omega}}} \left(\frac{\frac{\alpha d}{2}}{1 - \exp\left(-\frac{\alpha d}{2}\right)}\right) \quad (4.3)$$

where  $\alpha$  is optical absorption coefficient.



### 4.1.2 Kurtz – Perry

The streamlined model of Kurtz and Perry was developed for microcrystalline powders [4.3]. This model is based on the comparison of the macroscopic second-order nonlinear optical properties of the samples with reference material – yellow powder 3-methyl-4-nitropyridine-1-oxide, called formally POM:

$$\chi^{(2)} = \chi_{POM}^{(2)} \sqrt{\frac{I^{2\omega}}{I_{POM}^{2\omega}}} \quad (4.4)$$

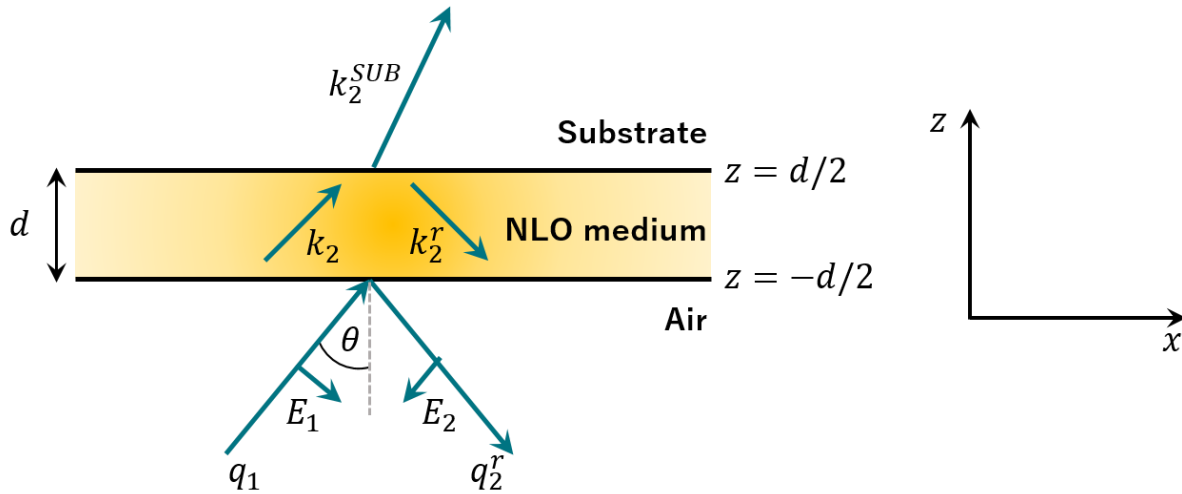
where:  $\chi^{(2)}$  and  $\chi_{POM}^{(2)} = (21 \pm 3) \cdot 10^{-9} \text{ esu}$  [4.4] are the second-order nonlinear optical susceptibilities of studied material and reference powder, respectively,  $I^{2\omega}$  and  $I_{POM}^{2\omega}$  are the maximum amplitudes of SHG of the investigated material and POM, respectively.

The main disadvantage of this simplistic model is the strong influence of the crystallinity of the investigated material on the intensities of the second harmonic signal measurements. Indeed, the size of the crystallites influences the phase agreement and therefore the intensity of the second harmonic signal. In this case, it is consequently essential to know the exact size of the crystallites.

### 4.1.3 Herman – Hayden

The model of Herman and Hayden is used for characterization of thin films and solid materials and was developed in 1995 [4.5]. This theoretical model has this advantage, unlike the model of Kurtz and Perry, of expressing the intensity of generated second harmonic by taking into account the absorption of the material at fundamental and generated second harmonic wavelengths. Model of Herman and Hayden assumes that the wave equation is solved for a homogeneous, nonmagnetic and nonlinear medium in the form of a thin film deposited on a transparent substrate: Maker fringes form as the sample rotates relative to the direction of the fundamental beam. Measurement of the

$d_{ij}(i = 1 - 3; j = 1 - 6)$  for a nonlinear medium usually consists in measuring the complex arrangement of the substrate layer, as presented in Fig. 4.1.



**Figure 4.1:** Three-layer scheme of the second harmonic generation system with a nonlinear medium.

This model assumed that the electromagnetic wave with the frequency  $\omega$  falls on the studied medium from the bottom under angle  $\theta$  and the plane  $x - z$  is the plane of incidence. At the frequency  $m\omega$ , the refractive index of nonlinear medium with thickness  $d$  is equal to  $n_m$  and  $n_{ms}$  of substrate. When the electromagnetic wave, described by:

$$\vec{E}_{1v} = \hat{e}_v E_1 \exp[i(\vec{k}_1 \cdot \vec{r} - \omega t)] \quad (4.5)$$

where:

$$\hat{e}_v = (0, 1, 0) \text{ or } \hat{e}_v = (\cos \theta, 0, -\sin \theta) \text{ for } v = S \text{ or } v = P, \text{ and } \vec{k}_1 = \left(\frac{\omega}{c}\right) (\sin \theta, 0, \cos \theta),$$

therefore in P-polarized fundamental beam, the fields of generated second harmonic in these three areas (see Fig. 4.1) are described as:

$$\text{Air:} \quad \vec{E}_2 = R \hat{e}_p^r \exp \left\{ i \vec{k}_2^r \left[ \vec{r} + \left( \frac{d}{2} \right) \hat{z} \right] \right\} \quad (4.5)$$

$$\vec{H}_2 = - \left( \frac{ic}{2\omega} \right) \nabla \times \vec{W} = R \hat{e}_s^r \exp \left\{ i \vec{k}_2^r \left[ \vec{r} + \left( \frac{d}{2} \right) \hat{z} \right] \right\} \quad (4.6)$$

$$\text{Medium:} \quad \vec{E}_2 = \vec{e}_b \exp(i2\vec{k}_1 \cdot \vec{r}) + A \hat{e}_{2P} \exp(i\vec{k}_2 \cdot \vec{r}) + B \hat{e}_{2P}^r \exp(i\vec{k}_2^r \cdot \vec{r}) \quad (4.7)$$

$$\vec{E}_H = \vec{h}_b \exp(i2\vec{k}_1 \cdot \vec{r}) + n_2 A \hat{e}_{2S} \exp(i\vec{k}_2 \cdot \vec{r}) + n_2 B \hat{e}_{2S}^r \exp(i\vec{k}_2^r \cdot \vec{r}) \quad (4.8)$$

$$\text{Substrate:} \quad \vec{E}_2 = T \hat{e}_{2P}^{SUB} \exp \left[ i \vec{k}_2^{SUB} \cdot \left( \vec{r} - \left( \frac{d}{2} \right) \hat{z} \right) \right] \quad (4.9)$$

$$\vec{E}_2 = n_2 T \hat{e}_{2S}^{SUB} \times \exp \left[ i \vec{k}_2^{SUB} \cdot \left( \vec{r} - \left( \frac{d}{2} \right) \hat{z} \right) \right] \quad (4.10)$$

where  $\hat{e}_s^r = (0,1,0)$  and  $\hat{e}_p^r = (-\cos \theta, 0, -\sin \theta)$  and is called by unit polarization vector of the reflected second harmonic field in the air,  $A$  and  $B$  are complex amplitudes of the second harmonic generation of free waves in a nonlinear medium, running forward and backward, respectively,  $R$  and  $T$  correspond to these amplitudes in substrate and air, respectively. The unit polarization vectors in nonlinear medium are described by:  $\hat{e}_{2P}^{SUB} = (0,1,0)$ ; and  $\hat{e}_{2S}^{SUB} = (c_{2S}, 0, s_{2S})$ . The vector waves are equal to:

$$\text{Air:} \quad \vec{k}_2^r = \left( \frac{2\omega}{c} \right) (\sin \theta, 0, -\cos \theta)$$

$$\text{Medium:} \quad \vec{k}_m = \left( \frac{m\omega n_m}{c} \right) (s_m, 0, c_m)$$

$$\vec{k}_m^r = \left( \frac{m\omega n_m}{c} \right) (s_m, 0, -c_m)$$

$$\text{Substrate:} \quad \vec{k}_m^{SUB} = \left( \frac{2\omega n_s}{c} \right) (s_{2S}, 0, c_{2S})$$

where:  $s_m = \frac{1}{n_m} \sin \theta$  and  $c_m = \sqrt{1 - s_m^2}$ . Stimulated wave is described by:

$$\vec{e}_b = \frac{4\pi}{n_1^2 - n_2^2} \left[ \vec{P}^{NL} - \frac{\vec{k}_b (\vec{k}_b \cdot \vec{P}^{NL})}{|\vec{k}_2|^2} \right] \quad \text{where} \quad \vec{k}_2 = 2\vec{k}_1 \quad (4.11)$$

$$\vec{h}_b = n_1 \vec{k}_1 \times \vec{e}_b \quad (4.12)$$

$$\vec{P}^{NL} = |E_1|^2 \vec{d} : \hat{e}_1 \hat{e}_2 \quad (4.13)$$

In this case, the power of generated second harmonic passing through the isotropic nonlinear medium (see Fig. 4.1) without dispersion is expressed by:

$$P_{2\omega}^{(\gamma \rightarrow P)} = \frac{128 [t_{af}^{(1\gamma)}]^4 [t_{fs}^{(2P)}]^2 [t_{sa}^{(2P)}]^2}{cA n_2^2 c_2^2} P_\omega^2 \left( \frac{2\pi d}{\lambda} \right)^2 d_{eff}^2 \frac{\frac{\sin^2 \Phi}{\Phi^2} + [r_{af}^{(2P)}]^2 R^2 \frac{\sin^2 \Psi}{\Psi^2} - 2 [r_{af}^{(2P)}] R \frac{\sin \Phi \sin \varphi}{\Phi \varphi} \cos 2\phi_2}{1 + [r_{af}^{(2P)}]^2 [r_{fs}^{(2P)}]^2 + 2 [r_{af}^{(2P)}] [r_{fs}^{(2P)}] \cos 4\phi_2} \quad (4.14)$$

where  $t$  and  $r$  are the standard Fresnel coefficients for transmission and reflection, respectively, the indices  $af$  are air-medium ( $f$ - film),  $fs$  are medium-substrate, and  $sa$  are substrate-air, and:

$$R = \frac{d_{eff}^r}{d_{eff}} \quad \text{where} \quad d_{eff} = \vec{d} : \hat{e}_1 \hat{e}_2$$

$$\varphi = \frac{2\pi d}{\lambda} (n_1 c_1 - n_2 c_2)$$

$$\Phi = \frac{2\pi d}{\lambda} (n_1 c_1 + n_2 c_2)$$

$$\phi_2 = \frac{2\pi d}{\lambda} n_2 c_2$$

In the case of non-zero absorption in the medium, complex equation of refractive index is included in equation (4.14):

$$\tilde{n}_m = n_m + i\kappa_m \quad (4.15)$$

where  $\kappa_m$  is extinction coefficient of the nonlinear medium at the frequency of  $m\omega$ . Therefore, equation (4.14) for the absorbing medium, neglecting reflection from the layer, takes the form:

$$P_{2\omega}^{(\gamma \rightarrow P)} = \frac{128}{cA} \frac{[t_{af}^{(1\gamma)}]^4 [t_{fs}^{(2P)}]^2 [t_{sa}^{(2P)}]^2}{n_2^2 c_2^2} P_\omega^2 \left(\frac{2\pi d}{\lambda}\right)^2 d_{eff}^2 \times \exp[-2\delta_1 + \delta_2] \frac{\sin^2 \Phi}{\Phi^2} + \frac{\sinh^2 \Psi}{\Psi^2} \quad (4.16)$$

where:

$$\Psi = \delta_2 - \delta_1 = \frac{2\pi d}{\lambda} \left( \frac{n_1 \kappa_1}{c_1} - \frac{n_2 \kappa_2}{c_2} \right) \quad (4.17)$$

Assuming that the studied medium in the form of a layer and the substrate are transparent, that is, that the transmission coefficients are approximately equal to 1, then the relationship describing the second-order nonlinear susceptibility for the nonlinear medium is given in form [4.5 – 4.6]:

$$I_{2\omega}(\theta) = \left( \frac{128\pi^5}{n_{2\omega}^2 \cos^2 \theta_{2\omega} \lambda_\omega^2 c} \right) (\chi_{eff}^{(2)} I_\omega d)^2 \left( \frac{\sin^2 \Phi + \sinh^2 \Psi}{\Phi^2 + \Psi^2} \right) \quad (4.18)$$

$\Phi$  and  $\Psi$  are phase angles and can be described as:

$$\Phi = \frac{2\pi d}{\lambda_\omega} (n_\omega \cos \theta_\omega - n_{2\omega} \cos \theta_{2\omega}) \quad (4.19)$$

$$\Psi = \frac{2\pi d}{\lambda_\omega} \left( \frac{n_\omega \kappa_\omega}{\cos \theta_\omega} - \frac{n_{2\omega} \kappa_{2\omega}}{\cos \theta_{2\omega}} \right) \quad (4.20)$$

where  $I_\omega$  and  $I_{2\omega}$  are the intensities of fundamental and generated second harmonic waves, respectively,  $\lambda_\omega$  is fundamental wavelength beam,  $d$  is the thickness of studied medium,  $\theta_\omega$  and  $\theta_{2\omega}$  are angles of fundamental and generated second harmonic wave, respectively,  $n_\omega$  and  $n_{2\omega}$  describe indexes of refraction at fundamental and generated second harmonic wavelength, respectively,  $\kappa_\omega$  and  $\kappa_{2\omega}$  are extinction coefficients of fundamental and generated second harmonic wavelength, respectively.

#### 4.1.4 Kubodera – Kobayashi

The Kubodera-Kobayashi model [4.7] is used to calculate  $\chi^{(3)}$ . This model consists in directly comparing the maximum amplitude of the light intensity generated third harmonic by diagnosed

medium with the maximum amplitude of the light intensity obtained in the measurement of 1 mm of silica which is used as a reference material:

$$\chi^{(3)} = \chi_{Silica}^{(3)} \left(\frac{2}{\pi}\right) \left(\frac{L_{Silica}^{coh}}{d}\right) \sqrt{\frac{I^{3\omega}}{I_{Silica}^{3\omega}}} \quad (4.21)$$

where  $d$  is a film thickness,  $I^{3\omega}$  and  $I_{Silica}^{3\omega}$  are THG intensities of the sample and the silica, respectively,  $\chi_{Silica}^{(3)} = 2 \cdot 10^{-22} m^2 \cdot V^{-2}$  [4.8],  $L_{Silica}^{coh} = 6,7 \mu m$  is the coherent length of silica:

$$L_{Silica}^{coh} = \frac{\lambda_{\omega}}{6 \cdot |n_{3\omega} - n_{\omega}|} \quad (4.22)$$

where  $\lambda_{\omega}$  is the wavelength of the fundamental beam, while  $n_{3\omega}$  and  $n_{\omega}$  are refractive indexes of the reference material for the fundamental beam and the generated third harmonic, respectively. When the optical absorption is not negligible, the relation (4) includes the linear absorption coefficient  $\alpha$  and takes the form:

$$\chi^{(3)} = \chi_{Silica}^{(3)} \left(\frac{2}{\pi}\right) \left(\frac{L_{Silica}^{coh}}{d}\right) \sqrt{\frac{I^{3\omega}}{I_{Silica}^{3\omega}}} \left(\frac{\frac{\alpha d}{2}}{1 - \exp\left(-\frac{\alpha d}{2}\right)}\right) \quad (4.23)$$

#### 4.1.5 Reintjes

The Reintjes model [4.9] was the first model in which attempts were made to explain the phenomena that is responsible for the formation of so-called Maker's fringes [4.10 – 4.11]. In this model, it is assumed that the wave propagates in a homogeneous, nonconductive, nonmagnetic, nonlinear medium. To express the intensity of the third harmonic generation, it is necessary to solve the wave equation in such a medium:

$$\vec{\nabla} \times \vec{\nabla} \times \vec{E} + \frac{n^2(3\omega)}{c^2} \frac{\partial^2 \vec{E}}{\partial t^2} = -\frac{4\pi}{c^2} \frac{\partial^2 \vec{P}^{NL}}{\partial t^2} \quad (4.24)$$

where  $c$  is speed of light and  $\vec{P}^{NL}$  is nonlinear polarization of medium. This model also assumes that:

$$\vec{E} = \frac{1}{2} \{ E_1 \exp[-i(\omega_1 t)] \vec{e}_1 + E_3 \exp[-i(\omega_3 t)] \vec{e}_3 + c. c. \} \quad (4.25)$$

as well as:

$$\vec{P}^{NL} = \frac{1}{2} \{ P_1^{NL} \exp[i(k_1 z - \omega_1 t)] \vec{e}_1 + P_3^{NL} \exp[i(k_3 z - \omega_3 t)] \vec{e}_3 + c. c. \} \quad (4.26)$$

Acquire that  $E_i = A_i \exp(ik_i z)$  then equation (4.25) takes form:

$$\vec{E} = \frac{1}{2} \{ A_\omega \exp[i(k_1 z - \omega_1 t)] \vec{e}_1 + A_{3\omega} \exp[i(k_3 z - \omega_3 t)] \vec{e}_3 + c. c. \} \quad (4.27)$$

where  $A_\omega$  and  $A_{3\omega}$  denote the amplitudes of the fundamental beam field and the generated third harmonic, respectively. If we consider only the components along the  $z$  axis, then we get the following relation:

$$\frac{\partial^2 \vec{E}}{\partial z^2} = \frac{1}{2} \frac{\partial^2}{\partial z^2} \{ A_\omega \exp[i(k_1 z - \omega_1 t)] \vec{e}_1 + A_{3\omega} \exp[i(k_3 z - \omega_3 t)] \vec{e}_3 + c. c. \} \quad (4.28)$$

therefore:

$$\begin{aligned} \frac{\partial^2 \vec{E}}{\partial z^2} = & \nabla^2 A_\omega + ik_\omega \frac{\partial A_\omega}{\partial z} \exp[i(k_1 z - \omega_1 t)] - \frac{1}{2} A_\omega k_\omega^2 \exp[i(k_1 z - \omega_1 t)] + \nabla^2 A_{3\omega} + \\ & + ik_\omega \frac{\partial A_{3\omega}}{\partial z} \exp[i(k_3 z - \omega_3 t)] - \frac{1}{2} A_{3\omega} k_{3\omega}^2 \exp[i(k_3 z - \omega_3 t)] + c. c. \end{aligned} \quad (4.29)$$

Moreover, second expression on the left side of the equation (4.24) can be written as:

$$\begin{aligned} \frac{n^2(3\omega)}{c^2} \frac{\partial^2 \vec{E}}{\partial t^2} = & \frac{1}{2} \frac{n^2(3\omega)}{c^2} \frac{\partial^2}{\partial t^2} \{ A_\omega \exp[i(k_1 z - \omega_1 t)] + A_{3\omega} \exp[i(k_3 z - \omega_3 t)] + c. c. \} = \\ = & \frac{1}{2} \frac{n^2(3\omega)}{c^2} \{ A_\omega \omega_1^2 \exp[i(k_\omega z - \omega_1 t)] + A_{3\omega} \omega_3^2 \exp[i(k_{3\omega} z - \omega_3 t)] \} \end{aligned} \quad (4.30)$$

Assume that  $k = \frac{n\omega}{c}$  and  $k_i^2 = \frac{n_i^2 \omega_i^2}{c^2}$  we obtain the following relation:

$$\frac{n^2(3\omega)}{c^2} \frac{\partial^2 E}{\partial t^2} = \frac{1}{2} A_\omega k_\omega^2 \exp[i(k_\omega z - \omega_1 t)] + \frac{1}{2} A_{3\omega} k_{3\omega}^2 \exp[i(k_{3\omega} z - \omega_3 t)] + c. c. \quad (4.31)$$

Inserting equation (4.29) to (4.31) we get:

$$\begin{aligned} \frac{\partial^2 \vec{E}}{\partial z^2} + \frac{n^2(3\omega)}{c^2} \frac{\partial^2 E}{\partial t^2} &= \\ &= ik_\omega \frac{\partial A_{3\omega}}{\partial z} \exp[i(k_{1z} - \omega_1 t)] \vec{e}_1 + ik_{3\omega} \frac{\partial A_\omega}{\partial z} \exp[i(k_{3z} - \omega_3 t)] \vec{e}_3 + c. c. \end{aligned} \quad (4.32)$$

Moreover:

$$-\frac{4\pi}{c^2} \frac{\partial^2 \vec{P}^{NL}}{\partial t^2} = -\frac{1}{2} \frac{4\pi}{c^2} \frac{\partial^2}{\partial t^2} \left\{ P_{NL}^{(1)} \exp(-i\omega_1 t) \vec{e}_1 + P_{NL}^{(3)} \exp(-i\omega_3 t) \vec{e}_3 + c. c. \right\} \quad (4.33)$$

However, from equations (4.26) and (4.32) the following relationship is obtained:

$$\begin{cases} 2ik_\omega \frac{\partial A_\omega}{\partial z} = -\frac{4\pi}{c^2} \omega_1^2 \frac{\partial^2 P_{NL}^{(1)}}{\partial t^2} \\ 2ik_{3\omega} \frac{\partial A_{3\omega}}{\partial z} = -\frac{4\pi}{c^2} \omega_3^2 \frac{\partial^2 P_{NL}^{(3)}}{\partial t^2} \end{cases} \quad (4.34)$$

According to the general expression of polarization, we can write:

$$P_{NL}^{(3)}(\omega) = \sum_{\omega=\omega_1+\dots+\omega_3} \left\{ \chi^{(3)}(\omega; \omega_1; \dots; \omega_2) \vec{E}_1(\omega_1) \dots \vec{E}_3(\omega_3) \right\} \quad (4.35)$$

In the case of the THG technique, the polarization then takes form:

$$P_{NL} = \frac{1}{4} \chi^{(3)} A_\omega^3 [\exp(ik_\omega z)]^3 \quad (4.36)$$

Using the equations (4.34) and (4.36), the following expression is obtained:



$$\begin{aligned}
2ik_{3\omega} \frac{\partial A_{3\omega}}{\partial z} &= -\frac{4\pi}{c^2} \omega_3^2 \frac{\partial^2}{\partial t^2} \left\{ \frac{1}{4} \chi^{(3)} A_\omega^3 \exp(3ik_\omega z) \right\} \exp(-ik_{3\omega} z) = \\
&= -\frac{\pi}{c^2} \omega_3^2 \chi^{(3)} A_\omega^3 \exp[-i(k_{3\omega} - 3k_\omega)z]
\end{aligned} \tag{4.37}$$

Therefore we get:

$$\frac{\partial A_{3\omega}}{\partial z} = i \frac{\pi}{2c^2} \frac{\omega_3^2}{k_{3\omega}} \chi^{(3)} A_\omega^3 \exp[-i\Delta k z] \tag{4.38}$$

Taking into account that  $k = \frac{n\omega}{c}$  and  $\omega = \frac{2\pi c}{\lambda}$  we can replace:

$$\frac{\omega^2}{k} = \frac{\omega^2 c}{n\omega} = \frac{\omega c}{n} = \frac{2\pi c^2}{\lambda} \tag{4.39}$$

As a result we get following expression:

$$\frac{\partial A_{3\omega}}{\partial z} = i \frac{\pi^2}{\lambda_{3\omega} n_{3\omega}} \chi^{(3)} A_\omega^3 \exp[-i\Delta k z] = i \frac{3\pi^2}{\lambda_\omega n_{3\omega}} \chi^{(3)} A_\omega^3 \exp[-i\Delta k z] \tag{4.40}$$

where  $n_{3\omega}$  denotes refractive index for  $3\omega$ , and  $\Delta k$  describes phase shift vector for the process of third harmonic. By integrating equation (4.40) between 0 and L we get relation:

$$A_{3\omega} = \int_0^L i \frac{3\pi^2}{\lambda_\omega n_{3\omega}} \chi^{(3)} A_\omega^3 \exp[-i\Delta k z] dz = \frac{3\pi^2}{\lambda_\omega n_{3\omega}} \chi^{(3)} A_\omega^3 \left[ \frac{1 - \exp(-i\Delta k L)}{\Delta k} \right] \tag{4.41}$$

However, the intensity of the wave can be expressed as:

$$I_{i\omega} = \frac{n_{i\omega} c}{2\pi} |A_{i\omega}|^2 \tag{4.42}$$

Thus, the intensity of the generated third harmonic with the amplitude described by equation (4.41)

takes the form:

$$I_{3\omega} = \frac{n_{3\omega} c}{2\pi} \left( \frac{3\pi^2}{\lambda_\omega n_{3\omega}} \right)^2 \left( \frac{2\pi}{n_\omega c} \right)^3 I_\omega^3 |\chi^{(3)}|^2 \left| \frac{1 - \exp(-i\Delta k L)}{\Delta k} \right|^2 \tag{4.43}$$

or written as:

$$I_{3\omega} = \frac{576\pi^6}{n_{3\omega}n_{\omega}^3\lambda_{\omega}^2c^2} I_{\omega}^3 |\chi^{(3)}|^2 L^2 \left| \frac{\sin\left(\frac{\Delta kL}{2}\right)}{\frac{\Delta kL}{2}} \right|^2 \quad (4.44)$$

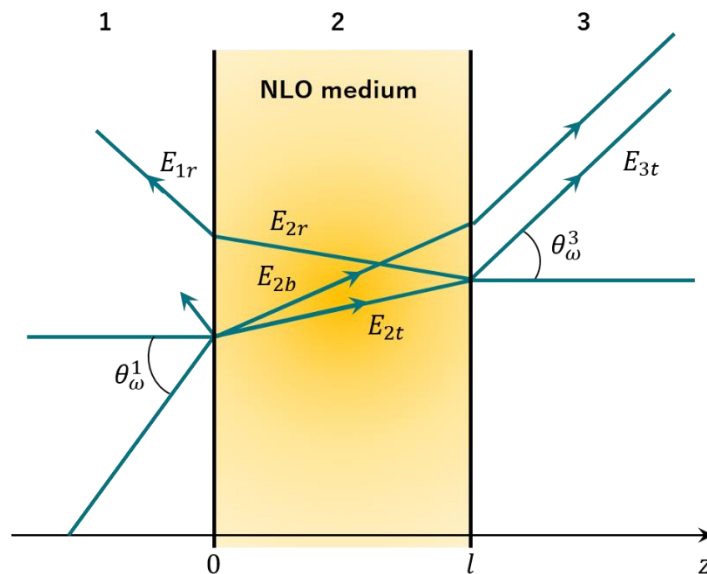
where  $I_{\omega}$  and  $I_{3\omega}$  designate the fundamental and harmonic light intensities, respectively, and  $|\chi^{(3)}|$  describes the electronic contribution of the third order nonlinear susceptibility of the nonlinear medium. In the case where the sample is not absorbing, the intensity of the third harmonic depends on the phase shift, that means:

$$\Delta\Psi = \Delta kL = \left(\frac{6\pi\Delta n}{\lambda_{\omega}}\right)L = \left(\frac{\pi}{L_C}\right)L \quad (4.45)$$

where:

$$\Delta n = n_{3\omega} - n_{\omega}; \quad \text{and} \quad L_C = \frac{\lambda_{\omega}}{6(n_{3\omega} - n_{\omega})} \quad (4.46)$$

#### 4.1.6 Kajzar – Messier



**Figure 4.2:** Propagation of a harmonic wave in a nonlinear medium placed between two linear media.

The Kajzar – Messier model can be considered in two cases [4.12 – 4.13]. The first of these is the case when the investigated sample is an isotropic medium. The propagation of the harmonic wave in a nonlinear medium takes place according to the representation of Fig. 4.2. The harmonic electric field created in a nonlinear medium with parallel faces 2 placed between two considered linear media (1 and 3) is the sum of a forced wave  $b$  and two free waves  $t$  and  $r$ :

$$E_2^{3\omega} = E_{2t}^{3\omega} \exp[-i(3\omega t - k_{3\omega}^{2f} r)] + E_{2r}^{3\omega} \exp[-i(3\omega t - k_{3\omega}^{2f} r)] + E_{2b}^{3\omega} \exp[-i(3\omega t - k_{\omega}^{2b} r)] + c. c. \quad (4.47)$$

Taking into account polarized light perpendicular to the incident plane, the third harmonic electric field is created:

$$E_{3t}^{3\omega} = E_{2b}^{3\omega} A \exp(ik_{2t}^{3\omega} l) \{ \exp[i(k_{2b}^{3\omega} - k_{2t}^{3\omega})l] - 1 \} \quad (4.48)$$

where:  $E_{2b}^{3\omega} = \frac{4\pi P_{NL}^{(2)}}{\Delta\varepsilon}$  and nonlinear polarization is given by:  $P_{NL}^{(2)} = \frac{1}{4}\chi^{(3)}(E_2^\omega)^3$ . This assumption leads to:

$$E_{2b}^{3\omega} = \frac{\pi\chi^{(3)}}{\Delta\varepsilon} (E_2^\omega)^3 = \frac{\pi\chi^{(3)}}{\Delta\varepsilon} (t_{12}^\omega E^\omega)^3 \quad (4.49)$$

Moreover, factor  $A$  is defined by:

$$A = \frac{N_2^{3\omega} + N_2^\omega}{N_2^{3\omega} + N_3^{3\omega}} \Rightarrow N_j^{\omega,3\omega} = n_j^{\omega,3\omega} \cos \theta_j^{\omega,3\omega} \quad \wedge \quad j = 1,2,3 \quad (4.50)$$

where the fundamental wave transmission coefficient  $t_{12}^\omega$  between medium 1 and the input surface of the nonlinear medium is determined by:

$$t_{12}^\omega = \frac{2n_1 \cos \theta_1}{n_1 \cos \theta_1 + n_2^\omega \cos \theta_2^\omega} \quad (4.51)$$

where:  $E^\omega$  and  $E^{2\omega}$  are the amplitudes of the optical electric fields in centres 1 and 2, respectively, the indicators  $b$  and  $t$  refer to harmonic waves transmitted by force and free space,  $l$  thickness of the nonlinear medium,  $\theta_j$  propagation angle in the middle  $j$ ,  $\Delta\varepsilon = \varepsilon^\omega - \varepsilon^{3\omega}$  describes dielectric constant dispersion,  $n^{\omega,3\omega} = \sqrt{\varepsilon^{\omega,3\omega}}$  denotes refractive indexes, and  $k^{\omega,3\omega}$  is the amplitude of the wave vectors that fulfil the relation:

$$k_{2b}^{3\omega} = 3k_2^\omega = \frac{3\omega N_2^\omega}{c} \text{ and } k_{2t}^{3\omega} = 3k_2^{3\omega} = \frac{3\omega N_2^{3\omega}}{c} \quad (4.52)$$

Setting the boundary conditions of the electric field on interfaces 1 – 2 and 2 – 3 and neglecting the waves reflected on the interfaces and the air share in relation to the vacuum, we get for the outgoing harmonic field:

$$E^{3\omega} = \frac{1}{\pi} \frac{\chi^{(3)}}{\Delta\varepsilon} T \exp(i\Psi^{3\omega}) (E^\omega)^3 [\exp(i\Delta_p) - 1] \quad (4.53)$$

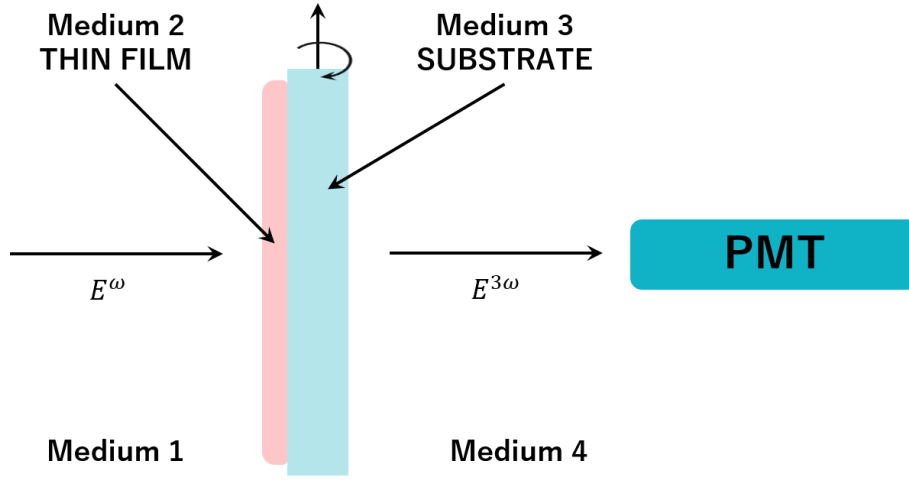
where:

$$\Delta_p = \Psi^\omega - \Psi^{3\omega} = \frac{3\omega l (N_2^\omega - N_2^{3\omega})}{c} \quad (4.54)$$

where  $E^\omega$  designates the incident electric field. Since  $\Delta_p$  varies depending on the angle of incidence, the harmonic field will change between the maximum value of  $2|A|$  for  $\Delta_p = (2m + 1)\pi$  (where  $m = 0, 1, 2, \dots$ ) and the minimum value for  $\Delta_p = 2m\pi$ . This change in the harmonic field causes Maker fringes during sample rotation.

The second case of Kajzar – Messier model is when we study a thin film deposited on the substrate [4.13]. In the case of a thin film deposited on the substrate and sandwiched between two media considered to be linear, we obtain the resulting electric field (see Fig. 4.3):

$$E_R^{3\omega} = E_S^{3\omega} t_3^{3\omega} + E_F^{3\omega} (t_1^\omega)^3 \quad (4.55)$$



**Figure 4.3:** Thin film deposited on a substrate and placed between two linear media.

Indicators  $S$  and  $F$  refer to the substrate and thin film, respectively,  $t_1^\omega$  is the fundamental wave transmission coefficient between air and thin film, and  $t_3^{3\omega}$  the harmonic wave transmission coefficient between the substrate and air. Intensity of generated harmonic for transparent thin film is defined as:

$$I^{3\omega} = \frac{64\pi^4}{c^2} \left| \frac{\chi^{(3)}}{\Delta\epsilon} \right|_S^2 (I_\omega)^3 \exp[i(\Psi_S^{3\omega} - \Psi_F^\omega)] \{ T_1 [\exp(i\Delta\Psi_S) - 1] + \rho \exp(i\phi) T_2 [1 - \exp(-i\Delta\Psi_F)] \} + C_{air}^2 \quad (4.56)$$

where:

$$\rho \exp(i\phi) = \frac{\left[ \frac{\chi^{(3)}}{\Delta\epsilon} \right]_F}{\left[ \frac{\chi^{(3)}}{\Delta\epsilon} \right]_S} \quad (4.57)$$

where  $\Delta\epsilon_S$  and  $\Delta\epsilon_F$  are the dispersion of the dielectric constant in the substrate and the thin layer, respectively and are given in following form:

$$\Delta\varepsilon_S = \varepsilon_S^\omega - \varepsilon_S^{3\omega} = 7.753 \cdot 10^{-2} [F \cdot m^{-1}]; \quad \Delta\varepsilon_F = \varepsilon_F^\omega - \varepsilon_F^{3\omega} \quad (4.58)$$

The difference of phase angles  $\Delta\Psi_S$  and  $\Delta\Psi_F$  in substrate and in a thin film, respectively, can be written in the form:

$$\Delta\Psi_S = \Psi_S^\omega - \Psi_S^{3\omega} = \frac{3\omega l_S}{c} (n_S^\omega \cos \theta_S^\omega - n_S^{3\omega} \cos \theta_S^{3\omega}) \quad (4.59)$$

$$\Delta\Psi_F = \Psi_F^\omega - \Psi_F^{3\omega} = \frac{3\omega l_F}{c} (n_F^\omega \cos \theta_F^\omega - n_F^{3\omega} \cos \theta_F^{3\omega}) \quad (4.60)$$

where  $l_S$  and  $l_F$  are the substrate thickness and the thin layer, respectively. Moreover, the factors  $T_1$  and  $T_2$  entered are determined by:

$$T_1 = (t_{12}^\omega t_{23}^\omega)^3 \frac{N_2^\omega + N_2^{3\omega}}{N_2^{3\omega} + N_3^{3\omega}} \quad \wedge \quad T_2 = (t_{12}^\omega)^3 t_{34}^{3\omega} \frac{N_3^\omega + N_3^{3\omega}}{N_3^{3\omega} + N_4^{3\omega}} \quad (4.61)$$

where  $N_j^{\omega,3\omega} = n_j^{\omega,3\omega} \cos \theta_j^{\omega,3\omega}$  for  $j = 1,2,3,4$  and transmission coefficients  $t_{ij}^{\omega,3\omega}$  for fundamental and harmonic wave between media  $i$  and  $j$  are given by (in polarization ss):

$$\begin{aligned} t_{12}^\omega &= \frac{2n_1 \cos \theta_1}{n_1 \cos \theta_1 + n_2^\omega \cos \theta_2^\omega} \\ t_{23}^\omega &= \frac{2n_2^\omega \cos \theta_2^\omega}{n_2^\omega \cos \theta_2^\omega + n_3^\omega \cos \theta_3^\omega} \\ t_{23}^{3\omega} &= \frac{2n_2^{3\omega} \cos \theta_2^{3\omega}}{n_2^{3\omega} \cos \theta_2^{3\omega} + n_3^{3\omega} \cos \theta_3^{3\omega}} \\ t_{34}^\omega &= \frac{2n_3^\omega \cos \theta_3^\omega}{n_3^\omega \cos \theta_3^\omega + n_4^\omega \cos \theta_4^\omega} \\ t_{34}^{3\omega} &= \frac{2n_3^{3\omega} \cos \theta_3^{3\omega}}{n_3^{3\omega} \cos \theta_3^{3\omega} + n_4 \cos \theta_4} \end{aligned} \quad (4.62)$$

The dispersion of the refractive index  $\Delta n_{Air}$ ,  $\Delta n_S$  and  $\Delta n_F$  of air, substrate and thin film, respectively, are given by:

$$\Delta n_{Air} = n_{Air}^{\omega} - n_{Air}^{3\omega} = 1.085 \cdot 10^{-5} \quad \Delta n_S = n_S^{\omega} - n_S^{3\omega} \quad \Delta n_F = n_F^{\omega} - n_F^{3\omega} \quad (4.63)$$

For the fundamental wave at 1064 nm the  $\chi_S^{(3)}$  and  $\chi_{Air}^{(3)}$  values for silica and air, respectively, are equal to  $\chi_S^{(3)} = 2.0 \cdot 10^{-22} [m^2V^{-2}]$  [4.14 – 4.15],  $\chi_{Air}^{(3)} = 9.8 \cdot 10^{-26} [m^2V^{-2}]$  [4.12]. The contribution of air relative to vacuum  $C_{Air}$  is given in the following form:

$$C_{Air} = 0.24C' \{t_{23}^{3\omega} t_{34}^{3\omega} \exp[i(\Psi + \alpha)] - (t_{12}^{\omega} t_{23}^{\omega} t_{34}^{\omega})^3 \exp[-i(\Psi + \beta)]\} \quad (4.64)$$

where:

$$C' = \frac{\left[ \frac{\chi^{(3)}}{\Delta \varepsilon} \right]_{Air}}{\left[ \frac{\chi^{(3)}}{\Delta \varepsilon} \right]_S} \quad (4.65)$$

where  $\Psi$  is the phase of the air proportion parameter, and  $\alpha$  and  $\beta = \alpha + \Delta\Psi_S$  are the phase differences between the fundamental and harmonic waves for propagation in air, respectively, on the input and output sides of the sample.

## 4.2. SHG/THG Experiments

Experimental setup allowed for second- and third order nonlinear optical response measurements via Maker fringe technique is presented in Fig. 4.4. This technique is based on rotating sample and measuring intensity of generated harmonic in transmission manner as a function of incident angle [4.16 – 4.18]. Studied samples were rotated from  $-75^\circ$  to  $+75^\circ$  with step  $0.5^\circ$  in vertical (P) and horizontal (S) polarized fundamental laser beam. Parameters of apparatus used in this experiment are located in Tab. 4.1. As a light source is used pulsed Nd:YAG laser (Ekspla, PL2250) with a pulse duration of 30 ps with a power of several  $\mu J$ , generating wavelength 1064 nm and frequency

of 10 Hz. The fundamental beam of light exiting the laser passes through the beam splitter and then reflect to the photodiode. Then the light beam reaches the half-wavelength plate ( $\lambda/2$ ) and the Glan polarizer, which allow changing the polarization, and thus - the energy of the incident beam. The focusing lens with a focal length of 25 cm allows the beam to focus in such a way that its axis of rotation is near the focus. Then the beam reaches the sample placed on a rotational table, which permits to rotate the sample with high precision. The selective filter cuts off the fundamental wavelength transmitted at 1064 nm and allows the recording of the generated harmonic beam and keep only the wavelength of the harmonic generated: for SHG 532 nm, for THG 355 nm. This filter is placed before the photomultiplier tube, which records the generated harmonic signal.

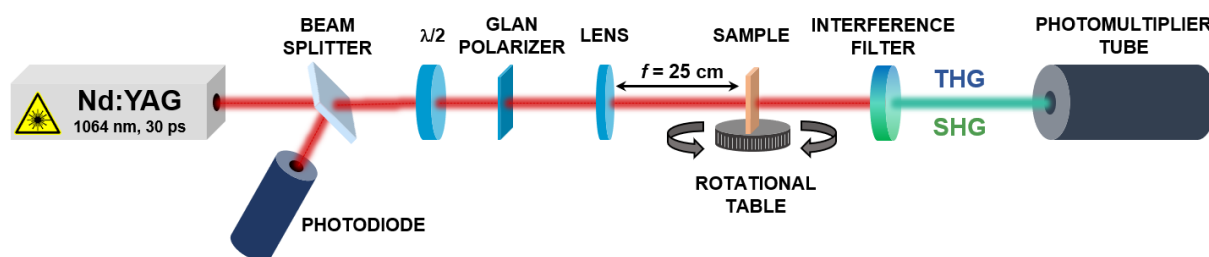


Figure 4.4: SHG and THG experimental setup via Maker fringe method.

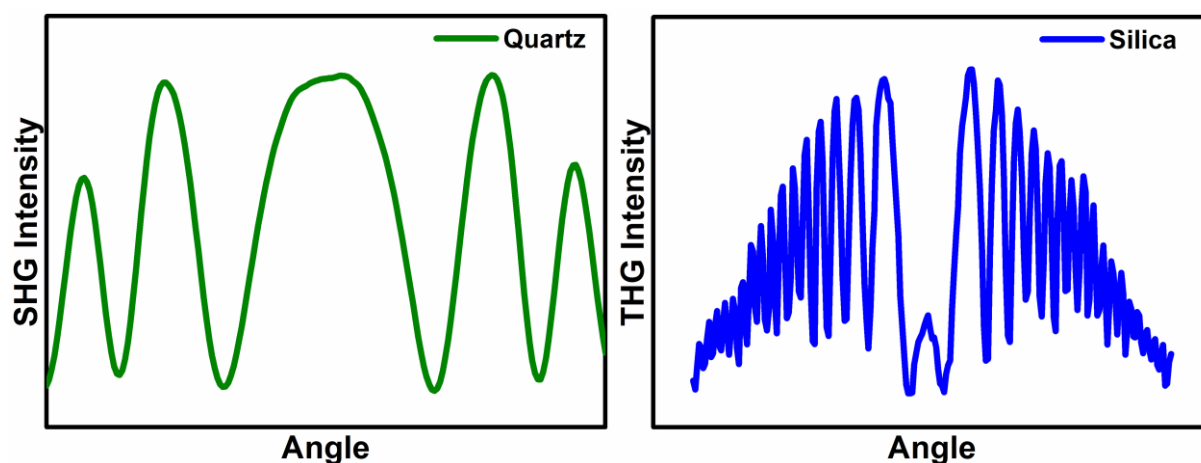


Figure 4.5: Typical Maker fringes for reference materials.

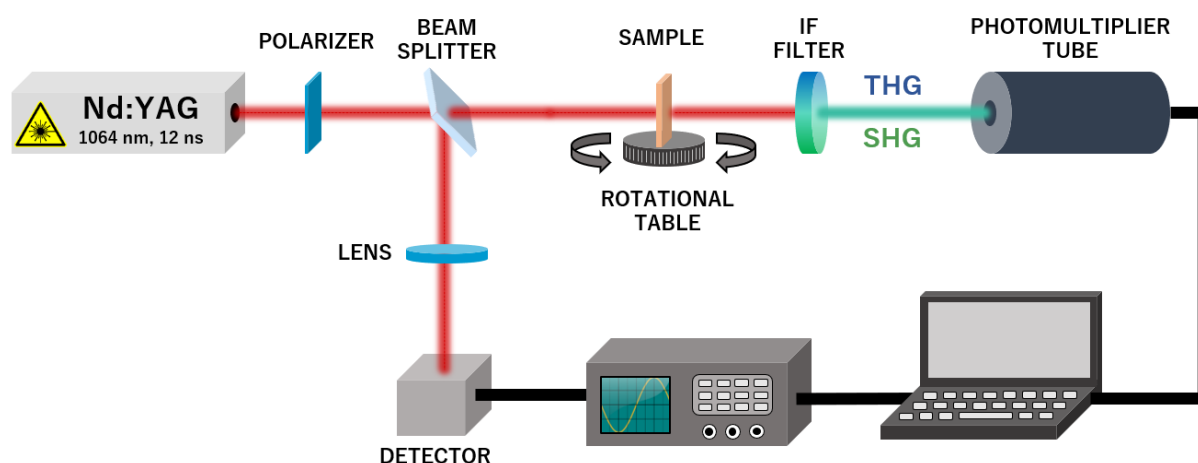
The intensity of the generated second and third harmonics is measured for each sample as a function of the incident angle. First, reference material is measured, which is Y-cut quartz crystal



(in the case of SHG measurements) and silica glass (in the case of THG measurements). Nonlinear electrical susceptibility is calculated in comparison of these reference materials. Exemplary SHG and THG intensities for reference materials are schematically shown in Fig. 4.5. It is important that the signal must be symmetrical in terms of angle  $0^\circ$ .

**Table 4.1.** Parameters of setup used in SHG/THG measurements.

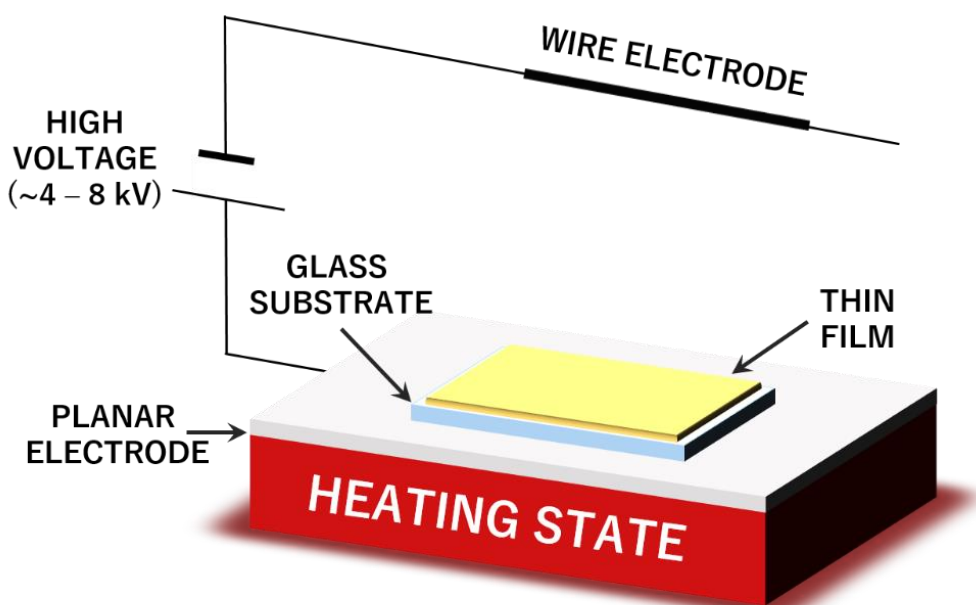
	Maker fringe	Laser energy dependence
Laser	Nd:YAG	Nd:YAG
Laser Wavelength	1064 nm	1064 nm
Laser Energy	80 $\mu$ J	60 mJ
Pulse duration	30 ps	12 ns
Repetition rate	10 Hz	12 Hz



**Figure 4.6:** Experimental setup measuring SHG and THG intensity relative to laser energy.

Moreover, second- and third order nonlinear optical effects as a dependence of laser energy were achieved by using experimental setup, presented in Fig. 4.6. Second and third harmonic generation were observed for s-p polarization of incident laser beam. As a light source was used Nd:YAG laser (Quanta-Ray Lab-Series) with fundamental wavelength 1064 nm, pulse duration 12 ns, repetition rate 12 Hz and energy 60 mJ [4.19]. The laser energy density was changed by rotating Glan polarizer up to  $200 \text{ J/m}^2$ . Parameters of laser used in this experiment are placed in Tab. 4.1.

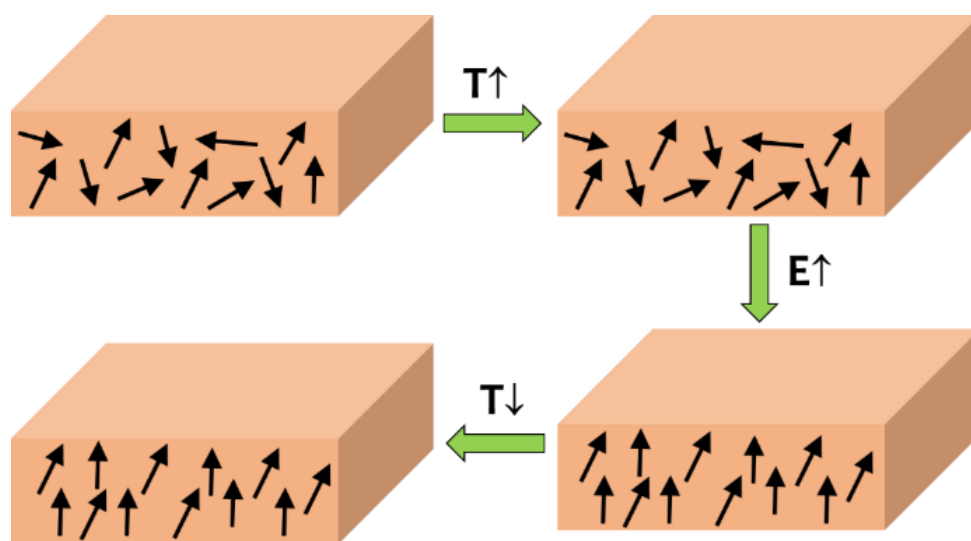
### 4.3. Corona Poling



**Figure 4.7:** Corona Poling setup.

Aforementioned, the generation of the second harmonic strongly depends on the symmetry of diagnosed material. Second harmonic generation in centrosymmetric materials is possible by creating macroscopic noncentrosymmetry. This is performed by applying an external electric field forcing the orientation of molecules which have dipole moments towards the electric field line. One of this method is the corona poling technique [4.20]. In this method, the sample is heated to change the orientation of molecules, while at the corona point a high voltage, about 4 – 8 kV, is used. Applied at this point the electric field accelerates the free electrons which ionizing the environment. Produced in this way ions, which have the same sign as the applied electric field, are orienting towards the surface of the material, where they forming an internal electric field along which the molecules are orienting. When high voltage is turned off, orientation remains suspended for particular time, depended on the chemical properties of the system. In the case of polymeric materials, it is important that the applied temperature have to be less than the glass transition temperature  $T_g$  of the material. Fig. 4.7. presents scheme of corona poling technique, while Fig. 4.8

describes orientation of dipole moment in polymer matrix. This technique, like any other, has advantages and disadvantages. First of all, the corona poling system is easy to use and has a fast charging process. Moreover, the main advantage is the ability to achieve macroscopic noncentrosymmetry in guest-host systems, thanks to which it is possible to obtain the SHG effect. On the other hand, the forced orientation of the dipole moments in molecules is achieved for an indefinite period of time, depending on the properties of the material. Due to the fact that the corona poling method is based on reducing the absorbance of a given material, in order to estimate the relaxation time, the absorption spectrum should be regularly measured after using this technique. Besides, other disadvantages of this method include the formation of surface roughness (not always), which has a direct impact on optical loss. According to Ref. [4.21], the ordering parameter in the corona poling method had value around  $f = 0.3$ , where the parameter  $f$  assumes a value from 0 to 1 depending on the degree of orientation. Considering that each molecule has different properties, the ordering parameter consists mainly of: dipole moment, absorption, guest-host concentration, isotropy, and other properties. One of the methods to determine this parameter is to measure the absorption spectrum of the thin film before and after the application of the corona poling method.



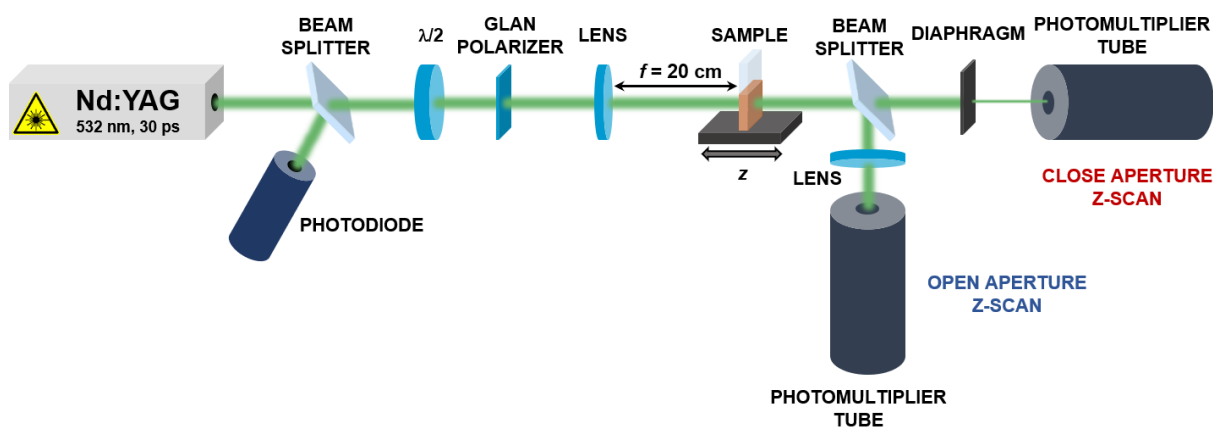
**Figure 4.8:** Orientation of dipole moment in polymer matrix during corona poling experiment.

#### 4.4. Z-scan Technique

During self-focusing of the intense Gaussian beam in the nonlinear medium, beam distortion occurs. The resulting distortion is measurable, and the information obtained allows us to extract the  $n_2$  value of the medium. In 1989, M. Sheik-Bahae [4.22] developed a method that focuses the laser beam on a thin sample. Light passing through a small hole is then detected in a distant field. When scanning the sample along the  $z$  direction through the lens focus, the far field aperture transmittance is measured, hence the name of the technique: Z-scan. To understand the Z-scan method, let's use a material that has a positive  $n_2$  and is located far from the lens. If the studied sample is thin, the intensity transmitted by the sample is low, whereas the energy passed through the hole is constant. As the sample approaches the focus, the intensity increases. When the intensity reaches a sufficiently high value, a positive lensing effect can be obtained. This effect causes, when scanning the sample, at a distance with  $z < 0$  in front of the focus, the beam approaching the focus, which results in spreading in a distant field. Therefore, the aperture transfer function decreases. Another situation occurs when focusing at a distance of  $z > 0$ . The added lensing effect reduces the beam divergence, and hence the aperture transmittance increases. Near  $z = 0$ , the lensing effect has little effect on the beam, as a result the iris transmittance returns to a low intensity value. As a result of the described phenomenon, a typical curve is obtained. An extraordinary useful feature of the Z-scan technique is that the nonlinear index sign is immediately obvious from the data.

Nonlinear optical properties were investigated by Z-scan technique [4.23 – 4.24] as well using frequency-doubled beam from pulsed Nd:YAG laser (Ekspla, PL2250) in transmission manner presented in Fig. 4.9. In this technique samples are usually investigated in form of liquids. This renowned technique allows in figure out nonlinear optical properties, such as nonlinear absorption and nonlinear refractive index, which are measured at the same time. Depending on the measured

nonlinear effect, three modes of this technique are distinguished: open aperture, closed aperture and divided Z-scan.

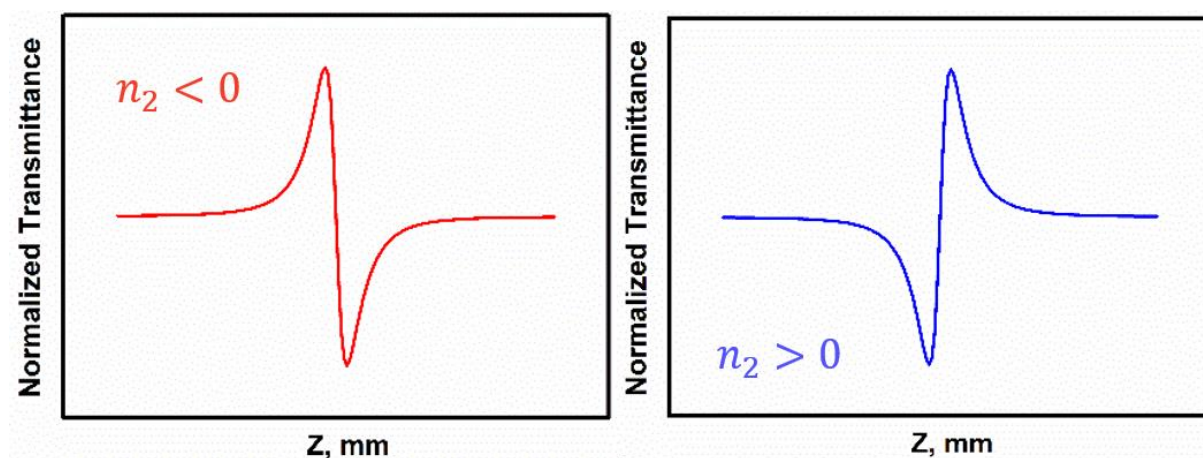


**Figure 4.9:** Z-scan experimental setup.

An extremely useful property of the Z-Scan technique is that the sign of the nonlinear absorption coefficient and the nonlinear refractive index is immediately obvious from the recorded transmittance curves. Besides, the analysis of this data is quick and simple, making it a good technique for studying new nonlinear materials. Moreover, in contrast to, for example, the third harmonic generation, thanks to the Z-scan we are able to determine both the real and the imaginary part of the nonlinear susceptibility  $\chi^{(3)}$ . Among other advantages is the simplicity of the method - single beam, there is no difficult alignment other than keeping the beam right in the centre of the aperture. However, the disadvantages of the technique include the fact that a very high quality Gaussian beam  $TEM_{00}$  is required to achieve absolute measurements, as well as thermal effects during the Z-scan experiment can cause a contribution to third-order NLO susceptibility determined from this technique, for example from thermal heating induced by laser beam pulse on the sample with time.

#### 4.4.1 Closed Aperture Z-scan

In this type of Z-scan method (CA) an aperture is located in front of the photodetector that partially prevents the access of the laser beam after passing through the nonlinear medium. The aperture causes only the central area of the light cone to reach the detector. Typically, the values of normalized transmittance are in the range  $0.1 < T < 0.5$ . This solution makes the detector extremely sensitive to any focusing or defocusing the laser beam that may be caused by the sample.



**Figure 4.10:** Typical closed aperture Z-scan curves for  $n < 0$  and  $n > 0$ .

The difference between the maximum and minimum transmission (“peak-valley”) is called  $\Delta T_{p-v}$ , where is negative in the “peak-valley” configuration and positive in the “valley-peak” configuration (Fig. 4.10).  $\Delta T_{p-v}$  value is given from:

$$\Delta T_{p-v} = 0,406 \frac{\Delta\Phi_0}{\sqrt{2}} (1 - S)^{0,25} \quad (4.66)$$

where  $(1 - S)^{0,25}$  is a parameter connected to the diameter of aperture placed before photomultiplier, and  $S$  is defined by:

$$S = 1 - \exp\left(-\frac{2r_a^2}{w_a^2}\right) \quad (4.67)$$

where  $r_a$  corresponds to radius of the aperture, and  $w_a$  corresponds to radius of the laser beam at the position of aperture. This relation (4.67) is applied when the distance between aperture and nonlinear medium is large and the radius of Gaussian beam does not change while passing through the medium. Moreover, in equation (4.66)  $\Delta\Phi_0$  describes the electric field nonlinear phase change, given in following form:

$$\Delta\Phi_0 = k\Delta n_0 L_{eff} \quad (4.68)$$

In equation (4.68)  $\Delta n_0$  is determined by following relation:

$$\Delta n_0 = \gamma' I_0 \quad (4.69)$$

and  $L_{eff}$  is described as:

$$L_{eff} = \frac{1 - e^{-L\alpha_0}}{\alpha_0} \quad (4.70)$$

where  $\alpha_0$  denotes linear absorption of the nonlinear medium. Taking into account the relation (4.68) and (4.69) in the equation (4.66) we obtain the following relationship:

$$\Delta T_{P-V} = 0,406 \frac{k\gamma' I_0 L_{eff}}{\sqrt{2}} (1 - S)^{0,25} \quad (4.71)$$

where intensity of the laser beam  $I_0$  in the centre, while passing through the focal plane, is expressed by:

$$I_0 = \frac{2E}{\pi w_0^2 \tau} \quad (4.72)$$

and  $E$  is the energy of laser beam measured by powermeter,  $\tau$  is the pulse duration (30 ns). Now, including this relation in (4.71), we obtain:

$$\Delta T_{P-V} = \frac{1,624\gamma' L_{eff} E (1 - S)^{0,25}}{\lambda \sqrt{2} w_0^2 \tau} \quad (4.73)$$

Transforming this equation with respect to  $\gamma'$ , we achieve:

$$\gamma' = \frac{\lambda \sqrt{2} w_0^2 \tau}{1,624 I_0 L_{eff} E (1 - S)^{0,25}} \Delta T_{P-V} \quad (4.74)$$

The above relation shows the relationship between the non-linear refractive index and the experimentally determined  $\Delta T_{p-v}$  parameter. Finally, the real value of  $\chi^{(3)}$  is determined from the following relation:

$$Re(\chi^{(3)}) = \frac{4n_0^2 \epsilon_0 c}{3} n_2 \quad (4.75)$$

#### 4.4.2 Open Aperture Z-scan

Open aperture Z-scan (OA), where all transmitted light is measured, allows to determine nonlinear absorption. We identify two types of nonlinear absorption: saturable absorption (SA) and reverse saturable absorption (RSA), which are determined during measurements in which we receive the transmission in the form of "peak" or "valley", respectively. In this case, the distribution of the intensity and the nonlinear phase shift at the output of the sample is given by the following relation:

$$T(z, S = 1) = \frac{1}{\sqrt{\pi} q_0(z, 0)} \int_{-\infty}^{+\infty} \ln[1 + q_0(z, 0) \exp(-\mu^2)] d\mu \quad (4.76)$$

where:



$$q_0(z, 0) = \frac{\beta I_0 L_{eff}}{1 + \left(\frac{z^2}{z_0^2}\right)} \quad (4.77)$$

where  $L_{eff}$  and  $I_0$  are given in the same conditions as described in relations (4.70) and (4.72), respectively. Determination the imaginary part of third order nonlinear susceptibility  $\chi^{(3)}$  is calculated using following expression:

$$Im(\chi^{(3)}) = \frac{n_0^2 \epsilon_0 c \lambda}{3\pi} \beta \quad (4.78)$$

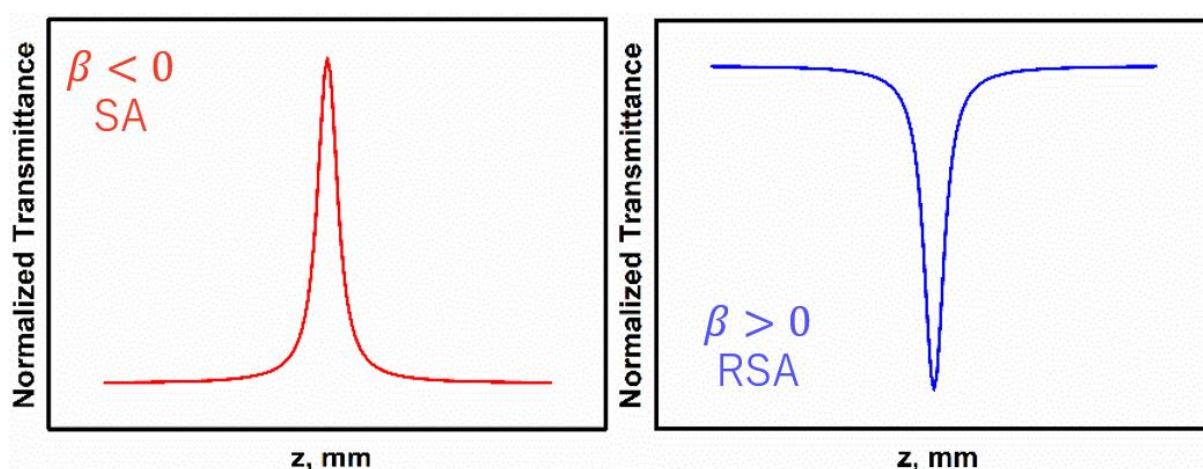


Figure 4.11: Typical open aperture Z-scan curves for  $\beta < 0$  and  $\beta > 0$ .

#### 4.4.3 Divided Z-scan

Supplementary to the aforementioned phenomena, it may happen that during closed aperture Z-scan the change in transmittance is induced by both effects - nonlinear refraction and nonlinear absorption. This is the occurrence in which nonlinear absorption cannot be ignored when calculating the nonlinear refractive index directly from data obtained from the closed aperture Z-scan. Removal of the nonlinear absorption is completed by dividing the received signal from the closed aperture Z-scan by the signal received from the open aperture Z-scan. The result is a divided Z-scan which shows the "peak – valley" or "valley – peak" for as close aperture Z-scan, but without

nonlinear absorption [4.22]. In case of impact of the nonlinear absorption during experiment of CA Z-Scan, the calculation of the nonlinear refractive index is completed using divided Z-Scan, where  $\Delta T_{p-v}$  is taken directly form divided Z-Scan.

#### 4.5. Spectroscopy Characterization



**Figure 4.12:** UV-1800 (Shimadzu) spectrometer.

The UV-1800 (Shimadzu) is an advanced high-resolution from 1100 nm to 190 nm spectrophotometer using a precise Czerny-Turner optical system. Due to the different modes it is possible to measure absorbance or transmittance at a single wavelength or at multiple (up to eight) wavelengths. When measuring multiple wavelengths, calculations can be made on data obtained for up to four wavelengths, including calculating the difference or ratio of the measurements obtained for the two wavelengths. In addition, it is possible to measure the change in absorbance, transmittance or energy as a function of time and calculate the value of the enzyme activity. In addition, it is possible to quantify up to eight ingredients mixed in one sample. Pure ingredients or mixtures of ingredients can be used as standard samples. Moreover, it can analyse DNA and proteins using several popular quantitative methods. Fig. 4.12 presents photograph of used UV-1800 spectrometer.

The spectrofluorometer is an instrument used in fluorescence measurements. The Horiba FluoroMax®-4 spectrometer is equipped with an excitation source, which is a 150 W xenon lamp. The light from the source is collected by an elliptical mirror and then focused on the tightly in-line monochromator. The lamp housing is separated from the excitation monochromator by a quartz window, which releases excess heat and protects against possible lamp failure. The next elements are two Czerny – Turner: excitation and emission monochromators, which allow to maintain high resolution in the entire spectral range, as well as minimize diffraction and spherical aberrations. An important part of the monochromator is a diffraction grating that dissipates the incident light. The spectrum is obtained by rotating the slits and recording the intensity value at each wavelength. The diffraction grating in FluoroMax®-4 contains 1200 slits per mm. Each of the monochromators has adjustable input and output slots. The width of the slits in the excitation monochromator passes the band of light falling on the sample, while the monochromator emission slots control – the intensity of the fluorescence signal recorded by the signal detector. The wider the gap, the more light falls on the sample and the detector, the resolution decreases at the same time. The beam starting from the excitation monochromator is focused on the toroidal mirror. Fluorescence from the sample is then collected and directed to the emission monochromator. The spectrofluorometer is equipped with two detectors. One of them is a photomultiplier operating in the range from 180 to 850 nm. The second one is a silicon photodiode which has a good response in the range of 190 to 980 nm. The apparatus is shown in Fig. 4.13. Photoluminescence measurements were recorded on FluoroMax-4 spectrofluorometer (Horiba), which allows the measurement of photoluminescence (fluorescence, phosphorescence) on samples in solid state (e.g. thin films) or in liquid form. This spectrofluorometer allows to record excitation, emission or both wavelengths simultaneously, measuring the intensity of photoluminescence and its changes with time, polarization and temperature. Knowing the excitation and emission wavelengths luminescence decay-times were obtained by pulse diode (with the excitation wavelength close to the excitation wavelength

characteristic for the sample, determined from the measurements) in Single Photon Counting Controller FluoroHub linked to FluoroMax-4 instrument.



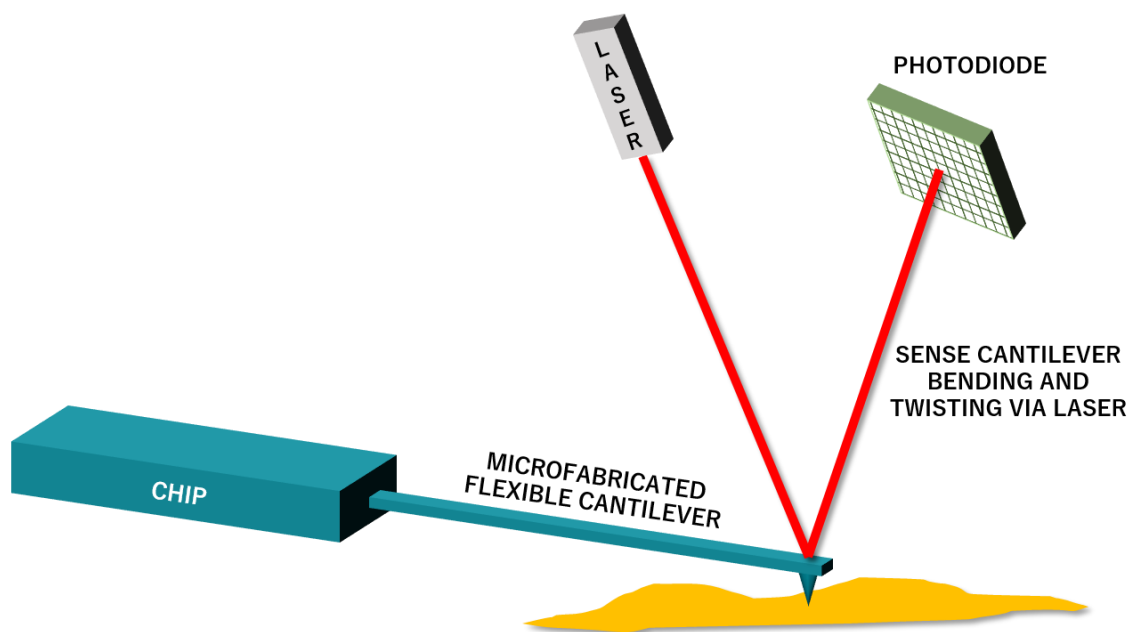
**Figure 4.13:** Photograph presents spectrofluorometer Horiba FluoroMax-4.

## 4.6. Atomic Force Microscopy

Atomic Force Microscopy (AFM) was first developed in 1986 by G. Binnig [4.25] and shortly after the discovery it became a leading technique in surface analysis, even on a molecular and atomic scale. AFM is a method that allows to observe the shape of the surface of the object under study in three dimensions at the nanometre scale. This technique is used to image the surface of any material, regardless of its transparency, hardness or conductivity. Atomic force microscopy has many advantages over other techniques, including electron microscopy techniques. The main advantage is its versatility in the field of measurement, for example in the air or fluid environment, not in a high vacuum, which allows the imaging of samples in their home state.

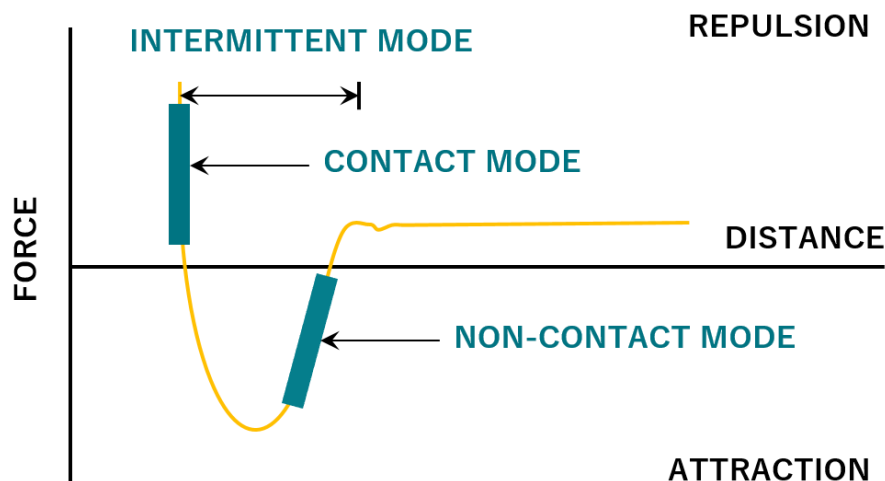
The typical atomic force microscope system is shown in Fig. 4.14 [4.26]. The most crucial element of this microscope is a sharp probe, most often V-shaped, placed near the end of an elastic cantilever. By scanning all surface of sample, the deflections of the cantilever are monitored, which allows obtaining a three-dimensional image of the topography of the sample in high resolution.

Due to the fact that all measurements made by using the AFM are based on the physical interaction between the probe and the sample, the shape of the probe is important to determine these interactions. In addition to the radius of curvature at the tip of the probe, the geometry of all parts that can interact with the sample is of great importance, especially when imaging or plummeting.



**Figure 4.14:** Schematic representation of the basic elements of the atomic force microscope. The probe is placed on the top of an elastic cantilever. The sample is most often placed on a piezoelectric table. The deviation of the cantilever is monitored by changing the laser light path deviated from the upper end of the beam by the photodiode. When the tip touches the surface, deflection is monitored. This deviation can then be used to calculate the impact forces of the probe and sample.

There are many different surface imaging modes available in AFM technique. Imaging may take place in contact mode, intermittent mode and also in non-contact mode [4.27]. These modes provide a range of different information about the surfaces to be tested.



**Figure 4.15:** Lennard – Jones potential zones in which three most common AFM imaging modes work.

Contact Mode Imaging means that the probe always stays in contact with the sample. As a result, the impact of the probe – the sample takes place in the repulsive are, as illustrated in Fig. 4.15. This is the simplest AFM operating mode and was originally used to scan the surface. There are two variations of this technique: the mode in continuous and variable power. In the constant mode, a feedback mechanism is used to maintain the deflection and thus the contact force mode of the cantilever. As the cantilever tilts, the height changes in the z-axis direction to restore the original deflection or “set point”. The position change in the z-axis direction is monitored, while the information obtained in the x and y position functions is used to create a topographic image of the sample surface. In the case of imaging the force of a variable, the feedback mechanisms are turned off so that the distance in the z-direction remains unchanged and the deviation is monitored in order to obtain a topographic image. This mode can only be used on samples that are relatively smooth, generally providing better resolution than constant mode.

The contact mode is usually chosen for imaging a hard and relatively flat surface due to the ease of use. However, there are a few drawbacks. Transverse force may occur when the probe moves to

the edge of the sample, which may damage the probe or the sample itself. Also, friction forces between the probe and the sample can lead to reduced image resolution. In addition, the relatively high forces with which the probe cooperates with the sample can cause sample deformation, which underestimates the height of the surface, and also increases the contact area between the probe and the surface. The contact area determines the resolution limit.

In order to combat the limitations of imaging in the contact mode, as mentioned earlier, the Intermittent Contact Mode (Tapping Mode) is used. In this mode, the cantilever can oscillate at a value close to the resonant frequency. When oscillations occur close to the surface of the sample, the probe will repeatedly couple to the surface, limiting the vibration amplitude. During surface scanning, the oscillation amplitude of the cantilever changes as different topographies are encountered. By using a feedback mechanism to change the height in the axis from the piezoelectric table and maintain a constant amplitude, the image of surface topography can be obtained in a similar manner as in the case of imaging in the contact mode. In this way, the probe scans the surface, and the occurrence of lateral forces is significantly reduced compared to the contact mode.

While surfaces with different mechanical and adhesive properties are scanned, the frequency of vibrations will change, causing the phase signal to shift between the frequency at which the cantilever actually oscillates. This phenomenon has been used to obtain phase images in addition to topographic images, which may show changes in the material properties of the surface being tested. Although the qualitative data provided by phase images is useful, it is difficult to extract quantitative information from them, because they are a complex result of many parameters, such as adhesion, scanning strength, load force, topography, flexibility and other.

In the Non-contact Mode, the image is oscillated, similar to the intermittent mode, but with a much smaller amplitude. When the probe approaches the surface of the sample, long-range interactions, such as van der Waals interactions or electrostatic forces, occur between atoms in the probe and

sample. This results in a detectable shift in the cantilever oscillation frequency. Detecting the phase shift between oscillation frequencies allows the positioning angle to be set in the z-axis direction to keep the cantilever in contact with the surface by feedback. Because the probe is not in contact with the surface of the sample in the repulsion zone, the impact surface is minimized, potentially allowing a higher surface resolution. As a result, in this mode it is an image that can best achieve true atomic resolution while testing the appropriate surface in the right conditions. However, in practice, obtaining high quality images is more difficult to produce than in intermittent mode. During air imaging, all but the most hydrophobic surface areas will have a significant layer of water that can be larger than the van der Waals force range.

A total samples were collected and their surfaces were analyzed by two different atomic force microscopes: Bioscope II AFM – Nanoscope V controller (Veeco) [4.28] with phosphorous n-doped Si cantilever in scanning area  $10 \times 10 \mu\text{m}^2$  and by Nanosurf Easyscan 2 AFM by monolithic silicon cantilever in scanning area  $1 \times 1 \mu\text{m}^2$  in contact mode. AFM images were then handled by Gwyddion 2.56 software. Fig. 4.16 presents photograph of Nanosurf Easyscan 2 AFM.



**Figure 4.16:** Photograph presenting Nanosurf Easyscan 2 Atomic Force Microscopy.



## 4.7. Ellipsometry

Ellipsometric spectroscopy is used to study the change in polarization of the electromagnetic wave reflected from the tested medium. The way in which the polarity changes depends on the optical parameters and the thickness of the material being tested. The name ellipsometry comes from the fact that a linearly polarized electromagnetic wave after reflection is elliptically polarized. This technique is very well known, among others in 1889 P. Drude was the first to investigate the optical properties of metals using an ellipsometer [4.29]. The scheme of the operation setup of the UVISEL Horiba Jobin Yvon ellipsometer is shown in Fig. 4.17. The xenon lamp operating in the spectrum 190 nm to 2100 nm, acting as a light source, is characterized by the fact that the outgoing light is monochromic and then linearly polarized by a polarizer and then reflected from the sample. The reflected beam goes to a photoelastic modulator, which allows to induce a modulated phase shift of the reflected beam. This photoelastic modulator is a fused silica bar exhibiting isotropic behaviour without applying stress, acting as a birefringence modulator. After the beam passes to the analyser, which transforms the polarization ellipse, and then moves to the detector.

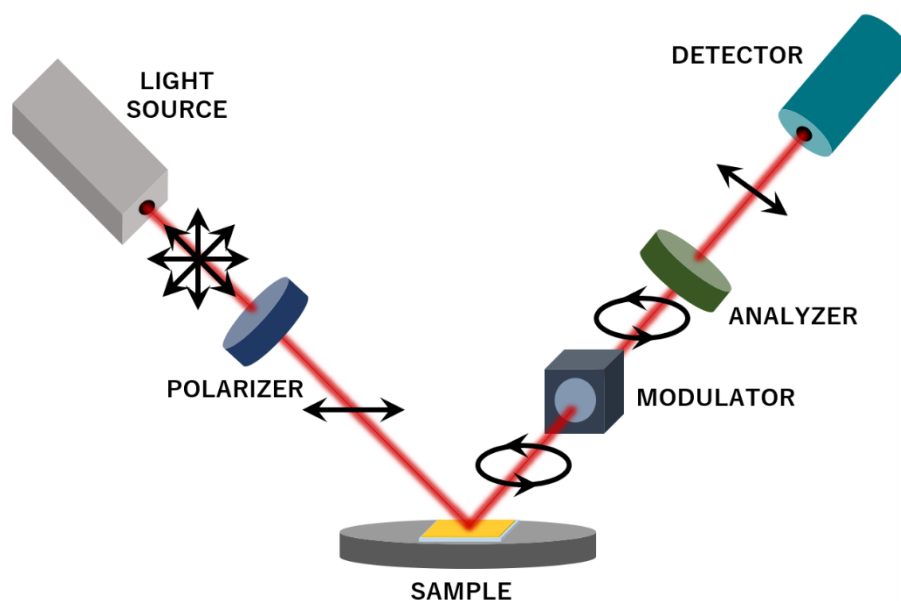
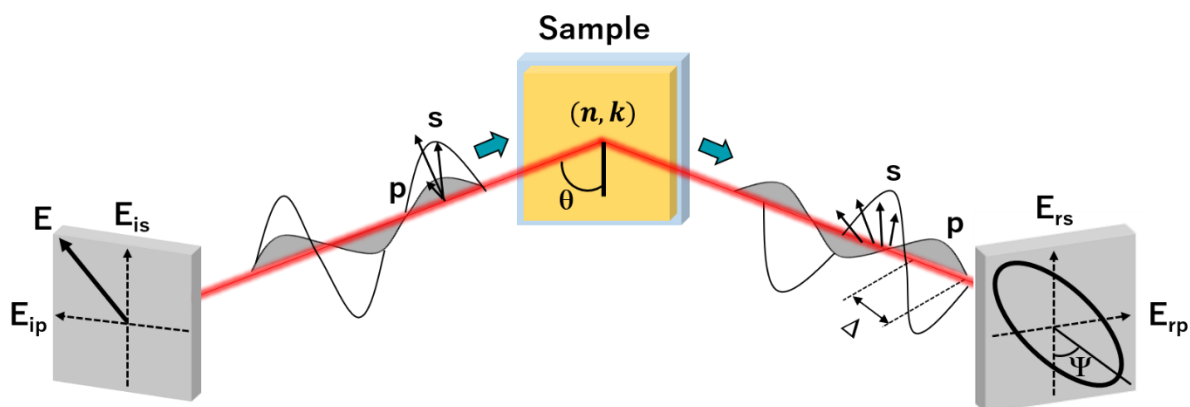


Figure 4.17: Scheme of the optical ellipsometry setup.

Let us consider the principle of operation of ellipsometry presented in Fig. 4.18. The beam waves polarized in the p- and s- directions are directed at the sample at Brewster's angle [4.30]. Optical parameters and the thickness of a thin sample layer are measured by changing the polarization state by light reflection. The directions of the electric field vectors (p- and s- polarization) are inverted on both the reflection and the incident side, and they overlap when  $\theta = 90^\circ$ . Since the phase difference between polarizations equals zero when the incident beam is polarized at an angle of 45 degrees to the  $E_{ip}$  axis, in this case  $E_{ip} = E_{is}$ . During reflection of the incident beam, the p- and s- polarizations are characterized by changes in amplitude and phase due to their amplitude reflectance differences related to electrical dipole radiation [4.30]. The ellipsometric spectroscopy measures values that express the ratio of these two parameters ( $\Psi, \Delta$ ) between the two polarizations. In the case when the structure of the studied material is simple, the amplitude coefficient  $\Psi$  is expressed by the refractive index  $n$ , while the delta is characterized by the extinction coefficient  $k$ . Both  $n$  and  $k$  are determined directly from both the  $\Psi$  and  $\Delta$  parameters obtained from the measurement using the Fresnel equations [4.30].



**Figure 4.18:** Principles of ellipsometry.

The coefficients ( $\Psi, \Delta$ ) determined during the measurement of ellipsometry are defined as the ratio of the amplitude reflection coefficients for both polarizations p- and s-:

$$\rho \equiv \tan \Psi e^{(i\Delta)} \equiv \frac{r_p}{r_s} \quad (4.79)$$

Substituting the reflection coefficients  $r_p$  and  $r_s$  as the ratio of the electric field vectors, we obtain the following relationship:

$$\rho \equiv \tan \Psi e^{(i\Delta)} \equiv \frac{r_p}{r_s} \equiv \left( \frac{E_{rp}}{E_{ip}} \right) / \left( \frac{E_{rs}}{E_{is}} \right) \quad (4.80)$$

As mentioned before,  $E_{ip} = E_{is}$ , therefore equation (4.82) can be simplified:

$$\rho \equiv \tan \Psi e^{(i\Delta)} \equiv (E_{rp}) / (E_{rs}) \quad (4.81)$$

Using polar coordinates as a record of the amplitude reflectance coefficients, we get the following relationship:

$$\tan \Psi = |r_p| / |r_s| \quad \text{and} \quad \Delta = \delta_{rp} - \delta_{rs} \quad (4.82)$$

Substituting  $R_p = |r_p|^2$  and  $R_s = |r_s|^2$ , we achieve:

$$\Psi = \tan^{-1}(|\rho|) = \tan^{-1} \left( \frac{|r_p|}{|r_s|} \right) = \tan^{-1} \left[ \left( \frac{R_p}{R_s} \right)^{1/2} \right] \quad (4.83)$$

While  $\Delta$  equals [4.30]:

$$\Delta = \arg(\rho) = \begin{cases} \tan^{-1}[Im(\rho)/Re(\rho)] & \text{for } Re(\rho) > 0 \\ \tan^{-1}[Im(\rho)/Re(\rho)] + 180^\circ & \text{for } Re(\rho) < 0, Im(\rho) \geq 0 \\ \tan^{-1}[Im(\rho)/Re(\rho)] - 180^\circ & \text{for } Re(\rho) < 0, Im(\rho) < 0 \end{cases} \quad (4.84)$$

It can be noticed that both dependencies correspond to the relationship defined by  $N \equiv n - ik$  (4.15), in which we express the refractive index and the extinction coefficient. These constants are determined from experimental data by using appropriate models, depending on the characteristics of the investigated material [4.30]. In this work, the most important aspect is the determination of the refractive indices of the thin layers under study for strictly defined

wavelengths, that is: 1064 nm, which corresponds to the wavelength, 532 nm, which corresponds to the generated second harmonic wavelength, and 355 nm corresponds to the generated third harmonic, in order to calculate nonlinear susceptibilities using the Herman-Hayden and Reintjes models described in subsection 4.1.

## Literature

[4.1] G. J. Lee, S. W. Cha, S. J. Jeon, J. -I. Jin, J.S. Yoon, Second-order nonlinear optical properties of unpoled bent molecules in powder and in vacuum-deposited film, *Journal of the Korean Physical Society*, 39(5), 912-915, 2001.

[4.2] S. K. Kurtz, J. Jerphagnon, M. M. Choy, Numerical Data and Functional Relationships in Science and Technology, New Series, Group III: Crystal and Solid State Physics, *Landolt-Bornstein New Ser.* 11, 671, 1979.

[4.3] S. K. Kurtz, T. T. Perry, A powder technique for the evaluation of nonlinear optical materials, *J. Appl. Phys.*, 39, 8, 3798-3813 (1968)

[4.4] J. Zyss, D. S. Chemla, J. F. Nicoud, Demonstration of efficient nonlinear optical crystals with vanishing molecular dipole moment: Secondharmonic generation in 3methyl4nitropyridine1oxide, *The Journal of Chemical Physics* 74, 4800 (1981)

[4.5] W. Herman, and L. Hayden, Maker fringes revisited: second-harmonic generation from birefringent or absorbing materials, *J. Opt. Soc. Am. B*, 12, 3, 416-427 (1995)

[4.6] B. Kulyk, Z. Essaidi, J. Luc, Z. Sofiani, G. Boudebs, B. Sahraoui, V. Kapustianyk, and B. Turko, Second and third order nonlinear optical properties of microrod ZnO films deposited on sapphire substrates by thermal oxidation of metallic zinc, *J. Appl. Phys.*, 102, 113113, 1-6 (2007)

- [4.7] K. Kubodera, H. Kobayashi, Determination of Third-Order Nonlinear Optical Susceptibilities for Organic Materials by Third-Harmonic Generation, *Molecular Crystals and Liquid Crystals Incorporating Nonlinear Optics*, 182:1, 103-113, 1990.
- [4.8] F. Kajzar, Y. Okada-Shudo, C. Merrit, Z. Kafafi, Second- and third-order non-linear optical properties of multilayered structures and composites of C60 with electron donors, *Synth. Met.* 117, 2001.
- [4.9] J. F. Reintjes, *Nonlinear Optical Parametric Processes in Liquids and Gases*, Inc., Quantum Electronics, Principles and applications, 1984.
- [4.10] J. Jerphagnon, K. Kurtz, Maker Fringes: A Detailed Comparison of Theory and Experiment for Isotropic and Uniaxial Crystals, *Journal of Applied Physics* 41, 1667 (1970)
- [4.11] P. D. Maker, R. W. Terhune, M. Nisenoff, C. M. Savage, Effects of dispersion and focusing on the production of optical harmonics, *Phys. Rev. Lett.* Vol. 8, N. 1, 1962.
- [4.12] F. Kajzar, and J. Messier, Third-harmonic generation in liquids, *Phys. Rev. A*, 32, 4, 2352-2363, 1985.
- [4.13] F. Kajzar, J. Messier, and C. Rosilio, Nonlinear optical properties of thin films of polysilane, *J. Appl. Phys.*, 60, 9, 3040-3044, 1986.
- [4.14] C. Bosshard, U. Gubler, P. Kaatz, W. Mazerant, and U. Meier, Non-phase-matched optical thirdharmonic generation in noncentrosymmetric media: Cascaded second-order contributions for the calibration of third-order nonlinearities, *Phys. Rev. B*, 61, 16, 10688-10701, 2000.
- [4.15] U. Gubler, and C. Bosshard, Optical third-harmonic generation of fused silica in gas atmosphere: Absolute value of the third-order nonlinear optical susceptibility  $\chi^{(3)}$ , *Phys. Rev. B*, 61, 16, 10702-10710, 2000.

- [4.16] B. Kulyk B, A. P. Kerasidou, L. Soumahoro, C. Moussallem, F. Gohier, P. Frère, B. Sahraoui, Optimization and diagnostic of nonlinear optical features of  $\pi$ -conjugated benzodifuran-based derivatives. *RSC Adv* 6:14439-14447, 2016.
- [4.17] A. Zawadzka, K. Waszkowska, A. Karakas, P. Plóciennik, A. Korcala, K. Wisniewski, M. Karakaya, B. Sahraoui, Diagnostic and control of linear and nonlinear optical effects in selected self-assembled metallophthalocyanine chlorides nanostructures. *Dyes Pig.*, Vol. 157, 151-162, 2018.
- [4.18] A. Zawadzka, P. Plóciennik, J. Strzelecki, M. Pranaitis, S. Dabos-Seignon, B. Sahraoui, Structural and nonlinear optical properties of as-grown and annealed metallophthalocyanine thin films, *Thin Solid Films* 545, 429–437, 2013.
- [4.19] E. Gondek, J. Nizioł, A. Danel, M. Kucharek, J. Jedryka, P. Krasinski, N. Nosidlak, A. A. Fedorchuk, „Synthesis, ellipsometry and non-linear optical features of substituted 1,3,5-triphenylpyrazolines”, *Dyes and Pigments*, Volume 162, Pages 741-745, 2019.
- [4.20] B. Sahraoui, J. Luc, A. Meghea, R. Czaplicki, J-L Fillaut, A. Migalska-Zalas, Nonlinear optics and surface relief gratings in alkynyl-ruthenium complexes, *J. Opt. A, Pure Appl. Opt.* 11, 2009.
- [4.21] H. Singh Nalwa, S. Miyata, *Nonlinear Optics of Organic Molecules and Polymers*, CRC Press, 1997.
- [4.22] M. Sheik-Bahae, A.A. Said, T.-H. Wei, D.J. Hagan, E. W. van Stryland, Sensitive measurement of optical nonlinearities using a single beam, *IEEE J. Quantum Electron.* 26, 760, 1990.

- [4.23] B. Kulyk, A. P. Kerasidou, L. Soumahoro, C. Moussallem, F. Gohier, P. Frere, B. Sahraoui, Optimization and diagnostic of nonlinear optical features of  $\pi$ -conjugated benzodifuran-based derivatives, *RSC Adv.*, 6, 14439, 2016.
- [4.24] B. Kulyk, D. Guichaoua, A. Ayadi, A. El-Ghayoury, B. Sahraoui, Metal-induced efficient enhancement of nonlinear optical response in conjugated azo-based iminopyridine complexes, *Organic Electronics* 36, 1-6, 2016.
- [4.25] G. Binning, C. F. Quate, Ch. Gerber, Atomic Force Microscope, *Phys. Rev. Lett.* Vol. 56, N. 9, 1986
- [4.26] G. Haugstad, Atomic Force Microscopy: Understanding Basic Modes and Advanced Applications, John Wiley & Sons, 2012
- [4.27] W. R. Bowen, N. Hilal, Atomic Force Microscopy in Process Engineering, Elsevier, 2009
- [4.28] D. Laskowski, J. Strzelecki, K. Pawlak, H. Dahm, A. Balter, Effect of ampicillin on adhesive properties of bacteria examined by atomic force microscopy. *Micron* 112, 84–90 (2018).
- [4.29] P. Drude, Ueber Oberflächenschichten. II. Theil, *Ann. Phys. Chem.* 36 (1889) 865.
- [4.30] H. Fujiwara, Spectroscopic Ellipsometry: Principles and Applications, John Wiley & Sons, England, 2007

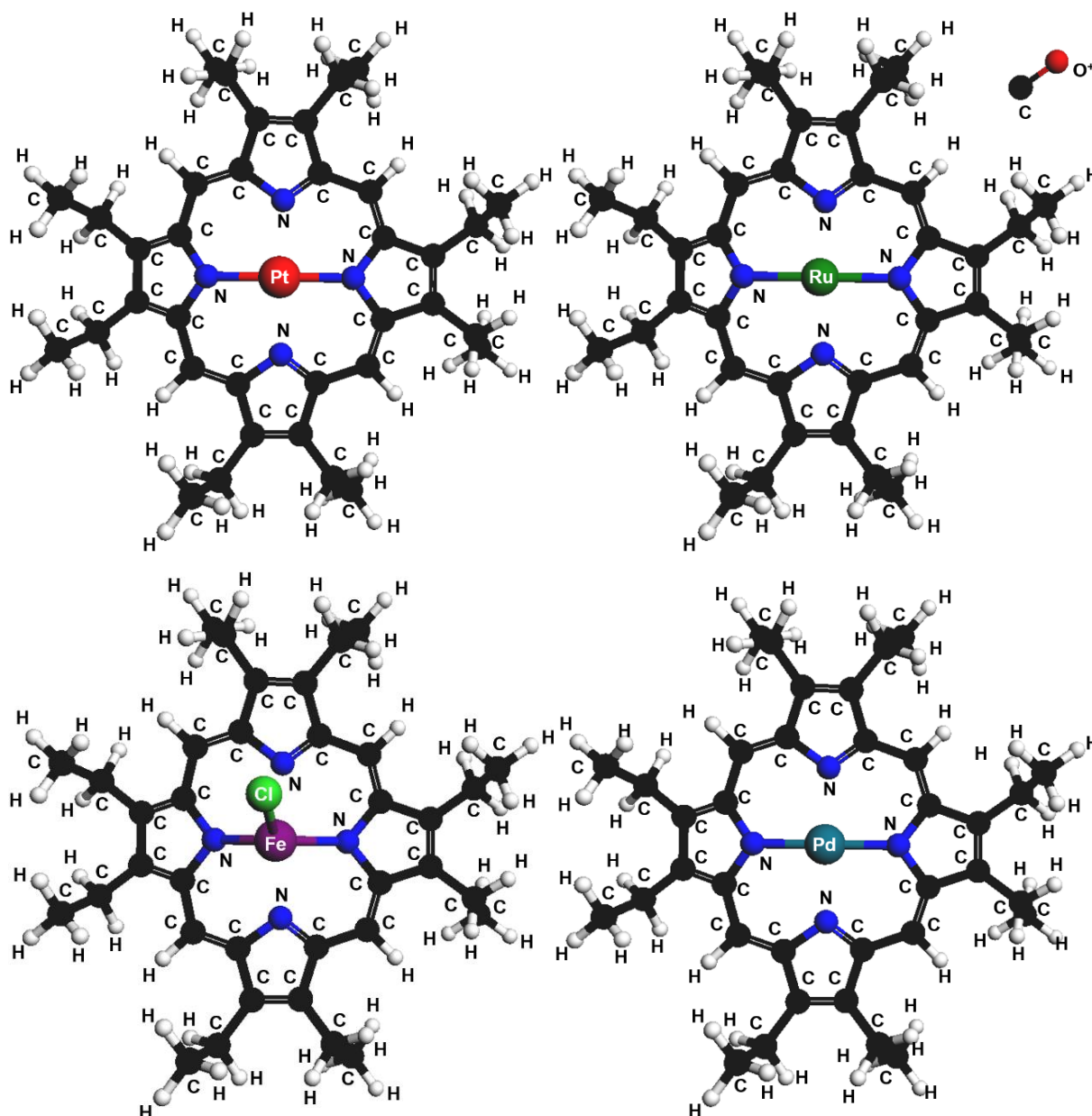
## CHAPTER 5: PORPHYRIN COMPLEXES

Porphyrins are the most studied and frequently used building blocks in supramolecular chemistry include systems based on the porphyrin backbone and related compounds. These compounds have interesting electrochemical and photochemical properties that can be easily modified, they also have the ability to form very stable transition metal chelate complexes. This research is devoted to, as well as nonlinear optical properties of porphyrin complexes build of different metal ions: platinum and palladium, atomic clusters: ruthenium carbonyl, and inorganic crystal: ferric chloride. Second and third harmonic generation was investigated via well-known Maker fringe technique, while nonlinear refraction and nonlinear absorption were carried out by Z-scan method. The second main objective of this research is relation between NLO response with study of surface, spectroscopic and photoluminescence properties of such porphyrin complexes. The motivation of this work was NLO research on basic mononuclear complexes as a models for NLO investigations on supramolecular assemblies.

### 5.1. Sample Preparation

A total of four porphyrin complexes have been purchased from Sigma-Aldrich company: platinum(II) 2,3,7,8,12,13,17,18-octaethyl-21H,23H-porphyrin,  $C_{36}H_{44}N_4Pt$  (**PtOEP**), 2,3,7,8,12,13,17,18-octaethyl-21H,23H-porphine ruthenium(II) carbonyl,  $C_{37}H_{44}N_4ORu$  (**RuOEP**), 2,3,7,8,12,13,17,18-octaethyl-21H,23H-porphine iron(III) chloride,  $C_{36}H_{44}ClFeN_4$  (**FeOEP**), 2,3,7,8,12,13,17,18-octaethyl-21H,23H-porphine palladium(II),  $C_{36}H_{44}N_4Pd$  (**PdOEP**), and their chemical structures are presented in Fig. 5.1. Samples were used without any modification and orientation by electric field, and were dissolved in 1 ml of  $CHCl_3$  with 50 mg of poly(methyl methacrylate) using as a matrix, forming 10%wt solutions of octaethylporphyrin to polymer, which were next applied on previously cleaned glass substrate and deposited on spin-coater (Spin200i, POLOS) with 2000 rpm.



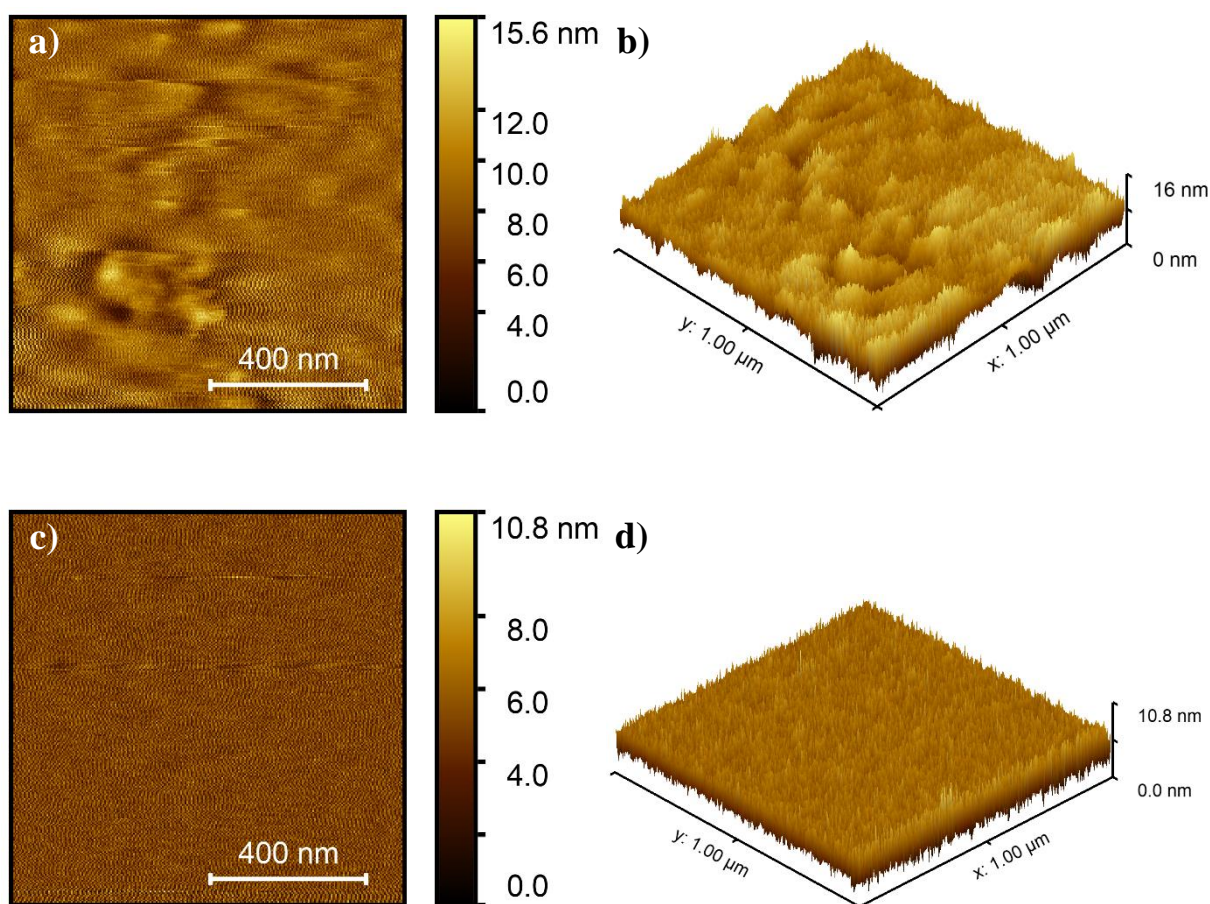


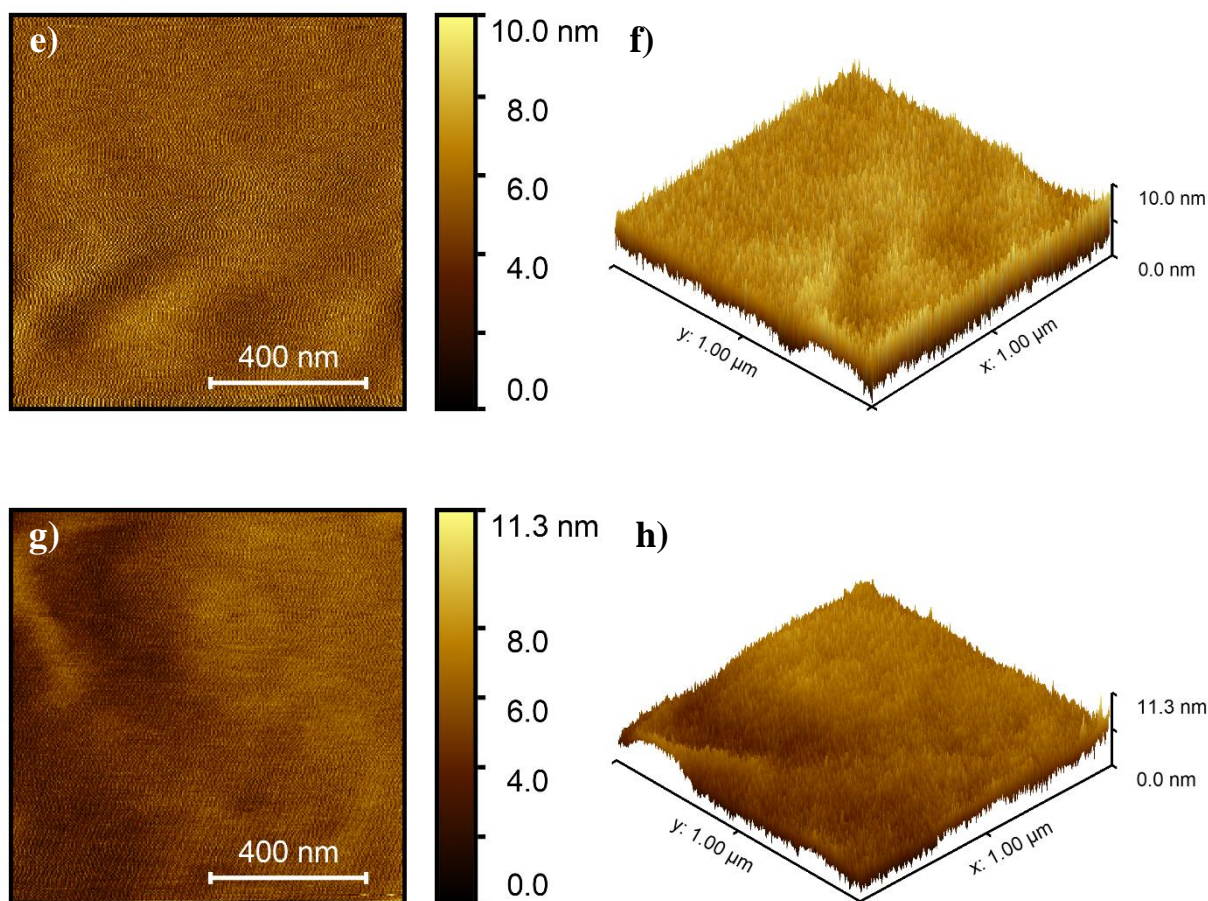
**Figure 5.1:** Chemical structures of porphyrin complexes: **PtOEP**, **RuOEP**, **FeOEP** and **PdOEP**.

## 5.2. Surface Characterization

The thickness of guest-host systems was measured by profilometer (Dektak 6M) and found as 1650 nm, 1200 nm, 1150 and 1430 nm for **PtOEP**, **RuOEP**, **FeOEP** and **PdOEP** respectively. The numerical values of the linear refractive index and extinction coefficients depending on the wavelength (1064 nm, 532 nm, 355 nm) are included in Tab. 5.1. Thin films topography was

investigated using the atomic force microscope (AFM) in the contact mode described in Section 4.6. Fig. 5.2 shows the AFM images with a resolution of  $1 \times 1 \mu\text{m}^2$  in two- and three-dimensional representation. It can be noticed that the surface of the samples is not very different from each other, they are as homogeneous and smooth as possible, what is very important in the nonlinear optical phenomena measurements, because any defects affect the quality and symmetry of the NLO signal, however some slight roughness and disturbances in the structure can be distinguished and they do not have a significant impact on optical research. Therefore, the average roughness was determined and for individual samples is equal to: 4.402 nm (**PtOEP**), 0.371 nm (**RuOEP**), 2.294 nm (**FeOEP**), 0.539 nm (**PdOEP**). It can be noticed that the difference in surface roughness is small, which was also illustrated as the AFM surface profiles of the studied thin films in Fig. 5.3.





**Figure 5.2:** Atomic force microscopy (AFM) images of studied metalporphyrin thin films: **PtOEP** a) 2-dimensional, b) 3-dimensional; **RuOEP** c) 2-dimensional, d) 3-dimensional; **FeOEP** e) 2-dimensional, f) 3-dimensional; **PdOEP** g) 2-dimensional, h) 3-dimensional.

**Table 5.1:** Thickness ( $d$ ), roughness ( $R_A$ ), linear refractive index values ( $n$ ) and extinction coefficients ( $\kappa$ ) of porphyrin complexes thin films.

	$d$ [nm]	$R_A$ [nm]	$n_{1064}$	$n_{532}$	$n_{355}$	$\kappa_{1064}$	$\kappa_{532}$	$\kappa_{355}$
<b>PtOEP</b>	1650	4.402	1.497	1.511	1.560	0.004	0.003	0.058
<b>RuOEP</b>	1200	0.371	1.486	1.490	1.495	0.015	0.034	0.032
<b>FeOEP</b>	1150	2.294	1.462	1.466	1.469	0.073	0.049	0.062
<b>PdOEP</b>	1430	0.539	1.464	1.478	1.488	0.037	0.0453	0.035

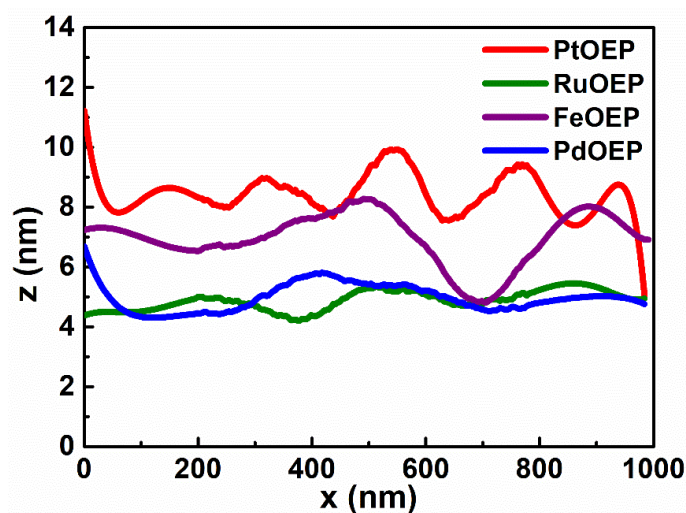


Figure 5.3: Atomic force microscopy profiles of studied metalloporphyrin thin films.

### 5.3. Spectroscopic Studies

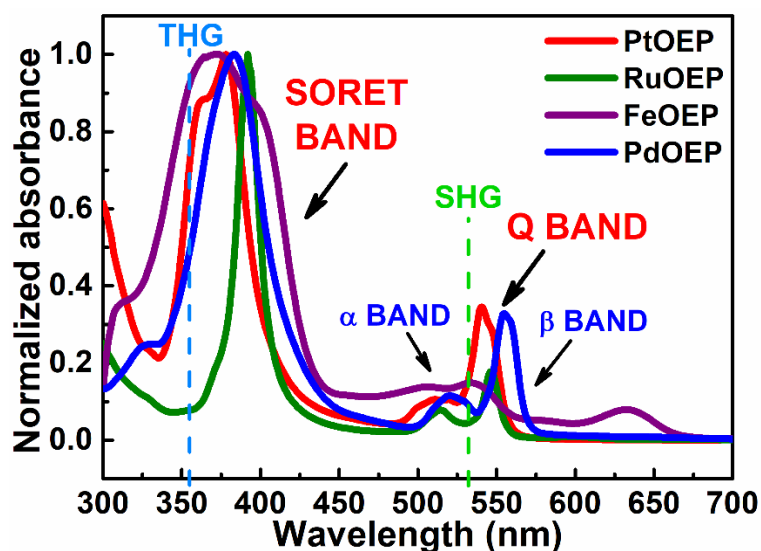


Figure 5.4: Normalized UV-Vis absorption spectra of investigated porphyrin complexes, including THG (355 nm) and SHG (532 nm) wavelengths.

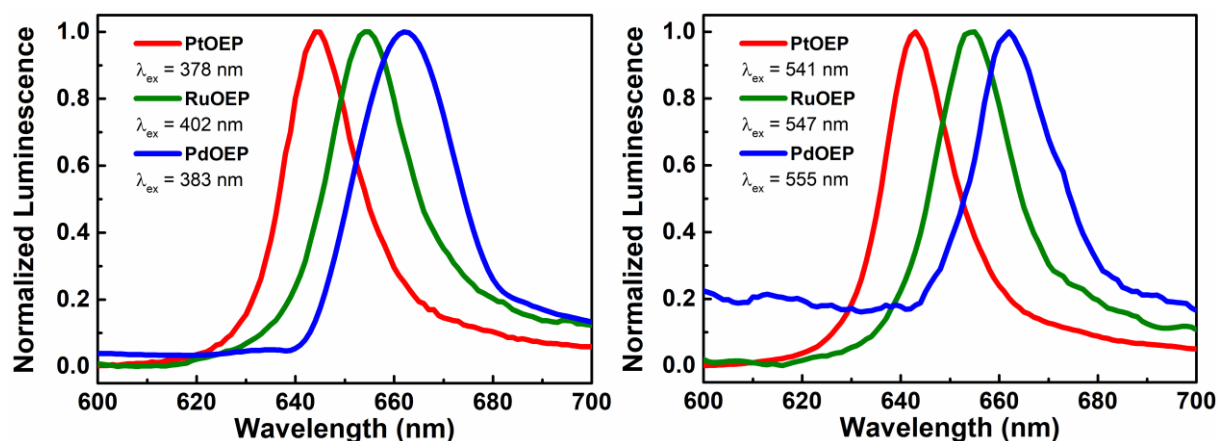
Generally, porphyrins have characteristic UV-Vis absorption spectra, in which two characteristic and intense absorption bands can be distinguished: strong Soret band in the range of 390–425 nm and a 10–15 times weaker Q band in the range of 480–700 nm [5.1]. Optical absorption spectra of studied guest-host thin films are presented in Fig. 5.4. We noticed high maxima of absorption in

range of blue light, positioned at 378 nm for **PtOEP**, 402 nm for **RuOEP**, 373 nm for **FeOEP** and 383 nm for **PdOEP** corresponding to Soret band transition  $\pi \rightarrow \pi^*$  metal-ligand charge transfer (MLCT), and slightly weaker in the range 480 - 680 nm in which the Q band is divided into two bands  $\alpha$  (480-525 nm with maximum around 515 nm) and  $\beta$  (530-560 nm with maximum around 545 nm). In the case of a sample of the porphyrin complex with iron (III) chloride, peak 633 nm corresponds to the transition  $n \rightarrow \pi^*$ . The values of the absorption peaks determined from the spectrum are presented in Tab. 5.2. Additionally, the energy gap values of the studied porphyrin complex compounds were determined from the absorption spectrum [5.2]. Generally, **PtOEP** is commonly used as a dye in OLED technology [5.3] with  $E_{g(Homo-Lumo)} = 2.1 \text{ eV}$  (due to SigmaAldrich characteristics), therefore additionally to this work  $E_{g(Homo-Lumo)}$  determined from the absorption spectrum as the ratio  $E_{g(Homo-Lumo)} = 1240/\lambda$ , where  $\lambda$  is the wavelength of the edge of absorption peak, and for each sample values are given in Tab.5.2.

In connection with the nonlinear optical properties of SHG and THG guest-host thin films, it is very important that these samples are optically transparent for the wavelength of the pumping beam 1064 nm, which means that the samples do not absorb laser radiation in any way. On the other hand, it can be observed that the absorbance at 532 nm (corresponding to SHG) and 355 nm (corresponding to THG) is significant. This means that the signal that is generated is absorbed to some extent at the same time. Therefore, when calculating the properties of SHG and THG, it is necessary to take into account the effects of absorption - that is, the absorption coefficients for these wavelengths. The determined values of these coefficients are included in Tab. 5.2.

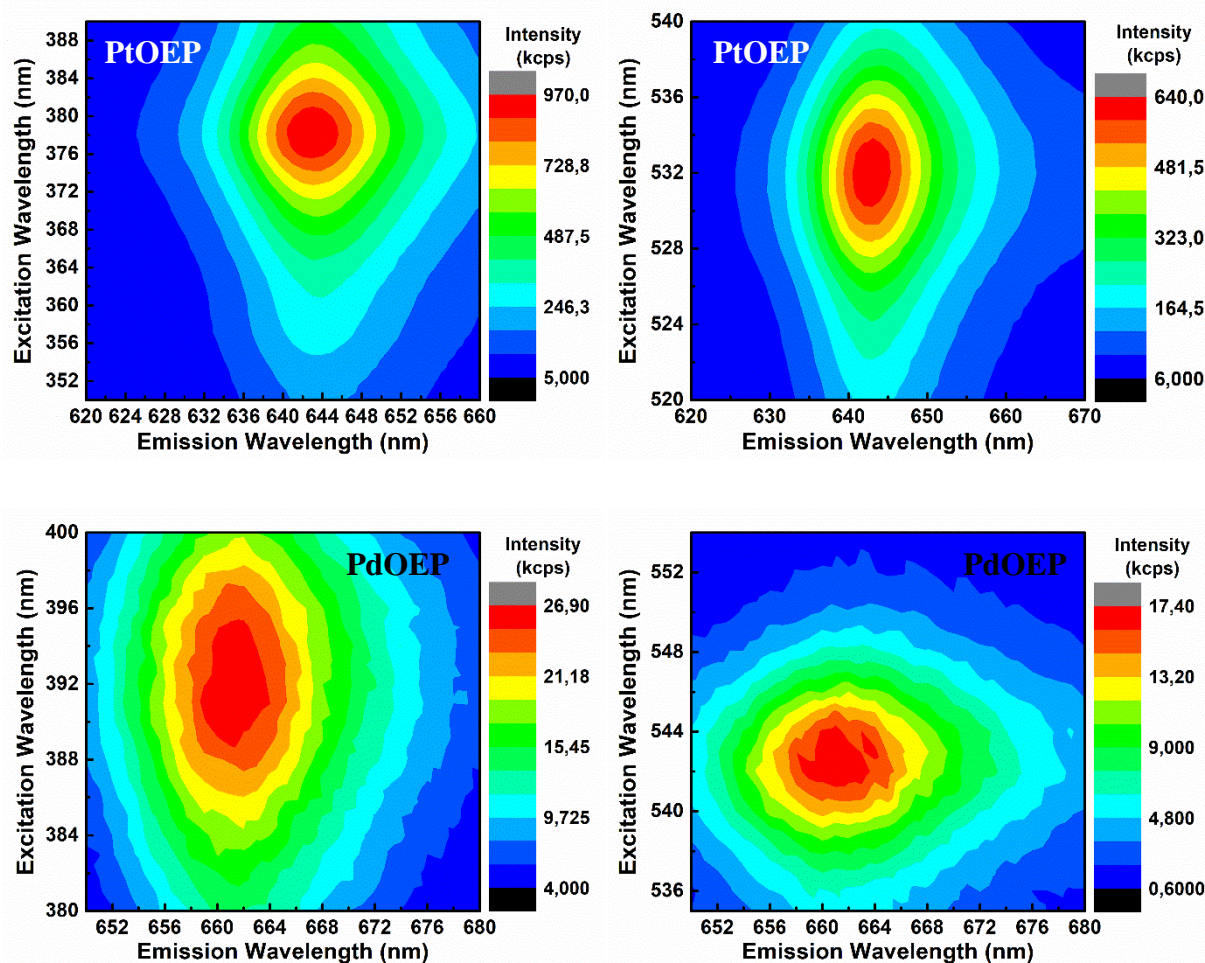
**Table 5.2:** Coefficients determined from absorption spectra of metalloporphyrin thin films.

Sample	$\lambda_{\text{abs}}$ [nm]	$\alpha$ [ $10^3 \text{ cm}^{-1}$ ]		$E_{\text{g(Homo-Lumo)}}$ [eV]
		355 nm	532 nm	
<b>PtOEP</b>	378, 519, 541	11.72	2.60	2.22
<b>RuOEP</b>	402, 515, 547	5.11	2.97	2.23
<b>FeOEP</b>	373, 534, 633	23.27	3.86	1.86
<b>PdOEP</b>	383, 520, 555	10.61	2.00	2.17

**Figure 5.5:** Normalized emission spectra for **PtOEP**, **RuOEP**, **PdOEP** thin films by exciting them with wavelengths corresponding to absorption peaks.

The emission spectra of studied metalloporphyrins which were excited with wavelengths corresponding to the absorption peaks are shown in Fig. 5.5. However, no emission spectra were obtained for the complex of porphyrin with iron(III) chloride due to fact that **FeOEP** in this case excites from single to triple state and does not emit anymore. Moreover, during the excitation of the samples with the wavelength coming from the  $\alpha$  band, a very weak emission spectrum was recorded, on the other hand, the excitation with the wavelength from the Soret band and the  $\beta$  band has the same emission wavelength, which only differs in intensity. The three-dimensional emission spectrum depending on the emission wavelength and intensity for **PtOEP** and **PdOEP** samples are presented in Fig. 5.6. The samples were excited with wavelengths in the range of 350-400 nm and 250-560 nm and the emission in the range of 620-680 nm was investigated. As in the

case of 2D plots, the maximum photoluminescence (PL) is located in the same wavelength, but with a much lower intensity. Generally, platinum is more emissive than palladium, hence more intense emission and longer lifetime were observed for the **PtOEP** sample. In this way, the approximately excitation and emission wavelengths for which maximum is located, were determined, and their values are presented in Tab. 5.3.



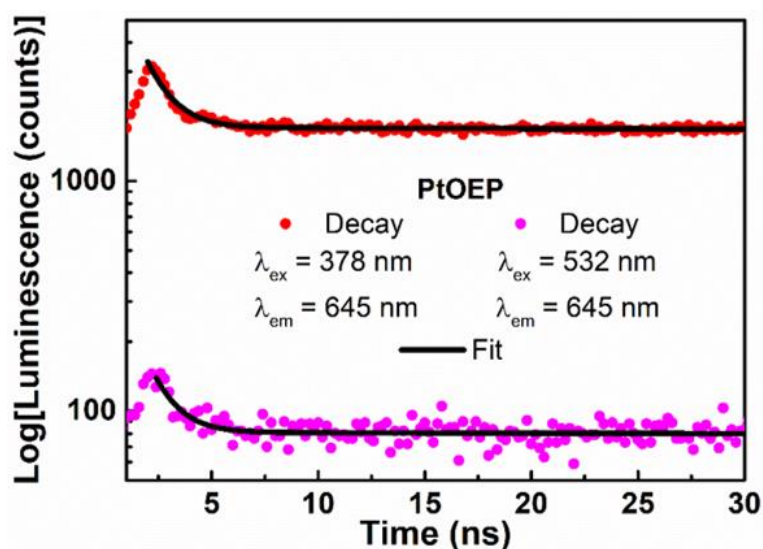
**Figure 5.6:** 3D representation of intensity of emission as a function of excitation wavelength of **PtOEP** and **PdOEP** thin films.

On this basis, the photoluminescence lifetime was measured at room temperature (see Fig. 5.7), however, for very low intensity wavelengths, this measurement was not recorded. Due to characteristics of the plots, the obtained responses were then fitted with the bi-exponential function

$y = y_0 + A_0 e^{-t/T_1} + A_1 e^{-t/T_2}$  [5.4], of which two lifetimes  $T_1$  and  $T_2$  were determined, which corresponds to fast and long transition from singlet excited state to ground state, and their values are presented in Tab. 2. The obtained luminescence lifetimes are very short,  $T_1$  ranges from 11 to 73 nanoseconds, while  $T_2$  ranges from 0.8 to 1.25 nanoseconds. In the case of the **PtOEP** sample for which the lifetime was recorded during the excitation with green light, the fluorescence is much lower than during the excitation with blue light. For the remaining samples, the lifetime was recorded only for the samples by excited them with blue light.

**Table 5.3:** Values of excitation and emission wavelengths also with fluorescence lifetimes of studied metalloporphyrins.

Sample	$\lambda_{\text{ex}}$ [nm]	$\lambda_{\text{em}}$ [nm]	$T_1$ [ns]	$T_2$ [ns]
<b>PtOEP</b>	378	645	$(72.7 \pm 1.9)$	$(1.23 \pm 0.04)$
	532	645	$(25.4 \pm 0.3)$	$(1.18 \pm 0.03)$
<b>RuOEP</b>	395	657	$(11.4 \pm 0.4)$	$(0.92 \pm 0.03)$
	547	657	-	-
<b>PdOEP</b>	392	660	$(22.9 \pm 0.5)$	$(0.86 \pm 0.05)$
	543	660	-	-



**Figure 5.7:** Luminescence decays for **PtOEP** thin film.



## 5.4. Second Harmonic Generation

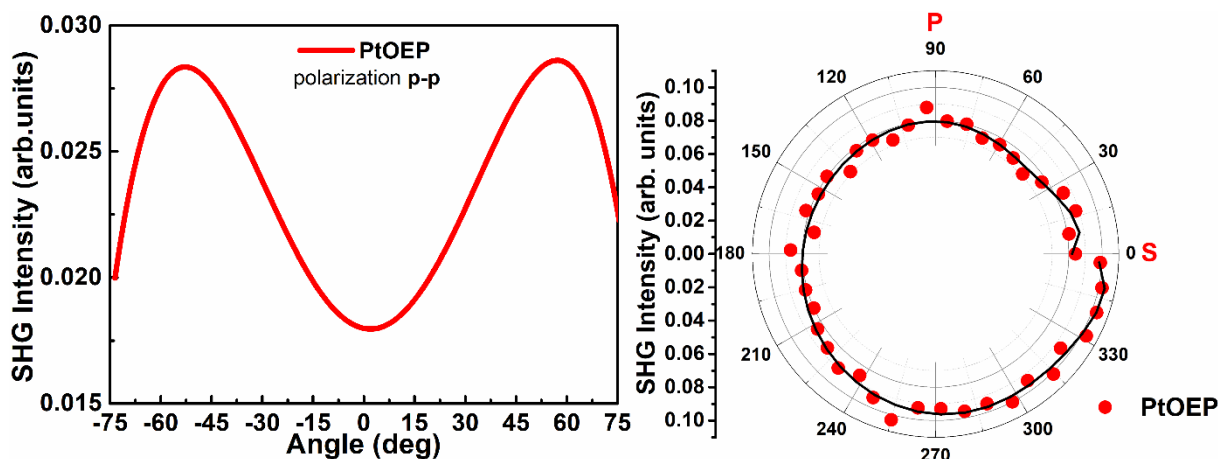


Figure 5.8: SHG intensities as a function of rotation angle in p-polarized laser beam (left) and as a dependence of laser polarization (right) of **PtOEP** thin film.

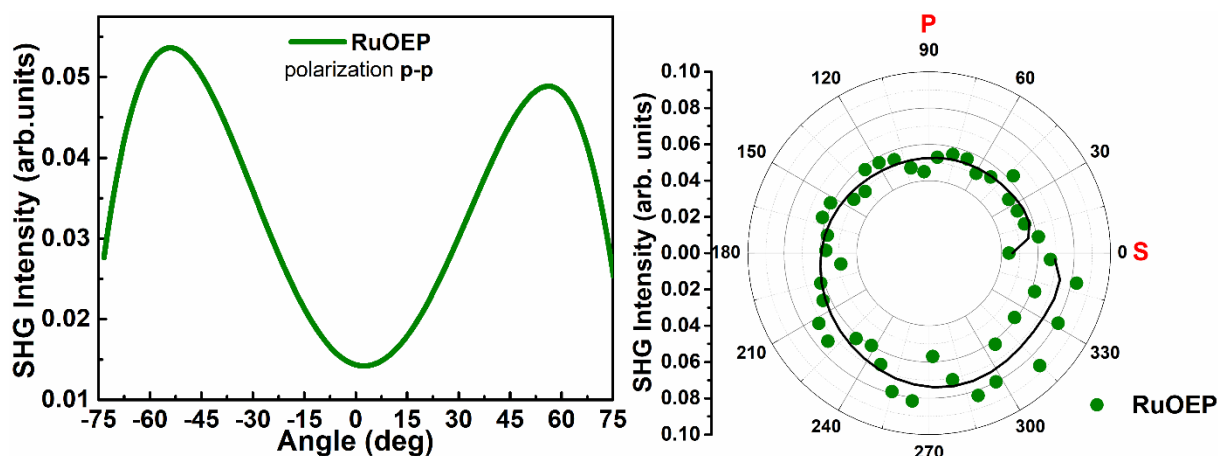


Figure 5.9: SHG intensities as a function of rotation angle in p-polarized laser beam (left) and as a dependence of laser polarization (right) of **RuOEP** thin film.

The studies of the second, as well as third harmonics, were carried out using the experimental setup presented in subchapter 4.2. The THG and SHG studies for the **PdOEP** sample are briefly presented in [5.5], which show the influence of the matrix polymer (PMMA, PVK, P1VN) on the nonlinear optical response. In this manuscript, we focused on the differences resulting from the use of selected substituents in the complexes of the studied porphyrins. Generally, obtained guest-

host metalloporphyrin thin films with PMMA did not show the SHG effect, thus it was necessary to use corona poling technique to orient the molecules in the polymer matrix in one direction. Moreover, from the polarization plots, no difference in SHG signal intensity was observed between the applied polarization (see Figs. 5.8-5.11) except for the **FeOEP** sample, which is strongly polar. This means that the remaining samples, in combination with the polymer matrix, form an isotropic system in which NLO response is independent on the direction.

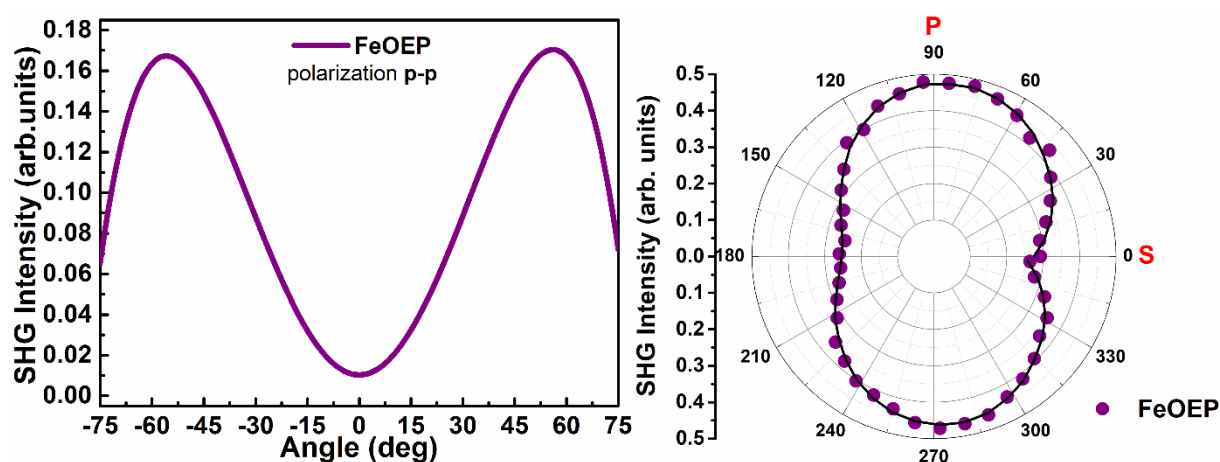


Figure 5.10: SHG intensities as a function of rotation angle in p-polarized laser beam (left) and as a dependence of laser polarization (right) of **FeOEP** thin film.

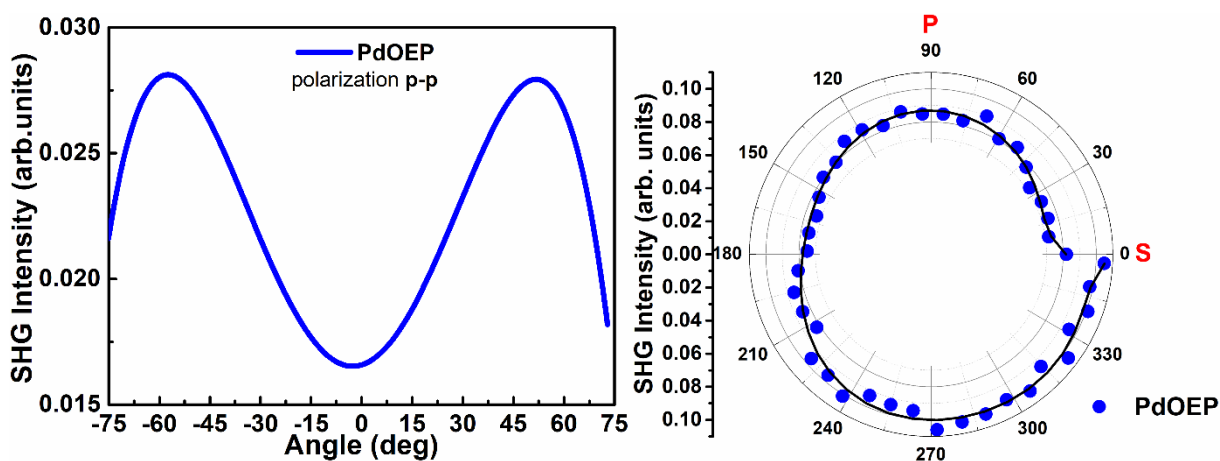
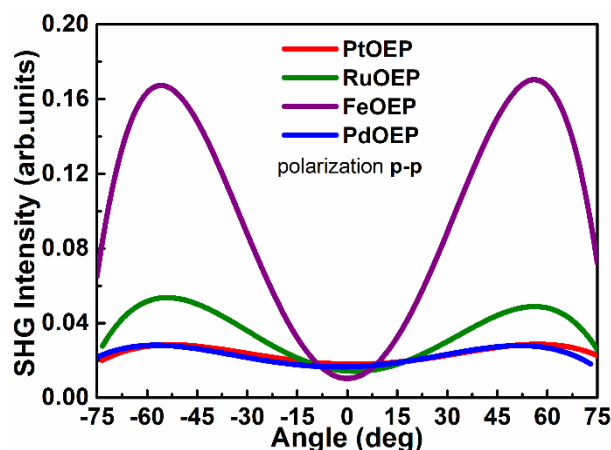


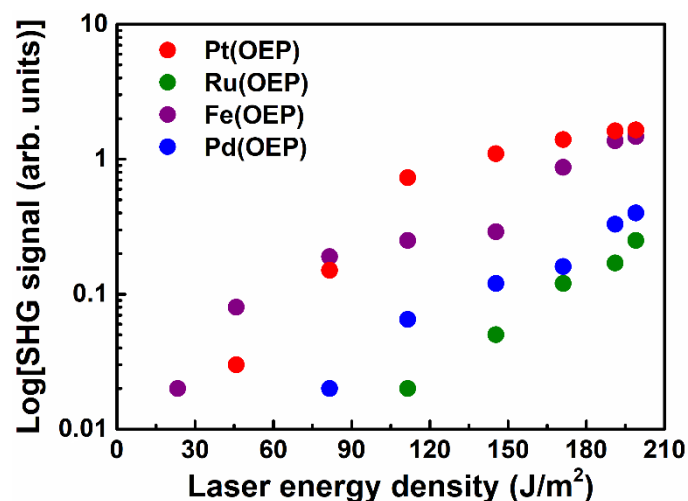
Figure 5.11: SHG intensities as a function of rotation angle in p-polarized laser beam (left) and as a dependence of laser polarization (right) of **PdOEP** thin film.



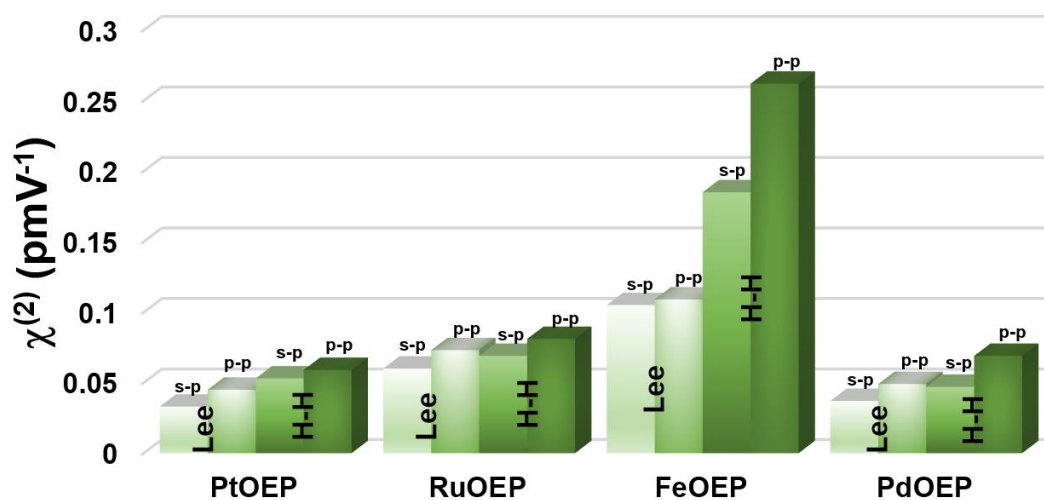
**Figure 5.12:** Comparison of SHG intensities for all studied porphyrin complexes in p-polarized laser beam.

By comparing the SHG intensity of the signal between the studied samples (see Fig. 5.12), it was noticed that the strongest NLO response was obtained with the **FeOEP** sample, due to the fact that this sample has nonplanar structure and moreover is more polar than the rest of the studied porphyrins. On the other hand, **RuOEP** also has a nonplanar structure, however the FeCl substituent is more electronegative than RuCO, therefore the **RuOEP** sample has a weaker SHG signal intensity than **FeOEP**. The remaining porphyrin samples **PtOEP** and **PdOEP** have planar structure, besides they are from the same group of the periodic table where the sum of dipoles is equal to zero, therefore these samples are characterized by a weaker SHG signal than nonplanar structures, and the intensity does not differ much between these samples. On the other hand, Fig. 5.13 shows the dependence of the SHG signal as a function of laser energy density, measured at Czestochowa University of Technology, which was mentioned in Chapter 4. Here, the strongest SHG signal was observed for the **PtOEP** sample, however, it is related to strong linear absorption samples for a wavelength of 532 nm. It can also be seen that on a logarithmic scale above the laser energy density  $100 \text{ J/m}^2$ , the SHG signal for this sample becomes saturated. Tab. 5.4 shows the calculated second-order NLO susceptibility values for both laser beam polarizations using the Lee theoretical models (subsection 4.1.1) and Herman-Hayden (subsection 4.1.3). According to the

obtained NLO graphical responses, the highest  $\chi^{(2)}$  values were obtained for the **FeOEP** sample. Due to the fact that the H-H model contains parameters characterizing the sample and parameters depending on the polarization, the calculated values of  $\chi^{(2)}$  in this case are higher, and the calculation error determined from the total differential is not too large. For better contrast, the calculated values are visualized graphically in the form of histogram in Fig. 5.14.



**Figure 5.13:** SHG signal as a function of laser energy density of studied metalloporphyrin thin films.

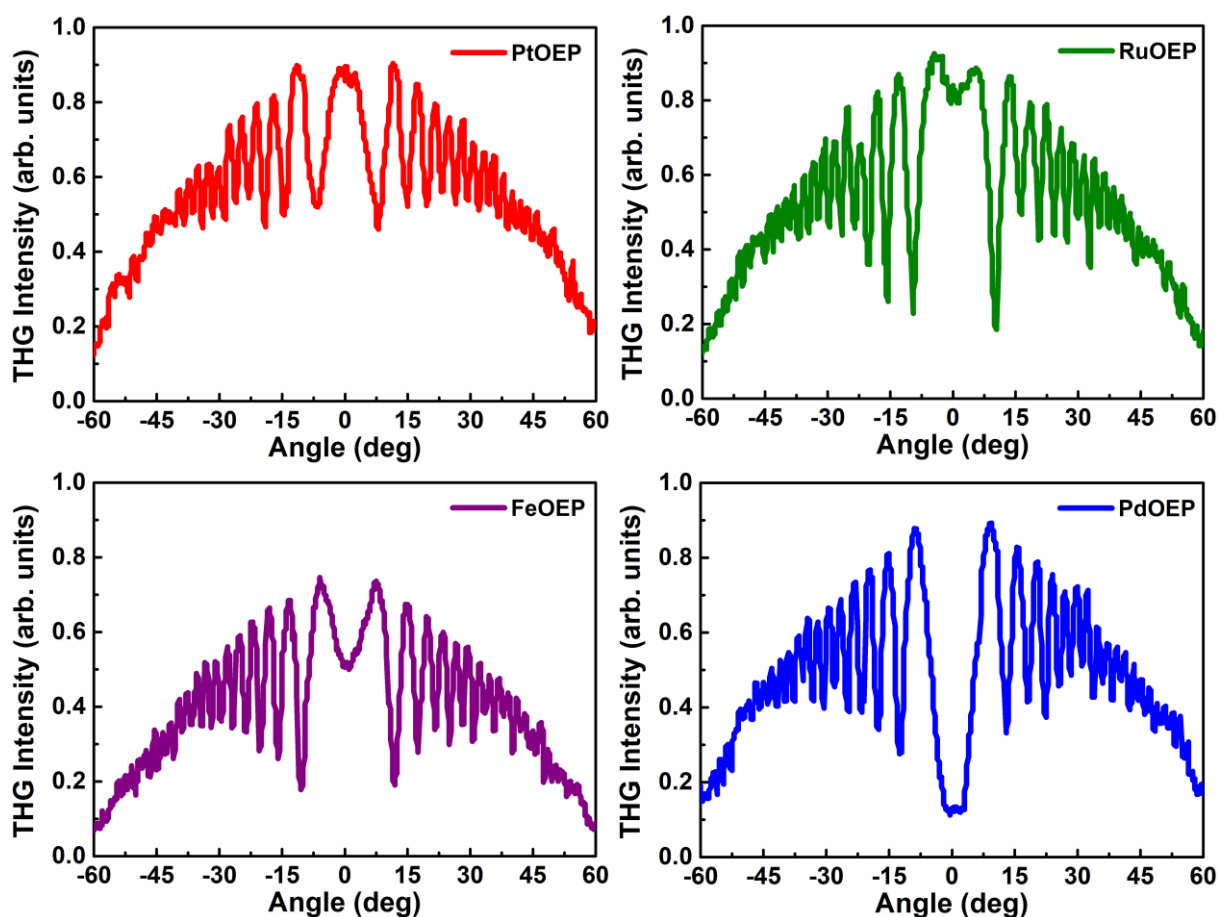


**Figure 5.14:** Histogram representing values of second-order nonlinear susceptibilities calculated via theoretical models.

**Table 5.4:** Values of second-order nonlinear susceptibilities calculated by theoretical models.

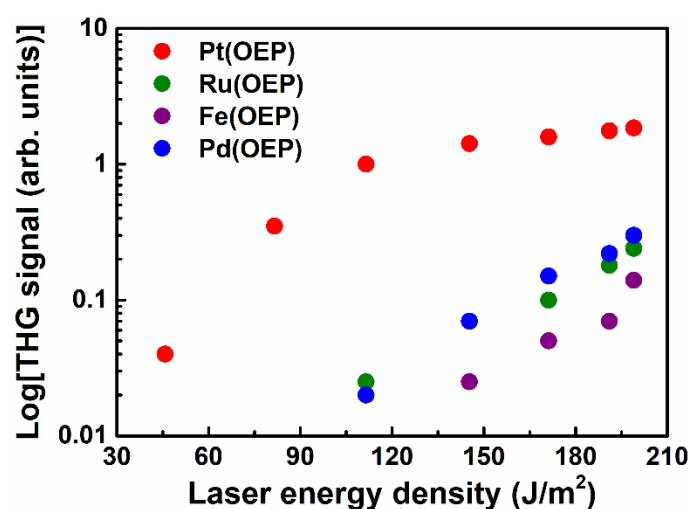
	Model	$\chi^{(2)}$ [pmV <sup>-1</sup> ]	
		s-p	p-p
PtOEP	Lee	(0.033 ± 0.002)	(0.045 ± 0.002)
	Herman-Hayden	(0.053 ± 0.002)	(0.059 ± 0.005)
RuOEP	Lee	(0.060 ± 0.001)	(0.073 ± 0.002)
	Herman-Hayden	(0.069 ± 0.002)	(0.081 ± 0.001)
FeOEP	Lee	(0.105 ± 0.003)	(0.109 ± 0.012)
	Herman-Hayden	(0.185 ± 0.001)	(0.262 ± 0.013)
PdOEP	Lee	(0.037 ± 0.001)	(0.049 ± 0.002)
	Herman-Hayden	(0.047 ± 0.002)	(0.069 ± 0.001)

### 5.5. Third Harmonic Generation



**Figure 5.15:** THG intensities as a function of incident angle of studied porphyrin complexes in s-polarized laser beam.

In the case of THG studies, there are no structure constraints, thus corona poling was not required to obtain a third-order nonlinear optical response. Fig. 5.15 shows the third harmonic signal for all investigated metalloporphyrins in s-polarized laser beam. The third-order nonlinear optical response was also unaffected by the applied polarization, the signal for s- and p-polarized wave is almost identical. In the case of the samples, also no huge difference between the signal was noticed. Therefore, the values of the third-order ( $\chi^{(3)}$ ) nonlinear susceptibilities were estimated using theoretical models Kubodera-Kobayashi (subsection 4.1.4) and Reintjes (subsection 4.1.5).



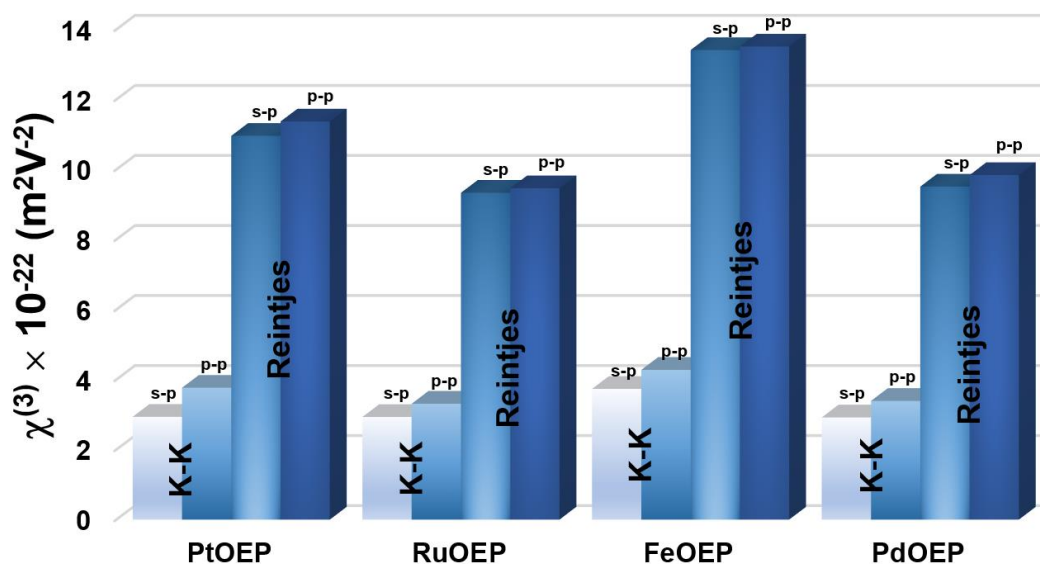
**Figure 5.16:** THG signal as a function of laser energy density of studied metalloporphyrin thin films.

Besides, Fig. 5.16 presents the dependence of the intensity of the generated third harmonic as a function of the laser energy made at Częstochowa University of Technology, presented in subsection 4.2 in Fig. 4.6. Similarly, to the SHG studies, due to the linear absorption for the 355 nm wavelength, the THG signal above 100 J/m<sup>2</sup> becomes supersaturated for the **PtOEP** sample. Moreover, as it was mentioned previously, due to the high absorbance at 355 nm, it is necessary to take into account the absorption coefficient in the calculations, the values of which are presented in Tab. 5.2. Earlier it was mentioned that no difference to the polarization was noticed during the recording of SHG signals, however the values are given in Tab. 5.5 are diverse. This is due to the

fact that when changing the polarization of laser beam by the half-wave plate, the power of the laser beam slightly changed, in fact these values should be very similar to each other. In case of THG measurements, similarly to SHG results, the highest values were obtained for the **FeOEP** sample, and much higher calculated by Reintjes model due to parameters depending on the sample properties. For better contrast, the calculated values are visualized graphically in the form of histogram in Fig. 5.16.

**Table 5.5:** Values of third-order nonlinear susceptibilities calculated by theoretical models.

	Model	$\chi^{(3)} \times 10^{-22} [\text{m}^2\text{V}^{-2}]$	
		s-p	p-p
<b>PtOEP</b>	Kubodera-Kobayashi	$(2.936 \pm 0.105)$	$(3.765 \pm 0.121)$
	Reintjes	$(10.960 \pm 0.222)$	$(11.370 \pm 0.235)$
<b>RuOEP</b>	Kubodera-Kobayashi	$(2.931 \pm 0.098)$	$(3.310 \pm 0.101)$
	Reintjes	$(9.335 \pm 0.136)$	$(9.463 \pm 0.142)$
<b>FeOEP</b>	Kubodera-Kobayashi	$(3.733 \pm 0.087)$	$(4.277 \pm 0.086)$
	Reintjes	$(13.410 \pm 0.196)$	$(13.510 \pm 0.203)$
<b>PdOEP</b>	Kubodera-Kobayashi	$(2.917 \pm 0.122)$	$(3.390 \pm 0.123)$
	Reintjes	$(9.510 \pm 0.158)$	$(9.840 \pm 0.166)$



**Figure 5.17:** Histogram representing values of third-order nonlinear susceptibilities calculated via theoretical models.

## 5.6. Z-Scan Results

The investigations of nonlinear refraction and nonlinear absorption were carried out by using Z-Scan experimental alignment shown in Fig. 4.9 in subsection 4.4. Powders of pure metalloporphyrin without the addition of polymer were dissolved in chloroform  $\text{CHCl}_3$  forming a solution with concentrations 0.5 mM, 0.4 mM, 0.3 mM and 0.2 mM. After introducing the solutions into 1 mm quartz cuvettes and placing them on the stage, the nonlinear absorption (OA Z-Scan) and the nonlinear refraction (CA Z-Scan) from -10 mm to 10 mm with a step of 0.1 mm were measured, where point 0 is corresponding to the focus point, by changing the energy of the laser pumping beam from 0.5 to 2.0  $\mu\text{J}$  with step 0.25  $\mu\text{J}$ . The signals recorded from OA and CA Z-Scan are shown in Fig. 5.18 – 5.19, from which the nonlinear absorption coefficients and the nonlinear refractive indexes were then determined. Due to the fact that chloroform is characterized by quite high nonlinearity during the CA Z-scan measurement (Fig. 5.19a) [5.6], its influence was taken into account in the calculations in which the NLO susceptibility of the  $\text{CHCl}_3$  is subtracted from the NLO susceptibility of the solution. From the data obtained during the measurement of nonlinear absorption, the NLO absorption cross section  $\sigma$  was calculated, which determines the efficiency of a single molecule in the ground state to approach the excited state during the multiphoton absorption process, using the appropriate relation [5.7 – 5.8]:

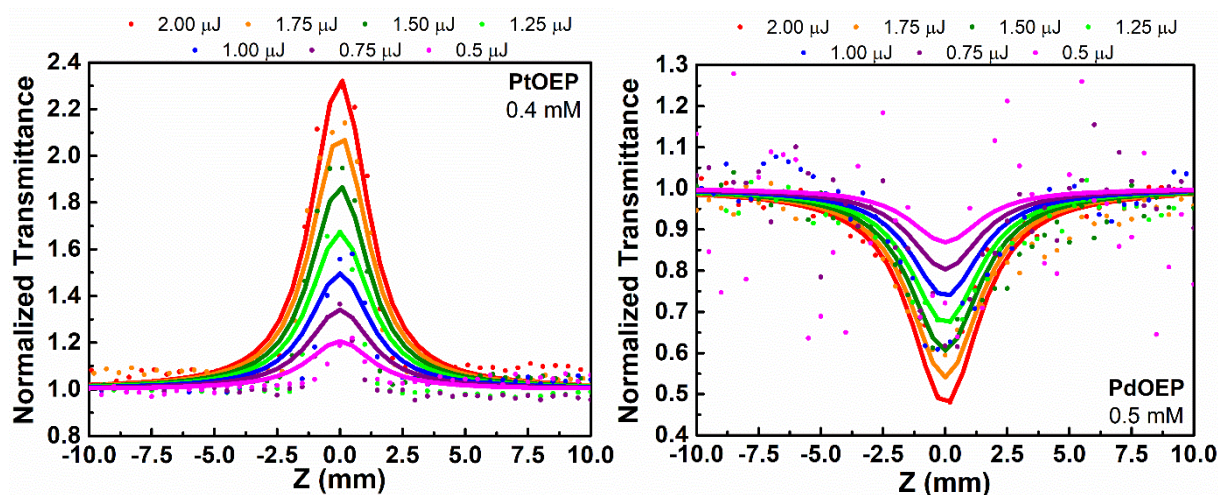
$$\sigma = \frac{\hbar\omega\beta}{N_A\rho} \quad (5.1)$$

where:  $\hbar$  - Planck's constant,  $N_A$  - Avogadro's number,  $\rho$  - concentration of solution [mole per volume]. The calculation results are presented in Tab. 5.6.



**Table 5.6:** Calculated values of NLO refractive index  $n_2$ , NLO absorption coefficient  $\beta$ , NLO absorption cross section  $\sigma$ , real and imaginary part of third order NLO susceptibility  $\text{Re}(\chi^{(3)})$ ,  $\text{Im}(\chi^{(3)})$  of studied porphyrin complexes.

	$\rho$ [mM]	$n_2 \times 10^{-19}$ [m <sup>2</sup> W <sup>-1</sup> ]	$\beta \times 10^{-12}$ [mW <sup>-1</sup> ]	$\sigma \times 10^{-54}$ [m <sup>4</sup> s]	$\text{Re}(\chi^{(3)}) \times 10^{-21}$ [m <sup>2</sup> V <sup>-2</sup> ]	$\text{Im}(\chi^{(3)}) \times 10^{-21}$ [m <sup>2</sup> V <sup>-2</sup> ]
<b>PtOEP</b>	0.5	1.23	-3.52	-4.36	0.91	-1.09
	0.4	2.51	-13.34	-20.67	1.84	-4.14
	0.3	5.30	-30.86	-67.90	3.88	-10.21
	0.2	7.87	-58.07	-179.99	5.77	-18.04
<b>RuOEP</b>	0.5	1.73	1.76	2.18	1.27	0.55
	0.4	1.09	1.17	1.81	0.80	0.36
	0.3	0.82	0.95	1.96	0.61	0.29
	0.2	0.48	0.52	1.61	0.35	0.16
<b>FeOEP</b>	0.5	-3.79	-0.82	-1.01	2.78	-0.25
	0.4	-1.25	-0.55	-0.85	0.92	-0.17
	0.3	-0.78	-0.39	-0.80	0.57	-0.12
	0.2	-0.57	-0.20	-0.62	0.42	-0.62
<b>PdOEP</b>	0.5	7.14	10.63	13.18	5.23	3.30
	0.4	2.79	3.59	5.56	2.05	1.12
	0.3	1.80	2.87	5.93	1.32	0.89
	0.2	1.18	1.65	5.11	0.87	0.51



**Figure 5.18:** Normalized OA Z-scan characteristics for porphyrin complexes at different input laser energy.

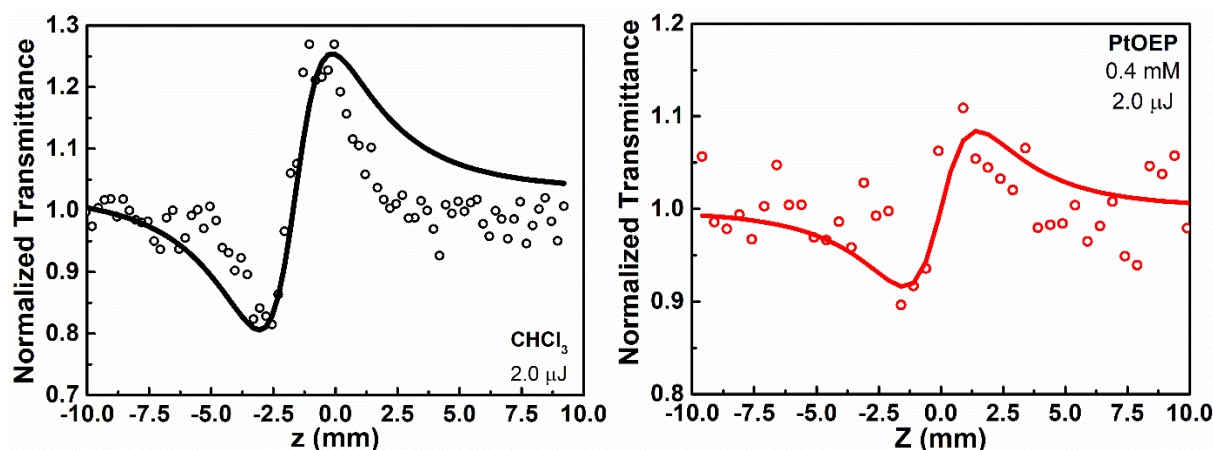


Figure 5.19: Normalized CA Z-scan characteristics for **CHCl<sub>3</sub>** and **PtOEP** at input laser energy 2.0 μJ.

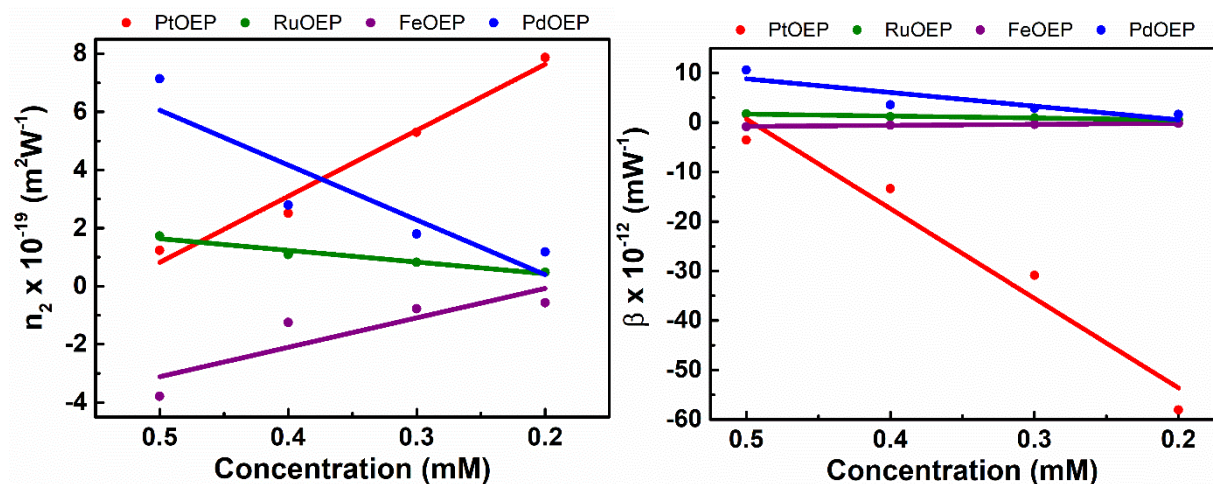
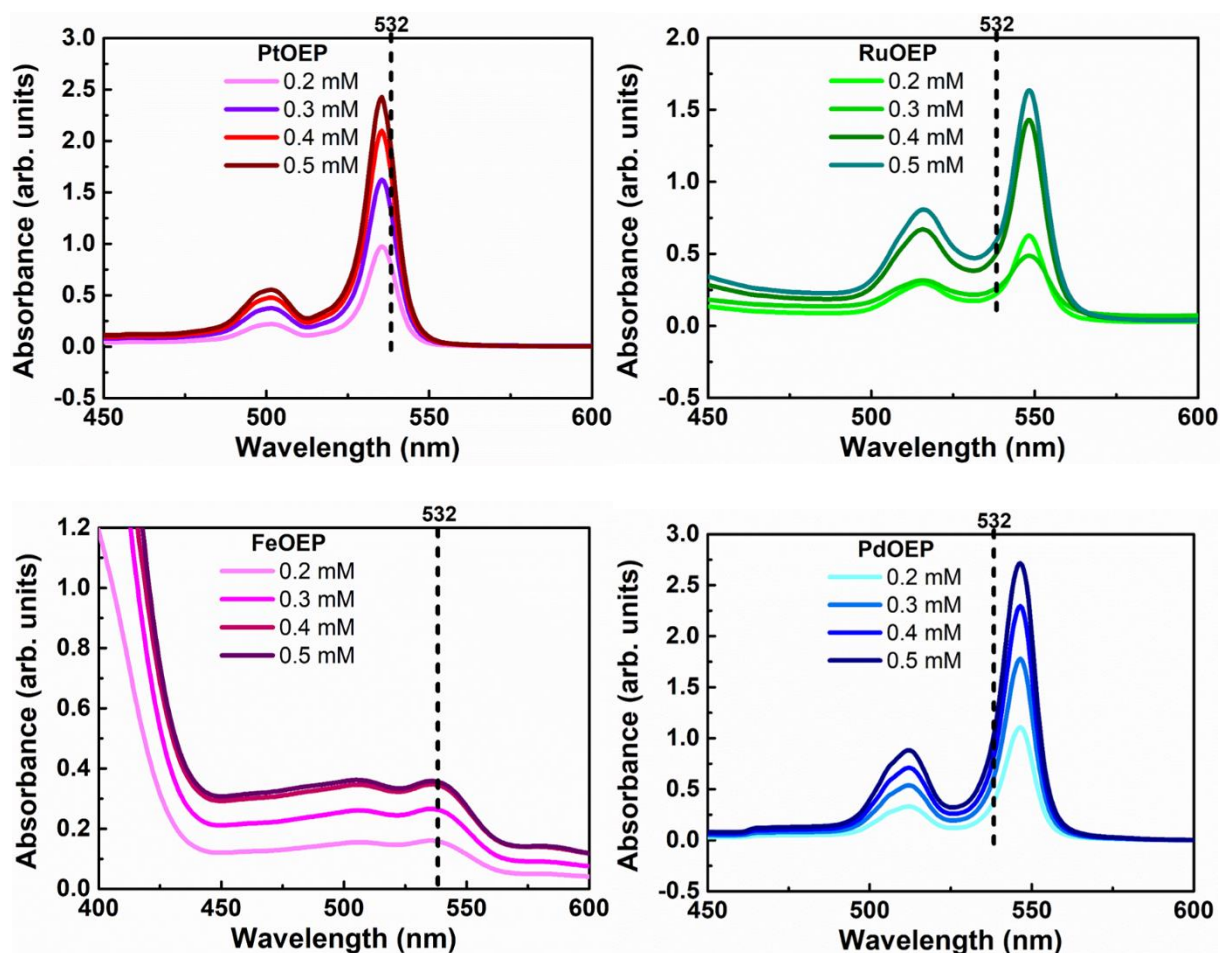


Figure 5.20: Values of nonlinear refractive index (left) and nonlinear absorption coefficient (right) as a function of solution concentration of porphyrin complexes in chloroform **CHCl<sub>3</sub>**.

As can be clearly seen in Fig. 5.18 – 5.19 and Tab. 5.6, the investigated porphyrin complexes are self-focusing ( $n_2 > 0$ ) and self-defocusing ( $n_2 < 0$ ) materials, as well as characterized by saturable absorption SA ( $\beta < 0$ ) and reverse saturable absorption RSA ( $\beta > 0$ ). For the **PtOEP** sample, along with the dilution of the solution, the effects of nonlinear refraction and saturable absorption began to increase significantly, in contrast to the remaining samples, where decreasing the

concentration of the solution resulted in the decreasing of the studied nonlinear effects. The calculated values of the nonlinear refractive index and the nonlinear absorption coefficient are given in Tab. 5.6 is shown schematically with the graphs in Fig. 5.20.



**Figure 5.21:** Absorption spectra of 0.5 mM, 0.4 mM, 0.3 mM and 0.2 mM solutions of porphyrin complexes in chloroform  $\text{CHCl}_3$  with the marked wavelength of the laser light source (532 nm).

To understand the behavior of **PtOEP** sample, UV-vis absorption of the studied solutions with different molar concentrations was measured. The results are shown in Fig. 5.21. From the obtained absorption spectra and the calculated nonlinear parameters, it can be noticed that with higher absorbance for samples **RuOEP**, **FeOEP** and **PdOEP**, the nonlinear effect becomes stronger. However, for the **PtOEP** sample, the effect is opposite and the absorbance is very high

and excitation laser wavelength 532 nm is close to resonance, which may mean that above the absorbance value of 1.0, the effect is saturated, that is why with dilution the effect becomes stronger. Moreover, the **PdOEP** sample is characterized by strong linear absorption at 532 nm, and in this case also the saturable absorption effect should occur during the Z-scan measurement, however we noticed opposite situation. Therefore, it is necessary to perform calculations on molecular orbitals to understand behavior in those studied samples. The best way to compare the Z-scan results for these samples is to compare them at the lowest concentration.

**Table 5.7:** Calculated values of NLO susceptibility  $\chi^{(3)}$  obtained from Z-scan data, compared with THG results of studied porphyrin complexes.

			<b>PtOEP</b>	<b>RuOEP</b>	<b>FeOEP</b>	<b>PdOEP</b>
$\chi^{(3)} \times 10^{-21}$ [m <sup>2</sup> V <sup>-2</sup> ]	<b>Z-scan</b>	<b>0.5 mM</b>	1.41	1.38	2.79	6.18
		<b>0.4 mM</b>	4.53	0.88	0.93	2.33
		<b>0.3 mM</b>	10.92	0.67	0.58	1.59
		<b>0.2 mM</b>	18.94	0.38	0.75	1.01
		<b>THG</b>	0.376	0.293	0.427	0.339

From the calculated real and imaginary parts of the nonlinear susceptibility, the total values of  $\chi^{(3)}$  was determined and are shown in Tab. 5.7 with comparison of  $\chi^{(3)}$  values determined from THG method in p-polarized laser beam. It can be noticed that, as in the case of the THG method, the **FeOEP** sample seemed to have the highest values of nonlinear susceptibility, and in the case of the Z-scan method, the values for this sample are lower than the other **PtOEP** and **PdOEP**. Moreover, as mentioned before, for these concentrations the NLO signal for the sample **PtOEP** becomes supersaturated, hence the large values of the NLO parameters occurred. Furthermore, the third harmonic generation method is distinguished by the fact that nonlinear susceptibility has only electronic contribution, and the Z-scan method is more accurate due to the contribution of nonlinear refraction (electronic element) and nonlinear absorption (molecular element), hence the  $\chi^{(3)}$  values determined from the Z-scan method are higher than the  $\chi^{(3)}$  values determined from

the THG method. Besides, it is important that nonlinear studies are performed under similar conditions. In the case of thin layers, it is difficult to obtain samples of the same thickness with the same concentration, but the Z-scan method allows us to perform research for the same concentration of solutions. Moreover different wavelengths of laser source have been used in those experiments: THG – 1064 nm and Z-Scan – 532 nm.

## 5.7. Conclusions

Summarizing, the above work presents the research on nonlinear optical and spectroscopic properties of selected porphyrin complexes **PtOEP**, **RuOEP**, **FeOEP** and **PdOEP** as a models for nonlinear optical research in supramolecular assemblies. The studies were performed on samples in state of thin films obtained by the spin-coating method and in solutions. Photoluminescence studies were carried out on thin films. During the excitation of the samples with a length corresponding to the maximum of the absorption peak, the investigated samples emit red light, and the lifetime time is very short, which indicates a fluorescence decay. Moreover, studies of the second and third order nonlinear optical properties were carried out using the second and third harmonic generation method, respectively. The results presented show that the samples have a strong nonlinear response for thin films due to chemical structure of studied metalloporphyrins. In addition, third-order nonlinear effects were investigated with the Z-scan technique, which allows the simultaneous measurement of nonlinear refraction and nonlinear absorption for different solution concentrations. All four samples have strong nonlinear saturable or reverse saturable absorption as well as positive or negative nonlinear refractive index. Each of these samples has unique spectroscopic and nonlinear optical properties. These interesting properties of porphyrin complexes result in them being of the most promising candidates for applications based on nonlinear optics, inter alia in data storage, as optical limiters and also appear to be ideal candidates for Q-switching.

## Literature

- [5.1] M. R. Dayer, A. A. Moosavi-Movahedi, M. S. Dayer, Band Assignment in Hemoglobin Porphyrin Ring Spectrum: Using Four-Orbital Model of Gouterman, *Protein & Peptide Letters*, 2010, 17, 473-479
- [5.2] P. Minutolo, G. Gambi, A. D'Alessio, The optical band gap model in the interpretation of the UV-visible absorption spectra of rich premixed flames, *Symposium (International) on Combustion/The Combustion Institute*, 1996/pp. 951-957
- [5.3] T. Tsuboi, H. Murayama, A. Penzkofer, Photoluminescence characteristics of Ir(ppy)<sub>3</sub> and PtOEP doped in TPD host material, *Thin Solid Films*, Vol. 499 (1-2), 306-312, 2006
- [5.4] A. Zawadzka, P. Plóciennik, A. Korcala, P. Szroeder, Optical properties of chiral single-walled carbon nanotubes thin films, *Opt, Mater.* vol 96 (2019) 109295
- [5.5] K. Waszkowska, K. El Korchi, D. Guichaoua, A. Zawadzka, B. Sahraoui, Influence of Polymer Matrix on Nonlinear Optical Response in Octaethylporphine Palladium Derivative Thin Films, 21st International Conference on Transparent Optical Networks (ICTON), Angers, France, 2019, pp. 1-4.
- [5.6] K. Iliopoulos, D. Potamianos, E. Kakkava, P. Aloukos, I. Orfanos, and S. Couris. Ultrafast third order nonlinearities of organic solvents. *Optics Express* Vol. 23, Issue 19, pp. 24171-24176, 2015.
- [5.7] A. Ajami, W. Husinsky, R. Liska, N. Pucher, Two-photon absorption cross section measurements of various two-photon initiators for ultrashort laser radiation applying the Z-scan technique, *Journal of the Optical Society of America B* Vol. 27, Issue 11, pp. 2290-2297 (2010)

[5.8] J. Szeremeta, R. Kolkowski, M. Nyk, M. Samoc, Wavelength Dependence of the Complex Third-Order Nonlinear Optical Susceptibility of Poly(3-hexylthiophene) Studied by Femtosecond Z-Scan in Solution and Thin Film, *J. Phys. Chem. C* 2013, 117, 49, 26197–26203

## CHAPTER 6: TRIPLE STRANDED HELICATES

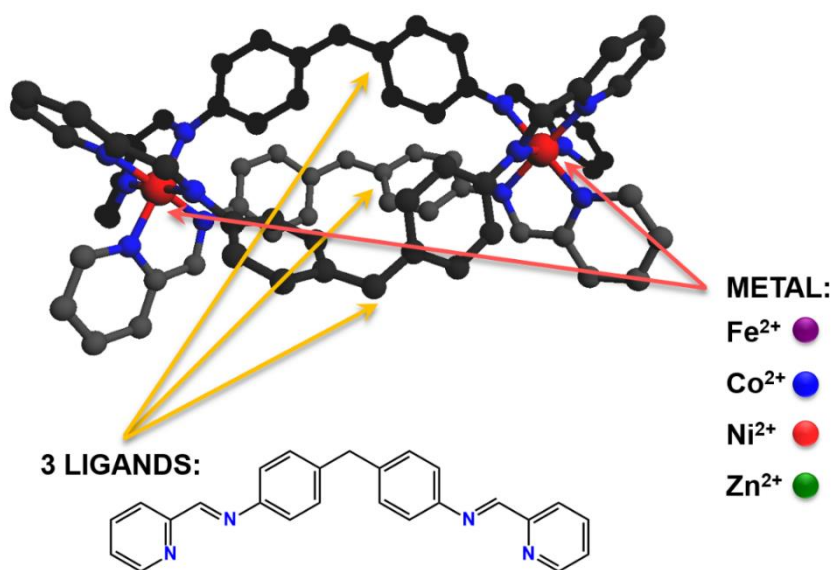
Motivation in this work is using self-assembly instead of mononuclear complexes and investigate influence of two metals on NLO properties. The work reported herein was devoted to study linear, photoluminescent and nonlinear optical properties of some selected metallo-supramolecular triple-stranded helicates and in particular to evaluate the influence of the metal cations over one period used during the self-assembly process such as iron(II), cobalt(II), nickel(II), zinc(II), on such physical properties. The determination of first and second-order hyperpolarizability of a molecule is often used to understand the affinity between the molecular structure and NLO properties. Therefore we present also the quantum chemical calculation of electronic delocalization through a  $\pi$ -conjugated molecular system. To explain the origin of the NLO phenomena occurring in the investigated supramolecular systems - calculations predicting: HOMO (Highest Occupied Molecular Orbital) and LUMO (Lowest Unoccupied Molecular Orbital), first and second-order hyperpolarizabilities were performed. The calculations of HOMO and LUMO are very important aspects to consider the molecular reactivity. The results presented below were published in [6.1].

### 6.1. Sample Preparation

The metal complexes in this research are triple stranded helicates which are resulting from the self-assembly process of three ligands based on iminopyridine fragments and two metal cations, as previously reported [6.2] and synthesized by Dr. Abdelkrim El-Ghayoury and Dr. Yohan Cheret. The metal cations being  $\text{Fe}^{2+}$  (**HelFe**),  $\text{Co}^{2+}$  (**HelCo**),  $\text{Ni}^{2+}$  (**HelNi**) and  $\text{Zn}^{2+}$  (**HelZn**). Fig. 6.1 the studied triple stranded metallo-helicates. **Hel-M** guest-host polymeric thin films were prepared using well-known spin coating method from solutions with acetonitrile (ACN) solvent and poly(methyl methacrylate) (PMMA). The concentration of the prepared solution was 10 wt% of

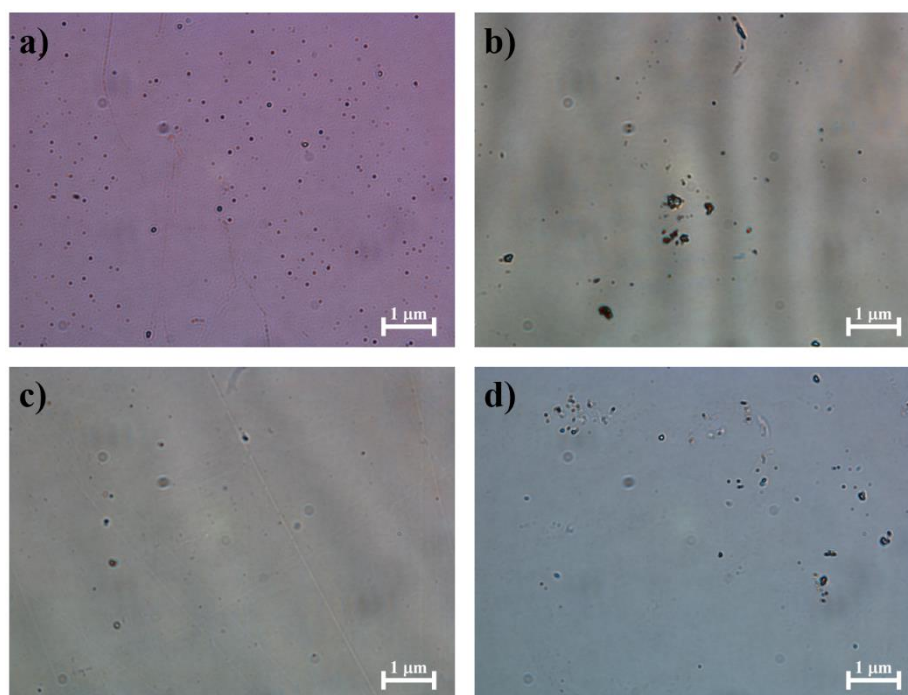


triple stranded helicate to polymer PMMA. Deposition were carried out on strictly cleaned 1 mm glass substrates using spin-coater (Spin200i, POLOS) at speed 2000 rpm.



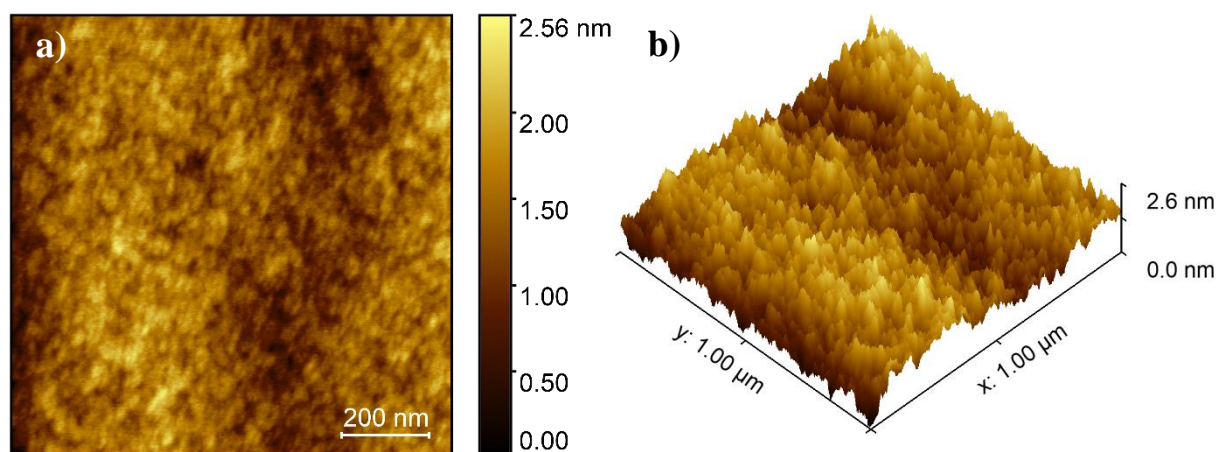
**Figure 6.1:** Schematic representation of the studied metallo-supramolecular assemblies.

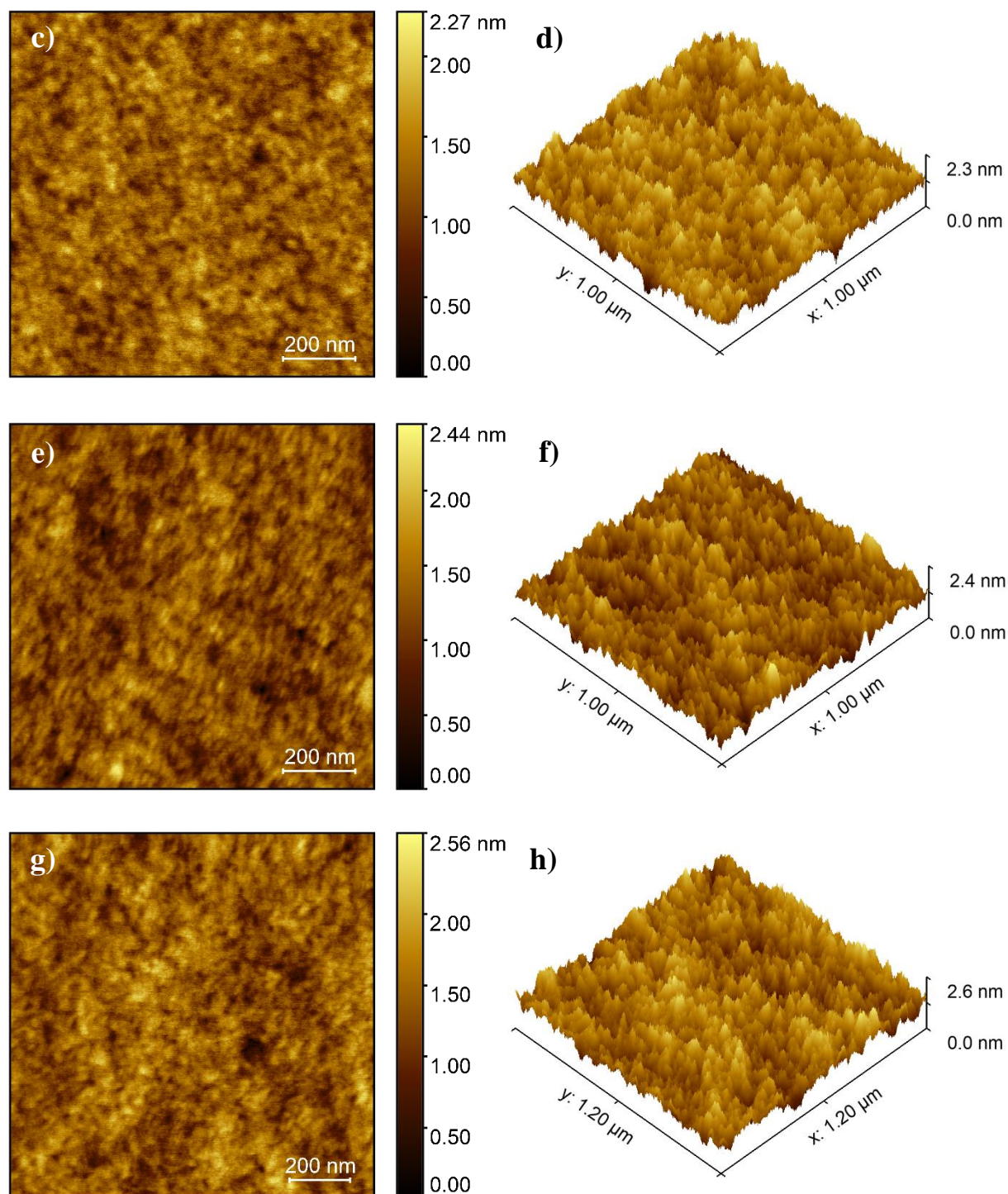
## 6.2. Surface Characterization



**Figure 6.2:** Photographs from optical microscope; a) **HelFe**; b) **HelCo**; c) **HelNi**; d) **HelZn**.

In the first order thickness of obtained thin films have been measured using profilometer (Dektak 6M, Veeco). Layers are thinner than 1 micron, and their exact values are given in Tab. 6.1. Afterwards, the photographs of the samples were taken with an optical microscope (Fig. 6.2). In addition to the different colors, some defects in the structure of the layer can also be seen, which were examined in detail using AFM microscope. Typical AFM images analyzed by Gwyddion software are presented in Fig. 6.3. Measurements were carried out in the range  $1\ \mu\text{m} \times 1\ \mu\text{m}$ . It was observed that films are quite homogenous and smooth, although some surface irregularities have been observed. The surface roughness was then measured and calculated. However, the unevenness is not significant - it is at the level of several hundred picometers, in the case of the **HelFe** sample almost one nanometer. This is important when measuring the second and third harmonics to obtain a periodic symmetric signal which is not affected by structure defects. The obtained values are located in Tab. 6.1. Moreover, in Tab. 6.1 the values of the linear refractive index and the extinction coefficient for the wavelengths corresponding to the wavelength of the pumping laser (1064 nm), generation of the second harmonic (532 nm) and generation of the third harmonic (355 nm), determined by means of an ellipsometric measurement, are presented.

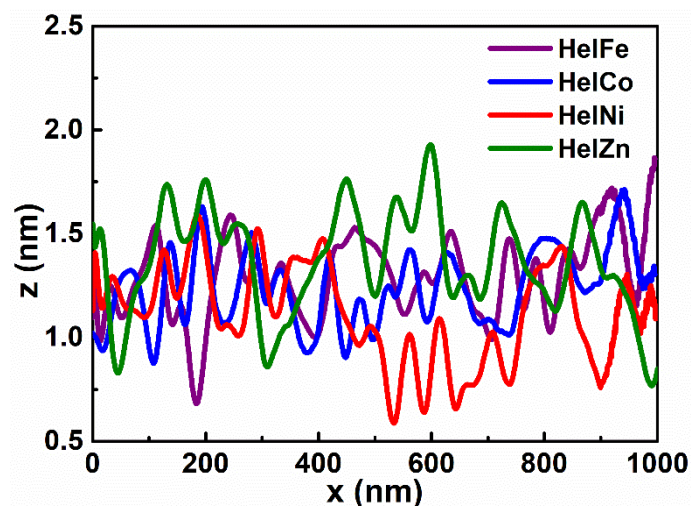




**Figure 6.3:** Atomic force microscopy (AFM) images of studied triple stranded helicates thin films: **HelFe** a) 2-dimensional, b) 3-dimensional; **HelCo** c) 2-dimensional, d) 3-dimensional; **HelNi** e) 2-dimensional, f) 3-dimensional; **HelZn** g) 2-dimensional, h) 3-dimensional.

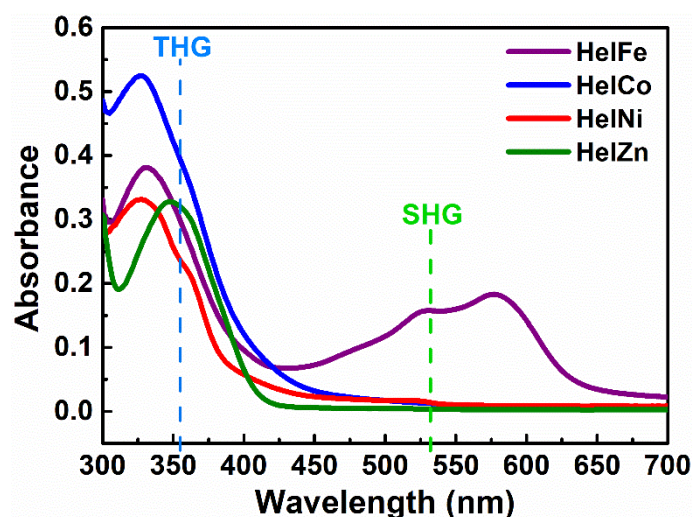
**Table 6.1:** Thickness ( $d$ ), roughness ( $R_A$ ), linear refractive index values ( $n$ ) and extinction coefficients ( $\kappa$ ) of triple stranded helicates thin films.

	$d$ [nm]	$R_A$ [nm]	$n_{1064}$	$n_{532}$	$n_{355}$	$\kappa_{1064}$	$\kappa_{532}$	$\kappa_{355}$
HelFe	820	0.984	1.522	1.528	1.540	0.004	0.014	0.038
HelCo	820	0.154	1.436	1.458	1.481	0.001	0.008	0.037
HelNi	660	0.157	1.426	1.443	1.464	0.072	0.069	0.067
HelZn	680	0.061	1.435	1.465	1.498	0.083	0.069	0.056



**Figure 6.4:** Atomic force microscopy profiles of studied triple stranded helicates.

### 6.3. Spectroscopic Studies



**Figure 6.5:** Absorption spectra of studied triple stranded helicates.

Absorption spectra (Fig. 6.5) of the studied thin films were measured by using UV-Visible spectrophotometer in the range 300-1000 nm. Cobalt(II), nickel(II) and zinc(II) exhibit one strong absorption band located at  $\lambda_{\max} = 355$  nm that can be assigned to the  $\pi \rightarrow \pi^*$  and  $n \rightarrow \pi^*$  interligand charge transfer (<sup>1</sup>ILCT) transitions. In the case of **HelFe** helicate, in addition to the band located at  $\lambda_{\max} = 331$  nm, the absorption spectrum exhibits a band located in the visible region which is assigned to metal to ligand charge transfer transition (<sup>3</sup>MLCT) as commonly observed for iron(II) N-heterocyclic ligands [6.3 – 6.4] due to *d-d* transitions in iron(III) complexes. Note that the absorbance at 1064 nm, that constitutes the fundamental wavelength of laser beam at SHG and THG measurements, is negligible. We also noted, that at wavelength corresponding to THG, which is 355 nm, the absorbance is significant which means that simultaneous THG generation is somewhat absorbed. For this reason, the calculations associated with THG experiment have included the absorption coefficient. On the other hand, in case of SHG wavelength, which is 532 nm, absorbance is not negligible for **HelFe** helicate, therefore for this material the calculations was performed by including the absorption coefficient as for THG. Moreover, with the appearance of linear absorption for a wavelength of 532 nm, we should also expect nonlinear absorption. The exact  $\lambda_{\max}$  with absorption coefficients for 532 nm (which corresponds to SHG) and 355 nm (which corresponds to THG) are presented in Tab. 6.2.

**Table 6.2:** Absorption peaks and values of absorption coefficients.

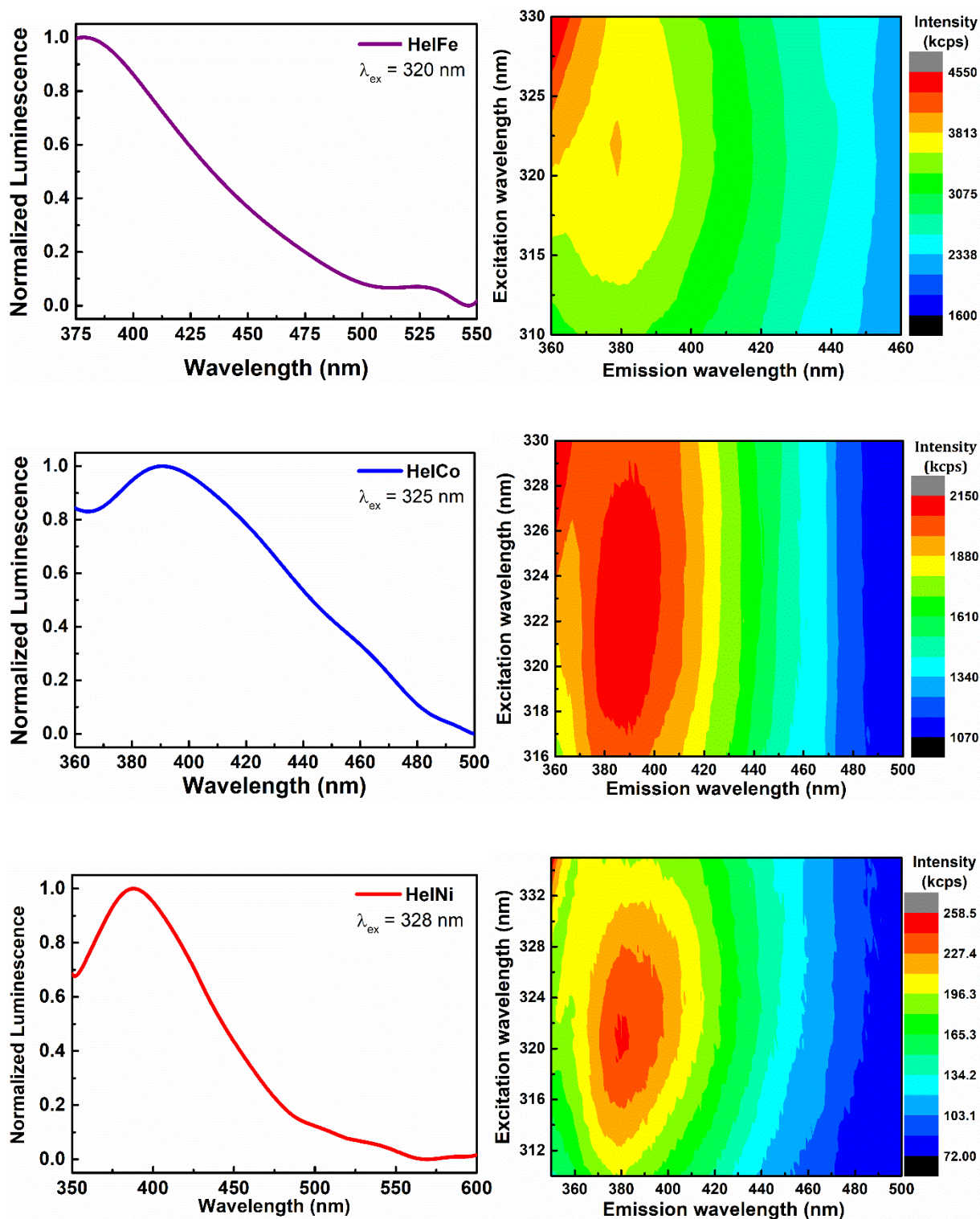
	$\lambda_{\text{abs}}$ [nm]	$\alpha$ [ $10^3 \text{ cm}^{-1}$ ]	
		532 nm	355 nm
<b>HelFe</b>	331, 531, 577	4.49	8.49
<b>HelCo</b>	327	0.35	11.22
<b>HelNi</b>	328	0.50	8.40
<b>HelZn</b>	348	0.12	10.94

Photoluminescence spectra of the studied triple stranded helicates thin films on glass substrates are presented in Fig. 6.6. It was observed that for all samples PL spectra indicate one maximal PL

peak in violet wavelength range positioned around 380-410 nm, which are result of ILCT transitions. During excitation at 532 nm and 577 nm sample containing iron(II) **HelFe**, no emission signal was recorded. This is due to the fact that the photoluminescence was carried on thin films containing only 10% of the studied material with the result that both absorption and emission for these compounds are not high intense. 3D photoluminescence spectra shows the intensity for a given emission wavelength as a function of the excitation wavelength. These PL spectra were carried out in the excitation wavelength range 310 nm to 340 nm and emission wavelength range from 350 nm to 500 nm for **HelFe**, **HelCo** and **HelNi**, sample containing zinc(II) was measured in excitation wavelength range from 310 nm to 390 nm and emission wavelength range from 400 nm to 500 nm. As we observed, the strongest enhancement of PL intensity was located near resonant region during excitation by UV light. However it was noted, that PL spectra is determined by asymmetrical shape which is caused by concentration of the samples. By determining the excitation and emission wavelengths for which the highest intensity occurs, the luminescence decay time was then measured using additional pulse diodes with wavelengths close to excitation wavelengths, which are presented on Fig. 6.7. The lifetime was measured in room temperature, and achieved results were fitted by double-exponential function  $y = y_0 + A_0e^{-t/T_1} + A_1e^{-t/T_2}$  [6.5], which implies two time decays short T1 and long T2, describing transition from excited single state to ground state. The estimated values of decay times are given in Tab. 6.3. The recorded decay times are very short, first around 1.5-2.0 ns and second around 20-40 ns, which signifies that these samples show fluorescent properties.

**Table 6.3:** Excitation, emission peaks and luminescence lifetimes of studied thin films.

	$\lambda_{\text{Excitation}}$ [nm]	$\lambda_{\text{Emission}}$ [nm]	T1 <sub>Decay</sub> [ns]	T2 <sub>Decay</sub> [ns]
<b>HelFe</b>	320	380	(1.562 ± 0.012)	(22.546 ± 0.226)
<b>HelCo</b>	325	400	(1.473 ± 0.011)	(37.872 ± 0.257)
<b>HelNi</b>	328	393	(1.408 ± 0.026)	(23.726 ± 0.242)
<b>HelZn</b>	380	410	(2.005 ± 0.052)	(24.420 ± 0.202)



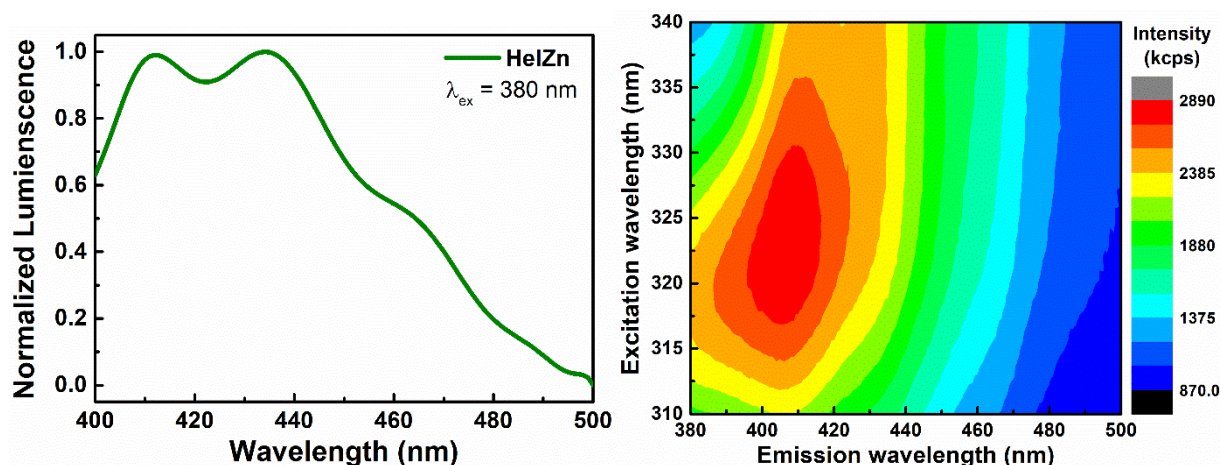


Figure 6.6: Photoluminescence spectra and 3D photoluminescence image of triple stranded helicates.

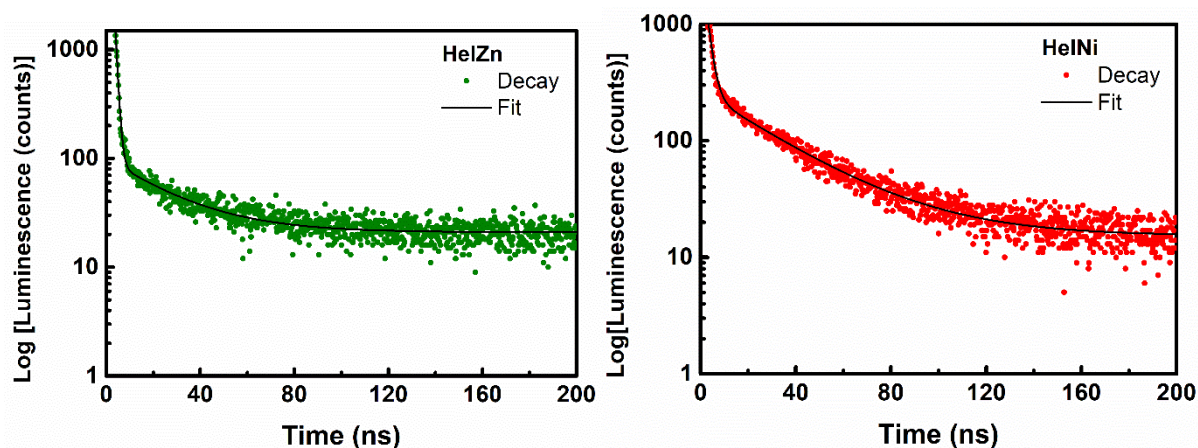


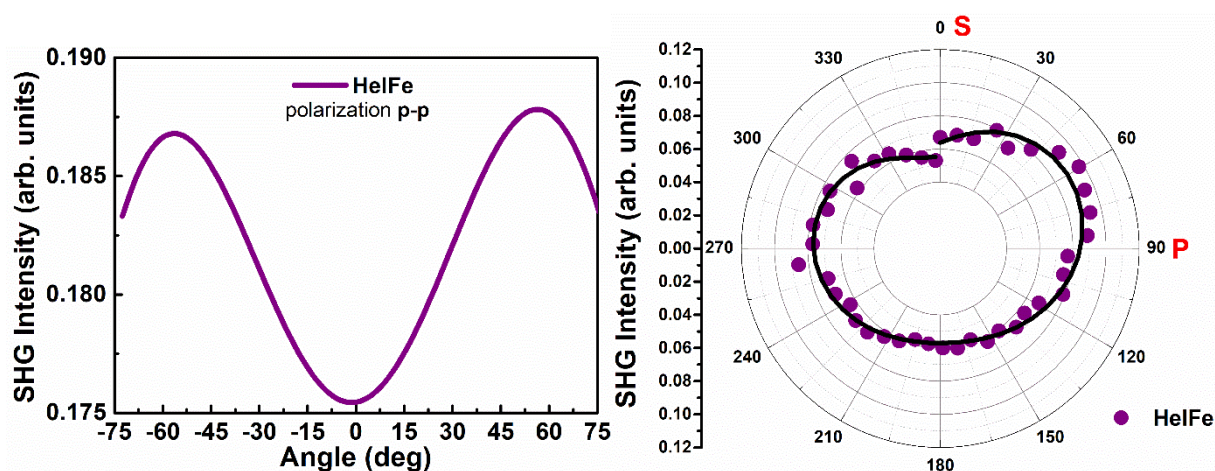
Figure 6.7: Typical luminescence lifetime decays of studied thin films.

#### 6.4. Second Harmonic Generation

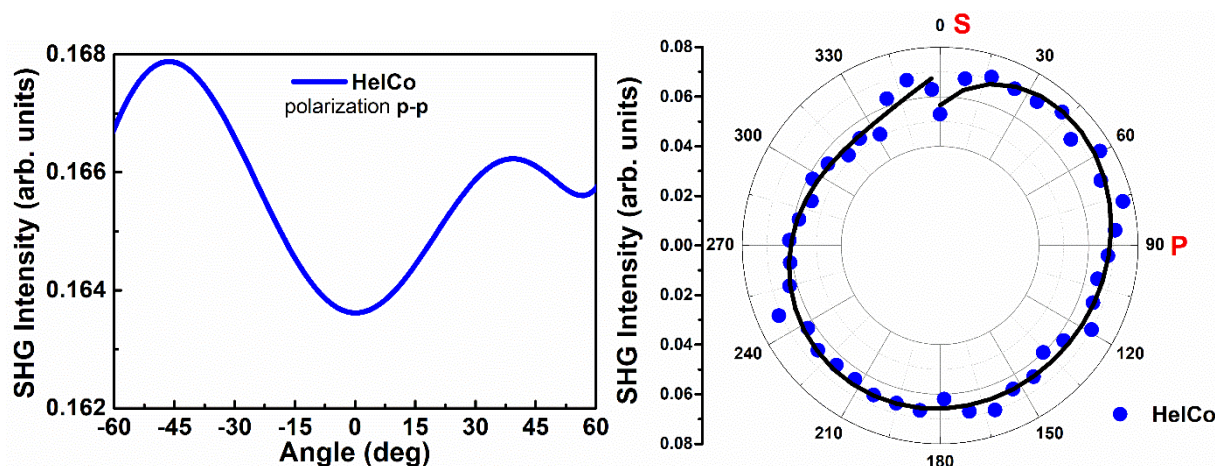
The measurements of the second, as well as third harmonic effects, were carried out using the experimental setup presented in subchapter 4.2. Y-cut quartz crystal was used as reference materials. Measurements were performed for vertical and horizontal polarization of fundamental laser beam. In this work, we focused on the differences in NLO effects resulting from the use of selected metal cations in the triple stranded helicates. According to the structural properties of guest-host systems, it was necessary to use the corona poling technique to obtain the second



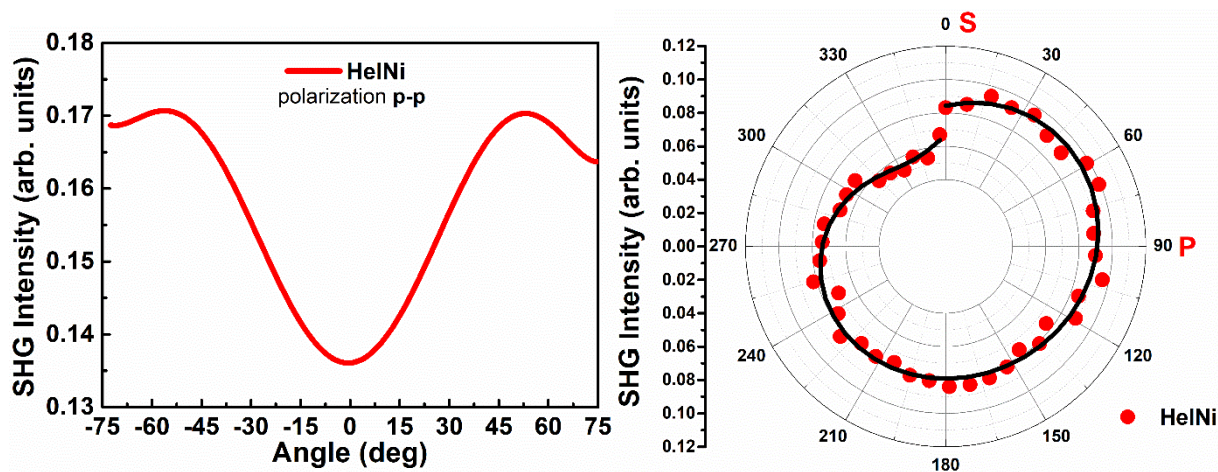
harmonic signal. SHG responses showed that the signal is not much dependent on polarization configuration (Fig. 6.8 – 6.11). The strongest signal of the generated second harmonic was obtained for the **HelNi** thin film. Additionally, Fig. 6.12 shows the dependence of the intensity of the generated second harmonic as a function of the laser energy made at Czestochowa University of Technology, presented in subsection 4.2 in Fig. 4.6. In this method, also the strongest response was obtained for the **HelNi** sample.



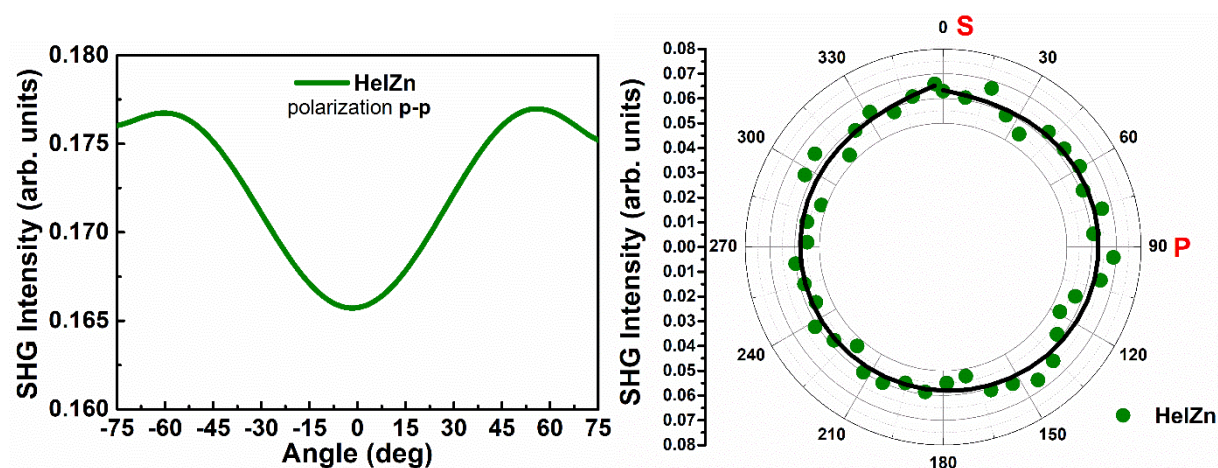
**Figure 6.8:** SHG intensities as a function of rotation angle in p-polarized laser beam (left) and as a dependence of laser polarization (right) of **HelFe** thin film.



**Figure 6.9:** SHG intensities as a function of rotation angle in p-polarized laser beam (left) and as a dependence of laser polarization (right) of **HelCo** thin film.



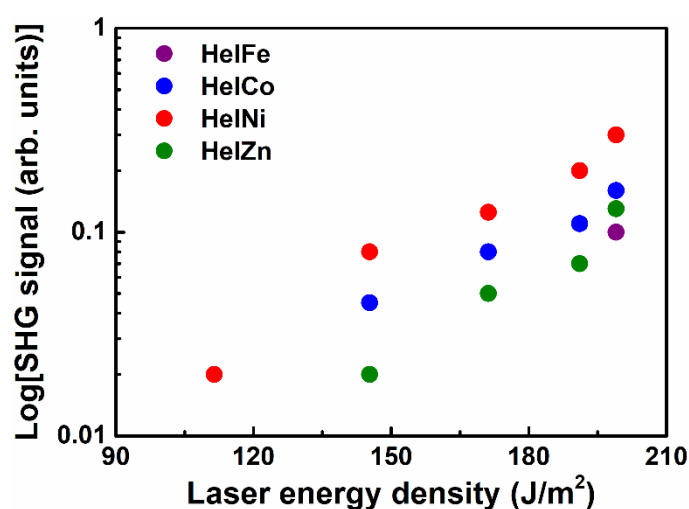
**Figure 6.10:** SHG intensities as a function of rotation angle in p-polarized laser beam (left) and as a dependence of laser polarization (right) of **HeINi** thin film.



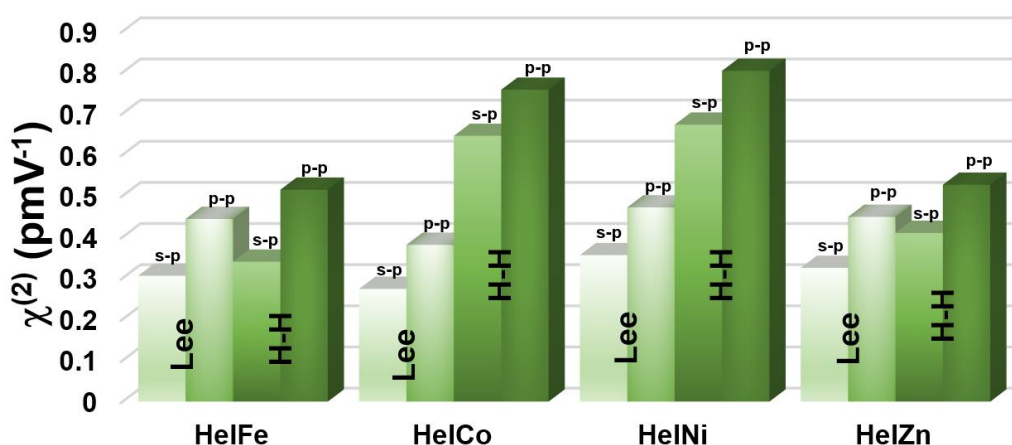
**Figure 6.11:** SHG intensities as a function of rotation angle in p-polarized laser beam (left) and as a dependence of laser polarization (right) of **HeIZn** thin film.

Tab. 6.4 shows the calculated values of the second order nonlinear susceptibilities for the s- and p-polarized laser beam using the Lee theoretical models (subsection 4.1.1) and Herman-Hayden (subsection 4.1.3). Herman-Hayden includes parameters dependent on the thin film and polarization properties, the values of second-order NLO susceptibilities are higher than for comparative model. However, values are not significantly different from each other for different polarization, which can also be seen in SHG signal versus laser polarization plots. This refers to

the fact that in the case of these supramolecular systems which are triple stranded helicates, when forming a guest-host system with polymer matrix, the system takes the form of an isotropic medium and the nonlinear response is independent on direction of polarized incident laser light. Moreover, outstanding differences were not noticed between the  $\chi^{(2)}$  values depending on the metal cation, due to the fact that metal cations are from over one period, and in fact their contribution to NLO properties is small. The highest values were obtained for the **HelNi** sample. For better contrast, the calculated values are visualized graphically in the form of histogram in Fig. 6.13.



**Figure 6.12:** SHG signal versus laser energy density of studied triple stranded helicate thin films.

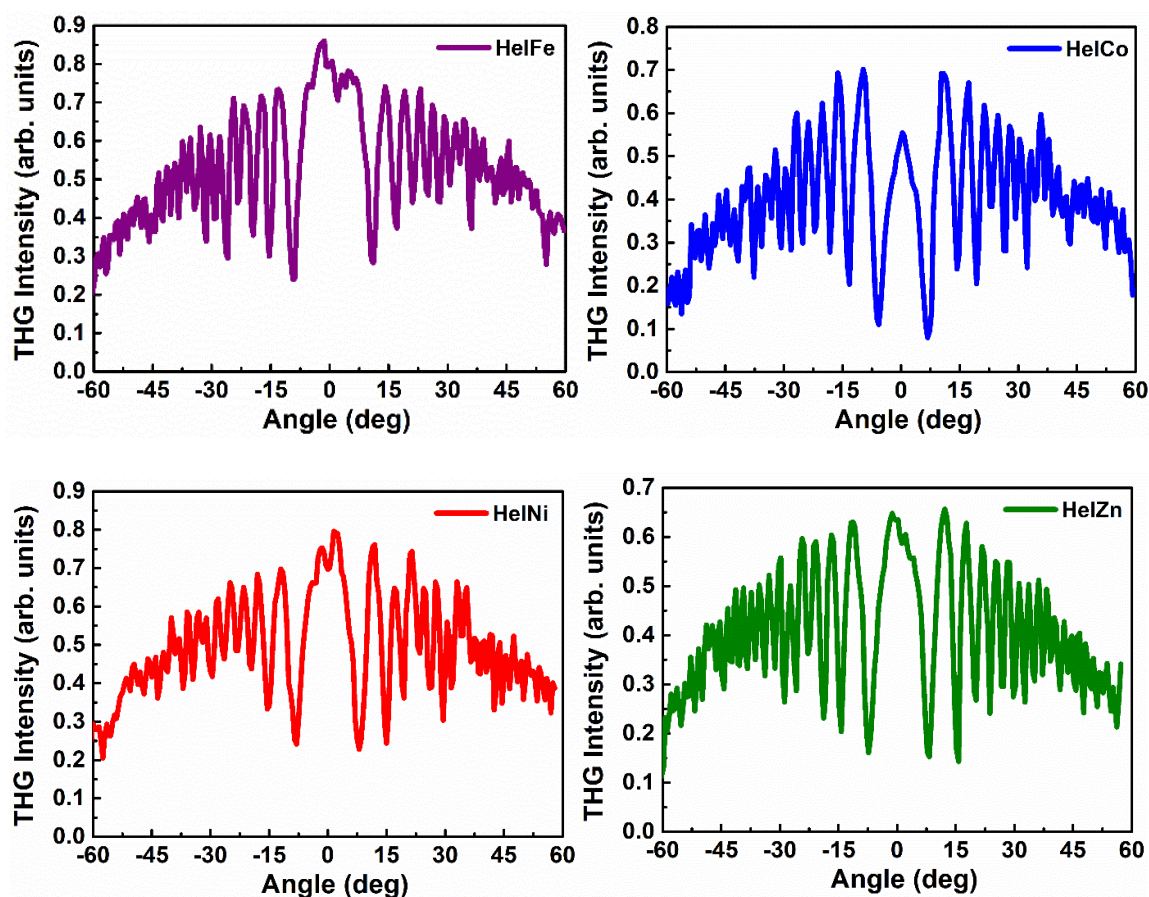


**Figure 6.13:** Histogram representing values of second-order nonlinear susceptibilities calculated via theoretical models.

**Table 6.4:** Values of second-order nonlinear susceptibilities calculated by theoretical models.

	Model	$\chi^{(2)}$ [pmV <sup>-1</sup> ]	
		s-p	p-p
HelFe	Lee	(0.306 ± 0.058)	(0.444 ± 0.036)
	Herman-Hayden	(0.340 ± 0.045)	(0.515 ± 0.098)
HelCo	Lee	(0.274 ± 0.023)	(0.381 ± 0.074)
	Herman-Hayden	(0.646 ± 0.025)	(0.758 ± 0.024)
HelNi	Lee	(0.356 ± 0.044)	(0.472 ± 0.063)
	Herman-Hayden	(0.673 ± 0.047)	(0.804 ± 0.038)
HelZn	Lee	(0.325 ± 0.015)	(0.449 ± 0.024)
	Herman-Hayden	(0.410 ± 0.026)	(0.527 ± 0.041)

### 6.5. Third Harmonic Generation



**Figure 6.14:** THG intensities as a function of incident angle of studied triple stranded helicates in s-polarized laser beam.

In the case of THG studies, there are no structure constraints, thus corona poling was not required to obtain a third-order nonlinear optical response. Fig. 6.14 shows the third harmonic signal for all investigated triple helicates in s-polarized laser beam. Additionally, Fig. 6.15 presents the dependence of the intensity of the generated third harmonic as a function of the laser energy made at Czestochowa University of Technology, presented in subsection 4.2 in Fig. 4.6.

**Table 6.5:** Values of second-order nonlinear susceptibilities calculated by theoretical models.

	Model	$\chi^{(3)} \times 10^{-22} [\text{m}^2\text{V}^{-2}]$	
		s-p	p-p
<b>HelFe</b>	Kubodera-Kobayashi	$(15.02 \pm 0.39)$	$(15.38 \pm 0.39)$
	Reintjes	$(17.95 \pm 0.20)$	$(18.18 \pm 0.19)$
<b>HelCo</b>	Kubodera-Kobayashi	$(15.85 \pm 0.14)$	$(15.45 \pm 0.14)$
	Reintjes	$(16.19 \pm 0.12)$	$(15.83 \pm 0.13)$
<b>HelNi</b>	Kubodera-Kobayashi	$(16.84 \pm 0.13)$	$(17.28 \pm 0.14)$
	Reintjes	$(18.32 \pm 0.36)$	$(18.55 \pm 0.35)$
<b>HelZn</b>	Kubodera-Kobayashi	$(14.74 \pm 0.23)$	$(14.98 \pm 0.26)$
	Reintjes	$(16.33 \pm 0.48)$	$(16.81 \pm 0.50)$

As it was mentioned previously, due to the high absorbance 355 nm, it is necessary to take into account the absorption coefficient in the calculations, the values of which are presented in Tab. 6.2. Basically, THG response is independent from polarization of fundamental beam, however slight differences between calculated values of  $\chi^{(3)}$  calculated by using Kubodera-Kobayashi and Reintjes model have been observed (see Tab. 6.5). This is due to small changes in the laser energy when changing polarization with a half-wave plate. Likewise SHG measurements, there was no significant difference observed for THG with the included metal cation, from the same reason. Nonetheless, the strongest responses in both experiments have been obtained for triple stranded helicate with nickel cation **HelNi**, however the obtained signal, as well as calculated third-order NLO values are not significantly different from other triple stranded helicates due to the fact that

contribution of metal cations to NLO properties, likewise in SHG experiment, is small. For better contrast, the calculated values are visualized graphically in the form of histogram in Fig. 6.16.

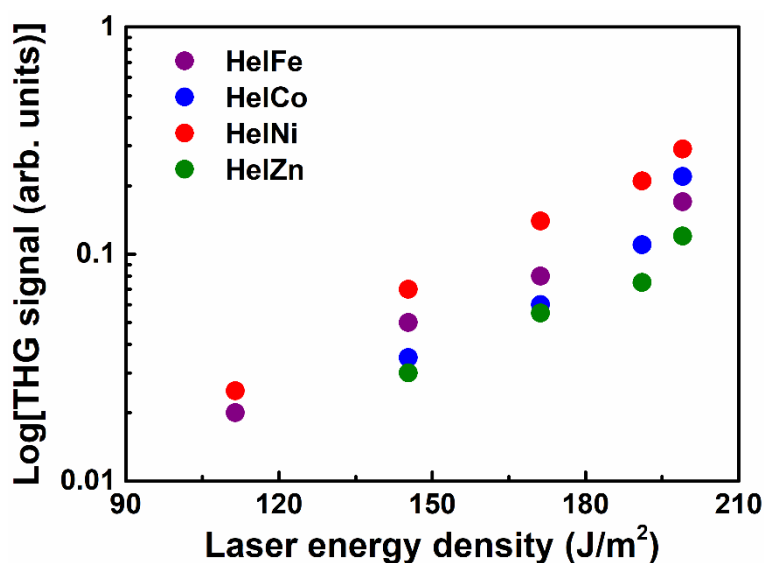


Figure 6.15: THG signal versus laser energy density of studied triple stranded helicate thin films.

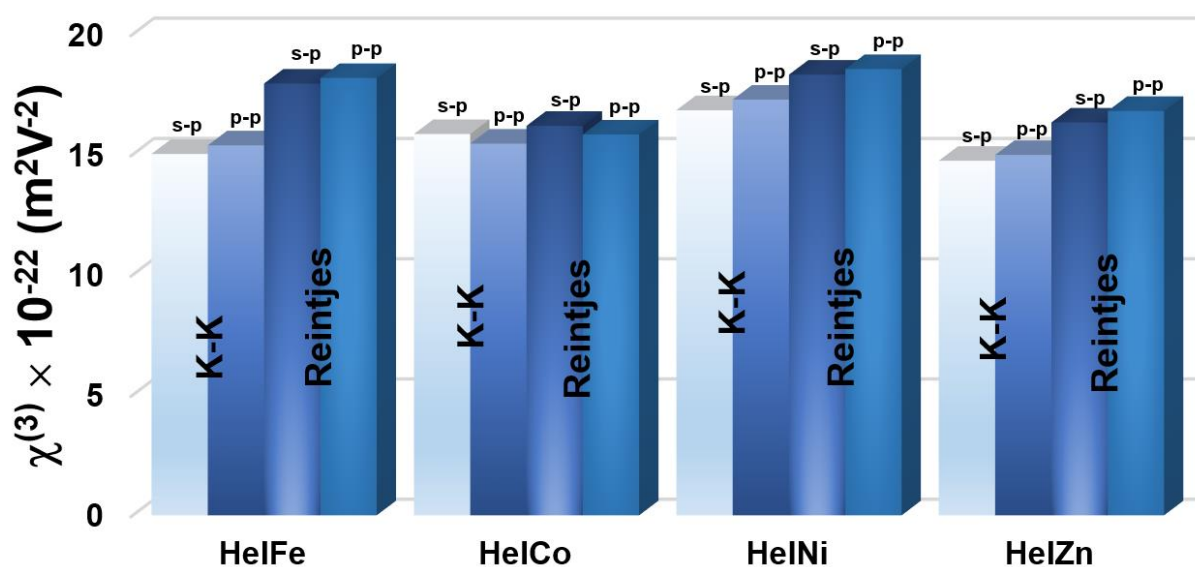


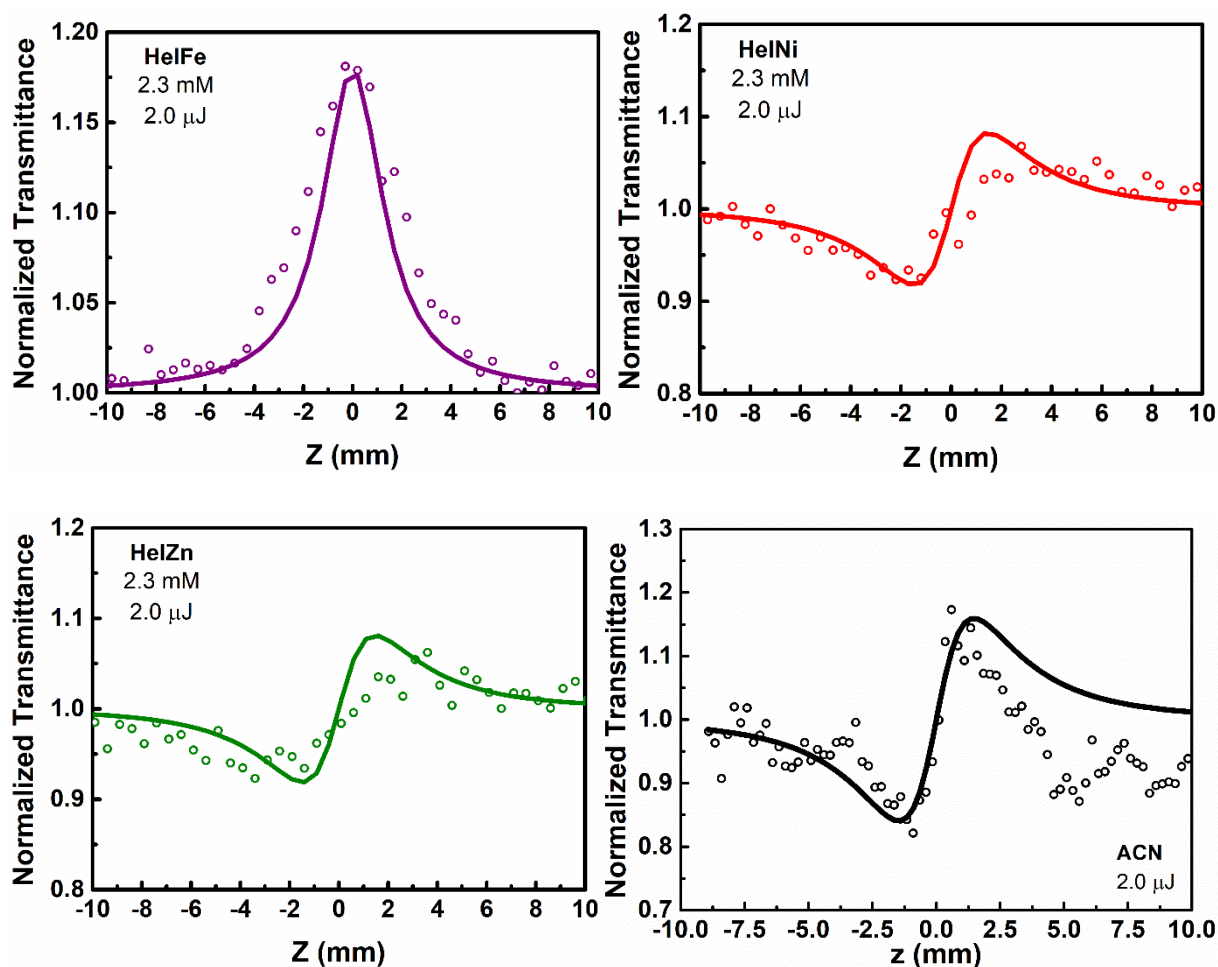
Figure 6.16: Histogram representing values of third-order nonlinear susceptibilities calculated via theoretical models.

## 6.6. Z-Scan Results

Analysis of nonlinear absorption and nonlinear refraction have been performed using Z-Scan experimental alignment shown in Fig. 4.9 in subsection 4.4. The triple stranded helicates were dissolved in acetonitrile forming solution with percentage concentration from 0.5% to 0.2%. However, due to the fact that in the following calculations the value of the molar concentration is needed, instead of the percentage, the following calculations were made, in which the percentage concentration corresponds to the molar concentration, i.e. 0.5% corresponds to 2.3 mM, 0.4% corresponds to 2.2 mM, 0.3% corresponds to 1.65 mM and 0.2% corresponds to 1.1 mM. The measurements were carried out for different laser energies from 0,5 to 2,0  $\mu\text{J}$ . Only the **HelFe** sample allowed for obtaining nonlinear absorption because it absorbs at 532 nm. Furthermore, **HelFe** sample showed no response in close aperture Z-scan. Achieved responses from OA and CA Z-scan are presented in Fig. 6.17. According to the fact that acetonitrile is characterized by quite high nonlinearity during the CA Z-scan measurement [6.6], its impact was taken into account in the calculations, where the third-order NLO susceptibility of the ACN is subtracted from the NLO susceptibility of the solution. From the data obtained during the measurement of nonlinear absorption for sample **HelFe**, the NLO absorption cross section  $\sigma$  was calculated, which determines the efficiency of a single molecule in the ground state to approach the excited state during the multiphoton absorption process, using the appropriate relation [6.7 – 6.8]:

$$\sigma = \frac{\hbar\omega\beta}{N_A\rho} \quad (6.1)$$

where:  $\hbar$  - Planck's constant,  $N_A$  - Avogadro's number,  $\rho$  - concentration of solution [mole per volume]. The calculation results are presented in Tab. 6.6.



**Figure 6.17:** CA Z-scan and OA Z-scan characteristics of ACN and triple stranded helicate complexes concentration 2.3 mM in ACN and laser energy 2.0 μJ.

Calculated values of  $n_2$  correspond to self-focusing behavior ( $n_2 > 0$ ). Triple stranded helicate **HelNi** is characterized by the highest total value of refractive index. Moreover, as previously mentioned, absorption coefficient  $\beta$  have been calculated only for **HelFe** complex from saturable absorption response ( $\beta < 0$ ), due to linear absorption properties at 532 nm. We have to take into account that  $\chi^{(3)}$  calculated from THG has only electronic contribution, as well as in Z-scan electronic and molecular. Besides, aforementioned, measurements were provided for different type of samples - in third harmonic generation experiments were carried out on thin films and in Z-scan technique we used liquid solutions. Furthermore, experiments were carried out in different laser



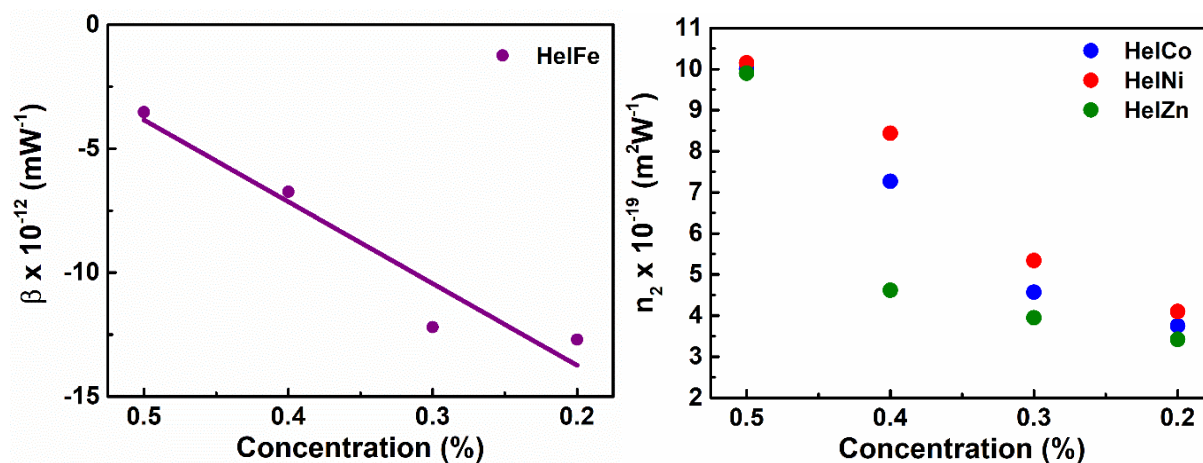
wavelength (1064 nm for THG and 532 nm for Z-scan). However, as in the case of THG studies, the parameters obtained using Z-scan proved to be the best for the **HelNi** sample, although they are not significantly different from the other helicates. The calculated values of the nonlinear refractive index and the nonlinear absorption coefficient are given in Tab. 6.6 is shown schematically with the graphs in Fig. 6.18.

**Table 6.6:** Calculated values of NLO refractive index  $n_2$ , NLO absorption coefficient  $\beta$ , NLO absorption cross section  $\sigma$ , real and imaginary part of third order NLO susceptibility  $\text{Re}(\chi^{(3)})$ ,  $\text{Im}(\chi^{(3)})$  of studied triple stranded helicates.

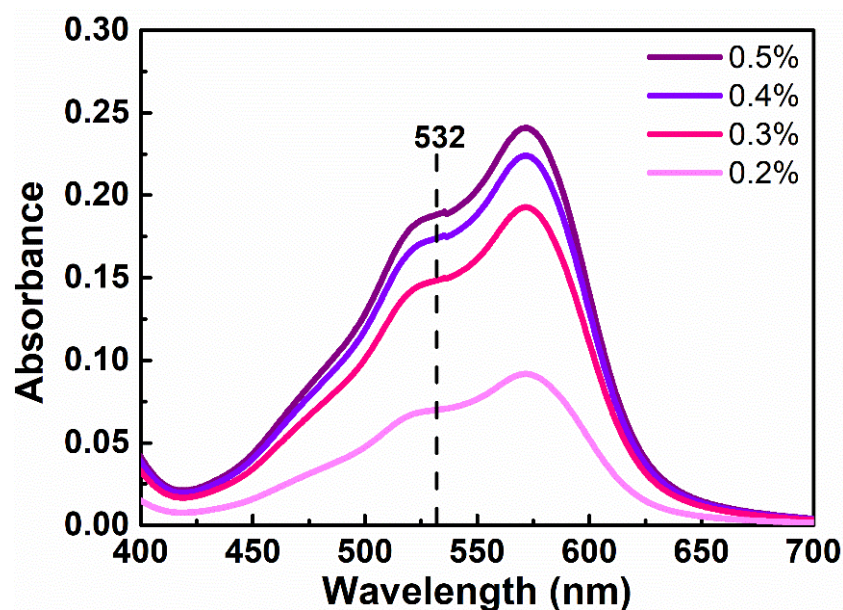
	$\rho$ [mM]	$n_2 \times 10^{-19}$ [m <sup>2</sup> W <sup>-1</sup> ]	$\beta \times 10^{-12}$ [mW <sup>-1</sup> ]	$\sigma \times 10^{-54}$ [m <sup>4</sup> s]	$\text{Re}(\chi^{(3)}) \times 10^{-21}$ [m <sup>2</sup> V <sup>-2</sup> ]	$\text{Im}(\chi^{(3)}) \times 10^{-21}$ [m <sup>2</sup> V <sup>-2</sup> ]
<b>HelFe</b>	2.3	-	-3.52	-0.95	-	-0.95
	2.2	-	-6.74	-1.89	-	-1.81
	1.65	-	-12.2	-4.58	-	-3.28
	1.1	-	-12.7	-7.15	-	-3.41
<b>HelCo</b>	2.3	10.0	-	-	6.35	-
	2.2	7.27	-	-	5.33	-
	1.65	4.57	-	-	3.35	-
	1.1	3.75	-	-	2.75	-
<b>HelNi</b>	2.3	10.15	-	-	6.45	-
	2.2	8.44	-	-	6.19	-
	1.65	5.34	-	-	3.92	-
	1.1	4.10	-	-	3.01	-
<b>HelZn</b>	2.3	9.9	-	-	6.29	-
	2.2	4.62	-	-	3.39	-
	1.65	3.95	-	-	2.98	-
	1.1	3.42	-	-	2.51	-

The UV-vis absorption of the studied **HelFe** solutions with different concentrations was measured. The results are shown in Fig. 6.19. However, this sample behaves similar to the **PtOEP** sample described in Chapter 5, which, as the linear absorbance decreases, increases its nonlinear response, which means that NLO response is saturated for above concentration 0.2%. It is difficult to determine the optimal value for linear absorbance at wavelength 532 nm for which NLO

absorption response would be the strongest and signal would be not saturated. It depends primarily on the structure of the studied compound, on the solvent used, as well as on the molar (percentage) concentration.



**Figure 6.18:** Values of nonlinear refractive index (left) and nonlinear absorption coefficient (right) as a function of solution concentration of triple stranded helicates in acetonitrile ACN.



**Figure 6.19:** Absorption spectra of 0.5%, 0.4%, 0.3% and 0.2% solutions of **HelFe** in acetonitrile ACN with the marked wavelength of the laser light source (532 nm).

Moreover, the value of the third-order nonlinear susceptibility composed of the real and the imaginary parts was calculated. The results for individual samples and their concentrations are presented in Tab. 6.7. The results were also compared with the THG values obtained experimentally. However, it should be taken into account that both experiments were not carried out under the same conditions, i.e. a different laser wavelength was used, as well as a different method (thin layer and solution). However, it can be seen that, as in the case of THG, the highest values were obtained for the **HelNi** sample.

**Table 6.7:** Calculated values of NLO susceptibility  $\chi^{(3)}$  obtained from Z-scan data, compared with THG results of studied triple stranded helicates.

			<b>HelFe</b>	<b>HelCo</b>	<b>HelNi</b>	<b>HelZn</b>
$\chi^{(3)} \times 10^{-21}$ [m <sup>2</sup> V <sup>-2</sup> ]	<b>Z-scan</b>	<b>0.5 %</b>	0.95	6.35	6.45	6.29
		<b>0.4 %</b>	1.81	5.33	6.19	3.39
		<b>0.3 %</b>	3.28	3.35	3.92	2.98
		<b>0.2 %</b>	3.41	2.75	3.01	2.51
	<b>THG</b>			1.54	1.54	1.73

## 6.7. Quantum Chemical Calculations

The initial geometrical parameters of the metallohelicates were obtained from Single Crystal X-ray Diffraction refinement data [6.9]. The optimization of the molecular geometries leading to energy minima was achieved by using density functional dispersion-corrected DFT-D3 theory calculations using B3LYP/6-31+G(d,p) basis set and the UV-vis absorption spectra were computed applying b3lyp/6-31++g(d,p) methodology without dispersion-correction implemented in the GAUSSIAN 09 program package [6.10] in C1 symmetry. The geometry optimization was performed in gas-phase. Though density functional theory (DFT) is good enough for systems more than 200 atoms, standard semilocal (hybrid) density functional approximations do not describe well the London dispersion energy which is essential for accurate predictions of inter- and intramolecular

noncovalent interactions. Therefore dispersion-corrected DFT provides a unique tool for the analysis of complex aromatic systems [6.11]. The modelled structures were used to calculate HOMO-LUMO energies, frequency-dependent first and second hyperpolarizabilities. It should be mentioned that the empirical dispersion correction mainly affects the geometry of the molecule but is not effective for the other calculated parameters. The frequency-dependent  $\beta(-2\omega, \omega, \omega)$  and  $\gamma(-3\omega, \omega, \omega, \omega)$  parameters at considered  $\omega = 0.04282$  a.u. ( $\lambda = 1064$  nm wavelength) were calculated using GAMESS [6.12] program by B3LYP/lanl2DZ basis set. Analyzing the values of the position of the absorption maximum  $\lambda_{\max}$  calculated theoretically and determined experimentally presented in Tab. 6.8, one can notice a bathochromic shift of the experimental spectra in relation to the theoretical ones. Which may be related to both the calculation method and the fact that the experimental spectra were made in the solid phase.

**Table 6.8:** The computed quantum chemical parameters including: HOMO, LUMO, energy gap ( $E_g$ )<sub>HOMO-LUMO</sub>, UV-VIS absorption peak position spectra computed applying b3lyp/6-31++g(d,p) methodology and measured for of studied thin films.

	HOMO [eV]	LUMO [eV]	( $E_g$ ) <sub>HOMO-LUMO</sub> [eV]	$\lambda_{\text{abs exp}}$ [nm]	$\lambda_{\text{abs th}}$ [nm]
HelFe	-3.50	-2.18	1.32	331, 531, 577	272
HelCo	-2.82	-2.57	0.25	327	-
HelNi	-3.12	-1.71	1.41	328	280
HelZn	-4.96	-1.02	3.94	348	278

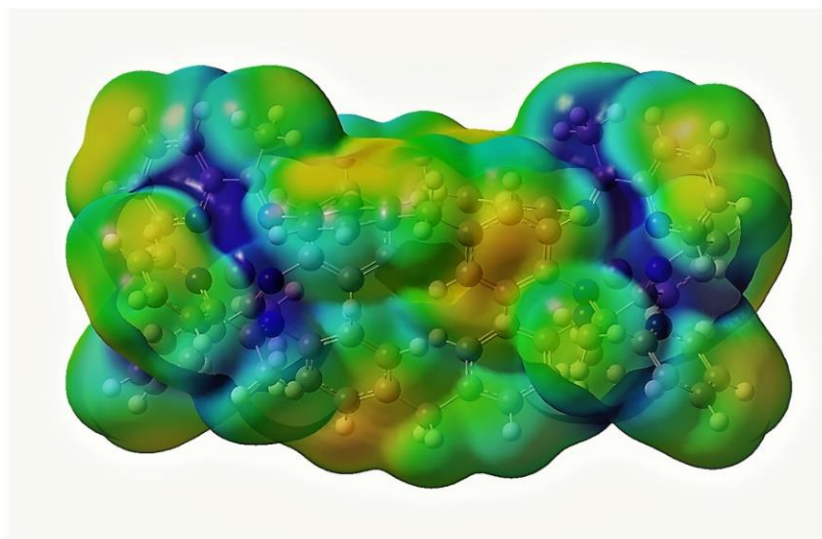
The highest occupied molecular orbital (HOMO) and lowest unoccupied molecular orbital (LUMO) are validity parameters to study the specific movements of electron transfer in molecules (see Tab. 6.8). The HOMO-LUMO gaps of **HelFe**, **HelCo** and **HelNi** are significantly smaller than the energy gap value for **HelZn**. A small energy gap suggested that these molecules are relatively more reactive and less stable than **HelZn**. The connection between the electric dipole moments of an organic molecule having donor – acceptor substituent and first order

hyperpolarizability is also very important. In the present case, the dipole moments,  $\mu$  (expressed in Debye units) for investigated complexes are very small which is due to the geometry of the molecule. The obtained results, both experimental and theoretical, suggest quite a good second-order nonlinear response (Tab. 6.10). All atoms and molecules (except S-state atoms) have one or more not disappearing permanent multipole moments. In the case of microcircuits with octahedral symmetry, there is a need to define higher-order multipoles and a hexadecapole system, the moment of which is determined by the fourth-rank tensor. The Tab. 6.9 shows the diagonal components of multipole moments for the tested molecules. With the high octahedral symmetry all other, except hexadecapole moment, multipole moments should be zero. In this case the also quadrupole moments- second rank tensor (determined by the charge distribution (see Fig. 6.20) have high values for all molecules and can play a crucial role in the obtained high hyperpolarizabilities. The Fig. 6.20 shows the charge distribution for **HelZn** resulting from the natural electrical properties of the system from which we can notice a positive and negative regions of the potential. The positive charges lie closer to the metal cationic center (blue region) the potential becomes positive in this region and their influence on the potential is greater while negative charges (orange region) is located at the ends and in the center of the molecule.

It is known that even in symmetrical systems, the process of polarization occurs under the influence of an external electric field, which gives rise to induced dipoles or dipoles of higher order. In the first approximation, the induced dipole moment  $D^{\text{ind}}$  is proportional to the external electric field  $E$ . In our case molecules have an asymmetric charge distribution and then the components of the dipole moment induced in different directions are different. The total moment induced in the system by the  $E$  field is the sum of the linear  $D^L$  moment and the non-linear moments  $D^{\text{NL}}$ .

$$D_i^{\text{ind}} = D_i^L + D_i^{\text{NL}} \quad (6.2)$$

Where:  $D_i^N = \alpha_{ij}\vec{E}_j$ ,  $D_i^{NL} = \frac{1}{2}\beta_{ijk}\vec{E}_j\vec{E}_k + \frac{1}{6}\gamma_{ijkl}\vec{E}_j\vec{E}_k\vec{E}_l$ ,  $\alpha_{ij}$  linear polarizability,  $\beta_{ijk}$ ,  $\gamma_{ijkl}$  hyperpolarizabilities.



**Figure 6.20:** Electrostatic charge distribution for **HelZn** - *positive* (blue) and *negative* (orange) regions. (b3lyp/6-31++g(d,p)).

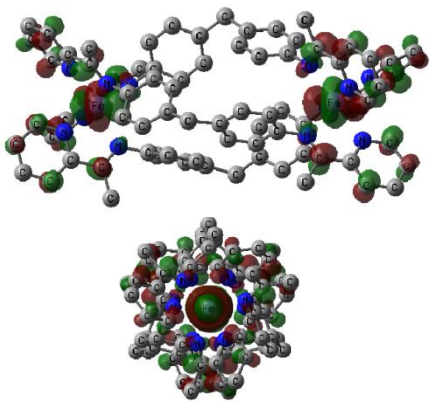
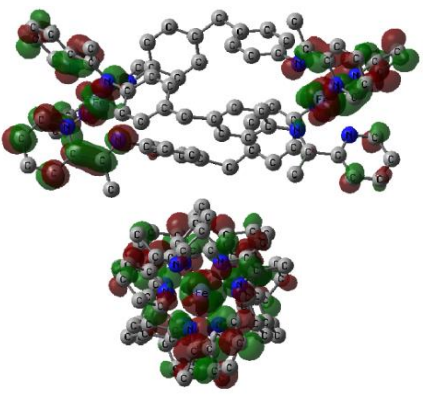
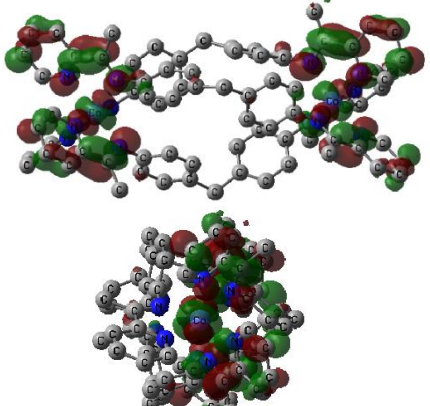
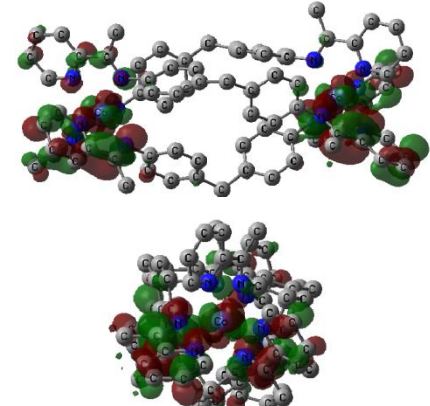
**Table 6.9:** The computed several components of multipole moment (b3lyp/6-31++g(d,p))

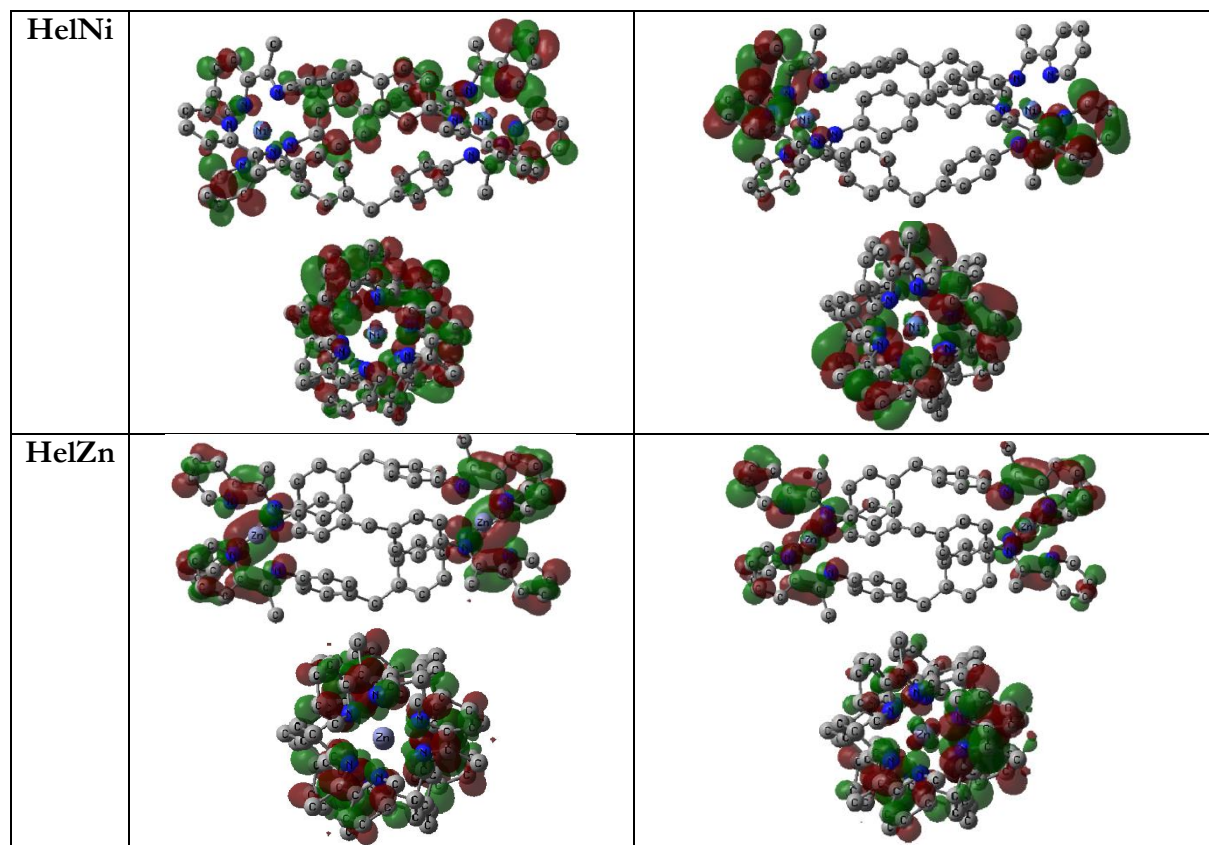
**HelFe, HelNi, HelZn, HelCo.**

	Dipole moment [D]	Quadrupole moment [ $D \cdot A^2$ ]	Octapole moment [ $D \cdot A^3$ ]	Hexadecapole moment [ $D \cdot A^4$ ]
HelFe	X=-0.0018 Y=0.0015 Z=-0.0015	XX= 385.2520 YY= -372.7489 ZZ= -372.7515	XXX=-0.2499 YYY=-64.3741 ZZZ=-48.0822	XXXX=-38918.5639 YYYY=-14408.8966 ZZZZ=-14406.8236
HelNi	X= 0.0010 Y= 0.0007 Z= -0.0005	XX= 395.2342 YY= 369.9974 ZZ= -370.0073	XXX= 0.1302 YYY= -37.8839 ZZZ= 99.7292	XXXX=-38367.2839 YYYY=-14643.4441 ZZZZ=-14642.8189
HelCo	X= -0.0626 Y= 0.1127 Z= -0.3155	XX= 374.4975 YY=-424.3843 ZZ=-426.5068	XXX= -3.6572 YYY=-86.5759 ZZZ= -35.5395	XXXX=45707.3996 YYYY=-15038.9663 ZZZZ=-15080.8357
HelZn	X= 0.0011 Y= 0.0002 Z= -0.0004	XX= 394.2931 YY= -369.7264 ZZ=-369.7332	XXX=0.1446 YYY=-103.6304 ZZZ=-44.5298	XXXX=-38363.2180 YYYY=-14593.7580 ZZZZ=-14592.9995

In this case the origin of second-order nonlinear optical properties comes from induced non-centrosymmetry in the charge density distribution. Tab. 6.10 shows the visualized structures of **HelFe**, **HelCo**, **HelNi**, **HelZn** compounds and depicts the intramolecular transfer of electron density. The maps clearly indicate interligand  $\pi \rightarrow \pi^*$  transmetallic charge-transfer (TTCT). The metal cation moiety has a donor nature and mostly there the HOMO orbital is located. Therefore we can observe the shift of electronic clouds from metal towards the iminopyridine fragment for all the investigated compounds. The first molecular hyperpolarizability  $\beta$  depends not only on the strength of the donor and acceptor groups but also on the nature of the  $\pi$ -conjugated spacer connecting these two groups [6.13].

**Table 6.10:** Frontier molecular orbitals of **HelFe**, **HelCo**, **HelNi**, **HelZn**, calculated at DFT/B3LYP/6-31G+(d,p) basis set level.

	HOMO	LUMO
<b>HelFe</b>		
<b>HelCo</b>		



**Table 6.11:** Frequency-dependent:  $\beta_{\text{tot}}(-2\omega;\omega,\omega)$  and  $\gamma_{\text{tot}}(-3\omega;\omega,\omega,\omega)$  values at  $\omega = 0.042827$  a.u.,  $\lambda = 1064$  nm, for **HelFe**, **HelZn**, B3LYP/lanl2DZ and comparison with experimental data

$\chi^{(2)}$  and  $\chi^{(3)}$ .

	$\beta_{\text{tot}} \times 10^{-30}$ esu	$\chi_{\text{exp}}^{(2)}$ , pmV <sup>-1</sup>	$\gamma_{\text{tot}} \times 10^{-36}$ esu	$\chi_{\text{exp}}^{(3)}$ , $\times 10^{-22}$ m <sup>2</sup> V <sup>-2</sup>
<b>HelFe</b>	210.078	0.444	-24167.288	15.38
<b>HelZn</b>	276.785	0.449	-3855.040	14.98

The obtained  $\beta$  values for molecules: **HelFe** and **HelZn** have the same order values. A slightly higher value was obtained for **HelZn** ( $\beta(-2\omega;\omega,\omega) = 276.785 \times 10^{-30}$  esu) molecule comparing to **HelFe** ( $\beta(-2\omega;\omega,\omega) = 210.078 \times 10^{-30}$  esu). Urea molecule is the most used reference material for comparison of second order nonlinear optical (NLO) properties of molecular systems. One can observe that the value of first hyperpolarizability  $\beta$  obtained for compound **HelZn** is four orders



higher than the one for urea (static first hyperpolarizability for urea molecule  $\beta(-2\omega;\omega,\omega) = 30.90 \times 10^{-32}$  esu) [6.14]. We can easily find a correlation between the parameters characterizing the electronic properties presented in Tab. 6.8 – 6.9 and the obtained second order hyperpolarizabilities (see Tab. 6.11).

As mentioned earlier, the HOMO-LUMO energy gap for **HelFe** is smallest than for **HelZn** hence the highest value of the second-order hyperpolarizability for **HelFe** is obtained. Decreasing the value of the energy gap increases the charge transfer within the molecule. As you can see from the Tab. 6.11 the second order hyperpolarizability of compound **HelFe** ( $\gamma=24167.288 \times 10^{-36}$  esu) is one order higher than for **HelZn** ( $\gamma=3855.040 \times 10^{-36}$  esu). We also compared our hyperpolarizabilities  $\gamma$  values with reported by Leupacher et al. [6.15] of methylene blue ( $\gamma=32.00 \times 10^{-36}$  esu) employing THG measurements and the value of  $\gamma$  for **HelFe** is three order higher. It should be noted that the determined theoretical values of  $\beta$  and  $\gamma$  are significantly higher than the values of NLO susceptibilities calculated from the experimental data. It should be taken into account that the experiment was carried out on thin layers with only 10 wt% of the studied material in relation to the polymer matrix. Moreover, guest-host systems has the disadvantage that losses of NLO response occur and are strongly dependent on the concentration of the material relative to the polymer.

## 6.8. Conclusions

Triple stranded helicates: **HelFe**, **HelCo**, **HelNi** and **HelZn** were synthesized and their corresponding thin films were prepared successfully using well-known spin-coating technique. AFM analysis have shown that the obtained thin films are relatively smooth and homogeneous, as demonstrated by the studies of the surface roughness. UV-Visible absorption spectra of the studied complexes showed that their absorption has a large impact on the NLO response. Moreover, in

spectroscopic studies ultraviolet emission was observed from photoluminescence studies, and the luminescence decay time is relatively fast, indicating fluorescence like emission. NLO response of the studied metallo-supramolecular triple stranded helicates have been performed using SHG and THG Maker fringe method and Z-scan technique. The highest quadratic and cubic nonlinear optical susceptibilities have been found for helicate containing nickel metal cations **HelNi**, even if these values for the other samples are not significantly different from each other. For Z-scan studies, only the **HelFe** complex exhibit nonlinear absorption, however, the NLO refraction for this sample has not been obtained. Finally, the highest value of NLO refractive index have been found for complex **HelNi**, which is consistent with THG results. The theoretically evaluated energy gap of the compounds showing the high rate of electron transfer from the ground to the excited state. However, a significant reduction in the energy gap in the molecule investigated compounds causes a large increase in third-order nonlinear properties. The interligand  $\pi \rightarrow \pi^*$  transmetallic charge-transfer (TTCT) supports noncentrosymmetric charge density distribution resulting in the molecules possessing second order NLO properties. The NLO properties obtained for the metallo-supramolecular triple stranded helicates, indicate that these assemblies can be promising candidates to be used in photonics and nonlinear optical devices applications. Moreover, the experimental results achieved in this work show the proof of using metallosupramolecules in nonlinear optics, with cooperative effect in metals in centers. However, no significant difference between a nonlinear response for metals from the same period was observed which indicate future perspectives, where modification of nature of metallosupramolecular assemblies will be interesting for NLO studies.

## Literature

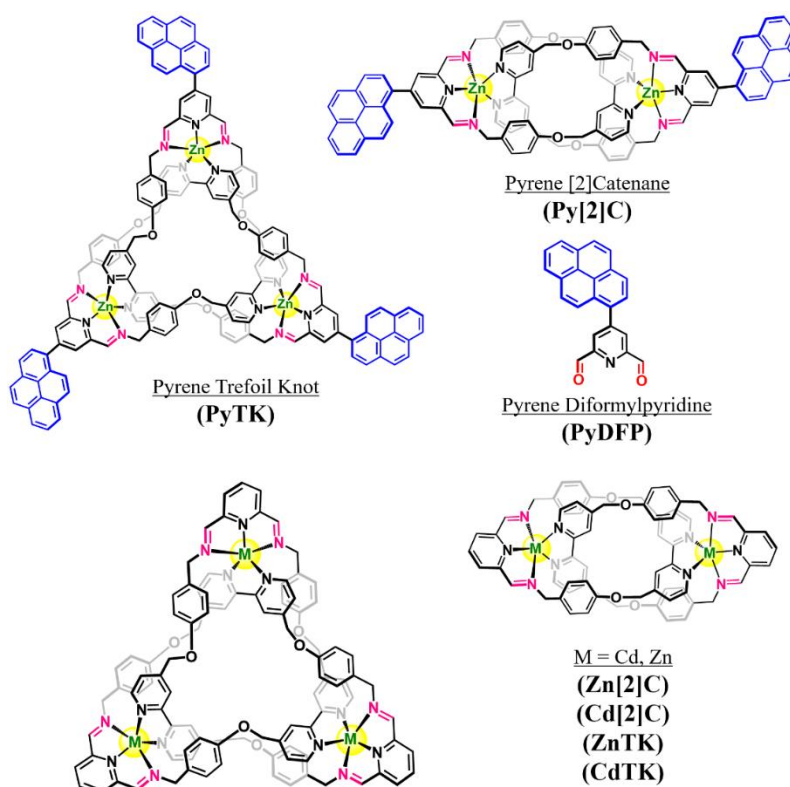
- [6.1] K. Waszkowska, Y. Cheret, A. Zawadzka, A. Korcala, J. Strzelecki, A. El-Ghayoury, A. Migalska-Zalas, B. Sahraoui. Photoluminescence and nonlinear optical properties of triple stranded helicates based metallo-supramolecular architectures. *Dyes and Pigments*, 186 (2021) 109036.
- [6.2] N. G. White, A Rapid and Straightforward Supramolecular Self-Assembly Experiment To Prepare and Characterize a Triple Helicate Complex, *Journal of Chemical Education* 2018 95 (4), 648-651
- [6.3] S. K. Vellas, J. E. M. Lewis, M. Shankar, A. Sagatova, J. D. A. Tyndall, B. C. Monk, C. M. Fitchett, L. R. Hanton, J. D. Crowley, [Fe<sub>2</sub>L<sub>3</sub>]<sup>4+</sup> Cylinders Derived from Bis(bidentate) 2-Pyridyl-1,2,3-triazole “Click” Ligands: Synthesis, Structures and Exploration of Biological Activity, *Molecules* 2013, 18, 6383-6407
- [6.4] S. E. Howson, L. E. N. Allan, N. P. Chmel, G. J. Clarkson, R. van Gorkum, P. Scott, Self-assembling optically pure Fe(A–B)<sub>3</sub> chelates, *Chem. Commun.*, 13, 2009, 1727–1729
- [6.5] A. Zawadzka, P. Plóciennik, A. Korcala, P. Szroeder, Optical properties of chiral single-walled carbon nanotubes thin films, *Opt, Mater.* vol 96 (2019) 109295
- [6.6] K. Iliopoulos, D. Potamianos, E. Kakkava, P. Aloukos, I. Orfanos, and S. Couris. Ultrafast third order nonlinearities of organic solvents. *Optics Express* Vol. 23, Issue 19, pp. 24171-24176, 2015.
- [6.7] A. Ajami, W. Husinsky, R. Liska, N. Pucher, Two-photon absorption cross section measurements of various two-photon initiators for ultrashort laser radiation applying the Z-scan technique, *Journal of the Optical Society of America B* Vol. 27, Issue 11, pp. 2290-2297 (2010)

- [6.8] J. Szeremeta, R. Kolkowski, M. Nyk, M. Samoc, Wavelength Dependence of the Complex Third-Order Nonlinear Optical Susceptibility of Poly(3-hexylthiophene) Studied by Femtosecond Z-Scan in Solution and Thin Film, *J. Phys. Chem. C* 2013, 117, 49, 26197–26203
- [6.9] Guo Dong, Pang Ke-liang, Duan Chun-ying, He Cheng, and Meng Qing-jin, Design and Crystal Structures of Triple Helicates with Crystallographic Idealized D<sub>3</sub> Symmetry: The Role of Side Chain Effect on Crystal Packing, *Inorganic Chemistry* 2002 41 (23), 5978-5985 DOI: 10.1021/ic0203623
- [6.10] Gaussian 09, Revision D.01, Gaussian, Inc., Wallingford CT, 2009
- [6.11] J. Moellmann and S. Grimme, Dispersion-Corrected Density Functional Theory for Aromatic Interactions in Complex Systems, *Acc. Chem. Res.* 46, 4, 916–926, 2013.
- [6.12] M. S. Gordon, M.W. Schmidt, Advances in electronic structure theory: GAMESS a Decade Later, C. E. Dykstra, G. Frenking, K.S. Kim, G.E. Scuseria, (eds.), in: *Theory and Applications of Computational Chemistry: the first forty years*, Elsevier, Amsterdam, 2005, 1167-1189.
- [6.13] F. Kajzar, Y. Okada-Shudo, C. Meritt and Z. Kafafi, Second- and third-order non-linear optical properties of multi-layered structures and composites of C<sub>60</sub> with electron donors, *Synth. Met.*, 117 (2001) 189-193.
- [6.14] M. Ferrero, Bartolomeo Civalleri, M. Rérat, R. Orlando, R. Dovesi, The calculation of the static first and second susceptibilities of crystalline urea: A comparison of Hartree–Fock and density functional theory results obtained with the periodic coupled perturbed Hartree–Fock/Kohn–Sham scheme “, *J. Chem. Phys.* 131 (2009) 214704).
- [6.15] W. Leupacher and A. Penzkofer, “Third-Order Nonlinear Susceptibilities of Dye Solutions Determined by Third-Harmonic Generation”, *Appl. Phys. B* 36, 25-31, 1985.

## CHAPTER 7: MODIFIED PYRENE-BASED COMPLEXES

This work is devoted to the study of the nonlinear optical properties of the new modified pyrene-based complexes. The motivation in this work are nonlinear optical studies on topologically nontrivial structures, metal-driven supramolecular architectures. This monograph compares the nonlinear responses of the two types of pyrene-based complexes, as well as the influence of the metal substituent on the nonlinear effect. The nonlinear effects in this chapter include second harmonic generation (SHG), third harmonic generation (THG), and nonlinear refraction by Z-scan method.

### 7.1. Sample Preparation



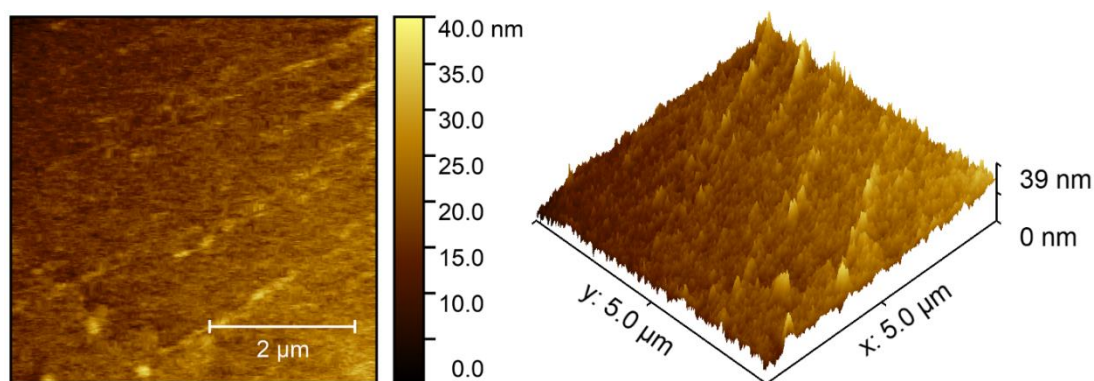
**Figure 7.1:** Chemical structures of **PyTK**, **Py[2]C** and **PyDFP**. The sixth coordination of each zinc metal ion in **PyTK** and **Py[2]C** is completed by a TFA or acetate anion, respectively, however TFA and acetate anions are omitted in the structures.

This work investigated the nonlinear optical properties of pyrene-containing compounds: pyrene trefoil knot (**PyTK**), containing zinc (**ZnTK**) and cadmium (**CdTK**), pyrene diformylpyridine (**PyDFP**), pyrene [2]catenane (**Py[2]C**), containing zinc (**Zn[2]C**) and cadmium (**Cd[2]C**) (Fig. 7.1), whose synthesis as well as physicochemical, crystallographic properties and computational modeling are described in [7.1 - 7.4], and were synthesized in collaboration with University of Strasbourg and New York University in Abu Dhabi. DFP (diformylpyridine) is characterized by starting material as one of the building ligands of TK and [2]C supramolecular complexes, which is then combined with DAB (diaminopyridine) and with  $Zn(OAc)_2$  (zinc acetate). The [2]catenane and trefoil knot in a single pot are then formed as a result of the self-assembly process. [2]catenane is characterized by the fact that it is composed of two identical macrocycles linked together by two zinc ions  $Zn(II)$ , and is also composed of one DFP and one DAB. On the other hand, trefoil knot is characterized by the fact that it is one structure composed of three crossings, and moreover is chiral. In addition to the above-mentioned physicochemical and crystallographic properties, [2]catenane and trefoil knot compounds have been studied for their applications in medicine, for example in pharmaceutical development in the diagnosis and treatment of cancer [7.5]. The following sections describe the studies of nonlinear optical effects carried out on these supramolecular complexes. A total of 7 samples were collected and dissolved with 50 mg of poly(methyl methacrylate) (PMMA) with average  $M_w \sim 120,000$  by GPC (Sigma-Aldrich) in dimethyl sulfoxide (DMSO) forming 10% wt guest-host solution of complex to the polymer. Subsequently, the solutions were applied to previously isopropanol vapor-cleaned glass substrates and thin layers were deposited in a vacuum-free spin-coater (Ossila) at 2000 rpm.

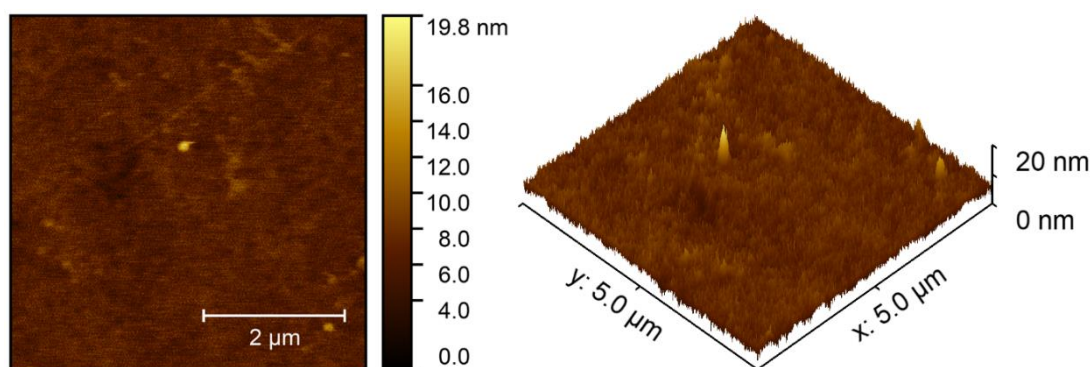
## 7.2. Surface Characterization

Thin layer thicknesses of modified pyrene-based complexes were measured using a profilometer (Dektak 6M) and their values are presented in Tab. 7.1. The films are statistically thin, between

200 nm and 400 nm, and the thickness is not drastically different between each other. Moreover, Tab. 7.1 includes the values of the linear refractive index and the extinction coefficient for the wavelengths corresponding to the wavelength of the pumping laser (1064 nm), generation of the second harmonic (532 nm) and generation of the third harmonic (355 nm), determined by means of an ellipsometric experiment. Typical (2D and 3D) AFM images analyzed by Gwyddion software are presented in Figs. 7.2 - 7.8 in the range  $5 \mu\text{m} \times 5 \mu\text{m}$ . It was observed that films are quite typically homogenous, although some surface irregularities are noticeable. The surface roughness was then measured and calculated and added to Tab. 7.1. In NLO studies is important that the sample is transparent, has no defects and is homogenous. The studied thin films of the modified pyrene-based supramolecular complexes have good quality for optical measurements, due to their low average roughness and smoothness.



**Figure 7.2:** Atomic force microscopy (AFM) images of studied **PyDFP** thin film.



**Figure 7.3:** Atomic force microscopy (AFM) images of studied **PyTK** thin film.

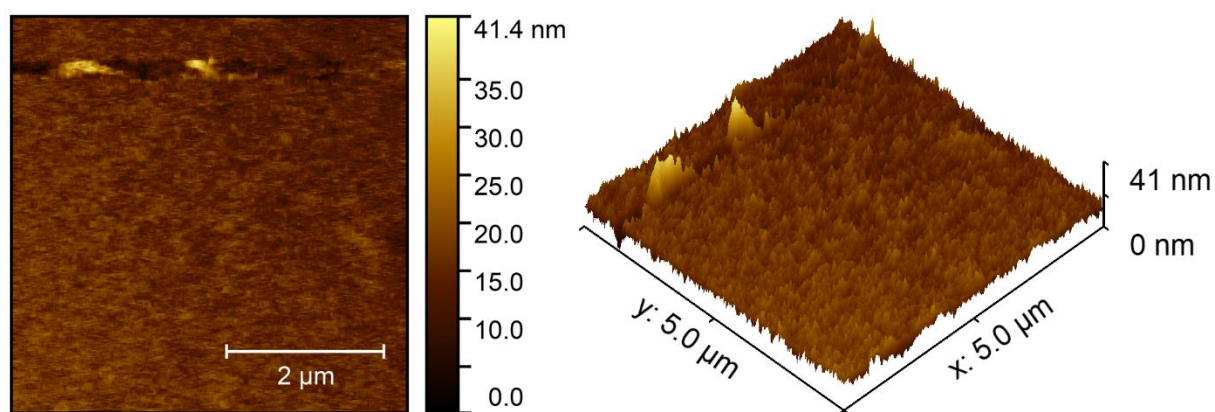


Figure 7.4: Atomic force microscopy (AFM) images of studied **ZnTK** thin film.

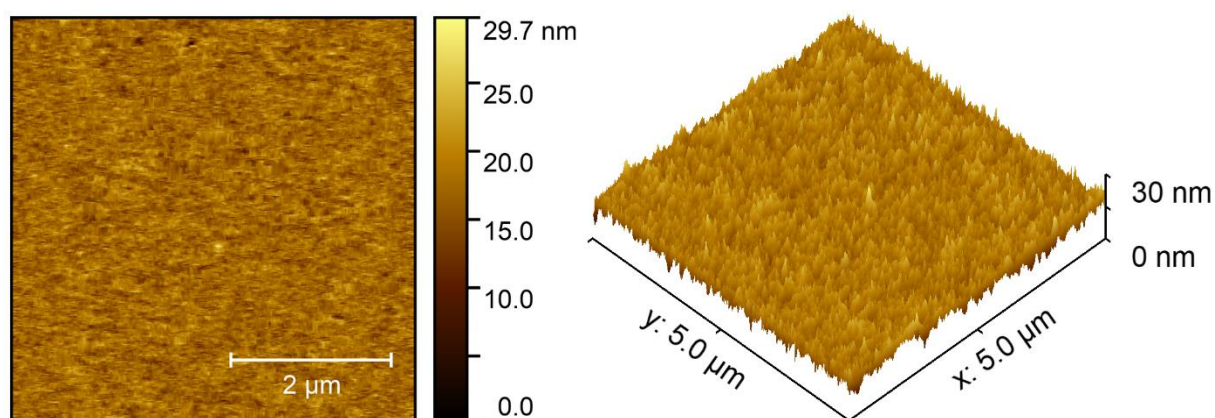


Figure 7.5: Atomic force microscopy (AFM) images of studied **CdTK** thin film.

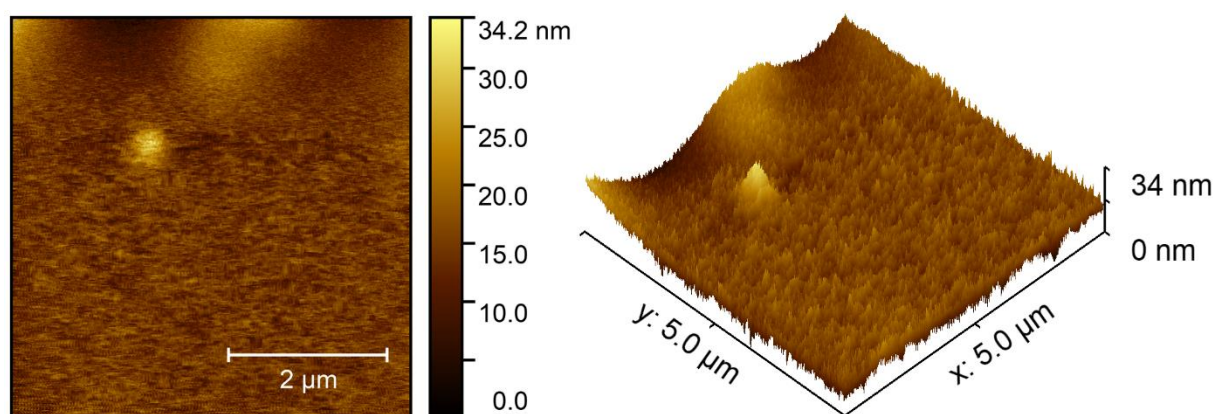
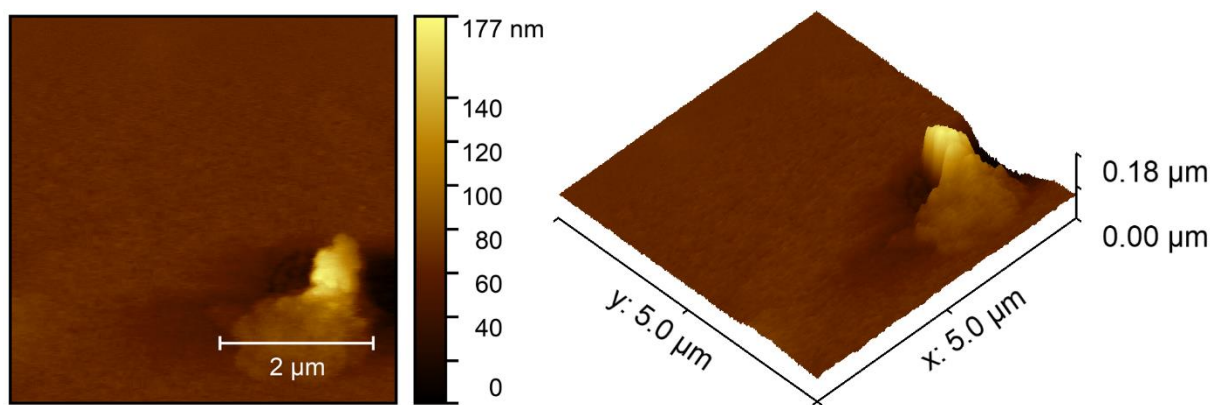
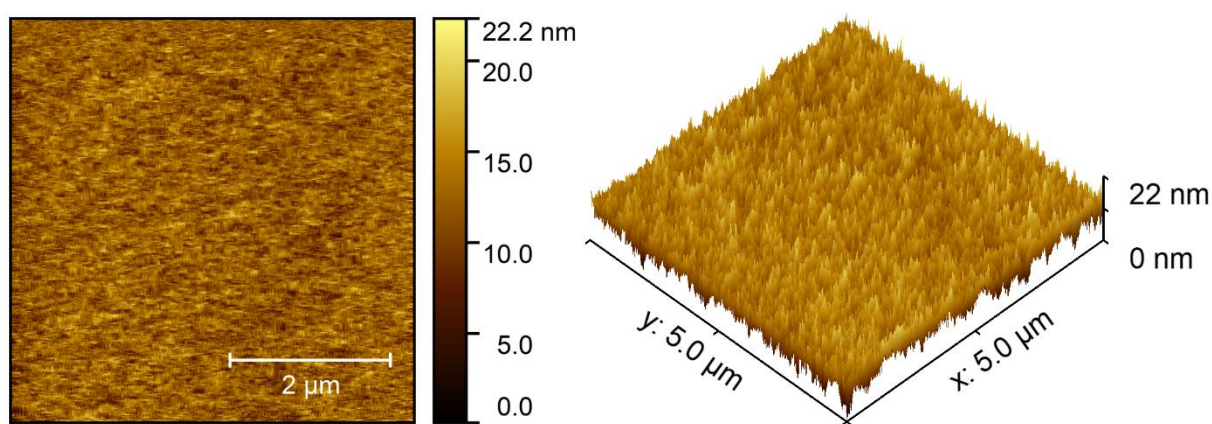


Figure 7.6: Atomic force microscopy (AFM) images of studied **Py[2]C** thin film.





**Figure 7.7:** Atomic force microscopy (AFM) images of studied **Zn[2]C** thin film.



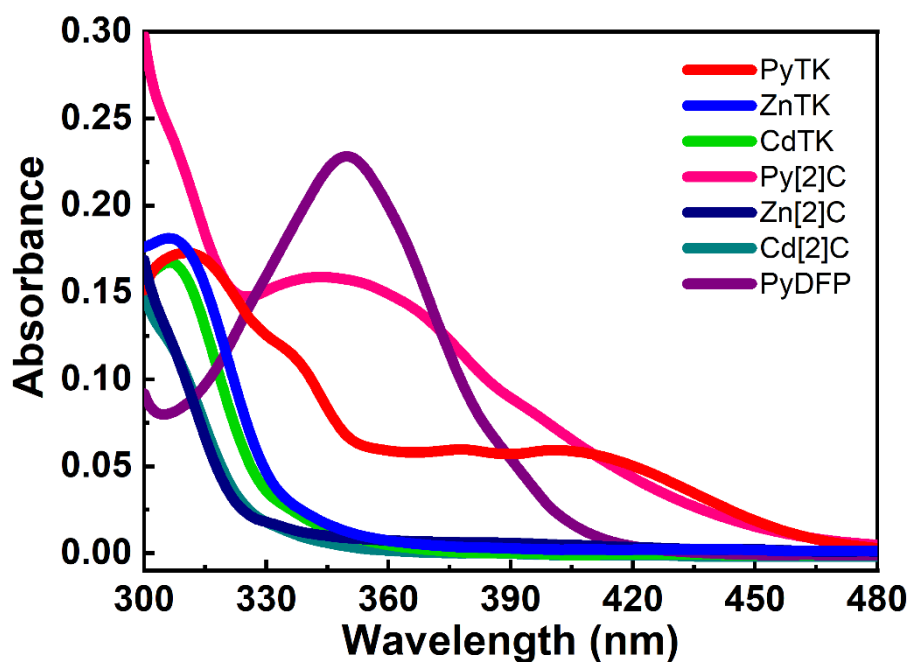
**Figure 7.8:** Atomic force microscopy (AFM) images of studied **Cd[2]C** thin film.

**Table 7.1:** Thickness ( $d$ ), roughness ( $R_A$ ), linear refractive index values ( $n$ ) and extinction coefficients ( $\kappa$ ) of modified pyrene-based guest-host thin films.

	$d$ [nm]	$R_A$ [nm]	$n_{1064}$	$n_{532}$	$n_{355}$	$\kappa_{1064}$	$\kappa_{532}$	$\kappa_{355}$
<b>PyDFP</b>	365	1.270	1.512	1.533	1.555	0.009	0.004	0.003
<b>PyTK</b>	330	0.667	1.505	1.511	1.518	0.041	0.011	0.005
<b>ZnTK</b>	290	1.267	1.490	1.508	1.456	0.004	0.026	0.067
<b>CdTK</b>	380	1.204	1.492	1.510	1.525	0.007	0.002	0.001
<b>Py[2]C</b>	215	1.175	1.484	1.514	1.561	0.001	0.004	0.014
<b>Zn[2]C</b>	300	1.266	1.495	1.505	1.488	0.001	0.005	0.028
<b>Cd[2]C</b>	320	1.209	1.516	1.504	1.572	0.007	0.005	0.002

### 7.3. Spectroscopic Studies

Spectroscopic studies of thin films of pyrene-based complexes were performed on the spectrometer in the range 1100-300 nm and the results are shown in Fig. 7.9. Due to the fact that the samples have a very high molar mass, and the concentration of the solutions from which the thin films were deposited is not too large, due to the limitations of the material possessed, the optical absorption is not intense. In general, these modified pyrene-based complexes are characterized by strong intramolecular metal-ligand  $\pi$ - $\pi$  stacking in modular systems [7.1] which correspond to the absorption peaks in Fig. 7.9. It can also be noticed that the samples above 500 nm are completely optically transparent, which means that for the wavelength of 1064 nm corresponding to the wavelength of the laser light source, during the measurement of the generation of the second and third harmonics, no absorption occurs, as well as the generated SHG with a wavelength of 532 nm is not simultaneously absorbed. In general, due to the fact that the probability of multi-photon processes, in this case of two-photon absorption (TPA), is many orders of magnitude smaller than that of single-photon processes, when measuring the Z-scan with excitation 532 nm, simultaneous absorption of two photons may be unlikely. In addition, TPA is also influenced by the intensity of the laser beam and the aforementioned concentration. It can also be seen from Fig. 7.9 that the absorption peaks are in the shorter wavelength direction, and their values are given in Tab. 7.2. In the case of **Zn[2]C** and **Cd[2]C**, the maximum absorption peaks are probably below 300 nm, however due to the very strong absorption of the glass substrate below this wavelength, the signal was not recorded. Moreover, it was observed that in the case of third harmonic generation (THG), the absorption is not negligible, which means that it has an influence on the size of the THG effect, as a reason of the signal generated is absorbed to some extent. Therefore, for this wavelength of 355 nm, the linear absorption coefficients  $\alpha$  were determined, and their values are given in Tab. 7.2.



**Figure 7.9:** UV-Vis absorption spectra of investigated modified pyrene-based guest-host thin films.

**Table 7.2:** Coefficients determined from absorption spectra of modified pyrene-based guest-host thin films.

Sample	$\lambda_{\text{abs}}$ [nm]	$\alpha_{355}$ [ $10^3 \text{ cm}^{-1}$ ]
PyDFP	360	13.95
PyTK	310; 403	4.30
ZnTK	308	0.74
CdTK	307	0.43
Py[2]C	301; 340	16.70
Zn[2]C	301	0.61
Cd[2]C	301	0.17

Photoluminescence spectra of the investigated modified pyrene-based thin films are shown in Figs. 7.10. - 7.16. Basically, the **PyDFP** sample, which acts as a ligand, emits very intense light in the blue wavelength, while the pyrene trefoil knot **PyTK** and pyrene[2]catenane **Py[2]C** are characterized by the emission spectrum shifted towards longer wavelengths, emitting very intense

green light visible by the naked eye. Moreover, samples containing metals of zinc and cadmium, in both cases trefoil knot and [2]catenane, are characterized by PL emission with weaker intensity shifted towards short waves, which is entirely due to the properties of the metal. Therefore, due to the fact that zinc and cadmium occur in the same group of the periodic table and *d* orbitals are fully occupied, there are no *d-d* transitions, no shift in the absorption spectrum and emission spectra in relation to samples containing metals was noticed. The exact values of the excitation and emission wavelengths determined from the 3D spectra are presented in Tab. 7.3.

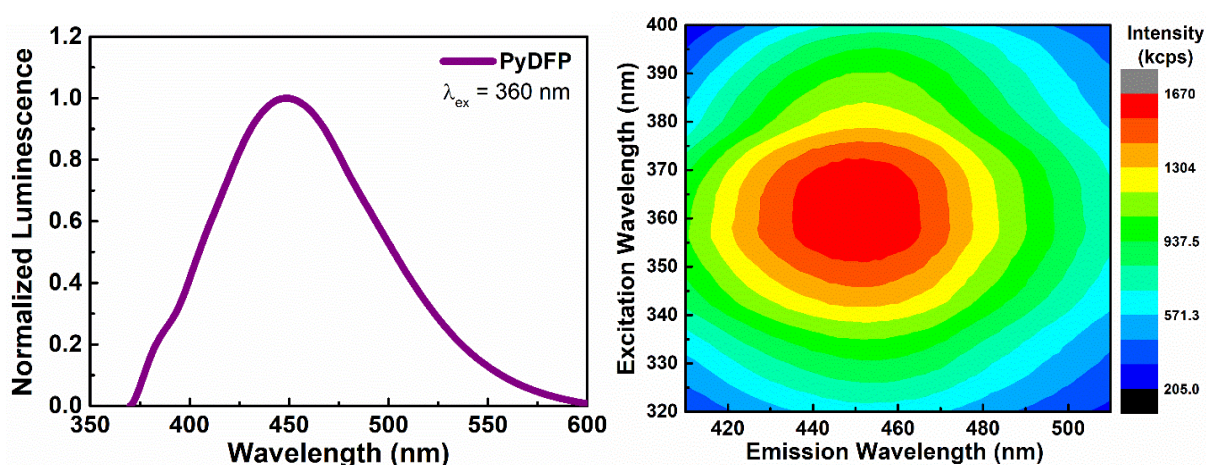


Figure 7.10: Photoluminescence spectra and 3D photoluminescence image of **PyDFP**.

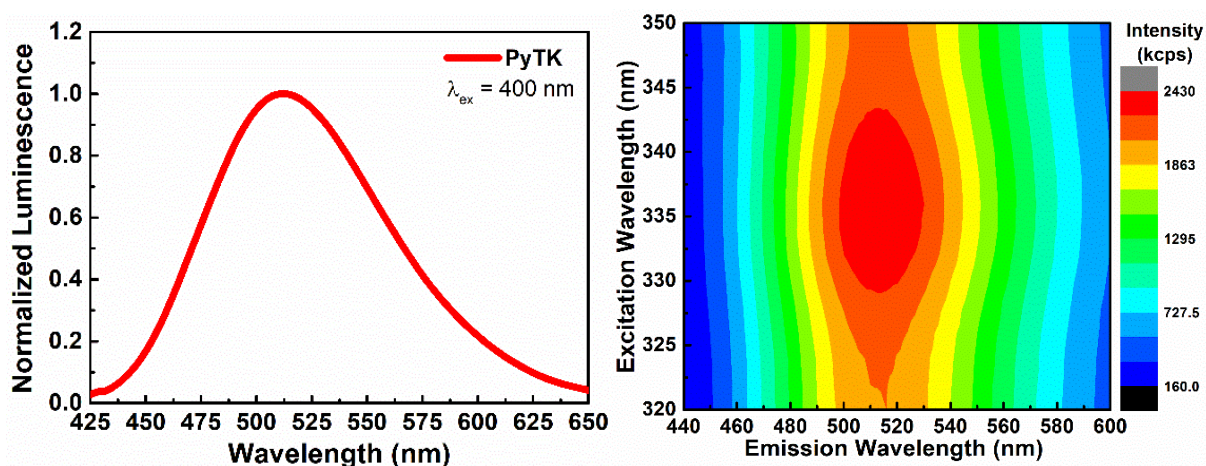


Figure 7.11: Photoluminescence spectra and 3D photoluminescence image of **PyTK**.

Therefore, the luminescence decay time was then measured using additional pulse diodes with wavelengths close to excitation wavelengths. The lifetime was measured in room temperature, and achieved results were fitted by double-exponential function  $y = y_0 + A_0e^{-t/T_1} + A_1e^{-t/T_2}$ , and implies two time decays  $T_1$  and  $T_2$ , which are characterized by a fast and long transition from the excited state to the ground state. The estimated values of decay times are given in Tab. 7.3. The resulting typical fluorescence lifetimes are shown in Fig. 7.17.

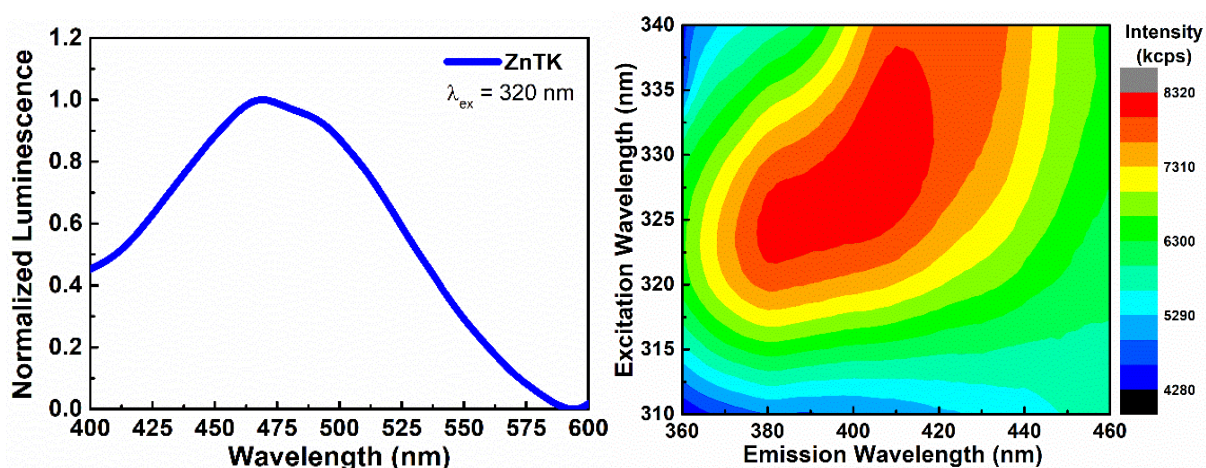


Figure 7.12: Photoluminescence spectra and 3D photoluminescence image of **ZnTK**.

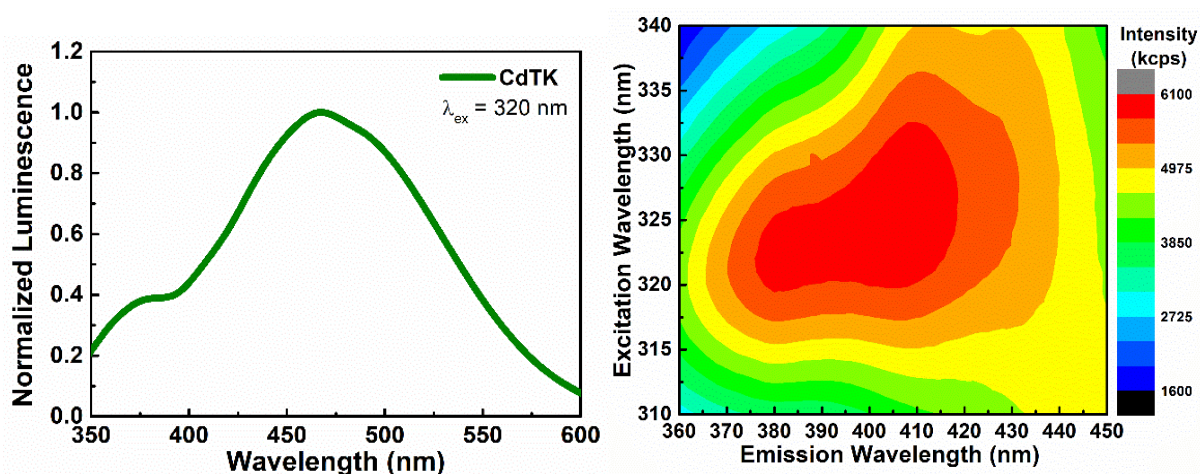


Figure 7.13: Photoluminescence spectra and 3D photoluminescence image of **CdTK**.

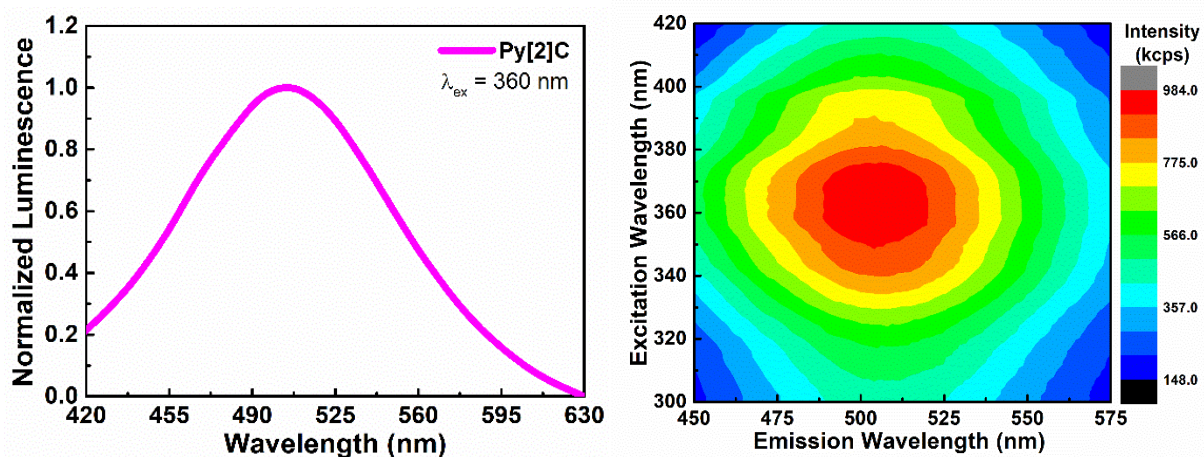


Figure 7.14: Photoluminescence spectra and 3D photoluminescence image of **Py[2]C**.

Table 7.3: Excitation, emission peaks and luminescence lifetimes of studied thin films.

	$\lambda_{\text{Excitation}}$ [nm]	$\lambda_{\text{Emission}}$ [nm]	$T_{1\text{Decay}}$ [ns]	$T_{2\text{Decay}}$ [ns]
<b>PyDFP</b>	286	450	$(18.62 \pm 0.29)$	$(4.14 \pm 0.02)$
	360		$(16.03 \pm 0.23)$	$(3.96 \pm 0.02)$
<b>PyTK</b>	330	520	$(17.73 \pm 0.70)$	$(7.19 \pm 0.02)$
	400		$(13.85 \pm 0.54)$	$(6.43 \pm 0.07)$
<b>ZnTK</b>	320	400	$(30.99 \pm 0.17)$	$(3.12 \pm 0.03)$
<b>CdTK</b>	320	400	$(30.97 \pm 0.16)$	$(2.97 \pm 0.02)$
<b>Py[2]C</b>	365	510	$(14.23 \pm 0.12)$	$(5.56 \pm 0.04)$
<b>Zn[2]C</b>	325	390	$(29.43 \pm 0.15)$	$(2.84 \pm 0.03)$
<b>Cd[2]C</b>	325	390	$(27.83 \pm 0.23)$	$(1.79 \pm 0.02)$

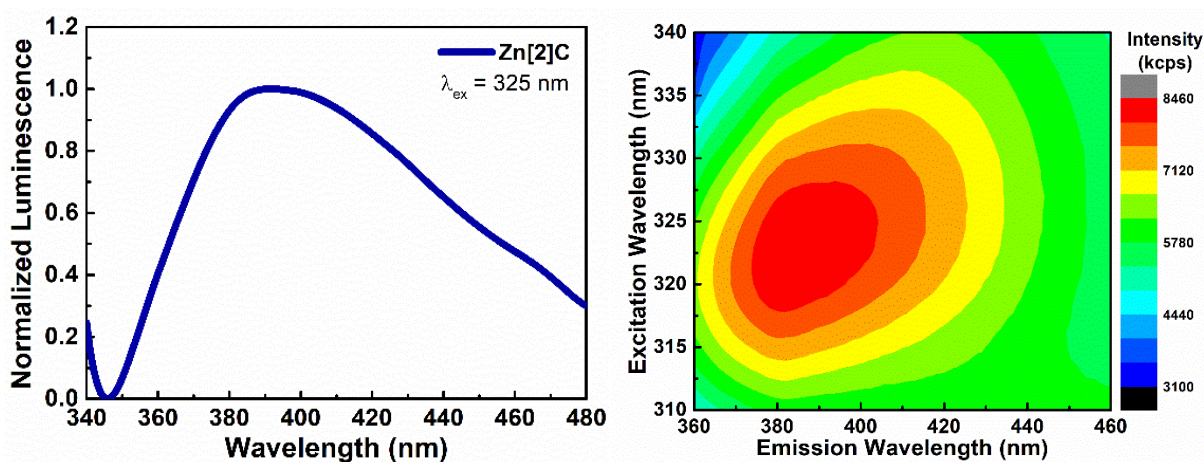


Figure 7.15: Photoluminescence spectra and 3D photoluminescence image of **Zn[2]C**.

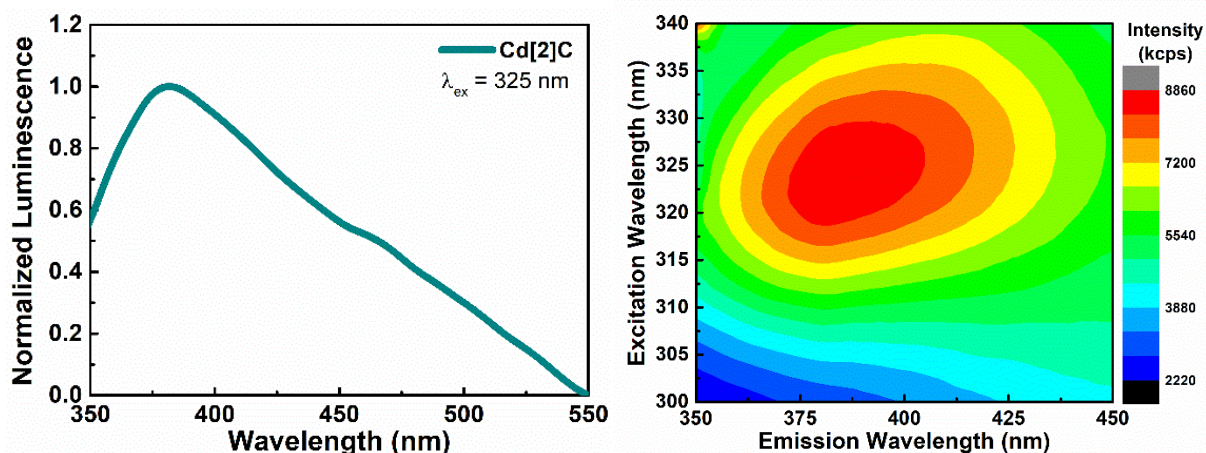


Figure 7.16: Photoluminescence spectra and 3D photoluminescence image of Cd[2]C.

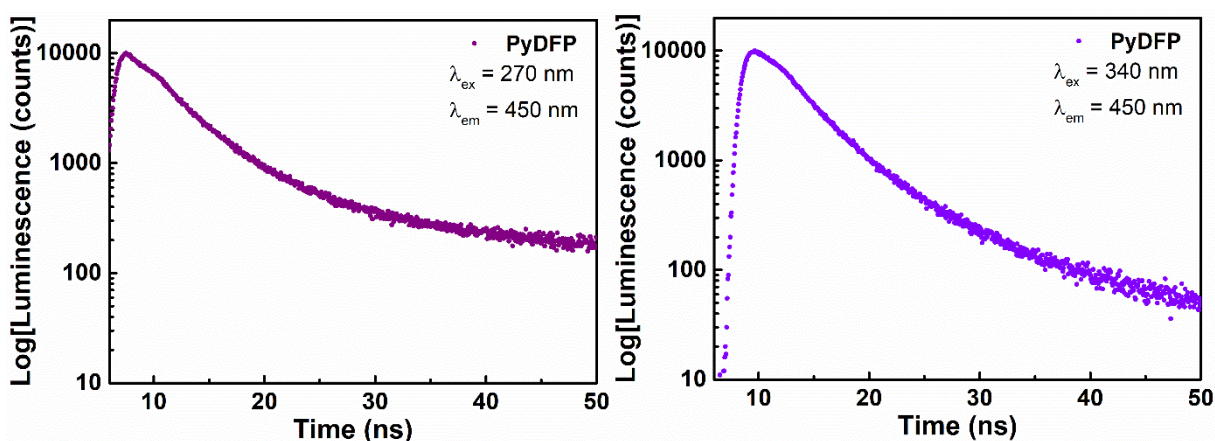
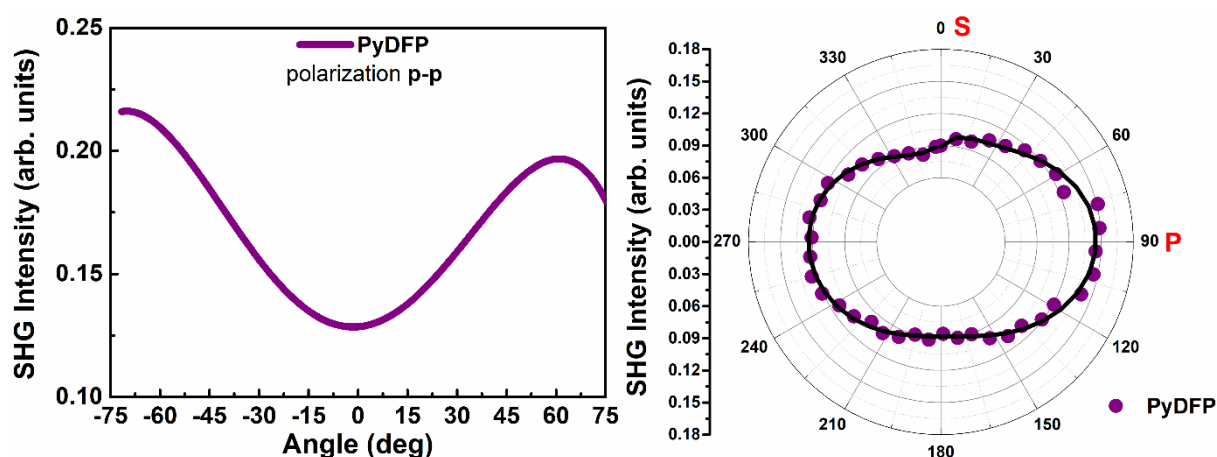


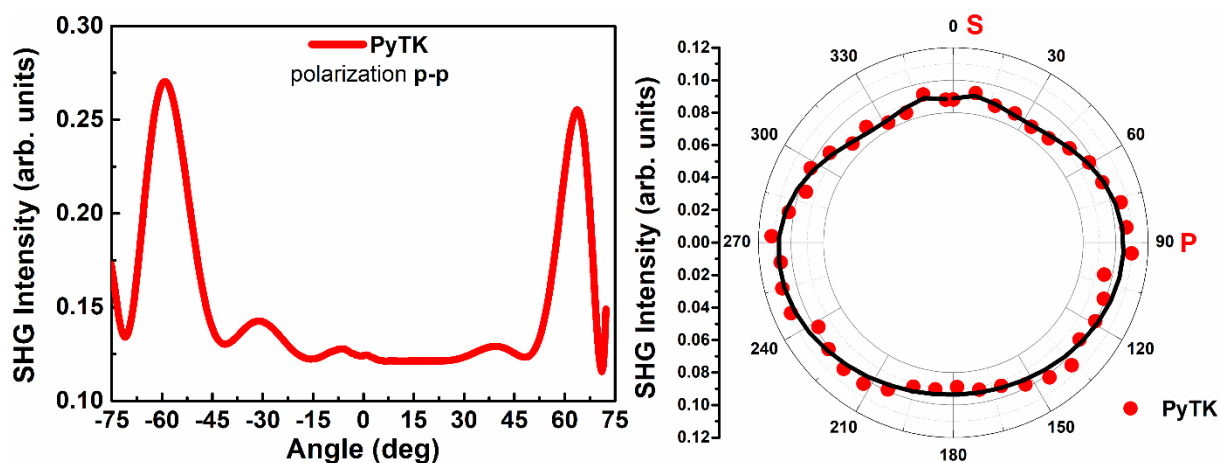
Figure 7.17: Typical luminescence lifetime decays of studied modified pyrene-based complexes.

#### 7.4. Second Harmonic Generation

Second and third order nonlinear effects describing the generation of the second and third harmonics, respectively, were carried out using the measuring equipment described in subsection 4.2. Y-cut quartz crystal was used as reference materials. Measurements were performed in vertical and horizontal polarization of fundamental laser beam. Moreover, as the resulting guest-host thin films do not show the same orientation of the dipole moments, it was necessary to use the corona poling technique to obtain the SHG signal.



**Figure 7.18:** SHG intensities as a function of rotation angle in p-polarized laser beam (left) and as a dependence of laser polarization (right) of **PyDFP** thin film.



**Figure 7.19:** SHG intensities as a function of rotation angle in p-polarized laser beam (left) and as a dependence of laser polarization (right) of **PyTK** thin film.

The second-order nonlinear optical response (SHG) for p-polarized laser light of modified pyrene-based complexes thin layers is shown in Figs. 7.18-7.24. Depending on the structure of the samples and their surface, which was examined with the AFM atomic force microscope, the SHG response varies in shape and intensity. In this experiment, as shown in the spectroscopic properties section, the absorption is neglected because in this 532 nm wavelength range the samples are optically transparent. Moreover, the above-mentioned figures also show the dependence of the intensity of



the generated second harmonic with as a function of the polarization. It was noticed that this response has an elliptical shape, as a rule, for the polarization S, the intensity is slightly lower than for the polarization P, which should coincide with the calculated values of the second-order nonlinear susceptibility, however similarly to previously investigated supramolecular complexes, these guest-host systems takes form of isotropic medium.

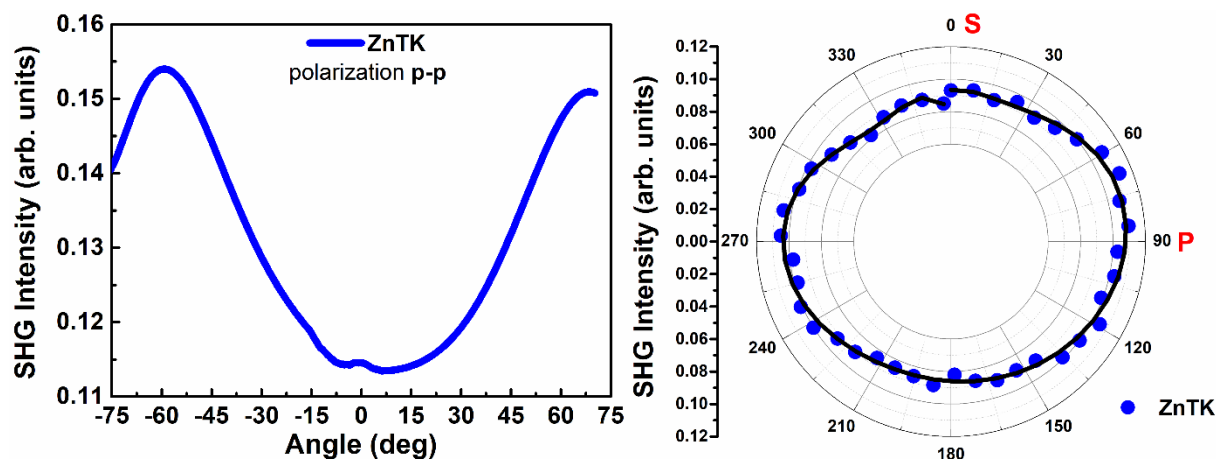


Figure 7.20: SHG intensities as a function of rotation angle in p-polarized laser beam (left) and as a dependence of laser polarization (right) of **ZnTK** thin film.

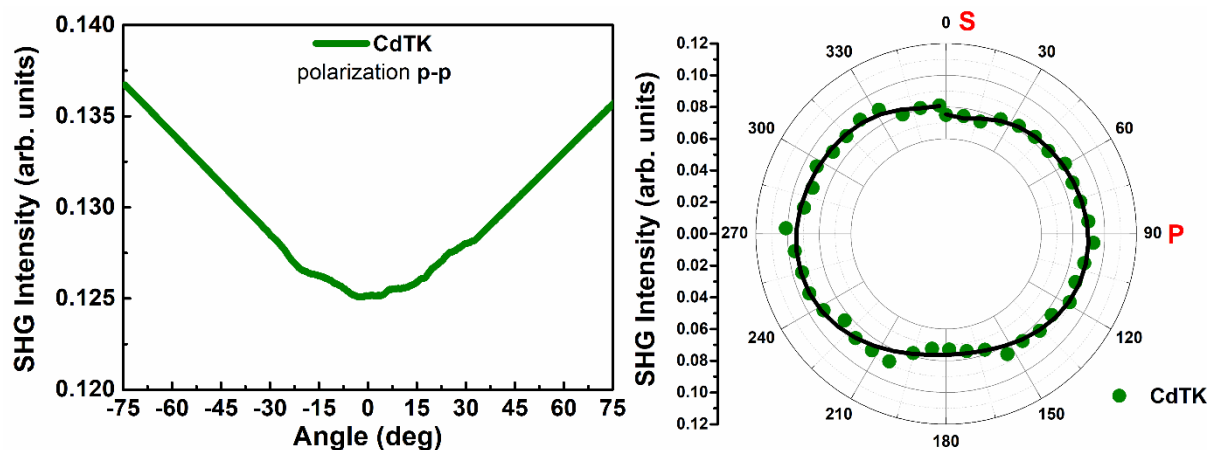


Figure 7.21: SHG intensities as a function of rotation angle in p-polarized laser beam (left) and as a dependence of laser polarization (right) of **CdTK** thin film.

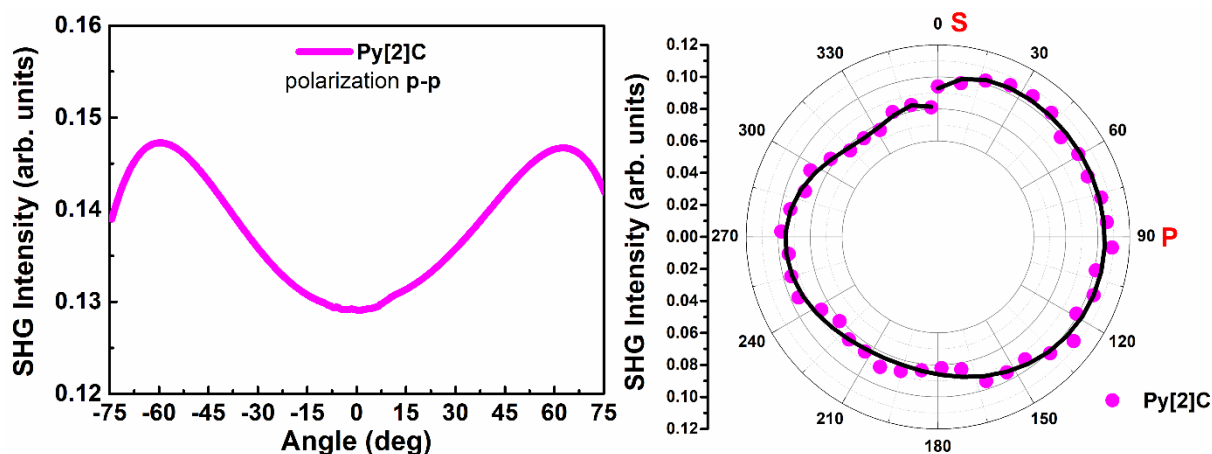


Figure 7.22: SHG intensities as a function of rotation angle in p-polarized laser beam (left) and as a dependence of laser polarization (right) of **Py[2]C** thin film.

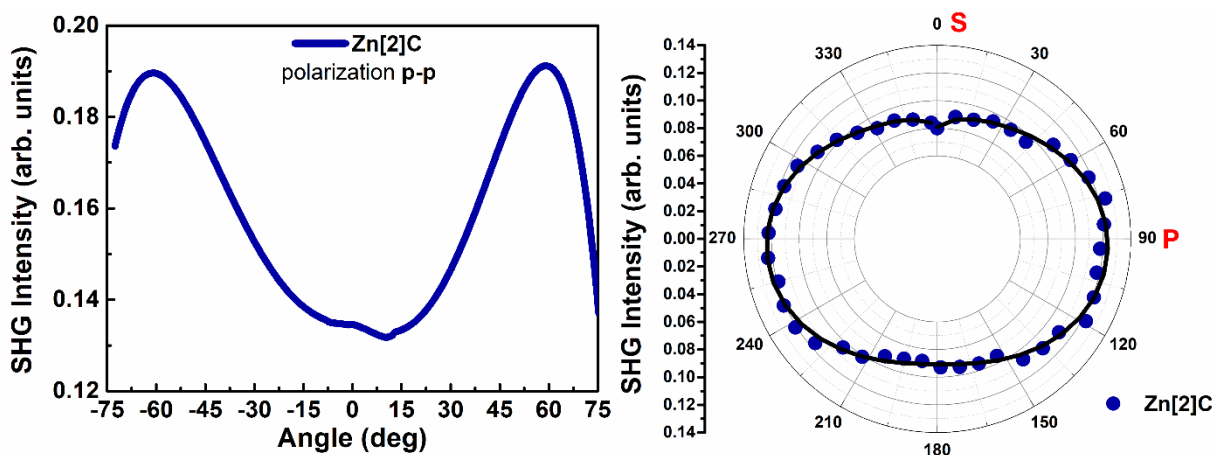
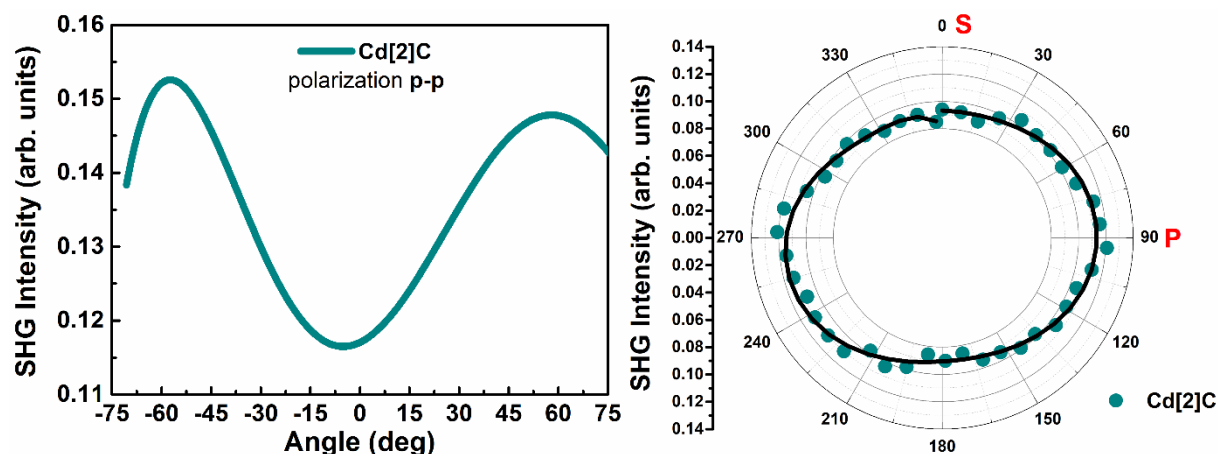


Figure 7.23: SHG intensities as a function of rotation angle in p-polarized laser beam (left) and as a dependence of laser polarization (right) of **Zn[2]C** thin film.

Table 7.4 shows the calculated values of the second order nonlinear susceptibilities for the s- and p-polarized laser beam using the Lee theoretical models (subsection 4.1.1) and Herman-Hayden (subsection 4.1.3). The highest values were obtained for the **Py[2]C** and **ZnTK** sample. Since the Herman-Hayden model requires parameters dependent on the sample polarization in the calculation, the NLO susceptibilities values are higher when this model was used. For better contrast, the calculated values are visualized graphically in the form of histogram in Fig. 7.25.

Moreover, from the obtained results, we can notice that by changing the nature of supramolecular assemblies, by changing the spacer, we can control NLO response, which was not observable in case of triple stranded helicates.



**Figure 7.24:** SHG intensities as a function of rotation angle in p-polarized laser beam (left) and as a dependence of laser polarization (right) of **Cd[2]C** thin film.

**Table 7.4:** Values of second-order nonlinear susceptibilities of modified pyrene-based guess-host thin films calculated by theoretical models.

	Model	$\chi^{(2)}$ [pmV <sup>-1</sup> ]	
		s-p	p-p
PyDFP	Lee	(0.449 ± 0.033)	(0.903 ± 0.039)
	Herman-Hayden	(0.559 ± 0.027)	(1.237 ± 0.022)
PyTK	Lee	(0.497 ± 0.037)	(1.059 ± 0.045)
	Herman-Hayden	(0.514 ± 0.024)	(1.248 ± 0.015)
ZnTK	Lee	(0.566 ± 0.043)	(1.024 ± 0.054)
	Herman-Hayden	(0.696 ± 0.033)	(1.281 ± 0.039)
CdTK	Lee	(0.432 ± 0.031)	(0.668 ± 0.039)
	Herman-Hayden	(0.569 ± 0.029)	(1.011 ± 0.019)
Py[2]C	Lee	(0.737 ± 0.063)	(1.211 ± 0.084)
	Herman-Hayden	(1.212 ± 0.044)	(2.187 ± 0.099)
Zn[2]C	Lee	(0.547 ± 0.041)	(0.989 ± 0.051)
	Herman-Hayden	(0.638 ± 0.028)	(1.350 ± 0.029)
Cd[2]C	Lee	(0.513 ± 0.038)	(0.814 ± 0.049)
	Herman-Hayden	(0.560 ± 0.031)	(0.972 ± 0.056)

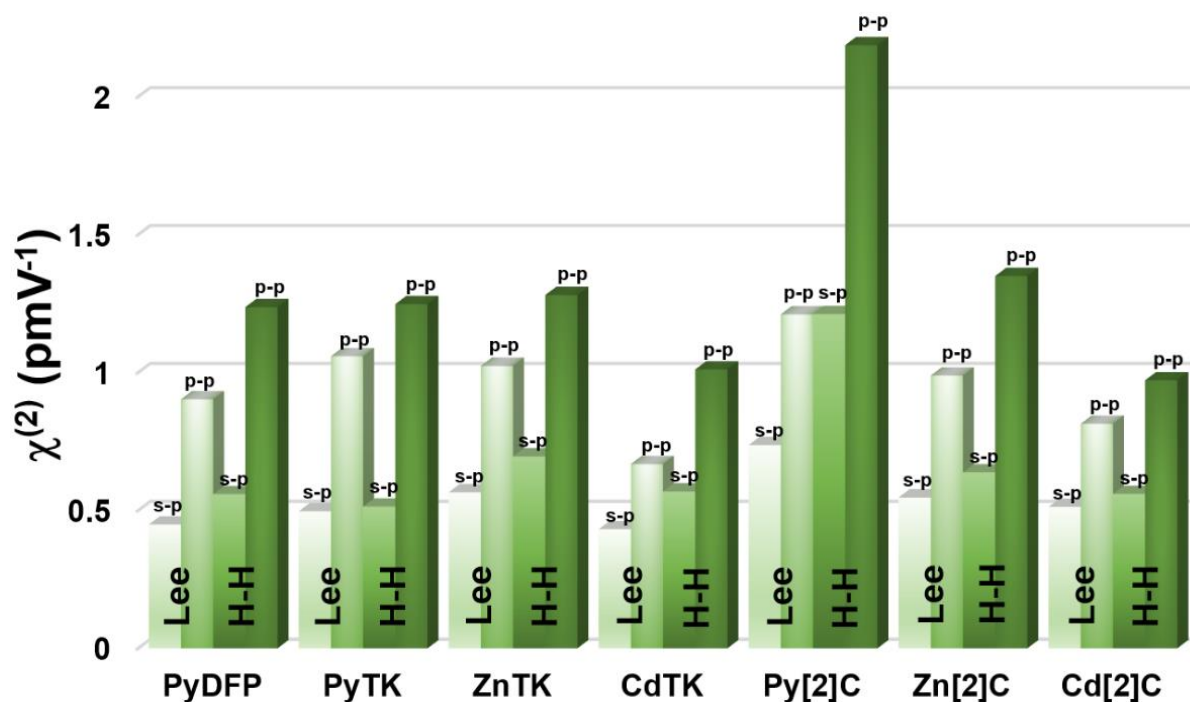


Figure 7.25: Histogram representing values of second-order nonlinear susceptibilities calculated via theoretical models.

### 7.5. Third Harmonic Generation

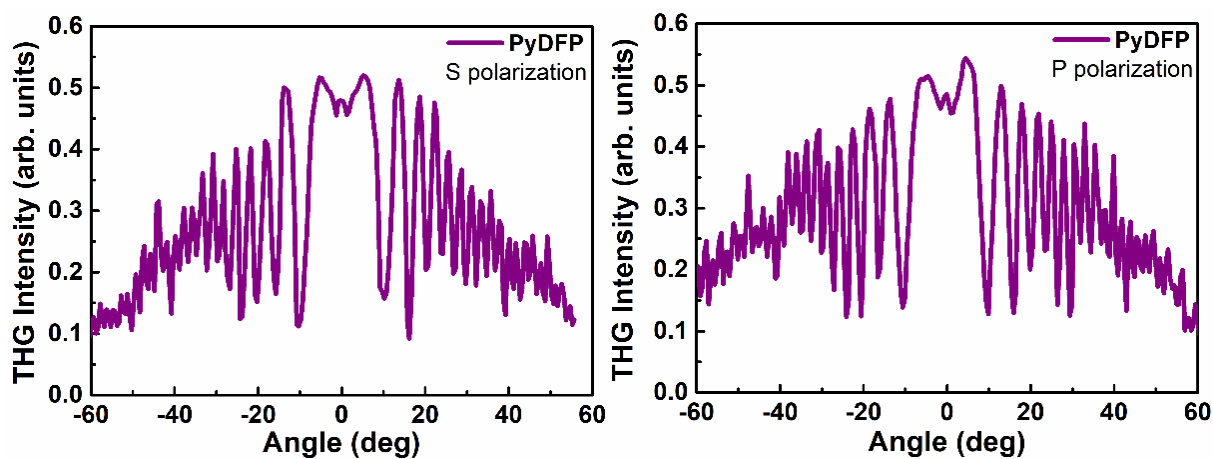
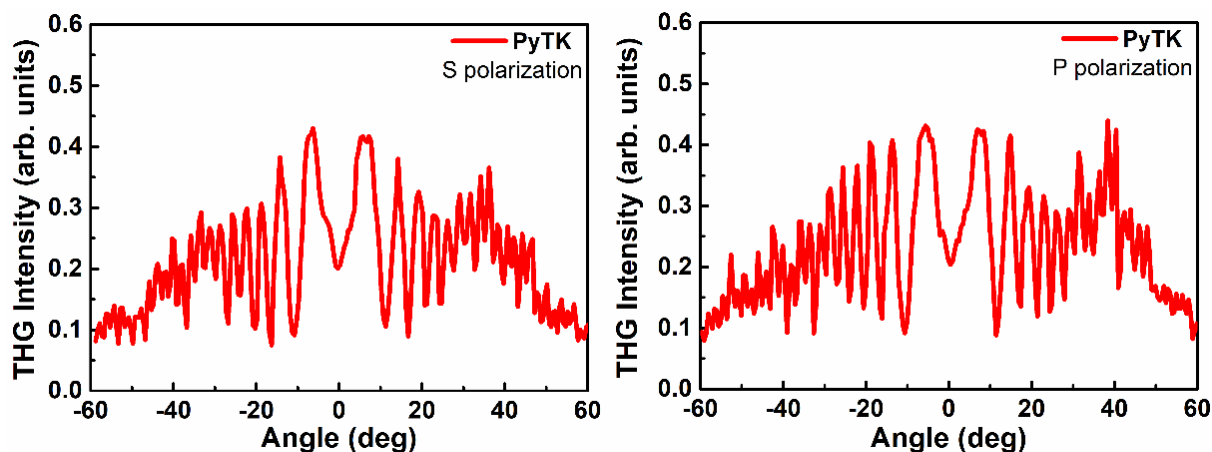
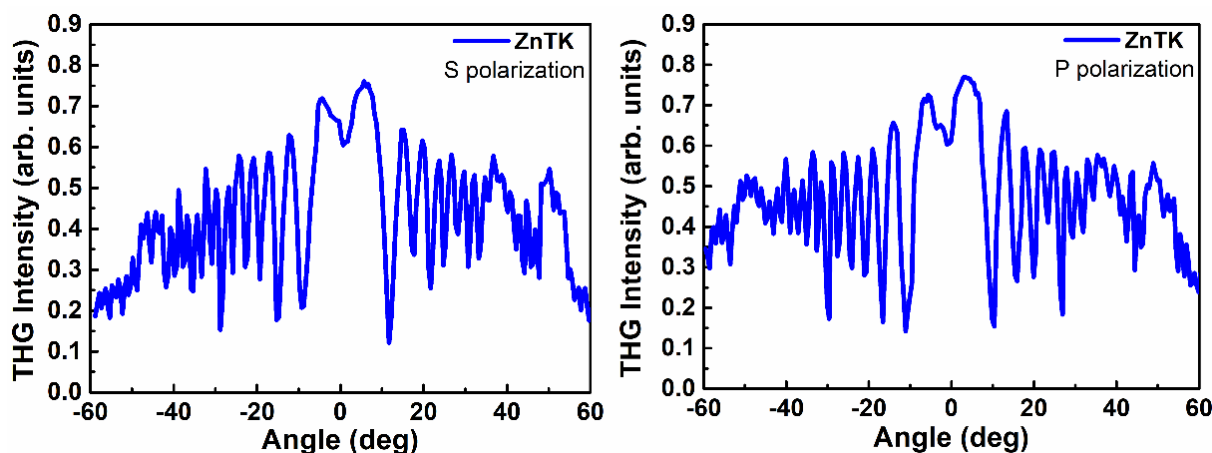


Figure 7.26: THG intensities as a function of incident angle of **PyDFP** thin film in s-polarized (left) and p-polarized (right) laser beam.



**Figure 7.27:** THG intensities as a function of incident angle of **PyTK** thin film in s-polarized (left) and p-polarized (right) laser beam.



**Figure 7.28:** THG intensities as a function of incident angle of **ZnTK** thin film in s-polarized (left) and p-polarized (right) laser beam.

As mentioned in previous chapters, the generation of the third harmonic THG does not require the use of the corona poling technique. Figs. 7.26-7.32 show THG response for thin layers of pyrene-based guest-host complexes. Similarly, as previously described supramolecular compounds, no significant difference was observed between the signal versus the applied polarization, which is also noticeable when calculating the NLO parameters. Thus, the values of  $\chi^{(3)}$  were calculated using theoretical models Kubodera-Kobayashi (subsection 4.1.4) and Reintjes (subsection 4.1.5)

and results are presented in Tab. 7.5. In the previous section about spectroscopic properties it was mentioned that absorption has no effect on the generation of the second harmonic, but has an effect on the generated third order nonlinear signal. Therefore, in the comparative model, the relation taking into account the absorption coefficient for the wavelength of 355 nm was used.

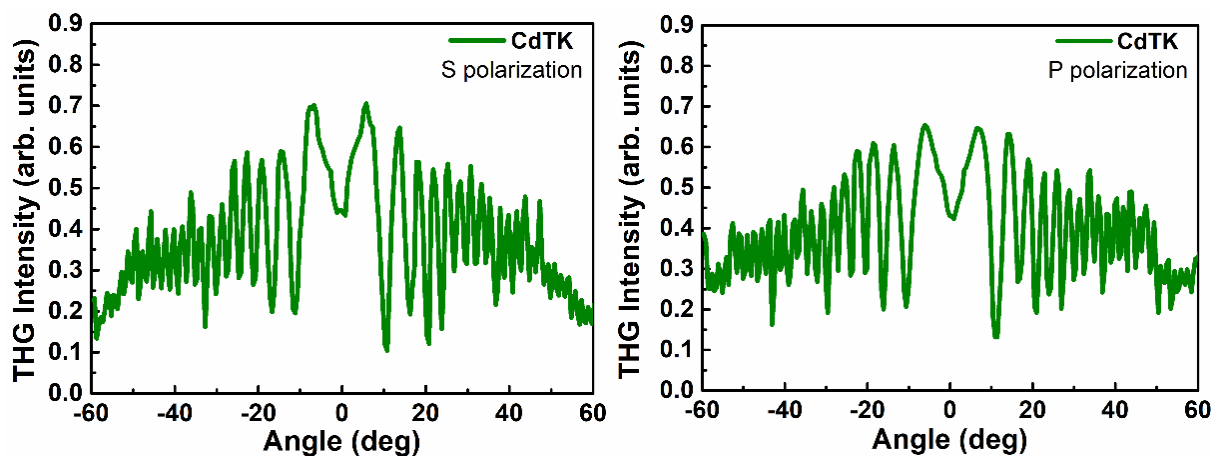


Figure 7.29: THG intensities as a function of incident angle of CdTK thin film in s-polarized (left) and p-polarized (right) laser beam.

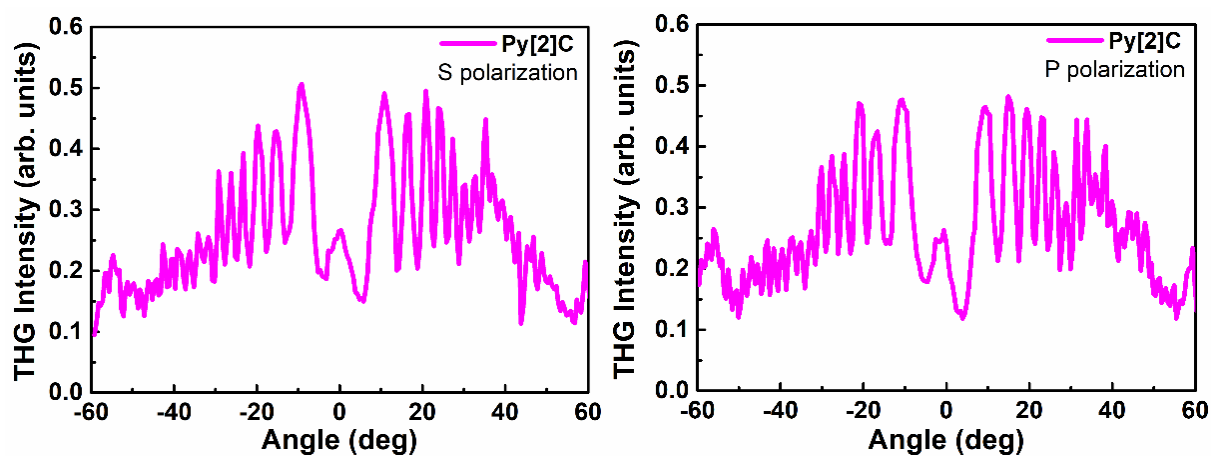


Figure 7.30: THG intensities as a function of incident angle of Py[2]C thin film in s-polarized (left) and p-polarized (right) laser beam.

From the histogram presented in Fig. 7.33 and from the values given in Tab. 7.5, it can be seen that the values calculated by the Reintjes model are higher than for the comparative model. This is

because, as described in Chapter 4, this model contains more parameters related directly to the properties of the sample, such as, for example, linear refractive index. Moreover, the discrepancies in the values related to the S and P polarization result from the fact that the polarization was changed by the optical system, which could have contributed to a slight change in the energy of the laser pulse. The strongest THG signal, similarly in SHG experiment, was observed for **ZnTK** and **Py[2]C** samples.

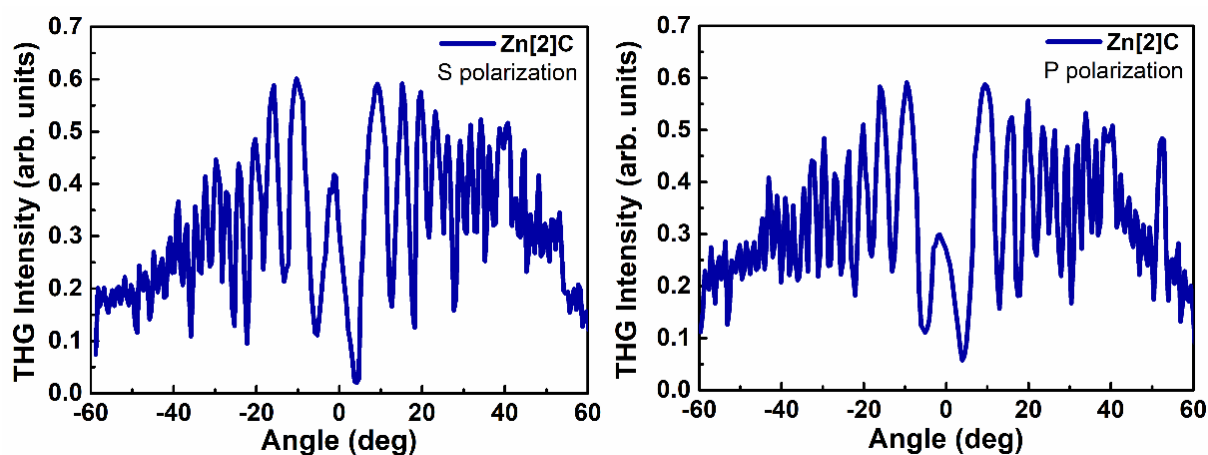


Figure 7.31: THG intensities as a function of incident angle of **Zn[2]C** thin film in s-polarized (left) and p-polarized (right) laser beam.

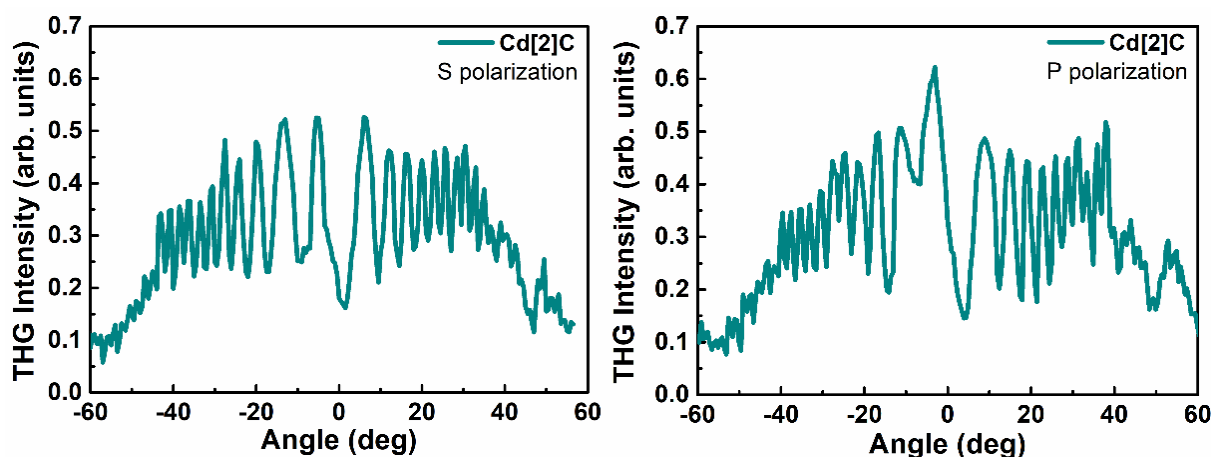
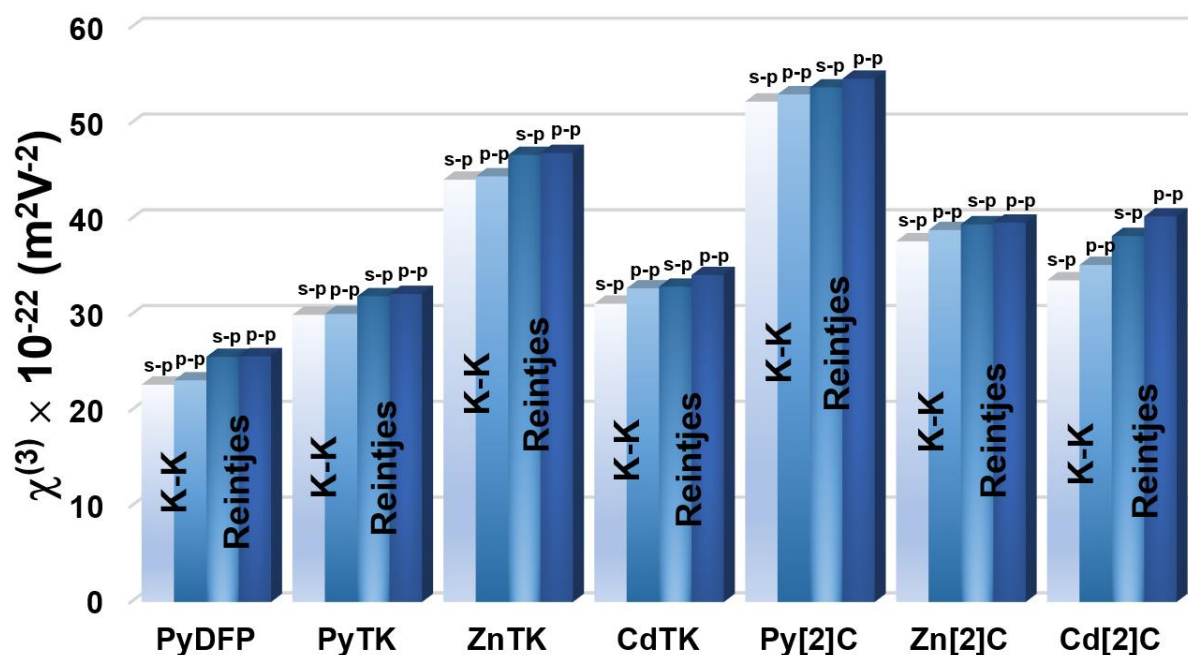


Figure 7.32: THG intensities as a function of incident angle of **Cd[2]C** thin film in s-polarized (left) and p-polarized (right) laser beam.

**Table 7.5:** Values of third-order nonlinear susceptibilities calculated by theoretical models.

	Model	$\chi^{(3)} \times 10^{-22} [\text{m}^2\text{V}^{-2}]$	
		s-p	p-p
PyDFP	Kubodera-Kobayashi	(22.70 ± 0.12)	(23.15 ± 0.12)
	Reintjes	(25.60 ± 0.11)	(25.66 ± 0.10)
PyTK	Kubodera-Kobayashi	(29.99 ± 0.13)	(30.08 ± 0.13)
	Reintjes	(31.93 ± 0.19)	(32.17 ± 0.14)
ZnTK	Kubodera-Kobayashi	(44.10 ± 0.18)	(44.45 ± 0.18)
	Reintjes	(46.69 ± 0.16)	(46.89 ± 0.12)
CdTK	Kubodera-Kobayashi	(31.15 ± 0.11)	(32.76 ± 0.13)
	Reintjes	(32.93 ± 0.12)	(34.14 ± 0.14)
Py[2]C	Kubodera-Kobayashi	(52.26 ± 0.28)	(53.02 ± 0.28)
	Reintjes	(53.73 ± 0.19)	(54.64 ± 0.19)
Zn[2]C	Kubodera-Kobayashi	(37.67 ± 0.15)	(38.84 ± 0.16)
	Reintjes	(39.44 ± 0.12)	(39.62 ± 0.15)
Cd[2]C	Kubodera-Kobayashi	(33.60 ± 0.14)	(35.20 ± 0.14)
	Reintjes	(38.22 ± 0.13)	(40.27 ± 0.20)

**Figure 7.33:** Histogram representing values of third-order nonlinear susceptibilities calculated via theoretical models.



## 7.6. Z-Scan Results

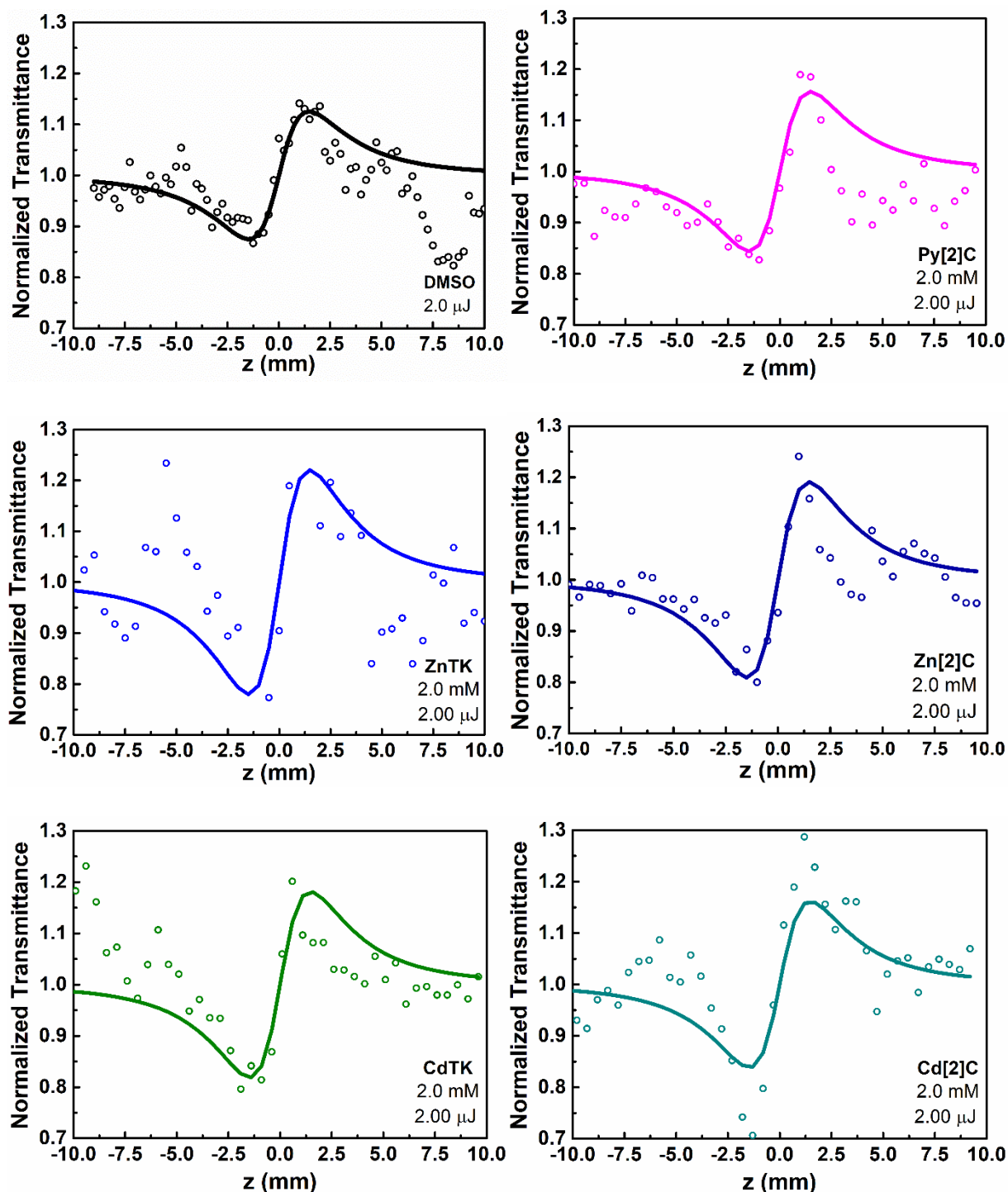


Figure 7.34: Typical normalized CA Z-scan characteristics for modified pyrene-based complexes and DMSO at laser energy 2.0 μJ.

The studies of nonlinear absorption and nonlinear refraction were performed by the Z-scan method with the excitation of laser light with wavelength 532 nm, described in the experimental section. Measurements were carried out for solutions placed in 1 mm quartz cuvettes, with a concentration of 2.0 mM, 1.5 mM, 1.0 mM and 0.5 mM dissolved in dimethyl sulfoxide (DMSO), depending on the input energy changed from 2.0  $\mu\text{J}$  to 0.5  $\mu\text{J}$  with steps of 0.25  $\mu\text{J}$ . The sample with the solution was placed on the stage moved in the direction of the Z axis from -10 mm to 10 mm with a step of 0.1 mm, where point 0 corresponds to the focus point. However, due to the aforementioned absorption properties, concentration of solutions and low intensity of the laser beam, the measurements of the two-photon absorption (TPA) in the open-aperture Z-scan (OA) were not achieved, while the close-aperture Z-scan (CA) has been registered successfully. Examples of the obtained CA Z-scan curves for the **Zn[2]C** sample with different solution concentrations and with the change of the laser beam energy are shown in Fig. 7.34. Due to the fact that solvent DMSO exhibits nonlinear refractive properties [7.6], its influence has been taken into account in the calculations, where the NLO susceptibility of the solvent is subtracted from the NLO susceptibility of the solution. The results of the calculated values of the nonlinear refractive index and the real value of the third-order nonlinear susceptibility for modified pyrene-based complexes with different concentrations are given in Tab. 7.6. Moreover, the calculated values of the nonlinear refractive index  $n_2$  depending on the concentration of the solutions are shown graphically in Fig. 7.35. From Tab. 7.6, it can be seen that the **Py[2]C** and **PyTK** samples have higher  $n_2$  values than **PyDFP**, which is the building block of these two complexes. Moreover, the zinc and cadmium cations found in these systems enhanced the effect of nonlinear refraction. The highest values, however, were observed for systems containing zinc metals **ZnTK** and **Zn[2]C**. It was also noticed that the NLO effect increases with the concentration of solution. In this case, absorption has no influence on the nonlinear refraction effect.

**Table 7.6:** Calculated values of NLO refractive index  $n_2$ , real part and total value of third order NLO susceptibility  $\text{Re}(\chi^{(3)})$ ,  $\chi^{(3)}$  of modified pyrene-based complexes in DMSO.

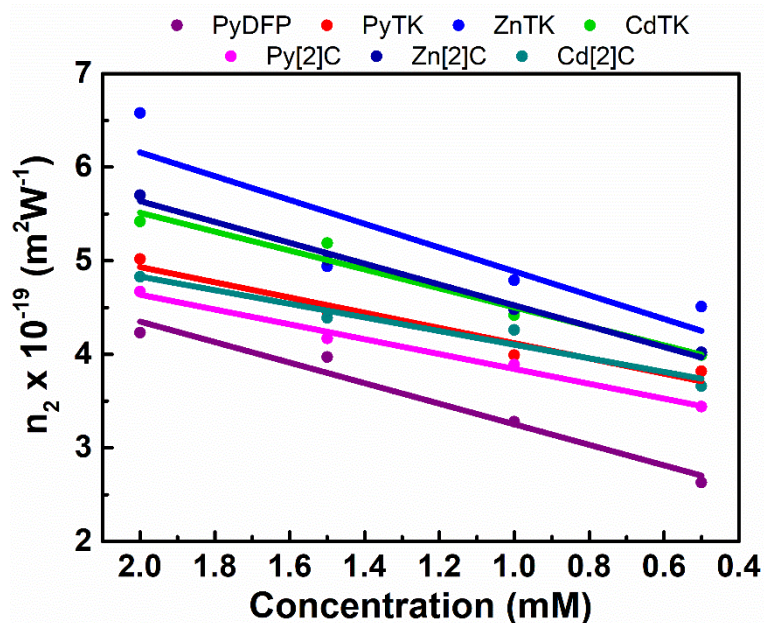
	$\rho$ [mM]	$n_2 \times 10^{-19}$ [m <sup>2</sup> W <sup>-1</sup> ]	$\text{Re}(\chi^{(3)}) \times 10^{-21}$ [m <sup>2</sup> V <sup>-2</sup> ]	$\chi^{(3)} \times 10^{-21}$ [m <sup>2</sup> V <sup>-2</sup> ]
PyDFP	2.0	4.23	3.21	3.21
	1.5	3.97	3.08	3.08
	1.0	3.28	2.54	2.54
	0.5	2.63	2.04	2.04
PyTK	2.0	5.02	3.89	3.89
	1.5	4.46	3.45	3.45
	1.0	3.99	3.09	3.09
	0.5	3.82	2.96	2.96
ZnTK	2.0	6.58	5.09	5.09
	1.5	4.94	3.83	3.83
	1.0	4.79	3.71	3.71
	0.5	4.51	3.49	3.49
CdTK	2.0	5.42	4.19	4.19
	1.5	5.19	4.02	4.02
	1.0	4.42	3.42	3.42
	0.5	3.99	3.09	3.09
Py[2]C	2.0	4.67	3.62	3.62
	1.5	4.17	3.23	3.23
	1.0	3.89	3.01	3.01
	0.5	3.44	2.67	2.67
Zn[2]C	2.0	5.70	4.42	4.42
	1.5	5.01	3.88	3.88
	1.0	4.48	3.47	3.47
	0.5	4.02	3.12	3.12
Cd[2]C	2.0	4.83	3.74	3.74
	1.5	4.39	3.40	3.40
	1.0	4.26	3.30	3.30
	0.5	3.66	2.84	2.84

As can be clearly seen in Fig. 7.34 and Tab. 7.6, the investigated modified pyrene-based supramolecular complexes are self-focusing ( $n_2 > 0$ ) materials. Moreover, the calculated values of the nonlinear refractive index given in Tab. 7.6 are presented schematically with on the Fig. 7.35. The results for this experiment are different from the THG experiment, which only has electronic contribution to the third-order NLO phenomena (see Tab. 7.7). Due to the fact that the investigated samples have the same concentration of solutions, where as in the case of thin layer

studied with the THG method, it is necessary to have the same concentration of molecules in layers, it is easier to compare the studied samples with each other. The total third order NLO susceptibility is influenced only by the real part of it as a result of the NLO refractive properties, the NLO susceptibility values determined by the THG technique do not differ significantly from the values determined from the Z-scan method, due to the lack of a molecular element, which is determined by NLO absorption. As it can be clearly seen, supramolecular compounds are characterized by an enhanced NLO signal compared with the **PyDFP** ligand. Moreover, the influence of the metal and the changes in the nature of the supramolecular complex by changing the spacer, have been noted, that is: in samples **ZnTK** and **CdTK** also **Zn[2]C** and **Cd[2]C**, the nonlinear response is stronger than for **PyTK** and **Py[2]C**, respectively. It also was noticed that the zinc cation is associated with stronger interactions than the cadmium cation, hence much higher values for the **ZnTK** sample relative to **CdTK** and **Zn[2]C** relative to **Cd[2]C**. In general, the presented supramolecular systems of new modified pyrene-based complexes are characterized by a high response of both the second and third order, moreover, they are characterized by strong NLO refraction with self-focusing properties, due to which they can be used, among others, in NLO devices based on self-phase modulation.

**Table 7.7:** Calculated values of NLO susceptibility  $\chi^{(3)}$  obtained from Z-scan data, compared with THG results of studied modified pyrene-based complexes.

		PyDFP	PyTK	ZnTK	CdTK	Py[2]C	Zn[2]C	Cd[2]C	
$\chi^{(3)} \times 10^{-21}$ [m <sup>2</sup> V <sup>-2</sup> ]	Z-scan	2.0 mM	3.21	3.89	5.09	4.19	3.62	4.42	3.74
		1.5 mM	3.08	3.45	3.83	4.02	3.23	3.88	3.40
		1.0 mM	2.54	3.09	3.71	3.42	3.01	3.47	3.30
		0.5 mM	2.04	2.96	3.49	3.09	2.67	3.12	2.84
	THG	2.32	3.01	4.45	3.28	5.30	3.88	3.52	



**Figure 7.35:** Values of nonlinear refractive index as a function of solution concentration of modified pyrene-based complexes in DMSO.

## 7.7. Conclusions

This chapter presented mainly nonlinear optics studies on new modified pyrene-based supramolecular complexes. The research focused on two types of pyrene compounds: trefoil knot and [2]catenane. The ligand forming these two types of supramolecular compounds **PyDFP** (pyrene diformylpyridine) and **PyTK** (pyrene trefoil knot) with zinc **ZnTK** cations and cadmium cations **CdTK**, and **Py[2]C** (pyrene [2]catenane) together with zinc cations were investigated **Zn[2]C** and cadmium cations **Cd[2]C**. The samples were successfully obtained according to the synthesis described in the literature. The research on nonlinear optics has been divided into two parts: the first one uses thin layers prepared with the spin-coating method, while the second one is based on studies in solutions. Thin layers were used to study nonlinear optics of second and third harmonic generation (SHG and THG, respectively) by the Maker fringe method. However, before the research into NLO was started, the spectroscopic properties of thin films were checked. It was found that in the case of these supramolecular compounds, the absorption only affects the third

order properties, which was taken into account in the subsequent determinations of the nonlinear optics parameters. The conducted studies of nonlinear optics have shown that the investigated supramolecular compounds are characterized by enhanced generation of the second and third harmonics. In addition, based on the Z-scan technique from the solution, NLO studies of the refractive index show that these complexes can be used in nonlinear optical devices, inter alia, as self-modulators. Due to the enhanced nonlinear properties of the second and third order, the most interesting compounds contain zinc cations: **ZnTK** and **Zn[2]C**. As the conclusion of this section, in this work the proof of using modified supramolecular nontrivial structures in nonlinear optics was achieved. By changing nature, spacer or substituent in supramolecular assemblies we can control NLO response.

## Literature

- [7.1] T. Prakasam, M. Lusi, M. Elhabiri, C. Platas-Iglesias, J.-C. Olsen, Z. Asfari, S. Cianferani-Sanglier, F. Debaene, L. J. Charbonniere, A. Trabolsi, Simultaneous Self-Assembly of a [2]Catenane, a Trefoil Knot, and a Solomon Link from a Simple Pair of Ligands, *Angew. Chem. Int. Ed.* 2013, 52, 9956 –9960
- [7.2] R. A. Bilbeisi, T. Prakasam, M. Lusi, R. El Khoury, C. Platas-Iglesias, L. J. Charbonniere, J.-C. Olsen, M. Elhabiri, A. Trabolsi, [C–H/anion] interactions mediate the templation and anion binding properties of topologically nontrivial metal–organic structures in aqueous solutions, *Chem. Sci.*, 2016, 7, 2524
- [7.3] T. Prakasam, R. A. Bilbeisi, R. El-Khoury, L. J. Charbonniere, M. Elhabiri, G. Esposito, J.-C. Olsen, A. Trabolsi, Topological transformation of a trefoil knot into a [2]catenane, *Dalton Trans.*, 2017, 46, 16474

- [7.4] T. Prakasam, R. A. Bilbeisi, M. Lusi, J.-C. Olsen, C. Platas-Iglesias, A. Trabolsi, Postsynthetic Modification of Cadmium-Based Knots and Links, *Chem. Commun.*, 2016, 52, 7398-7401
- [7.5] F. Benyettou, T. Prakasam, A. Ramidas Nair, I.-I. Witzel, M. Alhashimi, T. Skorjanc, J.-C. Olsen, A. Trabolsi, Potent and selective in vitro and in vivo antiproliferative effects of metal-organic trefoil knots, *Chem. Sci.*, 2019, 10, 5884-5892
- [7.6] K. Iliopoulos, D. Potamianos, E. Kakkava, P. Aloukos, I. Orfanos, and S. Couris. Ultrafast third order nonlinearities of organic solvents. *Optics Express* Vol. 23, Issue 19, pp. 24171-24176, 2015.

## CHAPTER 8: NANOPOROUS MEMBRANES

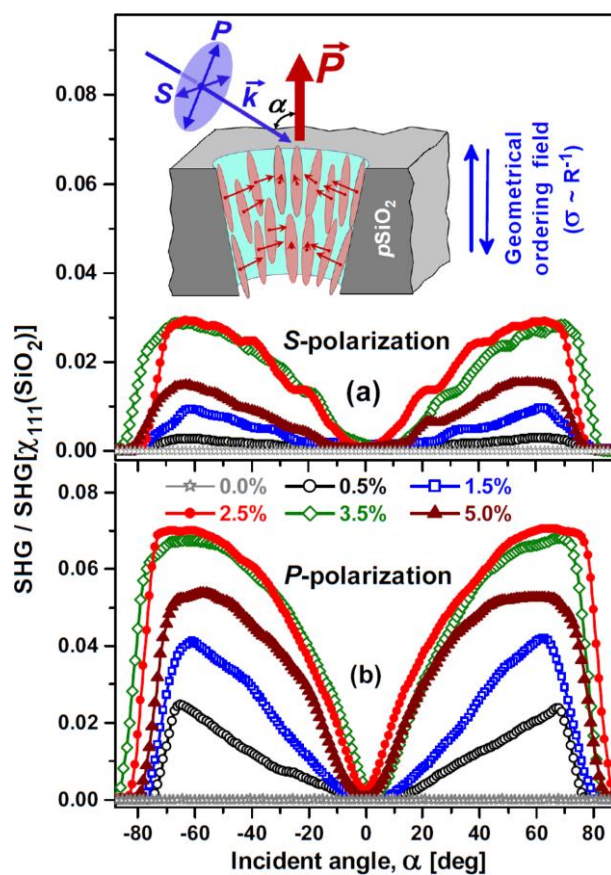
This chapter is devoted to the preparation of metamaterials composed of a nanoporous membrane and the studied supramolecular complex. From each type of investigated (metallo)supramolecular compounds, one of the most interesting was selected and a nanocomposite was prepared. **PtOEP** was selected from porphyrin complexes, **HelNi** was selected from triple helicates samples, and **ZnTK** also **Zn[2]C** were selected from modified pyrene-based complexes. The obtained nanocomposites were characterized by nonlinear optics studies.

### 8.1. Nanoporous Membranes versus Thin Films

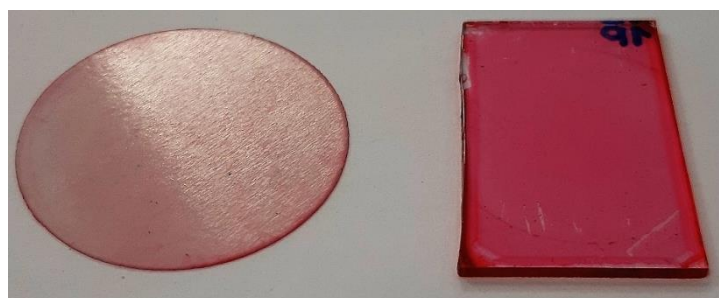
As already mentioned in this doctoral thesis, due to the unique properties of thin films, they are used in many fields of science, from optics, through electronics, to the aviation or space industry, giving rise to many inventions. As this monograph shows, thin films are widely used in the study of nonlinear optics [8.1 – 8.5]. This chapter describes the research of nonlinear optics, which was carried out not on thin films, but on alumina nanoporous membranes, in order to show their usefulness and potential use in future devices based on nonlinear optics. The NLO studies connected to nanocomposites consisting of a nanoporous membrane and the investigated compound described in [8.6 - 8.7] present the SHG studies with crystals already known in nonlinear optics, KDP and Ba(NO<sub>3</sub>)<sub>2</sub>. The results presented there clearly show that the generation of the second harmonic occurs by achieving forced orientation in each separate nanopore. On the other hand, when dealing with an organic compound that does not show a second-order effect without the use of the corona poling method creating macroscopic noncentrosymmetry, when such compounds are placed in a nanoporous membrane, as in the case of dimer in the silicone membrane described in [8.8], forced orientation of the dipole moments, thanks to which it is possible to achieve the SHG effect (see Fig. 8.1). From the above works, conclusions were drawn regarding the advantages and disadvantages of nanoporous membranes and thin films, which are presented



in Tab. 8.1. Moreover, Fig. 8.2 shows a photograph of both materials that are the subject of this subsection.



**Figure 8.1:** SHG intensities in s-polarized and p-polarized laser beam of  $p\text{SiO}_2$ : D1 nanocomposite [8.8].



**Figure 8.2:** Photograph presenting nanocomposite consisting of a porphyrin complex with  $\text{Al}_2\text{O}_3$  nanoporous membrane (left) and a guest-host thin film of porphyrin complex in PMMA on glass substrate (right).

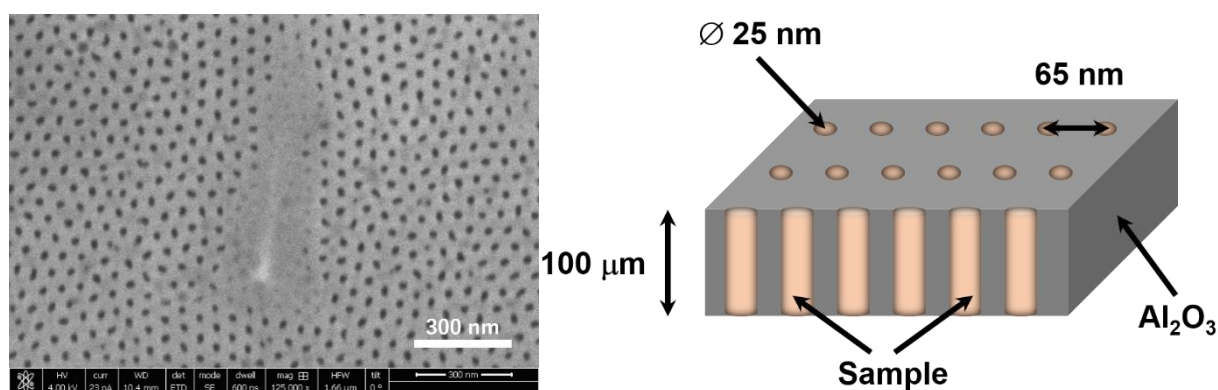
**Table 8.1:** Comparison the advantages and disadvantages of guest-host thin films with nanoporous membranes.

	<b>Advantages</b>	<b>Disadvantages</b>
<b>Guest-host thin films</b>	<ul style="list-style-type: none"> <li>• Easy and cheap sample preparation.</li> <li>• Sample size control: from small to larger areas.</li> <li>• Possibility of investigating various guest samples.</li> <li>• Variety of polymer matrix in use (PMMA, PVK, PVA, ...).</li> <li>• Capacity of symmetry breaking for SHG investigations.</li> </ul>	<ul style="list-style-type: none"> <li>• Thermal instability of thin films related to the properties of the guest material and the glass transition temperature <math>T_g</math> of the polymer.</li> <li>• Ambiguous lifetime of the SHG effect related to the relaxation time of dipole moments orientation after using the corona poling method.</li> <li>• Low NLO properties associated with the appropriate concentration and solubility of the guest material in relation to the polymer matrix.</li> </ul>
<b>Nanoporous membranes</b>	<ul style="list-style-type: none"> <li>• Ability to control the size of the nanopores.</li> <li>• Possibility of introducing various types of samples in nanopores: crystals, inorganic compounds, organic complexes, ...</li> <li>• Forced orientation of the chromophores in the nanopores: associated with the lack of the need to use the corona poling method.</li> </ul>	<ul style="list-style-type: none"> <li>• Mechanical instability of nanoporous membrane.</li> <li>• Time-consuming in the preparation of nanoporous matrices.</li> <li>• The orientation of molecules can be different in each nanopores.</li> </ul>

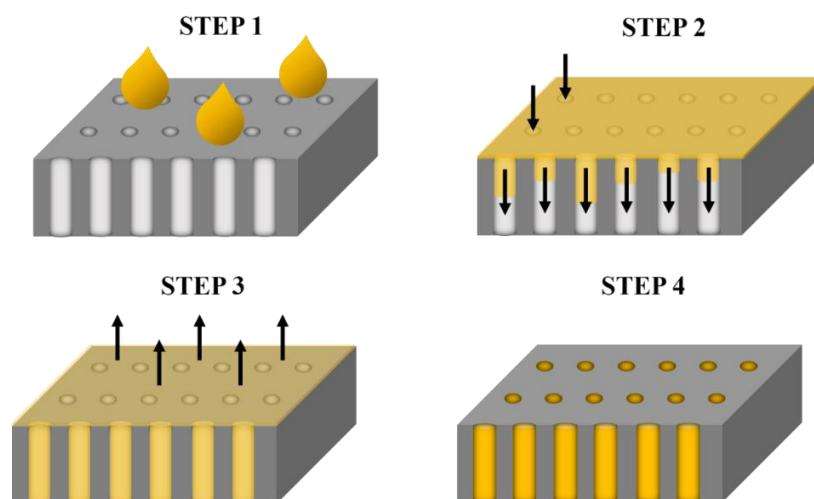
## 8.2. Samples Preparation

Additionally to the previously investigated thin films, nonlinear optical effects measurements have also been carried out on nanocomposites consisting of alumina  $Al_2O_3$  nanoporous membranes purchased from SmartMembranes Ltd. Company (Halle, Germany), with selected supramolecular complexes. Before proceeding with the preparation of the nanocomposite, the nanoporous membrane was examined using a scanning electron microscope SEM (Fig. 8.3).  $Al_2O_3$  membrane with thickness around 100  $\mu m$ , pore diameter  $\varnothing$  25 nm and interpore distance 65 nm (see Fig. 8.3) was firstly annealed for 2 hours in temperature around 200°C. Then, each of the selected

supramolecular samples was dissolved in an appropriate solvent, creating solutions with selected concentrations. Afterwards, the solutions were introduced into the nanoporous membranes and the prepared nanocomposites were annealed for 3h in less than 100°C to evaporate solvent. The entire process of obtaining a nanocomposite is shown schematically in Fig. 8.4. Moreover, Fig. 8.5 presents response during SHG experiment in pure  $\text{Al}_2\text{O}_3$  nanoporous membrane. It was noted, that SHG effect is not observable in pure membrane.



**Figure 8.3:** SEM image of nanocomposite (left); Schematic representation of a nanocomposite consisting of a nanoporous alumina membrane and supramolecular compound (right).



**Figure 8.4:** The process of preparing the nanocomposite. Step 1: Applying the solution to the membrane. Step 2: Absorbing the solution into the nanopores. Step 3: Solvent evaporation.

Step 4: Membrane with the material in nanopores.

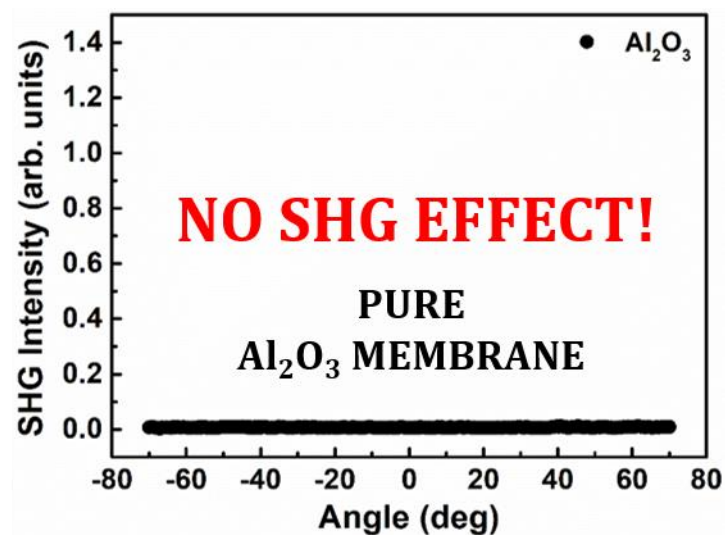


Figure 8.5: Lack of SHG response in pure nanoporous  $\text{Al}_2\text{O}_3$  membrane.

### 8.3. Porphyrin Complex Nanocomposite

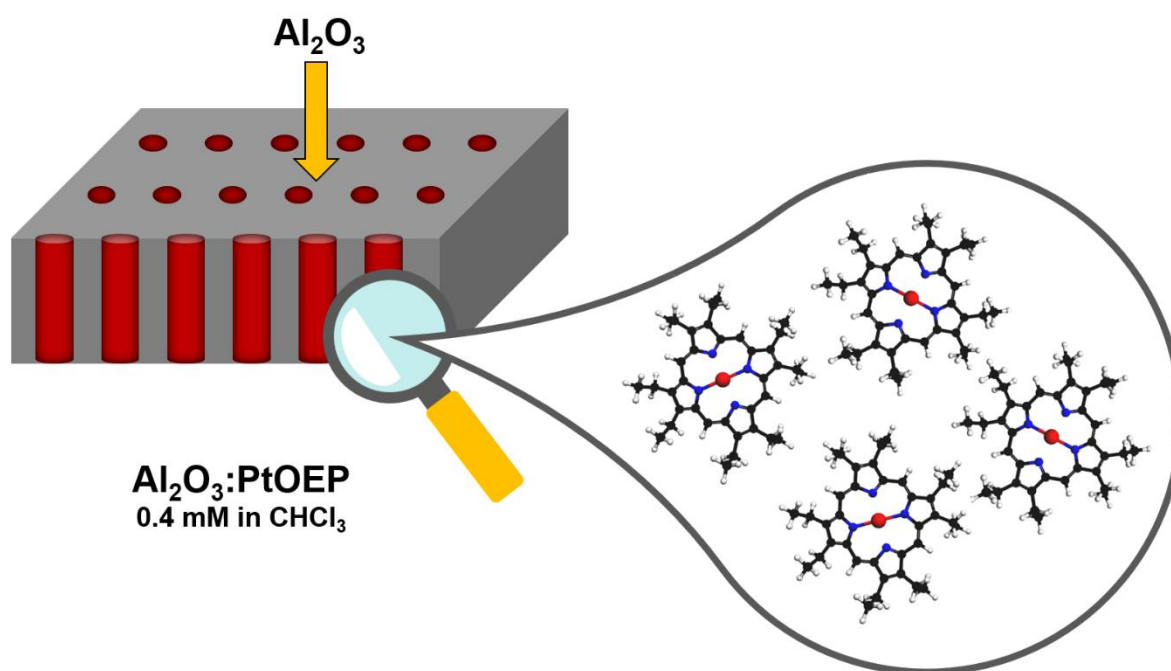
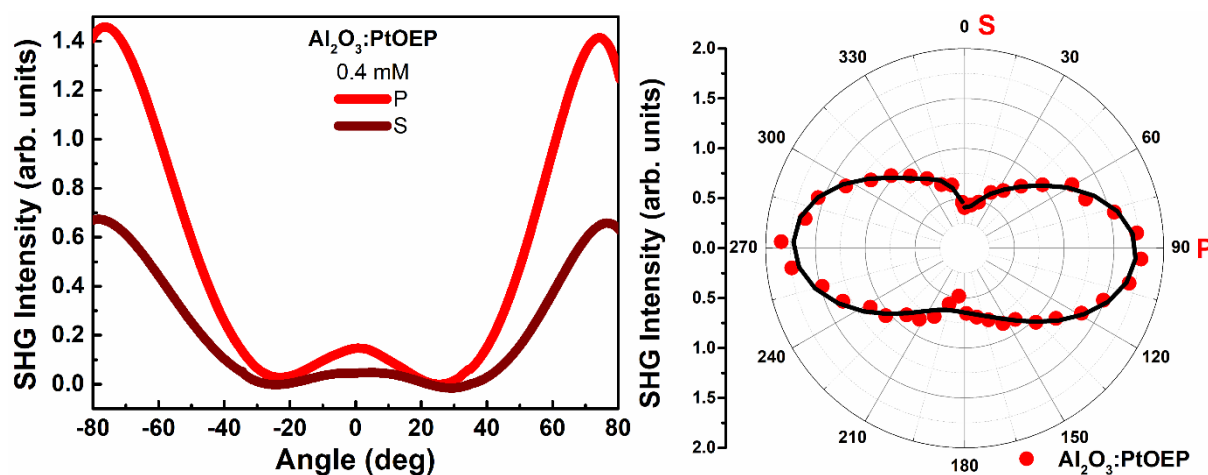


Figure 8.6: Schematic illustration of  $\text{Al}_2\text{O}_3:\text{PtOEP}$  nanocomposite.

Nanocomposite metamaterial consisting of an  $\text{Al}_2\text{O}_3$  nanoporous membrane and complex porphyrin with platinum metal **PtOEP** has been prepared from a solution with a concentration of

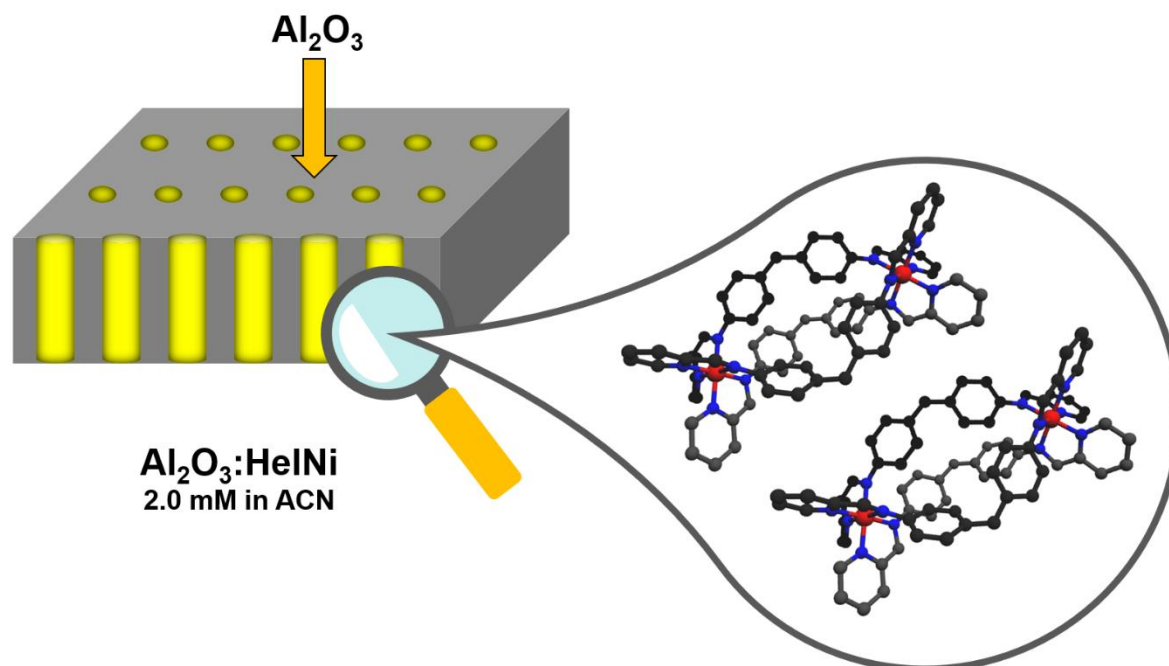
0.4 mM in chloroform  $\text{CHCl}_3$ . Such a concentration was selected on the basis of previous NLO studies described in Chapter 5. The obtained nanocomposite was schematically presented in Fig. 8.6. Inside nanopores are **PtOEP** molecules that are red colour, therefore a membrane that usually is colourless, but not transparent, has red reflections.

Moreover, Fig. 8.7 presents second-order NLO response of  **$\text{Al}_2\text{O}_3$ :PtOEP** nanocomposite investigated by means of second harmonic generation via Maker fringe technique. The determined dependence on polarization in this case was obtained, which was not noticed in the case of SHG measurement of the thin film **PtOEP**. Nevertheless, strong dependence on polarization can be clearly seen from Fig. 8.7b. However, nanopores in  $\text{Al}_2\text{O}_3$  membrane force molecules to orientation which is more likely to polarization P. **PtOEP** in general has planar structure however with nanoporous membrane, which is characterized by no second-order NLO effect (Fig. 8.5.), forms a nanocomposite which itself generate second order nonlinear effect by forced orientation of molecules. This strongly locates nanocomposites in their usefulness in devices based on nonlinear optics.



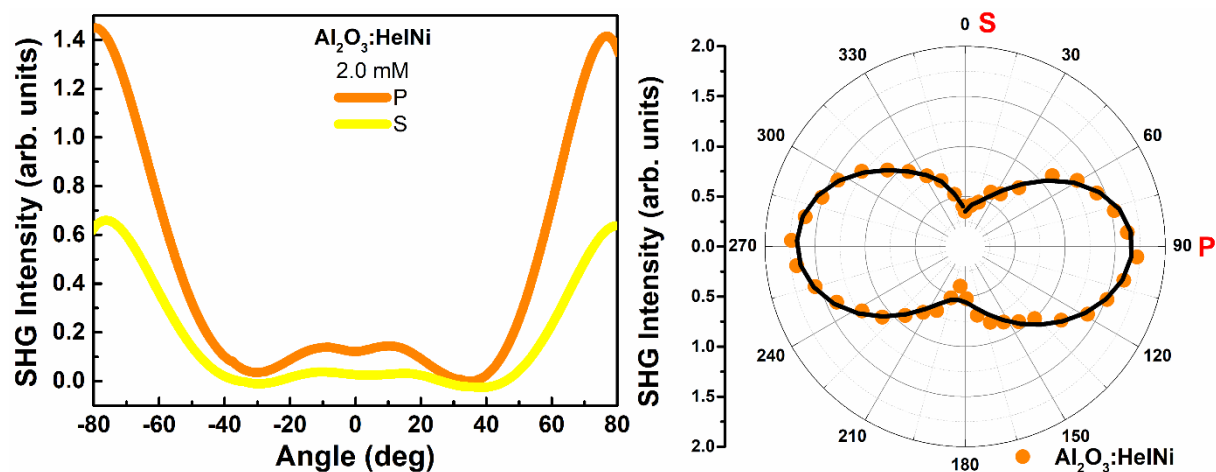
**Figure 8.7:** SHG intensities as a function of rotation angle in s- and p-polarized laser beam (left) and as a dependence of laser polarization (right) of  **$\text{Al}_2\text{O}_3$ :PtOEP** nanocomposite.

#### 8.4. Triple Stranded Helicate Nanocomposite



**Figure 8.8:** Schematic illustration of  $\text{Al}_2\text{O}_3:\text{HeINi}$  nanocomposite.

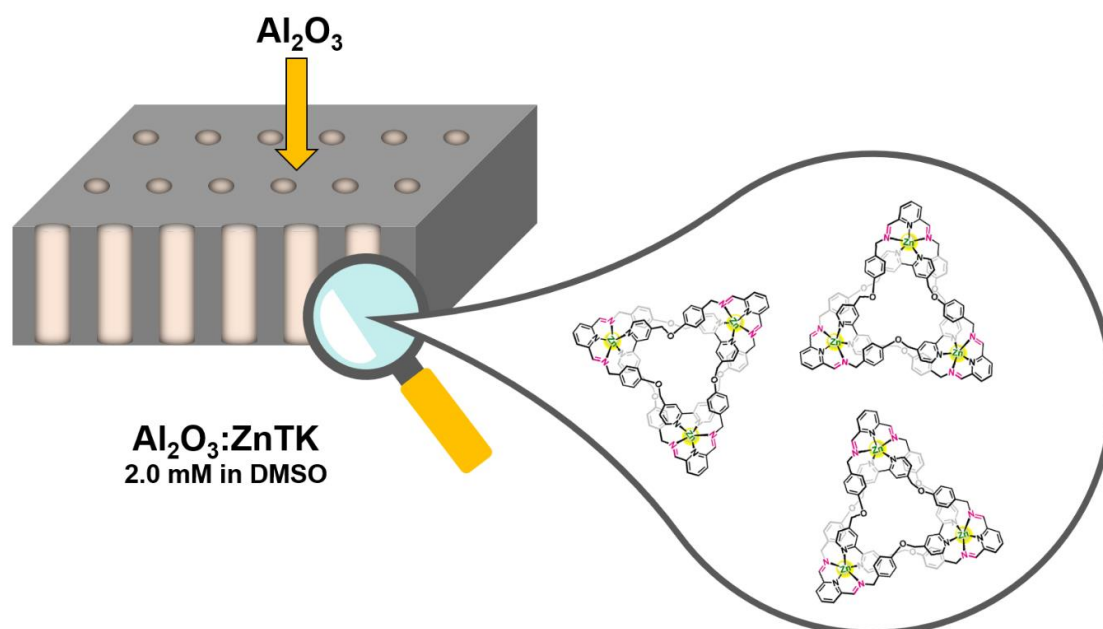
Similarly to the nanocomposite of the selected porphyrin complex, the metamaterial consisting of  $\text{Al}_2\text{O}_3:\text{HeINi}$  triple helicate with Ni(II) cation was obtained from the solution. Based on nonlinear optical research described in Chapter 6, the concentration of 2.0 mM in acetonitrile ACN solution was selected. The obtained nanocomposite, with a slight yellow colour, schematically shown in Fig. 8.8. Furthermore, the second-order nonlinear optical studies by Maker fringe method brought a similar result as in the case of the previous nanocomposite. Unlike the NLO investigations described in Chapter 6, carried out on thin films, there was no need to use corona poling technique, and SHG signal itself is enhanced and dependent on the applied polarization, which is visible in Fig. 8.9. This type of metamaterials can be widely used in NLO and nanophotonics devices that are dependent on polarization.



**Figure 8.9:** SHG intensities as a function of rotation angle in s- and p-polarized laser beam (left) and as a dependence of laser polarization (right) of  $\text{Al}_2\text{O}_3:\text{HeI Ni}$  nanocomposite.

### 8.5. Modified Pyrene-Based Complex Nanocomposite

Following the results of nonlinear optical investigations described in Chapter 7, nanocomposites containing modified-pyrene based complexes were obtained from solutions with a concentration of 2.0 mM in dimethyl sulfoxide DMSO.



**Figure 8.10:** Schematic illustration of  $\text{Al}_2\text{O}_3:\text{ZnTK}$  nanocomposite.

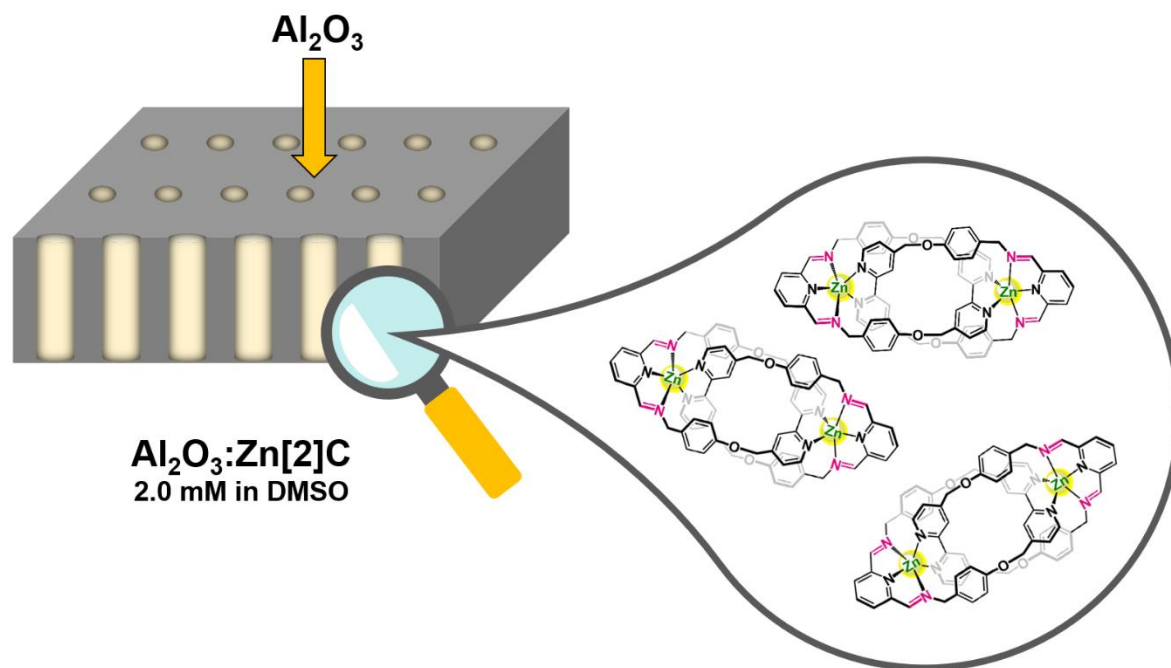


Figure 8.11: Schematic illustration of  $\text{Al}_2\text{O}_3:\text{Zn}[2]\text{C}$  nanocomposite.

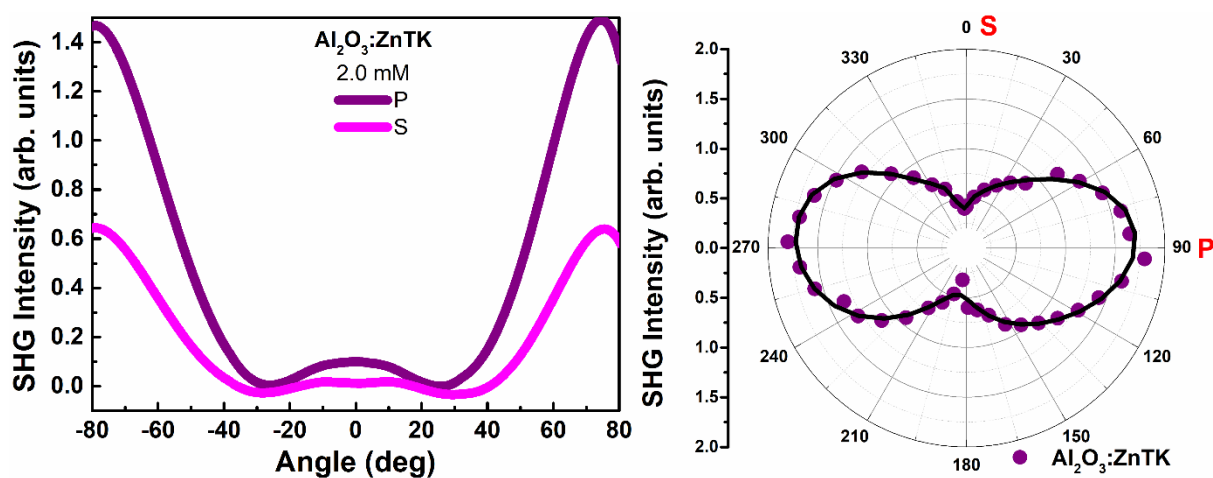
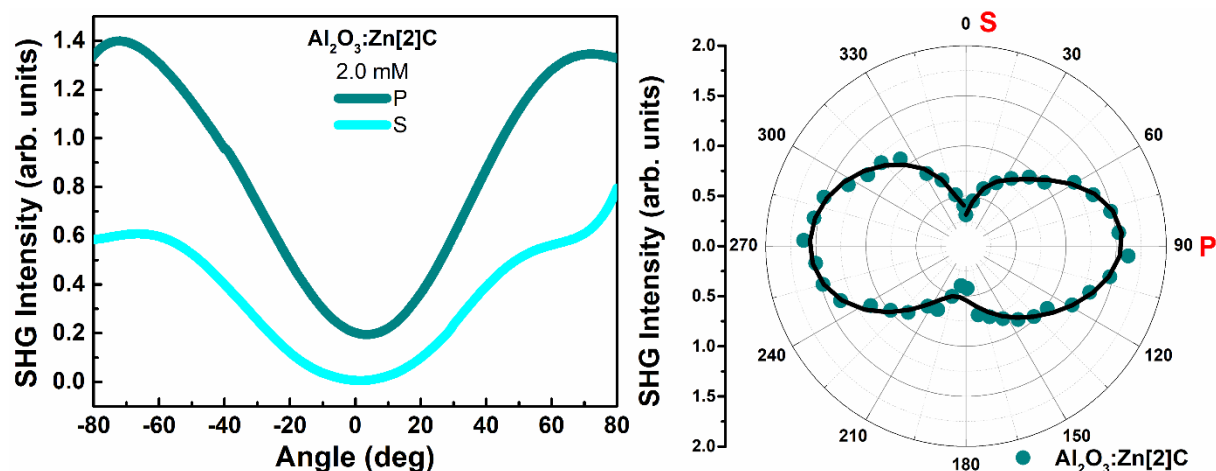


Figure 8.12: SHG intensities as a function of rotation angle in s- and p-polarized laser beam (left) and as a dependence of laser polarization (right) of  $\text{Al}_2\text{O}_3:\text{ZnTK}$  nanocomposite.

From the studied supramolecular complexes of this group, two compounds were selected, one  $\text{ZnTK}$  representing the trefoil knot group, and  $\text{Zn}[2]\text{C}$  representing the [2]catenane group. The



obtained  $\text{Al}_2\text{O}_3:\text{ZnTK}$  and  $\text{Al}_2\text{O}_3:\text{Zn}[2]\text{C}$  metamaterials are shown schematically in Figs. 8.10 - 8.11.

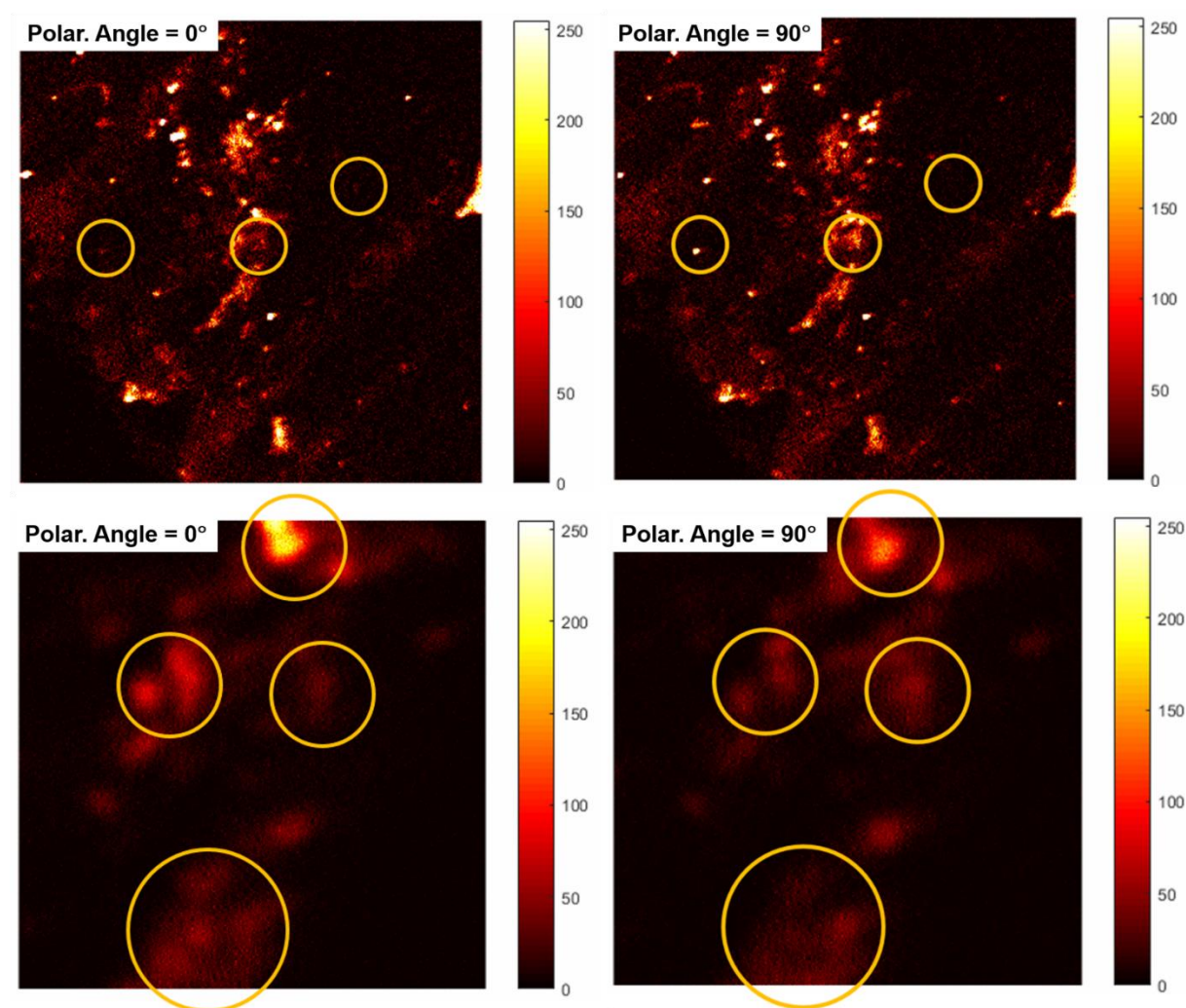


**Figure 8.13:** SHG intensities as a function of rotation angle in s- and p-polarized laser beam (left) and as a dependence of laser polarization (right) of  $\text{Al}_2\text{O}_3:\text{Zn}[2]\text{C}$  nanocomposite.

NLO research on the investigated nanocomposites was carried out on the basis of the SHG effect using the Maker fringe method. Figures 8.12 - 8.13 show the second-order nonlinear optical responses for the studied metamaterials. As in the case of the nanocomposites studied in this chapter, the nanocomposites containing modified-pyrene based supramolecular complexes show a strong dependence of the second harmonic generation in relation to the applied polarization of S and P. Moreover, the  $\text{Al}_2\text{O}_3:\text{Zn}[2]\text{C}$  nanocomposite is characterized by a slightly different signal shape from the previous ones studied samples. This is due to the fact that the investigated membranes do not show fully periodic distribution of nanopores, which can be seen in the SEM image of the membrane (see Fig. 8.3). There are also small places where there are no nanopores. Besides, the measurement of the second harmonic generation on nanoporous materials is not the easiest one, due to the above-mentioned properties. However, also in this case the signal is highly polarization dependent, which could be used in modulated nonlinear optics devices.

## 8.6. SHG Imaging

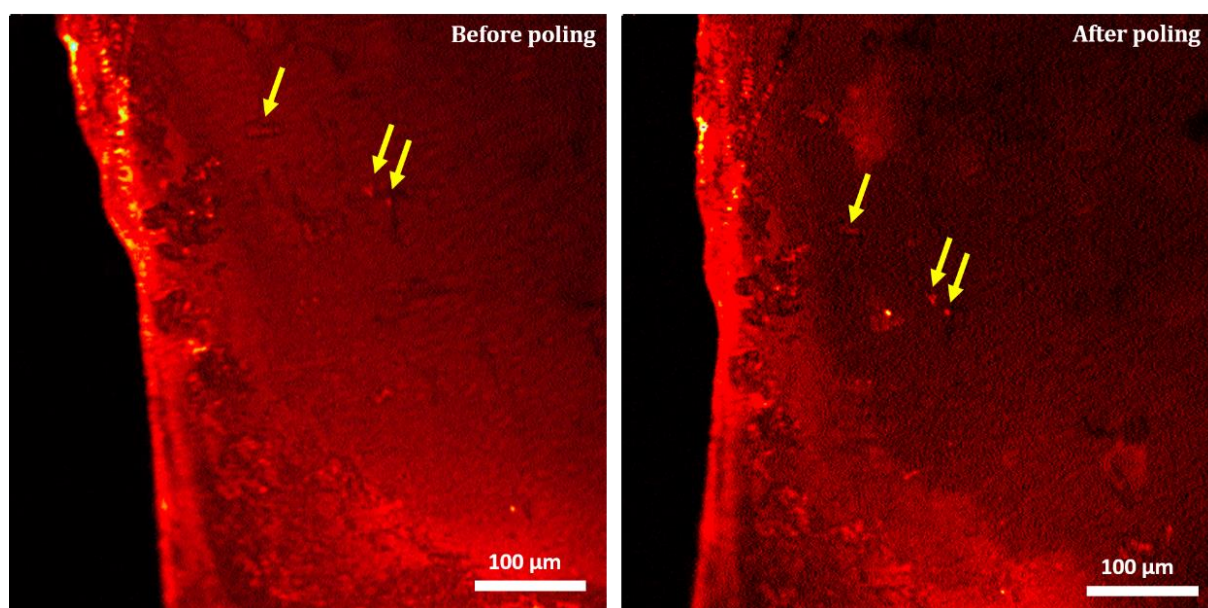
In addition to investigating the SHG effect by the Maker fringe method, the second-order nonlinear response of the nanocomposite surface was investigated using the experimental system described in Ref. [8.9]. Figs. 8.14 present the nonlinear SHG response of the  $\text{Al}_2\text{O}_3:\text{HeINi}$  nanocomposite surface depending on the polarization.



**Figure 8.14:** SHG responses on the  $\text{Al}_2\text{O}_3:\text{HeINi}$  nanocomposite surface dependent on polarization.

In the above SHG images, characteristic points are marked, which either become stronger when the polarity changes from S to P, or opposite. This means that molecules can orient themselves in

different directions in nanopores, which means that some places have a higher nonlinear SHG response for S polarization, while others for polarization P. In the Maker fringe method, the SHG signal is collected from a large area, which in the case of the studied nanocomposites SHG response in large area is more enhanced for the P polarization. Moreover, from the SEM image shown in Fig. 8.3a it can be seen that the nanopores are not periodically distributed, there are some "islands" of periodicity, which may also mean that for one area of the molecule they may orient themselves in another direction than for the adjacent area. Moreover, SHG imaging measurements were also performed before and after corona poling. The results are shown in Fig. 8.15. On the obtained microscope images, characteristic points are marked, which are not enhanced after the corona poling method. The conclusion of this experiment is that the corona poling of these nanocomposites does not affect the generated SHG signal.



**Figure 8.15:** SHG responses on the  $\text{Al}_2\text{O}_3:\text{HeI Ni}$  nanocomposite surface before and after applying corona poling technique.

## 8.7. Conclusions

This chapter presented studies of the nonlinear optics of nanocomposites with selected supramolecular compounds previously studied in this thesis. From each type of investigated compounds, one of the most interesting complexes was selected and introduced into a nanoporous alumina  $\text{Al}_2\text{O}_3$  membrane from solutions. From the complex porphyrins, platinum octaethylporphyrin **PtOEP** was selected, with a concentration of 0.4 mM in  $\text{CHCl}_3$  chloroform, from triple helicates compounds, a compound with nickel cations **HelNi** with a solution concentration of 2.0 mM in acetonitrile ACN was selected, while modified pyrene-based complexes represented trefoil knot with zinc metal **ZnTK** and [2]catenane with zinc metal **Zn[2]C** with concentrations of 2.0 mM solutions in dimethyl sulfoxide DMSO. Nonlinear optical studies were carried out on the basis of the Maker fringe method, examining the generation of the second harmonic SHG. Overall, the investigations achieved the SHG signal without applying the symmetry breaking method previously used in thin film studies. This macroscopic symmetry is achieved due to the forced orientation of the dipole moments in the nanopores of the membrane. This is an important action when using metamaterials in devices based on photonics and nonlinear optics. Moreover, it was noticed that the SHG signal is characterized by similar shape for each nanocomposite and the intensity is more or less at a similar level. This is most likely the result of the properties of the membrane, the significant distribution of nanopores, as well as their diameter. As a perspective for further work, it seems interesting to produce nanocomposites with different nanoporous membranes, i.e. with the arrangement of the nanopores, the diameter of the nanopores, the thickness of the membrane, etc. Moreover, the SHG imaging on the surface of nanocomposites studies showed that the orientation of the molecules in the nanopores can go in different directions and that the corona poling technique has no effect on the enhancement of the SHG response. Due to the fact that the obtained nanocomposites are neither crystals nor thin films, the  $\chi^{(2)}$  calculations for these samples were not provided on the basis of the theoretical

models described in this work in Chapter 4. Another perspective of this work is to determine the theoretical model that allows to calculate the parameters of nonlinear optics, including nonlinear susceptibility, which is already used in calculations for crystals as well as thin films.

## Literature

- [8.1] K. Waszkowska, T. Chtouki, O. Krupka, V. Smokal, V. Figa, B. Sahraoui, Effect of UV-Irradiation and ZnO Nanoparticles on Nonlinear Optical Response of Specific Photochromic Polymers, *Nanomaterials* 2021, 11, 492
- [8.2] P. Plóciennik, D. Guichaoua, A. Korcala, A. Zawadzka, Studies of aluminum oxide thin films deposited by laser ablation technique, *Optical Materials* 56 (2016) 49–57
- [8.3] A. Ayadi, A. Szukalski, A. El-Ghayoury, K. Haupa, N. Zouari, J. Myśliwiec, F. Kajzar, B. Kulyk, B. Sahraoui, TTF based donor- $\pi$ -acceptor dyads synthesized for NLO applications, *Dyes and Pigments* 138 (2017) 255e266
- [8.4] H. El Ouazzani, K. Iliopoulos, M. Pranaitis, O. Krupka, V. Smokal, A. Kolendo, B. Sahraoui, Second- and Third-Order Nonlinearities of Novel Push-Pull Azobenzene Polymers, *J. Phys. Chem. B* 2011, 115, 1944–1949
- [8.5] B. Kulyk, K. Waszkowska, A. Busseau, C. Villegas, P. Hudhomme, S. Dabos-Seignon, A. Zawadzka, S. Legoupy, B. Sahraoui, Penta(zinc porphyrin)[60]fullerenes: Strong reverse saturable absorption for optical limiting applications, *Applied Surface Science* 533 (2020) 147468
- [8.6] N. Andrushchak, B. Kulyk, P. Göring, A. Andrushchak, B. Sahraoui, Study of Second Harmonic Generation in KDP/Al<sub>2</sub>O<sub>3</sub> Crystalline Nanocomposite, *Acta Physica Polonica A*, No 4, Vol. 133, 2018.

- [8.7] K. Waszkowska, R. Wielgosz, T. Travers, M. Lelonek, P. Göring, D. Gindre, B. Sahraoui, Second-Order Nonlinear Optical Response of Ba(NO<sub>3</sub>)<sub>2</sub>/Al<sub>2</sub>O<sub>3</sub> Nanocomposite, 2020 22nd International Conference on Transparent Optical Networks (ICTON), 2020, pp. 1-4.
- [8.8] K. Waszkowska, P. Josse, C. Cabanetos, P. Blanchard, B. Sahraoui, D. Guichaoua, I. Syvorotka, O. Kityk, R. Wielgosz, P. Huber, A. V. Kityk, Anisotropic confinement of chromophores induces second-order nonlinear optics in a nanoporous photonic metamaterial, Optics Letters, 46 (4), 2021
- [8.9] D. Gindre, I. Ka, A. Boeglin, A. Fort, K. D. Dorkenoo, Image storage through gray-scale encoding of second harmonic signals in azo-dye copolymers, Applied Physics Letters 90, 094103, 2007.

## SUMMARY

The above monograph presented research of optical properties of selected supramolecular complexes as their usefulness in future applications, mainly in relation to nonlinear optics. In this doctoral thesis, three main types of supramolecular compounds have been selected, representing porphyrins, triple helicates and pyrene-based complexes. The research was divided into four parts: the first three presented studies on each separate group of investigation supramolecules, the last part, the fourth one presented research in the field of nanotechnology.

Porphyrins are one of the most interesting organic chemical compounds, find wide application for instance in medicine, include unique physicochemical properties, and often used to build supramolecular complexes: octaethylporphyrins with platinum **PtOEP**, with ruthenium **RuOEP**, with iron **FeOEP** and with palladium **PdOEP**. This work presented the spectroscopic and nonlinear optical properties of a group of four modified porphyrin complexes (so-called metalloporphyrins) with a simple chemical structure, which can be used as models for the construction of supramolecular compounds and NLO investigations. Spectroscopic studies carried out on thin film confirmed the emission of red color with a short lifetime of fluorescence and, in addition, concluded the influence of absorption on subsequent studies of nonlinear optics. The studies of nonlinear optics focused primarily on the usefulness of porphyrin complexes, as well as the influence of the substituent on the obtained NLO response. The second and third harmonic generation studies provided by the Maker fringe method proved the enhancement of both effects in relation to the samples. The most enhanced SHG and THG signals by the Maker fringe method were obtained for the **FeOEP** sample, however in another experiment the strongest response was found for the **PtOEP** sample, due to strong linear absorption at laser excitation wavelength. It was also concluded that the values of second order NLO susceptibilities in some cases, such as for the **FeOEP** sample, differ significantly from the applied calculation model, which require more

parameters related directly to the sample and parameters dependent on polarization. Therefore, a third experiment was carried out using the Z-scan method, in which solutions of the same concentration were used, thanks to which it was easier to compare the obtained results with each other. The obtained results clearly indicate the universality of each of the studied metalloporphyrin samples, as they are characterized by both strong saturable absorption (**PtOEP** and **FeOEP**) and reverse saturable absorption (**RuOEP** and **PdOEP**), while in nonlinear refraction properties they show strong self-focusing properties (**PtOEP**, **RuOEP** and **PdOEP**) and self-defocusing (**FeOEP**). Each of these samples can be used promisingly in devices based on nonlinear optics, as data storage devices, and also due to the strong nonlinear absorption properties, as optical limiters and in devices using Q-switching. Future work will be based on quantum chemical simulations, thanks to which it will be possible to more accurately analyze the experimentally obtained NLO results based on intermolecular interactions.

Apart from the above-mentioned metalloporphyrins, helicates are another very important group of supramolecular assemblies. One of the most important and intensively studied structure is the DNA double helix. In addition, other varieties of helicates are used in many fields of science, but from the perspective of this work, a triple helix with two metal cations was selected for nonlinear optical studies: iron(II) **HelFe**, nickel(II) **HelNi**, cobalt(II) **HelCo** and zinc(II) **HelZn**, to using self-assembly in NLO instead of mononuclear complexes. Similarly to metalloporphyrins, spectroscopic studies have shown that the generated harmonic signal in case of triple helicates is simultaneously absorbed by the sample, which translates into the use of theoretical models taking absorption into account. Using the Maker fringe method in the second and third harmonic generation studies, as well as the method based on the study of the intensity of the generated signal, in both cases and in both SHG and THG experiments, the most enhanced NLO response was obtained for the **HelNi** sample, however, the signals in the graphical form, as also the calculated second and third order NLO susceptibilities are not significantly different for the other triple



helicates samples. Moreover, no significant difference to the applied laser light polarization was noticed. In addition, the third-order NLO studies using the Z-scan method showed that the **HelFe** sample does not show NLO refractive properties, but is the only supramolecular complex of this group showing absorption properties, namely NLO saturable absorption, the effect of which increases with dilution of the solution. The remaining **HelCo**, **HelNi** and **HelZn** complexes are characterized by a self-focusing effect, where the most enhanced effect was again observed for the **HelNi** sample, however slightly different from the other samples. Furthermore, quantum chemical calculations were simulated to understand the NLO effects in these supramolecular complexes based on triple stranded helicates. The theoretically evaluated energy gap of the compounds showed the high rate of electron transfer from the ground to the excited state. However, a significant reduction in the energy gap in the molecule investigated compounds causes a large increase in third-order nonlinear properties. The interligand  $\pi \rightarrow \pi^*$  transmetallic charge-transfer (TTCT) supports noncentrosymmetric charge density distribution resulting in the molecules possessing second-order NLO properties. Moreover, the calculated theoretical values of second- and third-order hyperpolarizabilities were found to be in good agreement with the experimental response. Moreover, obtained results give proof of using supramolecular assemblies in nonlinear optics and modification of their nature will be interesting for NLO studies. Those unique NLO properties place supramolecular triple stranded helicates as one of the most promising candidates for applications based on nonlinear optics for instance as data storage materials.

Recently, a significant increase in research on metal-ligand organic coordination complexes has been noticed. This work focuses on the study of nonlinear optics in topologically nontrivial structures of two types of modified pyrene-based supramolecular complexes: trefoil knot and [2]catenane, also containing zinc or cadmium cations. Absorption studies showed a strong correlation for third-order NLO studies, however with longer wavelengths the samples were optically transparent emitting blue or green light, which had no direct impact on the generated

second harmonic signal. It was noticed that, as in the case of previously studied supramolecular compounds, thin films of modified pyrene-based complexes are characterized by an enhanced SHG and THG effects, slightly dependent on the polarization of laser light. Z-scan studies with solutions of various concentrations from 2.0 to 0.5 mM showed extraordinary dependence. All the complexes showed strong NLO refractive properties, but did not show the NLO absorption properties. In addition, a building material used as a ligand in both types of supramolecular compounds, pyrene diformylpyridine **PyDFP** has the weakest third-order NLO effect, while pyrene trefoil knot **PyTK** and pyrene [2]catenane **Py[2]C** exhibit an enhanced effect during the NLO Z-scan method. Moreover, supramolecular compounds containing zinc **ZnTK** and cadmium **CdTK** cations further enhance this effect in comparison to **PyTK**, and in the case of [2]catenane, the use of **Zn[2]C** and **Cd[2]C** is characterized by the enhancement of the effect compared to **Py[2]C**. These unique nonlinear optical properties of modified pyrene-based complexes prove that by changing nature of supramolecular systems we can control NLO response and they can be used in promising applications in NLO devices as, for example, self-modulators or data storage. The perspectives of this work are subsequent studies is an in-depth analysis of the obtained results of nonlinear optics based on quantum chemical simulations.

From the above-described three types of supramolecular compounds with unique properties, one of the most interesting complexes was selected from every group, creating a metamaterial, and second-order nonlinear properties were investigated. The metamaterials studied are nanocomposites consisting of a selected supramolecular compound placed in the nanopores of the  $\text{Al}_2\text{O}_3$  membrane. Each of these complexes was introduced to nanopores in the form of a solution with subsequent evaporation of the solvent: **PtOEP** with a concentration of 0.4 mM in  $\text{CHCl}_3$ , **HeINi** with a concentration of 2.0 mM in ACN and **ZnTK**, **Zn[2]C** with concentrations of 2.0 mM in DMSO. The Maker fringe SHG studies gave extraordinary results for each metamaterial. First of all, the generation of the second harmonic was possible without the use of the corona

poling method, because the orientation of dipole moments is already arranged in nanopores. Another quite important observation was the fact that the SHG signal, compared to thin films, is strongly enhanced and comes only from supramolecules. There is no loss in the NLO response, as is the case with thin film guest-host systems, when losses occur through the use of a polymer matrix (e.g. PMMA) where the concentration of studied material to polymer is typically 5-20%. Moreover, the obtained SHG response strongly depended on the applied laser light polarization. These unique properties of nanocomposites composed of supramolecular complexes and nanoporous membranes place them in potential applications in nonlinear optics and nanophotonics devices, including modulators. Moreover, another perspective of this research is to create a computational model of NLO parameters, such as nonlinear susceptibility, for samples consisting of a nanoporous membrane and the investigated material.

## LIST OF SYMBOLS

$A$	absorbance
$A_\omega$	amplitude of the fundamental beam
$A_{3\omega}$	amplitude of the generated third harmonic
$A$	complex amplitude of the second harmonic generation
$B$	complex amplitude of the second harmonic generation
$\vec{B}$	vector of magnetic induction
$C_{Air}$	contribution of air relative to vacuum
$c$	speed of light in vacuum
$c.c.$	complex conjugate
$c_0$	initial coating concentration
$\vec{D}$	vector of electric induction
$d$	thickness
$E$	energy
$E^\omega$	incident electric field
$E_F$	Fermi energy
$\vec{E}$	vector of electric field strength
$e$	evaporation rate
$\hat{e}^r$	unit polarization vector
$\vec{H}$	vector of magnetic field strength
$h$	Planck's constant
$I_\omega$	intensity of the incident light
$I^{2\omega}$	maximum amplitude of SHG of material
$I^{3\omega}$	maximum amplitude of THG of material
$I_{POM}^{2\omega}$	maximum amplitude of SHG of POM
$I_{Quartz}^{2\omega}$	maximum amplitude of SHG of quartz
$I_{Silica}^{3\omega}$	maximum amplitude of THG of silica
$\vec{J}$	vector of total current density
$K$	degeneration factor

$\vec{k}$	vector of fundamental wavelength
$k_B$	Boltzmann constant
$k_{nr}$	radiation transient velocity
$L_C$	coherence length
$L_{Silica}^{coh}$	coherent length of silica
$L_{Quartz}^{coh}$	coherent length of quartz
$l$	thickness
$\vec{M}$	vector of magnetic polarization
$n_0$	linear refractive index
$n_2$	nonlinear refractive index
$n_\omega$	refractive index for fundamental beam
$n_{2\omega}$	refractive index of generated second harmonic
$n_{3\omega}$	refractive index of generated third harmonic
$\vec{P}$	vector of electric polarity
$\vec{P}^{NL}$	nonlinear polarization of medium
$r$	coordinates
$r_a$	radius of the aperture
$S_0$	ground state
$S_1$	singlet excited level
$T$	temperature
$T$	transmittance
$T_1$	triplet excited level
$t$	time
$t^\omega$	fundamental wave transmission coefficient
$w_a$	radius of the laser beam
$\alpha$	linear absorption coefficient
$\beta$	nonlinear absorption coefficient
$\Gamma$	radiation emission rate
$\Delta k$	phase matching parameter
$\Delta T_{P-V}$	difference between the maximum and minimum transmission in CA Z-Scan
$\Delta \epsilon$	dispersion of the dielectric constant

$\Delta\Phi_0$	electric field nonlinear phase change
$\Delta\Psi$	difference of phase angles
$\delta_{ij}$	isotropic second-order tensor
$\varepsilon_0$	permittivity of free space
$\theta_j$	propagation angle
$\theta_\omega$	angle of fundamental wave
$\theta_{2\omega}$	angle of generated second harmonic wave
$\kappa$	extinction coefficient
$\kappa_m$	extinction coefficient of the nonlinear medium
$\kappa_\omega$	extinction coefficient of fundamental wavelength
$\kappa_{2\omega}$	extinction coefficient of generated second harmonic wavelength
$\lambda_\omega$	wavelength of the fundamental beam
$\mu$	magnetic permittivity of medium
$\nu$	frequency
$\nu_0$	initial kinetic viscosity
$\rho$	volumetric density of charge
$\tau_L$	luminescence lifetime
$\tau$	pulse duration
$\Phi$	phase angle
$\chi_e$	electrical susceptibility
$\chi_e^{(1)}$	linear electric susceptibility
$\chi_e^{(2)}$	second-order nonlinear optical susceptibility
$\chi_e^{(3)}$	third-order nonlinear optical susceptibility
$\chi_{elec}^{(3)}$	electronic component linked to the deformation of the electronic cloud
$\chi_m$	magnetic susceptibility
$\chi_{mol}^{(3)}$	molecular component linked to the movements of the molecule
$\chi'^{(3)}$	real part responsible for nonlinear variations in the refractive index
$\chi''^{(3)}$	imaginary part related to nonlinear absorption of light and stimulated scattering
$\chi_{ijk}^{(2)}$	three-rank tensor of nonlinear optical susceptibility
$\chi_{ijkl}^{(3)}$	four-rank tensor of nonlinear optical susceptibility

$\chi_{POM}^{(2)}$	nonlinear optical susceptibility of POM
$\chi_{Quartz}^{(2)}$	nonlinear optical susceptibility of quartz
$\chi_{Air}^{(3)}$	nonlinear optical susceptibility of air
$\chi_{Silica}^{(3)}$	nonlinear optical susceptibility of silica
$\Psi$	phase angle
$\omega$	frequency
$\omega_r$	angular rotation speed

# LIST OF FIGURES

## CHAPTER 1

<b>Figure 1.1:</b> The nucleus and the electron cloud are shifted relative to each other under the influence of light .....	<b>11</b>
<b>Figure 1.2:</b> Geometry of generated second harmonic and energy level diagram described SHG process .....	<b>12</b>
<b>Figure 1.3:</b> Geometric representation of the propagation of the fundamental and second harmonic waves in a nonlinear medium .....	<b>17</b>
<b>Figure 1.4:</b> Interaction geometry during the third harmonic generation process and energy level diagram described THG process .....	<b>18</b>
<b>Figure 1.5:</b> Schematic representation of two processes that can take place during interaction of three incident waves with nonlinear medium.....	<b>23</b>
<b>Figure 1.6:</b> Interaction of the electromagnetic field with a two-level system.....	<b>25</b>
<b>Figure 1.7:</b> Transmission in a medium of thickness $l$ .....	<b>27</b>
<b>Figure 1.8:</b> Numerous processes of multiphoton absorption .....	<b>28</b>
<b>Figure 1.9:</b> Schematic illustration of self-focusing ( $n_2 > 0$ ) and self-defocusing ( $n_2 < 0$ ) effect.....	<b>32</b>

## CHAPTER 2

<b>Figure 2.1:</b> NaCl as an examples of material with ion-ion interactions (a) and chemical structure of tris(diazabicyclooctane) used as a host to build supramolecular systems (b).....	<b>41</b>
---	-----------



<b>Figure 2.2:</b> Schematic structures of 12-crown-4-Lithium complex (LiSCN) and [Ru(BPy) <sub>3</sub> ] <sup>2+</sup> .....	42
<b>Figure 2.3:</b> Schematic example of dipole-dipole interaction. ....	43
<b>Figure 2.4:</b> Schematic examples of strong and weak hydrogen bonds.....	44
<b>Figure 2.5:</b> Schematic example of double helix DNA structure.....	44
<b>Figure 2.6:</b> Schematic example of Halogen bond interaction (red bond).....	44
<b>Figure 2.7:</b> Schematic example of van der Waals interactions.....	45
<b>Figure 2.8:</b> Schematic examples of complexes with face to face $\pi$ - $\pi$ stacking (a) and cation- $\pi$ interaction (sodium tetrabenzoyloxy-p-tert-butylcalix[4]arene (3NaI) complex) [2.28] (b).....	46
<b>Figure 2.9:</b> Schematically presented mechanism of forming supramolecular complex caused by hydrophobic effect.....	47
<b>Figure 2.10:</b> Schematic illustration of molecular recognition process.....	48
<b>Figure 2.11:</b> Scheme describing the formation of a supramolecule in guest-host interaction.....	48
<b>Figure 2.12:</b> Schematic example of guest-host supramolecular complex.....	49
<b>Figure 2.13:</b> Schematic example of crown ether complex (1,10-Diaza-18-Crown-6) with potassium.....	51
<b>Figure 2.14:</b> Schematic example of supramolecular cryptandium Li <sup>+</sup> complex.....	52
<b>Figure 2.15:</b> Schematic example of multi-layer chiral cyclophane.....	53
<b>Figure 2.16:</b> Schematic example of cyclodextrin complex.....	54
<b>Figure 2.17:</b> Schematically representation of rotaxanes.....	55

<b>Figure 2.18:</b> Schematic exemplary supramolecular calixarene structure with a $C_{60}$ molecule in centre.....	56
<b>Figure 2.19:</b> The schematic exemplary illustration of a supramolecular protein: on the left - presentation of the arrangement of individual atoms, on the right - a ribbon model.....	57
<b>Figure 2.20:</b> Schematic example of triple metallo-helicate.....	58
<b>Figure 2.21:</b> The structure of MOF-5 [2.96].....	60
<b>Figure 2.22:</b> Schematic example of supramolecular structure with porphyrin ring.....	61

### CHAPTER 3

<b>Figure 3.1:</b> Jabłoński diagram.....	78
<b>Figure 3.2:</b> Simplified Jabłoński diagram illustrating the fluorescence lifetime.....	80
<b>Figure 3.3:</b> Valence bands (highest occupied by electrons) and conduction bands (empty). The electrical properties of the solid depend on the energy gap between them (difference between HOMO - LUMO). A large energy gap is typical for an insulator, medium describes semiconductor, while a zero energy gap is typical for metals.....	83
<b>Figure 3.4:</b> Division of low-dimensional structures in terms of their general shapes and level of spatial restrictions.....	84
<b>Figure 3.5:</b> Spin coating technique.....	86
<b>Figure 3.6:</b> Types of layer growth: (A) Volmer - Weber island growth, (B) Frank - Van der Merwe layer growth, (C) Stranski - Krastanov island-layer growth.....	89
<b>Figure 3.7:</b> Schematic of forming island film on the substrate.....	89

<b>Figure 3.8:</b> Diagram showing the basic features of the vapor deposition system.....	<b>91</b>
<b>Figure 3.9:</b> Experimental setup for Pulsed Laser Deposition technique.....	<b>92</b>
<b>CHAPTER 4</b>	
<b>Figure 4.1:</b> Three-layer scheme of the second harmonic generation system with a nonlinear medium.....	<b>96</b>
<b>Figure 4.2:</b> Propagation of a harmonic wave in a nonlinear medium placed between two linear media.....	<b>104</b>
<b>Figure 4.3:</b> Thin film deposited on a substrate and placed between two linear media.....	<b>107</b>
<b>Figure 4.4:</b> SHG and THG experimental setup via Maker fringe method.....	<b>110</b>
<b>Figure 4.5:</b> Typical Maker fringes for reference materials.....	<b>110</b>
<b>Figure 4.6:</b> Experimental setup measuring SHG and THG intensity relative to laser energy.....	<b>111</b>
<b>Figure 4.7:</b> Corona Poling setup.....	<b>112</b>
<b>Figure 4.8:</b> Orientation of dipole moment in polymer matrix during corona poling experiment.....	<b>113</b>
<b>Figure 4.9:</b> Z-scan experimental setup.....	<b>115</b>
<b>Figure 4.10:</b> Typical closed aperture Z-scan curves for $n < 0$ and $n > 0$ .....	<b>116</b>
<b>Figure 4.11:</b> Typical open aperture Z-scan curves for $\beta < 0$ and $\beta > 0$ .....	<b>119</b>
<b>Figure 4.121:</b> UV-1800 (Shimadzu) spectrometer.....	<b>120</b>
<b>Figure 4.13:</b> Photograph presents spectrofluorometer Horiba FluoroMax-4.....	<b>122</b>

<b>Figure 4.14:</b> Schematic representation of the basic elements of the atomic force microscope. The probe is placed on the top of an elastic cantilever. The sample is most often placed on a piezoelectric table. The deviation of the cantilever is monitoring by changing the laser light path deviated from the upper end of the beam by the photodiode. When the top touches the surface, deflection is monitored. This deviation can then be used to calculate the impact forces of the probe and sample.....	<b>123</b>
<b>Figure 4.15:</b> Lennard – Jones potential zones in which three most common AFM imaging modes work.....	<b>124</b>
<b>Figure 4.16:</b> Photograph presenting Nanosurf Easyscan 2 Atomic Force Microscopy.....	<b>126</b>
<b>Figure 4.17:</b> Scheme of the optical ellipsometry setup.....	<b>127</b>
<b>Figure 4.18:</b> Principles of ellipsometry.....	<b>128</b>

## CHAPTER 5

<b>Figure 5.1:</b> Chemical structures of porphyrin complexes: <b>PtOEP</b> , <b>RuOEP</b> , <b>FeOEP</b> and <b>PdOEP</b> .....	<b>135</b>
<b>Figure 5.2:</b> Atomic force microscopy (AFM) images of studied metalloporphyrin thin films: <b>PtOEP</b> a) 2-dimensional, b) 3-dimensional; <b>RuOEP</b> c) 2-dimensional, d) 3-dimensional; <b>FeOEP</b> e) 2-dimensional, f) 3-dimensional; <b>PdOEP</b> g) 2-dimensional, h) 3-dimensional.....	<b>137</b>
<b>Figure 5.3:</b> Atomic force microscopy profiles of studied metalloporphyrin thin films.....	<b>138</b>
<b>Figure 5.4:</b> Normalized UV-Vis absorption spectra of investigated porphyrin complexes, including THG (355 nm) and SHG (532 nm) wavelengths.....	<b>138</b>
<b>Figure 5.5:</b> Normalized emission spectra for <b>PtOEP</b> , <b>RuOEP</b> , <b>PdOEP</b> thin films by exciting them with wavelengths corresponding to absorption peaks.....	<b>140</b>

---

<b>Figure 5.6:</b> 3D representation of intensity of emission as a function of excitation wavelength of <b>PtOEP</b> and <b>PdOEP</b> thin films.....	141
<b>Figure 5.7:</b> Luminescence decays for <b>PtOEP</b> thin film.....	142
<b>Figure 5.8:</b> SHG intensities as a function of rotation angle in p-polarized laser beam (left) and as a dependence of laser polarization (right) of <b>PtOEP</b> thin film.....	143
<b>Figure 5.9:</b> SHG intensities as a function of rotation angle in p-polarized laser beam (left) and as a dependence of laser polarization (right) of <b>RuOEP</b> thin film.....	143
<b>Figure 5.10:</b> SHG intensities as a function of rotation angle in p-polarized laser beam (left) and as a dependence of laser polarization (right) of <b>FeOEP</b> thin film.....	144
<b>Figure 5.11:</b> SHG intensities as a function of rotation angle in p-polarized laser beam (left) and as a dependence of laser polarization (right) of <b>PdOEP</b> thin film.....	144
<b>Figure 5.12:</b> Comparison of SHG intensities for all studied porphyrin complexes in p-polarized laser beam.....	145
<b>Figure 5.13:</b> SHG signal as a function of laser density of studied metalloporphyrin thin films....	146
<b>Figure 5.14:</b> Histogram representing values of second-order nonlinear susceptibilities calculated via theoretical models.....	146
<b>Figure 5.15:</b> THG intensities as a function of incident angle of studied porphyrin complexes in s-polarized laser beam.....	147
<b>Figure 5.16:</b> THG signal as a function of laser density of studied metalloporphyrin thin films....	148
<b>Figure 5.17:</b> Histogram representing values of third-order nonlinear susceptibilities calculated via theoretical models.....	149

<b>Figure 5.18:</b> Normalized OA Z-scan characteristics for porphyrin complexes at different input laser energy.....	151
<b>Figure 5.19:</b> Normalized CA Z-scan characteristics for <b>CHCl<sub>3</sub></b> and <b>PtOEP</b> at input laser energy 2.0 μJ.....	152
<b>Figure 5.20:</b> Values of nonlinear refractive index (left) and nonlinear absorption coefficient (right) as a function of solution concentration of porphyrin complexes in chloroform CHCl <sub>3</sub> .....	152
<b>Figure 5.21:</b> Absorption spectra of 0.5 mM, 0.4 mM, 0.3 mM and 0.2 mM solutions of porphyrin complexes in chloroform CHCl <sub>3</sub> with the marked wavelength of the laser light source (532 nm)..	153

## CHAPTER 6

<b>Figure 6.1:</b> Schematic representation of the studied metallo-supramolecular assemblies.....	159
<b>Figure 6.2:</b> Photographs from optical microscope; a) <b>HelFe</b> ; b) <b>HelCo</b> ; c) <b>HelNi</b> ; d) <b>HelZn</b> ...	159
<b>Figure 6.3:</b> Atomic force microscopy (AFM) images of studied triple stranded helicates thin films: <b>HelFe</b> a) 2-dimensional, b) 3-dimensional; <b>HelCo</b> c) 2-dimensional, d) 3-dimensional; <b>HelNi</b> e) 2-dimensional, f) 3-dimensional; <b>HelZn</b> g) 2-dimensional, h) 3-dimensional.....	161
<b>Figure 6.4:</b> Atomic force microscopy profiles of studied triple stranded helicates.....	162
<b>Figure 6.5:</b> Absorption spectra of studied triple stranded helicates.....	162
<b>Figure 6.6:</b> Photoluminescence spectra and 3D photoluminescence image of triple stranded helicates.....	166
<b>Figure 6.7:</b> Typical luminescence lifetime decays of studied thin films.....	166
<b>Figure 6.8:</b> SHG intensities as a function of rotation angle in p-polarized laser beam (left) and as a dependence of laser polarization (right) of <b>HelFe</b> thin film.....	167

<b>Figure 6.9:</b> SHG intensities as a function of rotation angle in p-polarized laser beam (left) and as a dependence of laser polarization (right) of <b>HelCo</b> thin film.....	167
<b>Figure 6.10:</b> SHG intensities as a function of rotation angle in p-polarized laser beam (left) and as a dependence of laser polarization (right) of <b>HelNi</b> thin film.....	168
<b>Figure 6.11:</b> SHG intensities as a function of rotation angle in p-polarized laser beam (left) and as a dependence of laser polarization (right) of <b>HelZn</b> thin film.....	168
<b>Figure 6.12:</b> SHG signal versus laser density of studied triple stranded helicate thin films.....	169
<b>Figure 6.13:</b> Histogram representing values of second-order nonlinear susceptibilities calculated via theoretical models.....	169
<b>Figure 6.14:</b> THG intensities as a function of incident angle of studied triple stranded helicates in s-polarized laser beam.....	170
<b>Figure 6.15:</b> THG signal versus laser density of studied triple stranded helicate thin films.....	172
<b>Figure 6.16:</b> Histogram representing values of third-order nonlinear susceptibilities calculated via theoretical models.....	172
<b>Figure 6.17:</b> CA Z-scan and OA Z-scan characteristics of ACN and triple stranded helicate complexes concentration 2.3 mM in ACN and laser energy 2.0 $\mu$ J.....	174
<b>Figure 6.18:</b> Values of nonlinear refractive index (left) and nonlinear absorption coefficient (right) as a function of solution concentration of triple stranded helicates in acetonitrile ACN.....	176
<b>Figure 6.19:</b> Absorption spectra of 0.5%, 0.4%, 0.3% and 0.2% solutions of <b>HelFe</b> in acetonitrile ACN with the marked wavelength of the laser light source (532 nm).....	176

<b>Figure 6.20:</b> Electrostatic charge distribution for <b>HelZn</b> - <i>positive</i> (blue) and <i>negative</i> (orange) regions. (b3lyp/6-31++g(d,p)).....	180
---	-----

## CHAPTER 7

<b>Figure 7.1:</b> Chemical structures of <b>PyTK</b> , <b>Py[2]C</b> and <b>PyDFP</b> . The sixth coordination of each zinc metal ion in <b>PyTK</b> and <b>Py[2]C</b> is completed by a TFA or acetate anion, respectively, however TFA and acetate anions are omitted in the structures.....	187
<b>Figure 7.2:</b> Atomic force microscopy (AFM) images of studied <b>PyDFP</b> thin film.....	189
<b>Figure 7.3:</b> Atomic force microscopy (AFM) images of studied <b>PyTK</b> thin film.....	189
<b>Figure 7.4:</b> Atomic force microscopy (AFM) images of studied <b>ZnTK</b> thin film.....	190
<b>Figure 7.5:</b> Atomic force microscopy (AFM) images of studied <b>CdTK</b> thin film.....	190
<b>Figure 7.6:</b> Atomic force microscopy (AFM) images of studied <b>Py[2]C</b> thin film.....	190
<b>Figure 7.7:</b> Atomic force microscopy (AFM) images of studied <b>Zn[2]C</b> thin film.....	191
<b>Figure 7.8:</b> Atomic force microscopy (AFM) images of studied <b>Cd[2]C</b> thin film.....	191
<b>Figure 7.9:</b> UV-Vis absorption spectra of investigated modified pyrene-based guest-host thin films.....	193
<b>Figure 7.10:</b> Photoluminescence spectra and 3D photoluminescence image of <b>PyDFP</b> .....	194
<b>Figure 7.11:</b> Photoluminescence spectra and 3D photoluminescence image of <b>PyTK</b> .....	194
<b>Figure 7.12:</b> Photoluminescence spectra and 3D photoluminescence image of <b>ZnTK</b> .....	195
<b>Figure 7.13:</b> Photoluminescence spectra and 3D photoluminescence image of <b>CdTK</b> .....	195
<b>Figure 7.14:</b> Photoluminescence spectra and 3D photoluminescence image of <b>Py[2]C</b> .....	196



<b>Figure 7.15:</b> Photoluminescence spectra and 3D photoluminescence image of <b>Zn[2]C</b> .....	196
<b>Figure 7.16:</b> Photoluminescence spectra and 3D photoluminescence image of <b>Cd[2]C</b> .....	197
<b>Figure 7.17:</b> Typical luminescence lifetime decays of studied modified pyrene-based complexes.....	197
<b>Figure 7.18:</b> SHG intensities as a function of rotation angle in p-polarized laser beam (left) and as a dependence of laser polarization (right) of <b>PyDFP</b> thin film.....	198
<b>Figure 7.19:</b> SHG intensities as a function of rotation angle in p-polarized laser beam (left) and as a dependence of laser polarization (right) of <b>PyTK</b> thin film.....	198
<b>Figure 7.20:</b> SHG intensities as a function of rotation angle in p-polarized laser beam (left) and as a dependence of laser polarization (right) of <b>ZnTK</b> thin film.....	199
<b>Figure 7.21:</b> SHG intensities as a function of rotation angle in p-polarized laser beam (left) and as a dependence of laser polarization (right) of <b>CdTK</b> thin film.....	199
<b>Figure 7.22:</b> SHG intensities as a function of rotation angle in p-polarized laser beam (left) and as a dependence of laser polarization (right) of <b>Py[2]C</b> thin film.....	200
<b>Figure 7.23:</b> SHG intensities as a function of rotation angle in p-polarized laser beam (left) and as a dependence of laser polarization (right) of <b>Zn[2]C</b> thin film.....	200
<b>Figure 7.24:</b> SHG intensities as a function of rotation angle in p-polarized laser beam (left) and as a dependence of laser polarization (right) of <b>Cd[2]C</b> thin film.....	201
<b>Figure 7.25:</b> Histogram representing values of second-order nonlinear susceptibilities calculated via theoretical models.....	202

<b>Figure 7.26:</b> THG intensities as a function of incident angle of <b>PyDFP</b> thin film in s-polarized (left) and p-polarized (right) laser beam.....	<b>202</b>
<b>Figure 7.27:</b> THG intensities as a function of incident angle of <b>PyTK</b> thin film in s-polarized (left) and p-polarized (right) laser beam.....	<b>203</b>
<b>Figure 7.28:</b> THG intensities as a function of incident angle of <b>ZnTK</b> thin film in s-polarized (left) and p-polarized (right) laser beam.....	<b>203</b>
<b>Figure 7.29:</b> THG intensities as a function of incident angle of <b>CdTK</b> thin film in s-polarized (left) and p-polarized (right) laser beam.....	<b>204</b>
<b>Figure 7.30:</b> THG intensities as a function of incident angle of <b>Py[2]C</b> thin film in s-polarized (left) and p-polarized (right) laser beam.....	<b>204</b>
<b>Figure 7.31:</b> THG intensities as a function of incident angle of <b>Zn[2]C</b> thin film in s-polarized (left) and p-polarized (right) laser beam.....	<b>205</b>
<b>Figure 7.32:</b> THG intensities as a function of incident angle of <b>Cd[2]C</b> thin film in s-polarized (left) and p-polarized (right) laser beam.....	<b>205</b>
<b>Figure 7.33:</b> Histogram representing values of third-order nonlinear susceptibilities calculated via theoretical models.....	<b>206</b>
<b>Figure 7.34:</b> Typical normalized CA Z-scan characteristics for modified pyrene-based complexes and DMSO at laser energy 2.0 $\mu\text{J}$ .....	<b>207</b>
<b>Figure 7.35:</b> Values of nonlinear refractive index as a function of solution concentration of modified pyrene-based complexes in DMSO.....	<b>211</b>

## CHAPTER 8

- Figure 8.1:** SHG intensities in s-polarized and p-polarized laser beam of  $p\text{SiO}_2$ : D1 nanocomposite [8.8].....215
- Figure 8.2:** Photograph presenting nanocomposite consisting of a porphyrin complex with  $\text{Al}_2\text{O}_3$  nanoporous membrane (left) and a guest-host thin film of porphyrin complex in PMMA on glass substrate (right).....215
- Figure 8.3:** SEM image of nanocomposite (left); Schematic representation of a nanocomposite consisting of a nanoporous alumina membrane and supramolecular compound (right).....217
- Figure 8.4:** The process of preparing the nanocomposite. Step 1: Applying the solution to the membrane. Step 2: Absorbing the solution into the nanopores. Step 3: Solvent evaporation. Step 4: Membrane with the material in nanopores.....217
- Figure 8.5:** Lack of SHG response in pure nanoporous  $\text{Al}_2\text{O}_3$  membrane.....218
- Figure 8.6:** Schematic illustration of  $\text{Al}_2\text{O}_3$ :PtOEP nanocomposite.....218
- Figure 8.7:** SHG intensities as a function of rotation angle in s- and p-polarized laser beam (left) and as a dependence of laser polarization (right) of  $\text{Al}_2\text{O}_3$ :PtOEP nanocomposite.....219
- Figure 8.8:** Schematic illustration of  $\text{Al}_2\text{O}_3$ :HelNi nanocomposite.....220
- Figure 8.9:** SHG intensities as a function of rotation angle in s- and p-polarized laser beam (left) and as a dependence of laser polarization (right) of  $\text{Al}_2\text{O}_3$ :HelNi nanocomposite.....221
- Figure 8.10:** Schematic illustration of  $\text{Al}_2\text{O}_3$ :ZnTK nanocomposite.....221
- Figure 8.11:** Schematic illustration of  $\text{Al}_2\text{O}_3$ :Zn[2]C nanocomposite.....222

---

<b>Figure 8.12:</b> SHG intensities as a function of rotation angle in s- and p-polarized laser beam (left) and as a dependence of laser polarization (right) of $\text{Al}_2\text{O}_3:\text{ZnTK}$ nanocomposite.....	222
<b>Figure 8.13:</b> SHG intensities as a function of rotation angle in s- and p-polarized laser beam (left) and as a dependence of laser polarization (right) of $\text{Al}_2\text{O}_3:\text{Zn}[2]\text{C}$ nanocomposite.....	223
<b>Figure 8.14:</b> SHG responses on the $\text{Al}_2\text{O}_3:\text{HeINi}$ nanocomposite surface dependent on polarization.....	224
<b>Figure 8.15:</b> SHG responses on the $\text{Al}_2\text{O}_3:\text{HeINi}$ nanocomposite surface before and after applying corona poling technique.....	225

## LIST OF TABLES

### CHAPTER 1

<b>Table 1.1.</b> Relation between indices $jk/l$ .....	16
---	----

### CHAPTER 4

<b>Table 4.1.</b> Parameters of setup used in SHG/THG measurements.....	111
---	-----

### CHAPTER 5

<b>Table 5.1:</b> Thickness ( $d$ ), roughness ( $R_A$ ), linear refractive index values ( $n$ ) and extinction coefficients ( $\kappa$ ) of porphyrin complexes thin films.....	137
--	-----

<b>Table 5.2:</b> Coefficients determined from absorption spectra of metalloporphyrin thin films.....	140
---	-----

<b>Table 5.3:</b> Values of excitation and emission wavelengths also with fluorescence lifetimes of studied metalloporphyrins.....	142
--	-----

<b>Table 5.4:</b> Values of second-order nonlinear susceptibilities calculated by theoretical models....	147
--	-----

<b>Table 5.5:</b> Values of third-order nonlinear susceptibilities calculated by theoretical models.....	149
--	-----

<b>Table 5.6:</b> Calculated values of NLO refractive index $n_2$ , NLO absorption coefficient $\beta$ , NLO absorption cross section $\sigma$ , real and imaginary part of third order NLO susceptibility $\text{Re}(\chi^{(3)})$ , $\text{Im}(\chi^{(3)})$ of studied porphyrin complexes.....	151
--	-----

<b>Table 5.7:</b> Calculated values of NLO susceptibility $\chi^{(3)}$ obtained from Z-scan data, compared with THG results of studied porphyrin complexes.....	154
---	-----

## CHAPTER 6

<b>Table 6.1:</b> Thickness ( $d$ ), roughness ( $R_A$ ), linear refractive index values ( $n$ ) and extinction coefficients ( $\kappa$ ) of triple stranded helicates thin films.....	<b>162</b>
<b>Table 6.2:</b> Absorption peaks and values of absorption coefficients.....	<b>163</b>
<b>Table 6.3:</b> Excitation, emission peaks and luminescence lifetimes of studied thin films.....	<b>164</b>
<b>Table 6.4:</b> Values of second-order nonlinear susceptibilities calculated by theoretical models....	<b>170</b>
<b>Table 6.5:</b> Values of second-order nonlinear susceptibilities calculated by theoretical models....	<b>171</b>
<b>Table 6.6:</b> Calculated values of NLO refractive index $n_2$ , NLO absorption coefficient $\beta$ , NLO absorption cross section $\sigma$ , real and imaginary part of third order NLO susceptibility $\text{Re}(\chi^{(3)})$ , $\text{Im}(\chi^{(3)})$ of studied triple stranded helicates.....	<b>175</b>
<b>Table 6.7:</b> Calculated values of NLO susceptibility $\chi^{(3)}$ obtained from Z-scan data, compared with THG results of studied triple stranded helicates.....	<b>177</b>
<b>Table 6.8:</b> The computed quantum chemical parameters including: HOMO, LUMO, energy gap ( $E_g$ ) <sub>HOMO-LUMO</sub> , UV-VIS absorption peak position spectra computed applying b3lyp/6-31++g(d,p) methodology and measured for of studied thin films.....	<b>178</b>
<b>Table 6.9:</b> The computed several components of multipole moment (b3lyp/6-31++g(d,p)) <b>HelFe, HelNi, HelZn, HelCo</b> .....	<b>180</b>
<b>Table 6.10:</b> Frontier molecular orbitals of <b>HelFe, HelCo, HelNi, HelZn</b> , calculated at DFT/B3LYP/6-31G+(d,p) basis set level.....	<b>181</b>

<b>Table 6.11:</b> Frequency-dependent: $\beta_{\text{tot}}(-2\omega;\omega,\omega)$ and $\gamma_{\text{tot}}(-3\omega;\omega,\omega,\omega)$ values at $\omega = 0.042827$ a.u., $\lambda = 1064$ nm, for <b>HelFe</b> , <b>HelZn</b> , B3LYP/lanl2DZ and comparison with experimental data $\chi^{(2)}$ and $\chi^{(3)}$ .....	<b>182</b>
--	------------

## CHAPTER 7

<b>Table 7.1:</b> Thickness (d), roughness ( $R_{\Lambda}$ ), linear refractive index values (n) and extinction coefficients ( $\kappa$ ) of modified pyrene-based guest-host thin films.....	<b>191</b>
<b>Table 7.2:</b> Coefficients determined from absorption spectra of modified pyrene-based guest-host thin films.....	<b>193</b>
<b>Table 7.1:</b> Excitation, emission peaks and luminescence lifetimes of studied thin films.....	<b>196</b>
<b>Table 7.4:</b> Values of second-order nonlinear susceptibilities of modified pyrene-based guest-host thin films calculated by theoretical models.....	<b>201</b>
<b>Table 7.5:</b> Values of third-order nonlinear susceptibilities calculated by theoretical models.....	<b>206</b>
<b>Table 7.6:</b> Calculated values of NLO refractive index $n_2$ , real part and total value of third order NLO susceptibility $\text{Re}(\chi^{(3)})$ , $\chi^{(3)}$ of modified pyrene-based complexes in DMSO.....	<b>209</b>
<b>Table 7.7:</b> Calculated values of NLO susceptibility $\chi^{(3)}$ obtained from Z-scan data, compared with THG results of studied modified pyrene-based complexes.....	<b>210</b>

## CHAPTER 8

<b>Table 8.1:</b> Comparison the advantages and disadvantages of guest-host thin films with nanoporous membranes.....	<b>216</b>
---	------------

---

**LIST OF PUBLICATIONS**

1. M. Lougdali, M. Zazoui, Y. Abboud, A. EL Bouari, A. Zawadzka, P. Plociennik, J. Strzelecki, K. Strzalkowski, A. Migalska-Zalas, **K. Waszkowska**, B. Sahraoui, Y. El kouari. Linear and nonlinear optical properties of Manganese bis-(8- hydroxyquinoline) thin films for optoelectronic devices: experimental and computational studies. *Journal of Molecular Structure*, 131558, **2021**. In Press. <https://doi.org/10.1016/j.molstruc.2021.131558>
2. D. Guichaoua, I. Syvorotka, I. Solskii, N. Syvorotka, **K. Waszkowska**, A. Andrushchak, B. Sahraoui. Specific complex-oxide crystals with strong nonlinear absorption and nonlinear refraction as promising optical materials. *Optical Materials* 112 (2021) 111493 <https://doi.org/10.1016/j.optmat.2021.111493>
3. **K. Waszkowska**, T. Chtouki, O. Krupka, V. Smokal, V. Figà, B. Sahraoui. Effect of UV-Irradiation and ZnO Nanoparticles on Nonlinear Optical Response of Specific Photochromic Polymers. *Nanomaterials* **2021**, 11(2), 492. <https://doi.org/10.3390/nano11020492>
4. **K. Waszkowska**, P. Josse, C. Cabanetos, P. Blanchard, B. Sahraoui, D. Guichaoua, I. Syvorotka, O. Kityk, R. Wielgosz, P. Huber, A. V. Kityk. Anisotropic Confinement of Chromophores Induces Second-Order Nonlinear Optics in Nanoporous Photonic Metamaterial. *Optics Letters* Vol. 46, Issue 4, pp. 845-848 (2021). <https://doi.org/10.1364/OL.416948>
5. **K. Waszkowska**, Y. Cheret, A. Zawadzka, A. Korcala, J. Strzelecki, A. El-Ghayoury, A. Migalska-Zalas, B. Sahraoui. Photoluminescence and nonlinear optical properties of triple stranded helicates based metallo-supramolecular architectures. *Dyes and Pigments*, 186 (2021) 109036. <https://doi.org/10.1016/j.dyepig.2020.109036>



6. H. Belahlou, **K. Waszkowska**, A. Bouraiou, El Bendeif, S. Taboukhat, K. Bouchouit, B. Sahraoui. New architecture of organo electronic chalcones derivatives: Synthesis, crystal structures and optical properties. *Optical Materials*, 108 (2020) 110188.  
<https://doi.org/10.1016/j.optmat.2020.110188>
7. S. Taboukhat, N. Kichou, J.-L. Fillaut, O. Alévêque, **K. Waszkowska**, A. Zawadzka, A. El-Ghayoury, A. Migalska-Zalas, B. Sahraoui. Transition metals induce control of enhanced NLO properties of functionalized organometallic complexes under laser modulations. *Scientific Reports* 10, 15292 (2020). <https://doi.org/10.1038/s41598-020-71769-2>
8. B. Kulyk, **K. Waszkowska**, A. Busseau, C. Villegasm P. Hudhomme, S. Dabos-Seignon, A. Zawadzka, S. Legoupy, B. Sahraoui. Penta(zinc porphyrin)[60]fullerenes: Strong reverse saturable absorption for optical limiting applications. *Applied Surface Science*, 533 (2020) 147468. <https://doi.org/10.1016/j.apsusc.2020.147468>
9. L. Mydlova, S. Taboukhat, **K. Waszkowska**, N. Ibrahim, A. Migalska-Zalas, B. Sahraoui, P. Frère, M. Makowska-Janusik. Selected molecules based on (-1-cyanovinyl)benzonitrile as new materials for NLO applications — Experimental and computational studies. *Journal of Molecular Liquids*, 314 (2020) 113622. <https://doi.org/10.1016/j.molliq.2020.113622>
10. **K. Waszkowska**, O. Krupka, O. Kharchenko, V. Figà, V. Smokal, N. Kutsevov, B. Sahraoui. Influence of ZnO nanoparticles on nonlinear optical properties. *Applied Nanoscience* 10, 4977–4982 (2020). <https://doi.org/10.1007/s13204-020-01373-3>
11. A. Aamoum, **K. Waszkowska**, S. Taboukhat, P. Plóciennik, M. Bakasse, Y. Boughaleb, J. Strzelecki, A. Korcala, Z. Sofiani, A. Zawadzka. Time-resolved photoluminescence and optical properties of a specific organic azo dye. *Optical and Quantum Electronics* 52, 35 (2020).  
<https://doi.org/10.1007/s11082-019-2147-7>
12. A. Migalska-Zalas, **K. Waszkowska**, B. Morzyk-Ociepa, B. Sahraoui. The role of d-electron metal ions complexation on the nonlinear-optical parameters of new trans-

dichloropalladium(II) complex. *Molecular Crystals and Liquid Crystals*, 695(1), 2019.

<https://doi.org/10.1080/15421406.2020.1723910>

13. A. Zawadzka, **K. Waszkowska**, A. Karakas, P. Plóciennik, A. Korcala, K. Wiśniewski, M. Karakaya, B. Sahraoui. Diagnostic and control of linear and nonlinear optical effects in selected self-assembled metallophthalocyanine chlorides nanostructures. *Dyes and Pigments*, 157 (2018), 151-162. <https://doi.org/10.1016/j.dyepig.2018.04.048>

---

## LIST OF COMMUNICATIONS

### CONFERENCE PAPERS

1. **K. Waszkowska**, R. Wielgosz, T. Travers, M. Lelonek, P. Göring, D. Gindre, B. Sahraoui. Second-Order Nonlinear Optical Response of Ba(NO<sub>3</sub>)<sub>2</sub>/Al<sub>2</sub>O<sub>3</sub> Nanocomposite. 22<sup>nd</sup> International Conference on Transparent Optical Networks (ICTON), Bari, Italy, **2020**, pp. 1-4, <https://doi.org/10.1109/ICTON51198.2020.9203228>
2. **K. Waszkowska**, D. Guichaoua, J. Jędryka, I. Syvorotka, N. Y. Syvorotka, A. V. Kityk; B. Sahraoui. Second- and Third-Order Nonlinear Optical Response of Perovskite LiTaO<sub>3</sub>. 22<sup>nd</sup> International Conference on Transparent Optical Networks (ICTON), Bari, Italy, **2020**, pp. 1-4. <https://doi.org/10.1109/ICTON51198.2020.9203454>
3. D. Guichaoua, R. Wielgosz, **K. Waszkowska**, K. El Korchi, B. Sahraoui. Luminescence Properties of Praseodymium-Doped Crystals. 21<sup>st</sup> International Conference on Transparent Optical Networks (ICTON), Angers, France, **2019**, pp. 1-4. <https://doi.org/10.1109/ICTON.2019.8839996>
4. **K. Waszkowska**, K. El Korchi, D. Guichaoua, A. Zawadzka, B. Sahraoui. Influence of Polymer Matrix on Nonlinear Optical Response in Octaethylporphine Palladium Derivative Thin Films. 2019 21st International Conference on Transparent Optical Networks (ICTON), Angers, France, **2019**, pp. 1-4. <https://doi.org/10.1109/ICTON.2019.8840459>
5. **K. Waszkowska**, O. Krupka, V. Smokal, O. Kharchenko, D. Guichaoua, B. Sahraoui. Third Harmonic Generation in Spin-Coated Styrylquinoline Based Polymer Thin Films. 21<sup>st</sup> International Conference on Transparent Optical Networks (ICTON), Angers, France, **2019**, pp. 1-4. <https://doi.org/10.1109/ICTON.2019.8840185>
6. S. Abed, H. Djaaboube, **K. Waszkowska**, K. El Korchi, R. Aouati, A. Bouabellou. Third Order Nonlinear Optical Properties of MgO Doped Co Thin Films by Dip Coating Technique. 21<sup>st</sup>

- International Conference on Transparent Optical Networks (ICTON), Angers, France, **2019**, pp. 1-4. <https://doi.org/10.1109/ICTON.2019.8840172>
7. **K. Waszkowska**, S. Slassi, A. Amine, A. El-Ghayoury, B. Sahraoui. Third Harmonic Generation of Azo-Based Thin Films. 20<sup>th</sup> International Conference on Transparent Optical Networks (ICTON), Bucharest, **2018**, pp. 1-4. <https://doi.org/10.1109/ICTON.2018.8473818>
  8. D. Guichaoua, **K. Waszkowska**, V. Smokal, O. Kharchenko, B. Kulyk, O. Krupka, A. Migalska-Zalas, B. Sahraoui. Functionalized Methacrylic Thiazolidinone Polymer for Optical Applications. 20<sup>th</sup> International Conference on Transparent Optical Networks (ICTON), Bucharest, **2018**, pp. 1-4. <https://doi.org/10.1109/ICTON.2018.8473860>
  9. A. Zawadzka, P. Plóciennik, **K. Waszkowska**, D. Guichaoua, B. Sahraoui. Nonlinear Optical Properties of Oxide Thin Films. 20<sup>th</sup> International Conference on Transparent Optical Networks (ICTON), Bucharest, **2018**, pp. 1-3. <https://doi.org/10.1109/ICTON.2018.8473614>
  10. **K. Waszkowska**, B. Kulyk, D. Guichaoua, A. Ayadi, A. El-Ghayoury, A. Zawadzka, B. Sahraoui. Effect of UV irradiation on nonlinear optical response of azo-based iminopyridine rhenium complexes. 2017 19<sup>th</sup> International Conference on Transparent Optical Networks (ICTON), Girona, **2017**, pp. 1-3. <https://doi.org/10.1109/ICTON.2017.8024899>
  11. **K. Waszkowska**, A. Zawadzka, B. Sahraoui. Diagnostic on nonlinear optical response of neodymium (III) oxide thin films. 19<sup>th</sup> International Conference on Transparent Optical Networks (ICTON), Girona, 2017, pp. 1-3. <https://doi.org/10.1109/ICTON.2017.8025110>
  12. A. Zawadzka, P. Plóciennik, **K. Waszkowska**, Z. Masewicz, A. Aamoum, J. Strzelecki, A. Korcala, B. Sahraoui. Physical Vapor Deposition technique and its application to thin organometallic films. 19<sup>th</sup> International Conference on Transparent Optical Networks (ICTON), Girona, **2017**, pp. 1-3. <https://doi.org/10.1109/ICTON.2017.8024901>

## ORAL PRESENTATIONS

1. **K. Waszkowska**, A. Zawadzka, B. Sahraoui. Metalloporphyrins as supramolecular models with potential application in nonlinear optics. 4<sup>th</sup> International Conference on Science & Engineering of Materials (ICSEM 2021), Greater Noida, India, **2021**.  
(Best oral presentation award)
2. **K. Waszkowska**, R. Wielgosz, T. Travers, M. Lelonek, P. Göring, D. Gindre, B. Sahraoui. Second-Order Nonlinear Optical Response of Ba(NO<sub>3</sub>)<sub>2</sub>/Al<sub>2</sub>O<sub>3</sub> Nanocomposite. 22<sup>nd</sup> International Conference on Transparent Optical Networks (ICTON), Bari, Italy, **2020**.
3. **K. Waszkowska**, P. Josse, C. Cabanetos, P. Blanchard, B. Sahraoui, D. Guichaoua, I. Syvorotka, O. Kityk, R. Wielgosz, P. Huber, A. V. Kityk. Optical nonlinearity of chromophores induced by geometrical field in nanochannels. 1<sup>st</sup> International Conference on Innovative Materials and Nanoengineering (IMNE'2019), Brenna, Poland, **2019**.
4. **K. Waszkowska**, Y. Cheret, A. El-Ghayoury, A. Zawadzka, B. Sahraoui. Design and elaboration of new multifunctional (supra)molecular architectures for nonlinear optical applications. XIV International Workshop Nonlinear Optical Applications (NOA), Wrocław, Poland, **2018**.

**POSTERS**

1. **K. Waszkowska**, D. Guichaoua, J. Jędryka, I. Syvorotka, N. Y. Syvorotka, A. V. Kityk; B. Sahraoui. Second- and Third-Order Nonlinear Optical Response of Perovskite  $\text{LiTaO}_3$ . 22<sup>nd</sup> International Conference on Transparent Optical Networks (ICTON), Bari, Italy, **2020**.
2. D. Guichaoua, R. Wielgosz, **K. Waszkowska**, K. El Korchi, B. Sahraoui. Luminescence Properties of Praseodymium-Doped Crystals. 21<sup>st</sup> International Conference on Transparent Optical Networks (ICTON), Angers, France, **2019**.
3. **K. Waszkowska**, K. El Korchi, D. Guichaoua, A. Zawadzka, B. Sahraoui. Influence of Polymer Matrix on Nonlinear Optical Response in Octaethylporphine Palladium Derivative Thin Films. 21<sup>st</sup> International Conference on Transparent Optical Networks (ICTON), Angers, France, **2019**.
4. **K. Waszkowska**, O. Krupka, V. Smokal, O. Kharchenko, D. Guichaoua, B. Sahraoui. Third Harmonic Generation in Spin-Coated Styrylquinoline Based Polymer Thin Films. 21<sup>st</sup> International Conference on Transparent Optical Networks (ICTON), Angers, France, **2019**.
5. S. Abed, H. Djaaboube, **K. Waszkowska**, K. El Korchi, R. Aouati, A. Bouabellou. Third Order Nonlinear Optical Properties of MgO Doped Co Thin Films by Dip Coating Technique. 21<sup>st</sup> International Conference on Transparent Optical Networks (ICTON), Angers, France, **2019**.
6. **K. Waszkowska**, B. Sahraoui. Diagnostic on nonlinear optical response of some selected supramolecular systems. Journée de l'Ecole doctorale 3M (JED) 2019-Brest, Brest, France **2019**.
7. **K. Waszkowska**, Y. Cheret, A. El-Ghayoury, A. Zawadzka, B. Sahraoui. Diagnostic of linear and nonlinear optical properties of some specific metallo-supramolecular thin films based on triple helicate. Journée de l'Ecole doctorale 3M (JED) 2018-Le Mans, Le Mans, France, **2018**.

8. **K. Waszkowska**, A. Zawadzka, B. Sahraoui. Diagnostic on nonlinear optical response of neodymium (III) oxide thin films. 19<sup>th</sup> International Conference on Transparent Optical Networks (ICTON), Girona, **2017**.





**Titre :** Etude et diagnostic des propriétés physicochimique de nouvelles architectures (métallo)supramoléculaires  $\pi$ -conjugués pour l'optique non linéaire.

**Mots clés :** optique non linéaire ; chimie supramoléculaire ; caractérisation des matériaux ; membranes nanoporeuses ; porphyrines ; triple hélicates ; complexes à base de pyrène ;

**Résumé :** Grâce aux propriétés physico-chimiques extraordinaires des assemblages supramoléculaires en général et des architectures (métallo)supramoléculaires  $\pi$ -conjugués en particulier sont de bons candidats pour l'optique non linéaire. Ce travail porte sur les propriétés optiques linéaires (incluant l'absorption UV-visible et la photoluminescence) de trois différents groupes de complexes supramoléculaires tels que les complexes métallo-porphyrines, les métallohélicates et les nœuds moléculaires, ainsi que sur leurs applications potentielles dans les dispositifs optoélectroniques. Les propriétés optiques de ces nouvelles architectures (métallo)supramoléculaires  $\pi$ -conjuguées ont été étudiées. Les études de la génération de la deuxième et troisième harmonique ont été réalisées sur la base des « franges de Maker » qui sont des techniques fiables et bien connues, ainsi que les intensités de SHG et THG en fonction de l'énergie laser incidente ont été étudiées. En outre nous avons obtenu une augmentation des

réponses optiques non linéaires (absorptions et réfractions) par le biais de la technique Z-scan. Les composés de type complexe de porphyrines, les triples hélices ainsi que les nœuds moléculaires fonctionnalisés par des pyrènes présentent des réponses optiques linéaires et non linéaires du troisième ordre très intéressantes et très prometteuses qui sont modulées par la nature du cation métallique utilisé dans les interactions métal/ligand. De plus, dans ce travail nous avons étudié l'influence de l'incorporation des assemblages métallo-supramoléculaires étudiés présentant la meilleure réponse ONL dans des membranes nanoporeuses innovantes sur la génération du second harmonique. Ainsi, les métallo-porphyrines, les triples hélices ainsi que les nœuds moléculaires contenant du pyrène ont été introduit dans les nanopores de la membrane  $Al_2O_3$ . Les premiers résultats obtenus sont très prometteurs en vue d'applications dans le domaine de la nanophotonique.

**Title :** Study and diagnostic of the physicochemical properties of new  $\pi$ -conjugated (metallo)supramolecular architectures for nonlinear optics.

**Keywords :** nonlinear optics ; supramolecular chemistry ; material characterization ; nanoporous membranes ; porphyrins ; triple helicates ; pyrene-based complexes ;

**Abstract :** Due to extraordinary physicochemical properties of the  $\pi$ -conjugated supramolecular assemblies in general and the metallosupramolecular architectures in particular are good candidates for nonlinear optical applications. The present work presents original studies of linear (including UV-visible absorption and photoluminescence) on three selected specific groups of metallosupramolecular complexes, as well as their potential nonlinear optical applications. Therefore, nonlinear optical properties of  $\pi$ -conjugated metallohelicates, knots and metalloporphyrins nonlinear have been investigated. The second and third harmonic generation are provided on the basis of the well-known Maker fringe method, as well as the intensities of SHG and THG versus laser energy are examined. Furthermore, the enhanced NLO absorption and refraction responses are obtained by means of Z-scan technique.

The investigated compounds of metalloporphyrines, similarly to triple stranded helicates and modified pyrene-based molecular knots, are characterized by large enhanced nonlinear effect both during the studies with the Maker fringe technique and with the Z-scan technique. The observed NLO properties, mainly depend on the used metal cation in these metallosupramolecular architectures. Moreover, in this work we studied the influence of the incorporation of the best NLO supramolecular complexes (investigated in this thesis) in innovative nanoporous membranes on the generation of the second harmonic (SHG). Thus, metalloporphyrins, triple stranded metallohelicates and the modified pyrene-based knots were introduced into nanopores of the  $Al_2O_3$  membranes. The first obtained results are very promising in terms of applications in the field of nanophotonics.